UMTRI-2001-07

Project D.7
Design, Development, and Testing of a New Pregnant Abdomen for the Hybrid III Small Female Crash Test Dummy

Final Report

University of Michigan Transportation Research Institute

Jonathan D. Rupp
Lawrence W. Schneider
Kathleen DeSantis Klinich

First Technology Safety Systems

Steve Moss
Jennifer Zhou

University of Michigan Medical School

Mark D. Pearlman

Submitted to General Motors and the National Highway Traffic Safety Administration
March, 2001

This file has been superceded.
See the file named 94356_rev2007.pdf in Deep Blue at http://hdl.handle.net/2027.42/1349.
Correction appears on page 101 of the report. The equation at the top of the page has been replaced with the following:

$\theta = 0.0021 P^{2.2512}$

This note added 02 October 2007.

Technical Report Documentation Page

1. Report No.	2. Government Accession No.	3. Recipient's Catalog No.
UMTRI-2001-07		

4. Title and Subtitle	5. Report Date
Design, Development, and Testing of a New Pregnant Abdomen for the Small Female Hybrid III Crash Test Dummy[1]	March 2001
	6. Performing Organization Code

7. Author(s)	8. Performing Organization Report No.
Rupp, J.D.[2], Schneider, L.W.[2], Klinich, K.D.[2], Moss, S.[3], Zhou, J.[3], and Pearlman, M.D.[4]	UMTRI-2001-07

9. Performing Organization Name and Address	10. Work Unit no. (TRAIS)
The University of Michigan Transportation Research Institute 2901 Baxter Road Ann Arbor, Michigan 48109-2150 U.S.A.	11. Contract or Grant No.

12. Sponsoring Agency Name and Address	13. Type of Report and Period Covered
General Motors Corporation 30500 Mound Rd. Warren, MI 48090-9055	Final Report
	14. Sponsoring Agency Code

15. Supplementary Notes

[1]The work covered by this report was financed by General Motors (GM) pursuant to an agreement with the U.S. Department of Transportation.
[2]University of Michigan Transportation Research Institute, Ann Arbor, Michigan
[3]First Technology Safety Systems, Plymouth, Michigan
[4]University of Michigan Medical School, Ann Arbor, Michigan

16. Abstract

A new prototype pregnant abdomen for the Hybrid III small-female ATD has been developed and evaluated in a series of component and whole-dummy tests. The new abdomen uses a fluid-filled silicone-rubber bladder to represent the uterus at 30-weeks gestation, and incorporates improved anthropometry with a midline contour that is more representative of the pregnant abdomen than that of the first pregnant dummy. The new abdomen has been designed with more humanlike mechanical response to dynamic rigid-bar, belt, and close-proximity airbag loading. An effort was made to instrument the fluid-filled abdomen to assess for the likelihood of fetal loss through two injury mechanisms that are believed to be the most likely causes of placental abruption in motor-vehicle crashes. Although the instrumentation problems could not be fully resolved within the time and funding constraints of the current program, the results obtained offer promise to future development efforts. The risk of fetal loss in the final prototype pregnant dummy, or MAMA-2B (Maternal Anthropomorphic Measurement Apparatus, version 2B) is determined by measuring the anterior pressure within the fluid-filled bladder. Peak internal bladder pressures measured in series of sled-test simulations of frontal crashes of different severities and occupant-restraint conditions have been correlated to the likelihood of fetal loss based on fetal-loss risk curves developed from real-world crash investigations.

17. Key Words	18. Distribution Statement
Trauma in pregnancy, fetal loss, Anthropomorphic Test Device, crash test dummy, pregnant abdomen, abdominal response, placental abruption	Unlimited

19. Security Classification (of this report)	20. Security Classi. (of this page)	21. No. of Pages	22. Price
None	None	205	

ACKNOWLEDGEMENTS

The research described in this report was financed by General Motors (GM) pursuant to an agreement between GM and the U.S. Department of Transportation.

The authors gratefully acknowledge the contributions of Steve Rouhana, Ali Elhagediab, and Tony Walbridge whose pioneering work in the development of a new fluid-filled silicon abdomen for the mid-size male Hybrid III ATD provided an invaluable resource for the current effort. Appreciation is also expressed to James Ashton-Miller and Laura Cowan, who provided information on the biomechanical properties of uterine and placenta tissue, and to Dave Smith for the fabrication of prototype abdomen components. Finally, the authors would like to thank several of the UMTRI staff for their engineering and technical assistance throughout the project. These include Monica Prasad, who spent long hours digitizing film and making plots, Warren Hardy, who assisted with many of the test and instrumentation problems; Miriam Manary, who assisted with the sled impact tests; and Brian Eby, Stewart Simonett, and Charles Bradley who provided invaluable technical, instrumentation, and fabrication support through the design, development, and testing phases of this program.

TABLE OF CONTENTS

ACKNOWLEDGEMENTS V

TABLE OF CONTENTS VII

TABLE OF FIGURES XI

LIST OF TABLES XVII

1.0 EXECUTIVE SUMMARY 1

2.0 INTRODUCTION 5

3.0 BACKGROUND 7

3.1 ANATOMY OF THE PREGNANT ABDOMEN 7

3.2 INJURIES UNIQUE TO PREGNANT OCCUPANTS IN MOTOR-VEHICLE CRASHES 8

3.3 RESTRAINT TESTING WITH PREGNANT ANIMALS 9

3.4 THE FIRST PREGNANT DUMMY 11

3.5 IMPACT RESPONSE OF THE ABDOMEN 12

3.5.1 Abdominal Response from Animal Tests 13

3.5.2 Results from Human Cadaver Tests 13

3.5.2.1 ABDOMEN RESPONSE TO RIGID IMPACTORS 13

3.5.2.2 ABDOMINAL RESPONSE TO BELT LOADING 16

3.5.2.3 OUT-OF-POSITION ABDOMINAL RESPONSE TO SURROGATE AIRBAG LOADING 17

3.6 FETAL INJURY RISK FROM CRASH INVESTIGATIONS 18

4.0 HYPOTHESIZED MECHANISMS OF PLACENTAL ABRUPTION 21

4.1 OVERVIEW OF INJURY TYPES 21

4.2 TISSUE TESTING TO DETERMINE CRITICAL STRAINS FOR PLACENTAL ABRUPTION 22

4.3 INVESTIGATION OF MECHANISMS OF PLACENTAL ABRUPTION 24

4.3.1 Fetus-Placenta Interaction 25

4.3.2 Inertial loading of the UPI by the Placenta 26

4.3.3 Shear Strains at the UPI due to Pressure-Induced Circumferential Strains in the Uterus 27

4.3.4 Tensile Loading at the UPI due to Pressure Gradients Generated by the Inertia of the Amniotic Fluid 29

4.3.5 Shear Strains in the UPI from Local Curvature Changes in the Uterus Due to Direct Loading of the Abdomen 31

4.4 LIKELY HYPOTHESIZED INJURY MECHANISMS 32

5.0 DESIGN SPECIFICATIONS 35

5.1 DESIGN GOALS AND CONSTRAINTS 35

5.2 ANTHROPOMETRY 35

5.2.1 Summary of Seated Anthropometry During Pregnancy 36

5.2.2 Selection of MAMA-2B External Contour from Anthropometric Data 40
5.2.3 Dummy Mass 41

5.3 RESPONSE CORRIDORS FOR THE NEW PREGNANT ABDOMEN 42

6.0 ABDOMEN DESIGN AND DEVELOPMENT 45

6.1 DESIGN APPROACH 45

6.2 FITTING THE PREGNANT ABDOMEN INTO THE SMALL-FEMALE HYBRID III ATD 46

6.3 EARLY DEVELOPMENT OF THE UTERINE COMPONENT 48

6.4 DUMMY MASS 51

6.5 CHEST JACKET AND BREAST DESIGN 51

6.6 TESTING AND DEVELOPMENT OF THE NEW PREGNANT ABDOMEN 52
6.6.1 Test Methods 52
6.6.1.1 RIGID-BAR IMPACT 52
6.6.1.2 DYNAMIC BELT-LOADING 53
6.6.1.3 INERTIAL LOADING 54
6.6.1.4 OUT-OF-POSITION AIRBAG LOADING 55
6.6.1.5 SLED TESTS 56
6.6.2 Evaluation and Further Development of the Pregnant Abdomen 56

6.7 SUMMARY OF MAMA-2B ABDOMINAL COMPONENT RESPONSE 71

7.0 INSTRUMENTATION DEVELOPMENT 75

7.1 INSTRUMENTATION OVERVIEW 75

7.2 MEASUREMENT OF BLADDER CURVATURE 77
7.2.1 Shape Tape Theory 78
7.2.2 Performance of Shape Tape in Quasi-Static Testing 79
7.2.3 Performance of Shape Tape in Rigid-Bar Impacts 83
7.2.4 Performance of Shape Tape for Out-of-Position Airbag Loading 85
7.2.5 Performance of Shape Tape in Full-Dummy Testing 87
7.2.6 Further Development of Shape Tape Transducer 89
7.2.7 Conclusions from Shape Tape Testing 91

7.3 MEASUREMENT OF INTERNAL BLADDER PRESSURES 92
7.3.1 Pressure Measurements from Rigid-Bar, Belt-Loading, and Bladder-Only Sled Tests 93
7.3.2 Pressure Measurements in Full Dummy Sled Tests 95

7.4 FINAL MAMA-2B INSTRUMENTATION 96

8.0 INJURY CRITERIA 97

8.1 OVERVIEW OF INJURY CRITERIA DEVELOPMENT 97

8.2 PRELIMINARY DEVELOPMENT OF PLACENTAL ABRUPTION THRESHOLDS FOR THE MAMA-2B 97

8.3 ALTERNATIVE METHOD OF INJURY PREDICTION BASED ON THE RISK OF FETAL LOSS IN MVC 98

8.4 REPEATABILITY OF INJURY PREDICTION 103

9.0 SUMMARY AND DISCUSSION 107

10.0 REFERENCES 111

APPENDIX A 115

EQUAL-STRESS, EQUAL-VELOCITY SCALING AS APPLIED TO THE PREGNANT DUMMY 115

APPENDIX B: PLOTS OF RELEVANT TEST SIGNALS 119

TABLE OF FIGURES

Figure 1. Anatomy of pregnant abdomen 7

Figure 2. Schematic of the structure of the utero-placental interface. 8

Figure 3. Pressure response from animal testing. Adapted from Crosby et al. (1968). 10

Figure 4. Original pregnant abdomen installed in pregnant dummy pelvis (right) and separated into fetal component, urethane casing, and urethane uterus (left). 12

Figure 5. Comparison of the 10 m/s Cavanaugh rigid-bar corridor and reanalyzed Nusholtz, Viano, and Stalnaker data. 15

Figure 6. Comparison of the 6 m/s Cavanaugh rigid-bar corridor and reanalyzed Nusholtz, Viano, Stalnaker, and Rouhana data. 15

Figure 7. Comparison of the 10 and 6 m/s rigid-bar Cavanaugh Corridors to the 3 m/s averaged response developed by Hardy et al. (2001). 16

Figure 8. Belt-loading corridor developed by Hardy et al. (2001). 17

Figure 9. Out-of-position airbag-loading corridor developed by Hardy et al. (2001). 18

Figure 10. Logistic regressions for adverse fetal outcome as a function of crash severity, for properly restrained (i.e., three-point belt or airbag and three-point belt) and improperly restrained (unbelted, airbag only, or shoulder belt only). Based on data from Klinich et al. (1999). 19

Figure 11. Shear testing of placenta, uterus, and UPI to determine UPI failure stresses and strains (from Ashton-Miller, unpublished). 23

Figure 12. Deformed state of FEM simulation (left) and physical uniaxial tensile testing (right) of intact uterus, placenta, and uteroplacental interface (Ashton-Miller, unpublished). 23

Figure 13. FE model of ellipsoid uterus with fetus comprised of solid elements in undeformed state (left) and deformed state during a simulated drop onto flat plate (right). 26

Figure 14. Spherical uterus model with placenta (shaded) used to study the effects of varying placental location on shear stress in the UPI under impact loading in an A-P direction. 27

Figure 15. Result from tensile testing of uterus (denoted 'UTExx') and placenta samples (denoted 'PLAxx') performed by Pearlman et al. (1999). 29

Figure 16. Stresses developed in FEM of human uterus under inertial loading conditions. 31

Figure 17. Direct loading of FEM uterus by 2.54 cm diameter hemispherical impactor. 32

Figure 18. Stress distribution in FEM of uterus after impact with hemispherical impactor. 32

Figure 19. Abdomen depth vs. stature (r=0.126) from Klinich et al. (1999). 37

Figure 20. Fundal height vs. stature (r=0.000) from Klinich et al. (1999). 37

Figure 21. Abdomen circumference vs. stature (r = 0.114) from Klinich et al. (1999). 38

Figure 22. Composite plot of average abdomen contours from the third test session. Lines connect points along the mid-sagittal contour of the abdomen from supersternale to pubic symphysis as well as from pubic symphysis to fundus. From Klinich et al. (1999). 39

Figure 23. Comparison of mean abdomen contours for the four analysis methods from Klinich et al. (1999). 40

Figure 24. Comparison of the midline abdomen contour for the new abdomen to that of the first pregnant dummy. From Klinich et al. (1999). 41

Figure 25. 6 m/s rigid bar loading corridor and 3 m/s averaged response scaled to the pregnant dummy mass using equal-stress, equal-velocity scaling. 43

Figure 26. Initial and modified belt-loading corridors developed by Hardy et al. (2001). Both corridors are scaled to the pregnant dummy mass of 58 kg from the reference mass used to develop the corridors (76 kg) using equal-stress, equal-velocity scaling (Eppinger, 1976). This allowed force-deflection responses of the new pregnant abdomen to be plotted in unscaled format..... 44

Figure 27. FEM showing geometry of modified Hybrid III ribcage. Stiffener plate runs from the sternum plate along the anterior and medial edges of the ribs..... 46

Figure 28. Comparison of FEM simulated responses to the 6.7 m/s pendulum calibration tests of the standard and modified small female ribcages. 47

Figure 29. Modified Hybrid III ribcage with spring-steel stiffeners connecting the ends of ribs 4 through 6 on each side (redesigned sternum plate not shown)..... 47

Figure 30. Force-deflection response for the modified and standard small-female ribcage to 6.7 m/s pendulum calibration tests. 48

Figure 31. Clay model of a 30-week uterus in small-female dummy with ribs 4 to 6 removed. Cardboard cutout provides abdomen midline contour based on results from Klinich et al. (1999)..... 49

Figure 32. Standard Hybrid III small-female pelvis (left) and first pregnant dummy pelvis (right). 49

Figure 33. Computer model of first prototype bladder and attachment cradles. 50

Figure 34. FEM of prototype uterus installed in dummy showing upper and lower mounting "cradles."..... 50

Figure 35. Photo of new pregnant dummy with neoprene jacket..... 52

Figure 36. Ballistic pendulum impact test setup. 53

Figure 37. Setup for dynamic belt-loading tests. Lines added to illustrate string pot and belt outline. 54

Figure 38. Sled test setup for inertial loading of prototype abdomen showing bladder prior to impact (left) and bladder with jacket material at maximum distention (right). 55

Figure 39. Test setup for surrogate airbag tests showing a side view of the cylindrical impactor (right) and the new pregnant abdomen (center)..... 56

Figure 40. Flow chart of bladder development process..... 60

Figure 41. Side view of urethane bladder showing attachment of upper and lower cradles..... 61

Figure 42. FEM showing side view of pregnant dummy with first prototype attachment cradles. 61

Figure 43. Force-deflection response to rigid-bar impact of Bladder 1 (25-durometer urethane bladder with rigid upper and full-profile lower-mounting cradles) at 6 m/s relative to scaled 6 m/s Cavanaugh corridor. 62

Figure 44. Force-deflection response to rigid-bar impact of Bladder 2 (30-durometer urethane bladder with soft upper and full-profile lower-mounting cradles) at 3 m/s relative to 3 m/s averaged cadaver response. 63

Figure 45. Bladder 2 failure due to shear at lower-mounting cradle during 6-m/s rigid-bar impact. 63

Figure 46. Force-deflection response of Bladder 3 (25-durometer urethane bladder with soft upper and partially reduced-profile lower-mounting cradles). All tests were conducted with the chest jacket except the 2.2 m/s impact..... 64

Figure 47. Belt loading response of Bladder 4 (30-durometer urethane bladder) with soft upper and reduced-profile lower-mounting cradles relative to scaled 3 m/s cadaver belt loading corridors (from Hardy, 2000). 65

Figure 48. Failure of Bladder 4 due to high strains near lower-mounting cradles during rigid-bar impact.... 65

Figure 49. Inertial loading of Bladder 5 (35-Durometer urethane) showing gross distention of the bladder under a 20-g deceleration..... 66

Figure 50. Force-deflection response of Bladder 6 (40-durometer silicone rubber) to belt loading in test GMP9919 relative to scaled 3 m/s belt loading corridor. 66

Figure 51. Force-deflection response of Bladder 6 (40-durometer silicone rubber) to rigid-bar loading from tests GMP9921-24 shown relative to scaled 6 m/s Cavanaugh Corridors and average 3 m/s average cadaver response. 67

Figure 52. Bladder 6 (40-durometer silicone rubber) with inextensible wrap 68

Figure 53. Bladder 6 (40-durometer silicone rubber) response to rigid-bar impacts with and without inextensible wrap relative to scaled 6 m/s Cavanaugh Corridor. 68

Figure 54. Force-deflection responses to rigid-bar impacts of Bladder 7 (thicker 40-durometer silicone rubber) in tests GMP9932-34 relative to scaled 6 m/s Cavanaugh Corridor and 3 m/s averaged cadaver response 69

Figure 55. Force-deflection responses of Bladder 8 (final MAMA-2B 50-durometer silicone rubber bladder) to rigid-bar impacts in tests GMP0012-15 relative to scaled 6 m/s Cavanaugh Corridor and 3 m/s averaged response. 70

Figure 57. Responses of MAMA-2B to out-of-position surrogate airbag loading response with and without chest jacket from tests GMP0048 and 0049 compared to out-of-position airbag loading corridor developed by Hardy et al. (2001). 71

Figure 58. Dynamic response of the first pregnant abdomen compared to scaled 6 m/s abdominal response corridor derived from Cavanaugh (1986) 73

Figure 59. "Top-hat" transducers. 76

Figure 60. Side view of test setup for quasi-static rigid-bar loading of the MAMA-2B bladder to evaluate top-hat transducer performance. Loading of the abdomen occurs when the rod-shaped indentor (the object covered with target tape) is uniaxially displaced into the bladder. 76

Figure 61. Laterally- and longitudinally- oriented top hat stretch measured during quasi-static indentation of the bladder away from the top-hat location, indicating that circumferential stretch caused by increased pressure in the bladder is small (approx. 0.04 in the figure above). 77

Figure 62. Shape Tape by Measurand, showing the curvature-sensitive section along with the curvature-insensitive lead length and the interface box. 78

Figure 63. "Nyquist Theorem" of curvature measurement. If the sensor length is ABC or greater, the sensor measures equal amounts of upwards and downwards curvature and consequently its averaged output is zero. If one sensor per monotonic curve is used (i.e., two sensors of length AB and BC, respectively) the correct curvature is measured. 79

Figure 64. Shape Tape installed on prototype bladder (left) and schematic of Shape Tape routing (right) 80

Figure 65. Quasi-static testing of Shape Tape installed in bladder. 81

Figure 66. Peak penetration of bladder during quasi-static indentation of MAMA-2B abdomen and associated deformed and undeformed Shape Tape results. (a) Picture of indentation. (b) Shape calculated using base-to-tip integration. (c) Shape calculated using tip-to-base integration. (d) Shape calculated by averaging base-to-tip and tip-to-base integrations. 82

Figure 67. Comparison of penetration calculated from static indentation of MAMA-2B bladder using base-to-tip, tip-to-base, and average of tip-to-base and base-to-tip algorithms to actual penetration measured from displacement of the indentor. 83

Figure 68. Peak penetration into bladder during pendulum impact of MAMA-2B with Shape Tape in test GMP0029. Deformed (right) and undeformed (left) shapes are shown at a time corresponding to maximum penetration. (a) Bladder deformation. (b) Shape calculated using base-to-tip integration. (c) Shape calculated using tip-to-base integration. (d) Shape calculated by averaging base-to-tip and tip-to-base integrations. 84

Figure 69. Peak deflection from out-of-position airbag loading of the MAMA-2B abdomen. Deformed (left) and undeformed (right) bladder shapes were taken at a test time that corresponds to maximum observed penetration. (a) Indentation shape. (b) Shape calculated using base-to-tip integration. (c) Shape calculated using tip-to-base integration. (d) Shape calculated by averaging base-to-tip and tip-to-base integrations. 86

Figure 70. Surrogate airbag penetration measured from Shape Tape using each of the three processing algorithms compared to the direct displacement measurement from the surrogate airbag device. 87

Figure 71. Side-view photo showing peak penetration of steering wheel and lap belt into upper and lower regions of the new pregnant abdomen in frontal sled test GMP0042. 88

Figure 72. Deformed and undeformed shapes calculated at peak deformation from steering wheel and lap belt contact in test GMP0042. (a) Shape calculated using base-to-tip integration. (b) Shape calculated using tip-to-base integration. (c) Shape calculated by averaging base-to-tip and tip-to-base integrations. 89

Figure 73. Quasi-static loading with tape routed inside the bladder to eliminate pressure sensitivity. 90

Figure 74. Quasi-static indentation of Shape Tape inside an unfilled bladder to eliminate pressure sensitivity. Tests were performed using 2.54 cm wide bar with rounded 2.54 cm diameter tip. (a) Deformed shape. (b) Shape calculated using base-to-tip integration. (c) Shape calculated using tip-to-base integration. (d) Shape calculated by averaging base-to-tip and tip-to-base integrations. 91

Figure 75. FEM of dummy with pressure transducer locations highlighted 92

Figure 76. Pressure histories from rigid-bar loading at 4.3 m/s in test GMP0012. 93

Figure 77. Pressure-time histories from belt loading at 3 m/s in test GMP0019 94

Figure 78. Anterior and posterior pressure transducer response from bladder-only sled test (GMP0009) using Bladder 6 94

Figure 79. Anterior and posterior pressure transducer responses from bladder-only sled test (GMP0046) using Bladder 8 (final prototype) 95

Figure 80. Pressure response from a whole-dummy sled test conducted at 47 kph/16 g with final MAMA-2B abdomen (GMP0042). 96

Figure 81. Process to develop injury criteria based on FE modeling and crash reconstructions. 98

Figure 82. Fetal outcome as a function of crash severity, controlling for proper (i.e., three-point belt or airbag and three-point belt) restraint use. From Klinich et al. (1999) 99

Figure 83. Relationship between peak anterior positive pressure and risk of adverse fetal outcome for three-point belted drivers (3pbdr), three-point belted passengers (3pbpass), three point belted and airbag-restrained drivers (3padr), and unrestrained drivers (unr dr). 101

Figure 84. Correlation between peak anterior positive pressure and risk of adverse fetal outcome for tests GMP0031-GMP0045. 102

Figure 85. Relationship between peak anterior positive pressure and crash severity for three-point-belted drivers (3pbdr), three-point-belted passengers (3pbpass), three-point-belted and airbag-restrained drivers (3padr), and unrestrained drivers (unr dr) 102

Figure 86. Anterior pressure transducer signals from tests GMP0039 and GMP0040 (three point belted driver). 103

Figure 87. Anterior pressure transducer signals from 4.3 m/s pendulum impacts in tests GMP0011 and GMP0012 104

Figure 88. Anterior pressure responses from 3 m/s lap belt loading tests (GMP0018 and GMP0019). Test GMP0018 was conducted with the chest jacket, while test GMP0019 was conducted without the jacket. 104

Figure 89. Anterior pressure transducer responses from surrogate-airbag loading tests (GMP0048 and GMP0049). Test GMP0048 was conducted without the chest jacket, while test GMP0049 was conducted with the jacket. 105

LIST OF TABLES

Table 1. Failure Conditions of Biological Tissues Used to Estimate UPI Failure Criteria 24

Table 2. UPI Shear Stress with Placenta Location Illustrating that Stresses Caused by Deformation are Much Higher than Those Caused by Placental Inertia 27

Table 3. Stature Group Ranges, Means, and Number of Subjects 36

Table 4. Dummy Development and Testing History 57

Table 5. Test Matrix for Developing Risk-Based Injury Criteria and Tolerance Thresholds 99

Table B1. Dummy Development Test History 120

1.0 EXECUTIVE SUMMARY

Based on crash statistics and birth rates, it has been estimated that about 130,000 women in the second half of pregnancy are involved in motor-vehicle crashes annually in the United States. Approximately 30,000 sustain treatable injuries, and 160 are killed. For the pregnant women who survive, it has been estimated that between 300 and 3800 will experience a fetal loss, most likely from placental abruption (the separation of the placenta from the uterine wall).

Despite the high relative incidence of fetal death, relatively little has been done to address the special circumstances associated with providing effective restraint for pregnant occupants. This is primarily because safety engineers have not had the tools to assess the unique injuries sustained by pregnant vehicle occupants, or to assess the effectiveness of restraint countermeasures. In response to this need, a first-generation pregnant crash test dummy was developed. However, this pregnant dummy has several shortcomings that make the dynamic interaction of the dummy with restraint systems and vehicle interior components questionable, and that limit its ability to predict the likelihood of fetal loss.

The goal of this project was to develop and test a new and improved pregnant version of the small-female Hybrid III ATD. Based on data from other projects, previous medical research on fetal injury and loss in motor-vehicle crashes, and recognized limitations and deficiencies with the first pregnant dummy, three primary objectives for the design and performance of the new pregnant dummy were established early in the project. These include:

1) improving the anthropometry of the pregnant abdomen to achieve more humanlike interaction with restraint systems and vehicle interiors,
2) enhancing the biofidelic response of the pregnant abdomen, and
3) implementing design features and instrumentation that will assess the likelihood of placental abruption in crash environments.

The project has resulted in a new prototype pregnant crash test dummy known as the Maternal Anthropomorphic Measurement Apparatus, version 2B (MAMA-2B). The design of the new pregnant abdomen uses a fluid-filled silicon bladder representing the human uterus at 30 weeks gestation. This size and shape is greatly improved from the first pregnant dummy, for which the abdomen protrudes much too far forward and does not extend upward to interact with the ribcage in an appropriate manner.

Incorporating the pregnant uterine-like bladder into the small-female Hybrid III dummy required trimming the 4th through 6th ribs at the front, but this was accomplished in a manner that ensured that the force-deflection response of the dummy's chest met the appropriate specification. The weight of the MAMA-2B is 9.1 kg greater than that of the small-female Hybrid III to account for typical weight gain during pregnancy. Ballast was added to the dummy in a manner that does not result in the mass decoupling that could occur in dynamic testing with the first pregnant dummy. Also, the weight distribution

was adjusted so that the seated-CG is located appropriately for a seated pregnant woman (about 8 mm forward and 10 mm above the seated non-pregnant whole-body CG).

The dynamic force-deflection response of the MAMA-2B abdomen is significantly improved from that of the first pregnant dummy. The new abdomen has been designed and tested for rigid-bar, belt, and close-proximity airbag loading, and the response of the MAMA-2B abdomen falls within force-deflection corridors established for each type of test. The abdomen also demonstrates rate sensitivity in its force-deflection response, although additional rate sensitivity would be desirable to better match the response of the human abdomen.

In attempting to design and instrument the abdomen to assess the risk of adverse fetal outcome due to placental abruption, two approaches were considered. The first approach involved an ambitious attempt to instrument the abdomen to measure response parameters needed for injury criteria that relate directly to hypothesized mechanisms of traumatic placental abruption. The second approach is more typical of injury criteria development, and involved establishing relationships between regional response measures to general levels of fetal outcome based on risk curves from real-world crash investigations, without concern for the specific mechanisms of injury or specific tissues injured.

Two mechanisms that are thought to be most responsible for placental abruption in motor-vehicle crashes are 1) tensile strain at the Uterine Placental Interface (UPI) due to an anterior-posterior fluid pressure gradient developed from inertial forces, and 2) shear strain or stress at the UPI due to uterus curvature changes caused by direct abdomen loading. A significant effort was made to successfully instrument the MAMA-2B with pressure transducers to measure anterior-posterior pressure gradients, and a curvature measurement device known as Shape Tape to measure strains resulting from changes in the curvature of the abdomen. However, results of numerous whole-dummy and isolated abdomen dynamic tests revealed problems that could not be resolved within the time and funding limitations of this study. While this approach offers promise with future improvements in instrumentation that appear feasible, it was necessary to abandon the prediction of the likelihood of placental abruption in favor of more traditional methods of injury criteria development.

The measure of fetal outcome developed using the second approach is based on pressure measured in the anterior region of the uterine-like MAMA-2B bladder. This pressure was measured in a matrix of sled tests designed to span the range of occupant-restraint and crash-severity conditions used in probability curves of adverse fetal outcome developed from real-world crashes and injuries. The peak anterior pressures in these tests were highly correlated to the expected risk of adverse fetal outcome. Therefore, a relationship was established between peak anterior pressure and the probability of adverse fetal outcome.

Although the MAMA-2B is considered to be in a prototype stage of development, whole-dummy testing under various restraint and crash-severity conditions indicates that the

new design is relatively durable and repeatable, and easy to use. Future work to improve MAMA-2B should focus on instrumentation issues. The rear pressure transducer should be replaced and sled tests conducted to determine if posterior pressure, or a combination of anterior and posterior pressure (e.g., pressure differential), better correlates to injury risk than peak anterior pressure. Proposed improvements to the shape tape should also be investigated to allow estimation of localized strain. Successful implementation of both the shape tape and dual pressure measures for expected abdomen loading scenarios along with additional tissue response data would allow the development and use of injury criteria that relate more directly to the hypothesized mechanisms of placental abruption.

Additional validation sled tests should also be conducted to determine how the MAMA-2B performs for a greater range of impact conditions, particularly for restraint misuse conditions, such as an improperly placed lap belt and out-of-position airbag loading. A second MAMA-2B should also be developed and tested to confirm and improve the fabrication process, and to verify that the MAMA-2B design is reproducible.

2.0 INTRODUCTION

Based on crash statistics and birth rates (Klinich et al. 1999), it is estimated that about 130,000 women in the second half of pregnancy are involved in motor-vehicle crashes annually in the United States. Approximately 30,000 sustain treatable injuries, and 160 are killed. For the pregnant women who survive, it has been estimated that between 300 to 3800 will experience a fetal loss, most likely from placental abruption (Klinich et al. 1999). Even the lower estimate of fetal deaths is greater than the number of infants killed (n=185) in motor-vehicle crashes in the U.S. each year (National Vital Statistics Reports, 1999).

In the past two decades, automotive safety engineers have made significant improvements in restraint systems that are designed to protect the general automotive occupant population. However, relatively little has been done to address the special circumstances associated with restraint of pregnant occupants. This is primarily because safety engineers have not had the tools to assess the unique injuries sustained by pregnant vehicle occupants. In response to this need, Viano et al. (1996) and Pearlman and Viano (1996) developed the first pregnant crash test dummy. However, the original pregnant dummy has several shortcomings that limit the ability to predict the likelihood of fetal loss and that make the dynamic interaction of the dummy with restraint systems and vehicle interior components questionable.

The goal of this project was to design, develop, and evaluate a new pregnant crash test dummy that will offer improved assessment of restraint-system performance for the pregnant occupant and the unborn fetus, and that will allow better prediction of the likelihood of fetal loss in frontal crashes. Based on the limitations of the original pregnant crash test dummy, three main objectives were identified for the design of the new pregnant dummy, hereafter referred to as the Maternal Anthropomorphic Measurement Apparatus, version 2B (MAMA-2B). These objectives are:

1. To incorporate realistic anthropometry and shape in the pregnant abdomen for more biofidelic interaction with restraint systems and vehicle interiors (particularly steering wheels),
2. To design the abdomen with a more humanlike force-deflection response, and
3. To provide instrumentation for assessing the risk of fetal loss due to placental abruption, the most common cause of fetal loss in motor-vehicle crashes (MVCs).

The design and development of MAMA-2B benefited from other GM/DOT settlement projects, including Project D.10 Seated Anthropometry During Pregnancy, D.8 Data Acquisition for Development of Uteroplacental Interface for the Second-Generation Pregnant Abdomen, and D.9 Investigations of Pregnancy Loss Resulting From Motor-Vehicle Crashes.

3.0 BACKGROUND

Prior to discussing the new pregnant crash test dummy, it is important to understand the anatomy of the pregnant abdomen as it may relate to abruption of the placenta, and to review and understand results of previous research on the impact response of the human abdomen and injuries to pregnant occupants. It is also important to understand the strengths and limitations of the first pregnant dummy.

3.1 Anatomy of the Pregnant Abdomen

Figure 1 illustrates the general anatomy of a pregnant abdomen near full term (Pritchard et al. 1985). The fetus is contained within the uterus, which is a muscular organ that grows in volume from about 5 mL to 5 to 10 L over the course of pregnancy. The uterine wall thickness at seven months is about 2 cm, and about 1 cm at full-term (40 weeks). Ligaments attach the cervical portion of the uterus to the sacrum and pelvic wall, but the uterus is otherwise free to move within the abdominal cavity. As the uterus grows, it displaces other abdominal organs and is in contact with both the anterior abdominal wall and the lumbar and sacral spines. The size of the uterus depends largely on the size of the fetus, and, since the weight of most newborns carried to full term is generally 2.7 to 3.6 kg (6 to 8 pounds), uterine size does not significantly vary with the stature or weight of the mother (Klinich, et al., 1999).

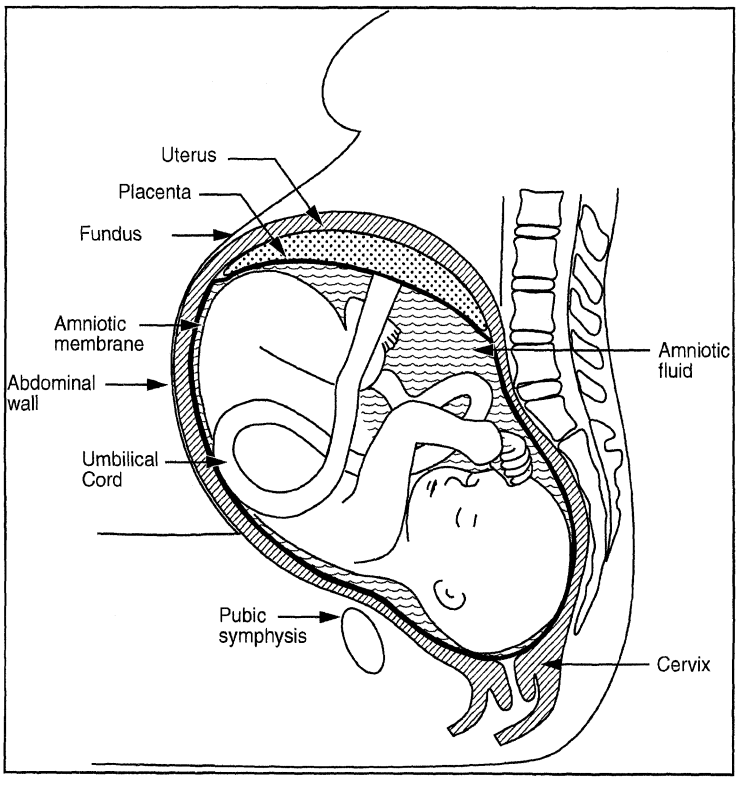

Figure 1. Anatomy of pregnant abdomen.

The placenta is a vascular organ within the uterus that exchanges oxygen, nutrients, and waste between the mother and the fetus. It is commonly called the afterbirth because it separates from the uterus and delivers spontaneously immediately after the baby is born. The placenta is roughly circular in shape, and is 2 to 2.5 cm thick during the last trimester of pregnancy. It covers approximately one-fourth of the internal surface area of the uterus throughout pregnancy. Eighty percent of placentas are located near the top (fundus) of the uterus by the third trimester (Fried, 1978). Figure 2 shows a schematic of the uterus, placenta, and uteroplacental interface, or UPI. Microvilli, which are finger-like projections approximately 50 μm in diameter, grow from the placenta into the superficial layers of the uterine wall during the early stages of fetal development and both anchor the placenta and facilitate nutrient transport. These microvilli are the sole attachment of the placenta to the uterine wall. Little is known about the strength of the villous attachment of the placenta to the uterus or the mechanisms that cause its failure (placental abruption); however, the uteroplacental interface is thought to be weaker than either the uterine or placental tissues.

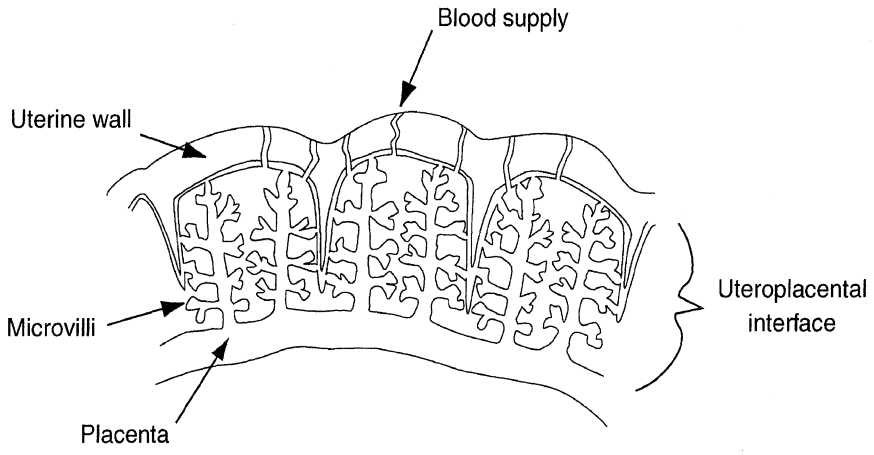

Figure 2. Schematic of the structure of the utero-placental interface.

The amniotic membrane lines the inner surfaces of the uterus and placenta, and surrounds the fetus and the amniotic fluid. The umbilical cord runs from the placenta through the wall of the membrane to the fetus. As the fetus grows, the relative proportion of the uterine volume filled with amniotic fluid decreases to about 10% at full term. By the last trimester, the fetus is positioned with its head down in over 95% of pregnancies.

3.2 Injuries Unique to Pregnant Occupants in Motor-Vehicle Crashes

Injuries that are unique to pregnant women involved in motor-vehicle crashes (MVCs) include placental abruption, uterine injury, and injury to the fetus. Of these injuries, placental abruption, which is a partial or complete failure of the uterine-placental

interface (UPI), occurs most frequently and is believed to account for 50 to 70% of fetal deaths in MVC (Pearlman, 1990).

Injuries to the uterus and fetus are believed to account for less than 10% of fetal losses in MVCs. When direct fetal injury occurs, the head is most frequently injured region because it is the largest part of the fetus. Fetal head injury often occurs in conjunction with pelvic fracture, which compromises the protective characteristics of the pelvic/abdominal cavity. Maternal death, maternal hypovolemic shock, and unknown causes account for the remaining 20-40% of fetal losses in MVCs.

A review of case studies in the literature, as well as cases investigated by Klinich et al. (1999), indicates that uterine and direct fetal injuries are usually accompanied by placental abruption, but that placental abruption often occurs without direct fetal or uterine injury. This implies that the threshold for placental abruption is lower than that for direct fetal or uterine injury, and suggests that reducing the potential for placental abruption will also reduce the probability of direct fetal and uterine injuries.

3.3 Restraint Testing with Pregnant Animals

The first series of animal tests to investigate restraint effectiveness for pregnant women was reported by Snyder et al. (1966). Seven sled tests using baboons as human surrogates are reported, in which three of the baboons were pregnant. An instrumented, artificial uterus was implanted in three of the non-pregnant animals prior to impact. All animals were restrained by only a lap belt and impacted in a seat position with the seat pan and seat back at angles of 45° from horizontal. Intrauterine pressure (at an unspecified location within the uterus), maternal EKG, fetal EKG (for the pregnant baboons), and maternal blood pressure were monitored. Subject kinematics were documented using high-speed film, and belt forces were measured.

The data show two peaks in positive uterine pressure. The first peak occurs immediately after sled deceleration begins and was attributed to the subjects tensing in anticipation of the impact. The second peak occurs when the mother's torso "jackknifed" over the uterus. All of the fetuses died within 2 hours of impact, although no direct fetal injuries were observed. Consequently, fetal death was attributed to maternal neurological shock. In most tests, the lap belt restraints functioned properly; however, in one test, the temporary shoulder strap used to limit torso motion prior to impact failed to release properly. As a result, the shoulder strap simulated a shoulder belt, which prevented jackknifing and consequently prevented the secondary pressure peak from occurring.

Crosby et al. (1968) conducted forward- and rearward-facing sled tests of pregnant baboons restrained by either a lap belt only or a three-point belt. Similar to the Snyder et al. data, Figure 3 illustrates that in the forward-facing, lap-belt only tests, intrauterine pressure showed two positive peaks. The first peak had an average magnitude of 67 kPa (9.7 psi or 500 mmHg) and occurred upon initial deceleration of the sled, before any forward movement of the torso began. This peak may be attributed to both inertia of the

pregnant abdomen and the restraint forces applied by the lap belt. The second pressure peak had an average magnitude of 47 kPa (6.8 psi or 350 mmHg) and occurred when the torso bent over the lap, compressing the uterus. In two tests conducted with the subjects forward-facing and restrained by a three-point belt, the results showed a single positive peak pressure of magnitude similar to that measured during tests with lap-belt-only restraints. This pressure peak was attributed to inertia of the pregnant abdomen.

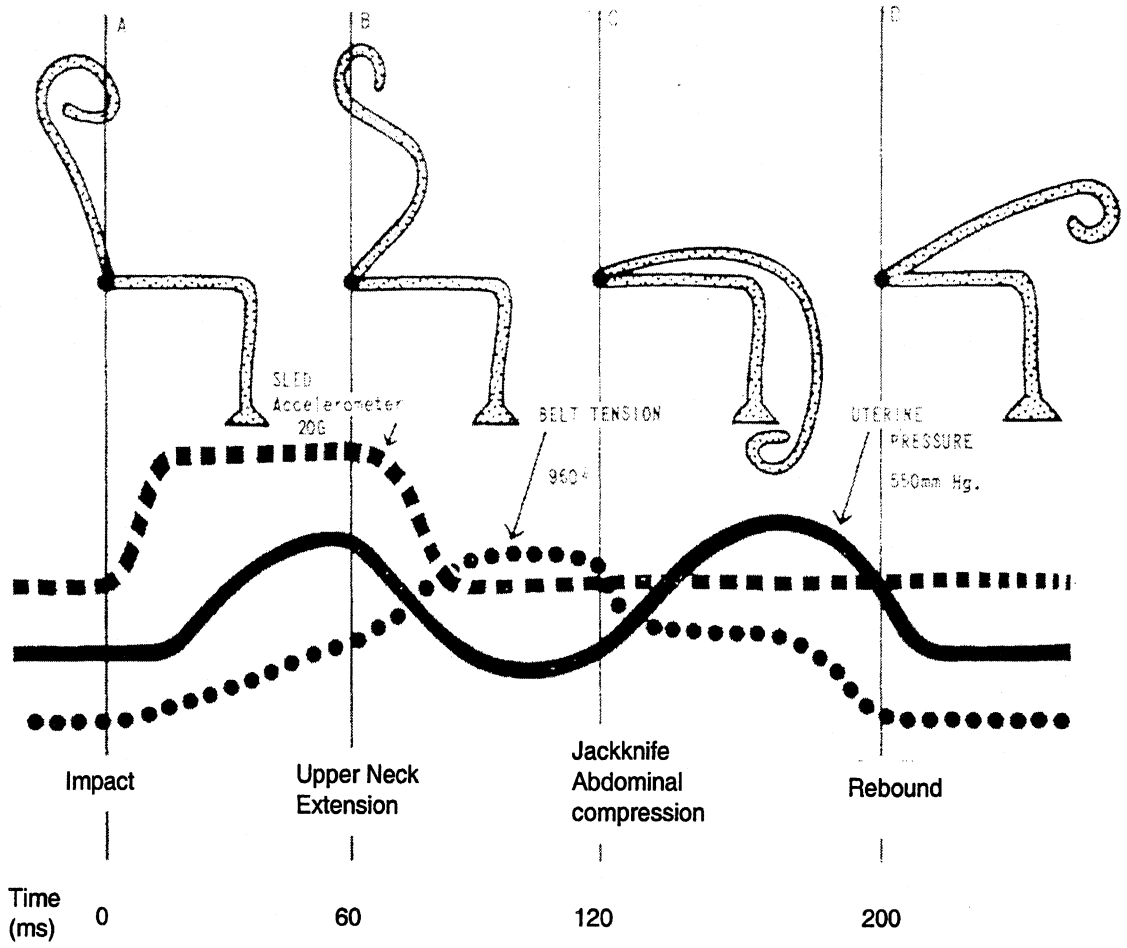

Figure 3. Pressure response from animal testing. Adapted from Crosby et al. (1968).

None of the fetuses survived, and three of the ten pregnant animals sustained significant injuries. The fetal deaths resulted from shock, placental separation, or direct fetal skull injury. The same levels of pressure increase occurred in both forward- and rear-facing tests. Three control animals that were not tested also underwent the surgical procedures to implant the instrumentation. All three also experienced fetal loss, implying that the observed fetal losses may have been caused by the instrumentation and/or surgical procedure, and not by the impact. However, injuries to the fetus, and separation of the placenta may still have been a result of, or been compounded by, impact.

King et al. (1972) conducted a series of forward-facing tests on twenty-two pregnant baboons to determine if three-point belts provide any additional benefit over lap belts.

Testing was performed approximately seven weeks prior to full term, which correlates to a gestational age of 28 weeks in a human. Uterine pressure was not measured, so the potentially traumatic effects of surgery to implant instrumentation did not affect results. Of the twelve subjects restrained by a three-point belt, one fetal loss occurred within several hours of the test, two fetuses died during birth from causes unrelated to the testing, and nine healthy infants were delivered. Of the ten subjects restrained with only a lap belt, five fetal losses occurred within a week of testing. The results of these tests support the use of properly positioned three-point belts for pregnant occupants.

Wiechel et al. (1989) documented a review of automotive/pregnancy literature, with an emphasis on animal testing. The authors compare results from the primate tests conducted by Crosby, King, Snow, and others. They include a qualitative discussion on how the kinematics expected with different restraint systems might affect a pregnant occupant, as well as a discussion of potential restraint effectiveness for pregnant women. The authors propose that pressure waves (i.e., a pressure gradient) within the uterus during impact can injure the uterus, the fetus, or the utero-placental interface.

Results from pregnant animal testing suggest that three-point belts are more effective than lap belts in protecting the pregnant abdomen and fetus. They also suggest that inertially generated intrauterine pressures may be responsible for fetal injury and loss with and without direct loading of the abdomen.

3.4 The First Pregnant Dummy

Viano et al. (1996) and Pearlman and Viano (1996) developed an abdominal insert for the Hybrid III small-female dummy to simulate pregnancy and assess the potential for fetal injury. This "pregnant" adaptation of the small female ATD was designed to evaluate the performance of different restraint systems by measuring forces applied directly to the pregnant abdomen. Figure 4 shows the first pregnant abdomen in a modified Hybrid III pelvis along with the separate pregnant abdomen components. The first pregnant abdomen consists of a surrogate urethane fetus that fits inside a solid-urethane egg-shaped casing, which is contained within a larger urethane uterus. These nested components are covered anteriorly by the external dummy torso/abdomen jacket. The fetus is equipped with triaxial accelerometers in the head and thorax. Ballast was added to pockets on the interior surface of the chest jacket so that the total mass of the original pregnant dummy was 58 kg. A force transducer is mounted to the lumbar spine behind the pregnant uterus to measure forces transmitted through the abdomen. The original pregnant dummy employs a modified version of the Hybrid III small female chest skin, which was contoured so that it blended with the superior surface of the abdominal insert.

Thirty-nine sled tests were conducted using the original pregnant dummy restrained by a three-point belt, restrained by only a lap belt routed across or below the abdomen, and unrestrained. Test velocities of 10, 15, 20, and 25 mph were used. The performance of airbag restraints was also evaluated in the restraint conditions discussed above and in out-of-position tests. Results obtained with proper belt placement were considered a baseline

response. Improper belt use (lap belt over the uterus, or lap belt only) resulted in three times as much force transmitted through the abdomen compared to proper belt usage. Fetal acceleration measurements increased as crash severity increased from 10 to 25 mph. Tests of an unbelted and belted ATD with an airbag deployment resulted in relatively low force transmitted through the uterus, but out-of-position airbag deployment tests resulted in high fetal accelerations and forces.

While the first pregnant dummy provides for measuring and comparing forces and accelerations applied directly to the pregnant abdomen under different crash and restraint scenarios, the relationship of these measures to the likelihood of fetal injury and loss is unknown, save that large increases in these measures intuitively should result in a greater likelihood of fetal loss. In addition, the first pregnant abdomen does not provide for assessing the risk of fetal injury and loss under crash/occupant scenarios that do not involve direct loading of the abdomen. Furthermore, the high, non-humanlike stiffness of the urethane components comprising this first pregnant abdomen, the exaggerated anterior contour of the pregnant abdomen, the unrealistic distribution of the mass in the dummy torso, and the tendency of the ballast weights in the chest jacket to decouple from the dummy torso during impact, likely result in an unrealistic interaction of the pregnant abdomen with restraints and vehicle components. This, consequently, would alter injury measurements by changing the conditions under which the abdomen is directly loaded.

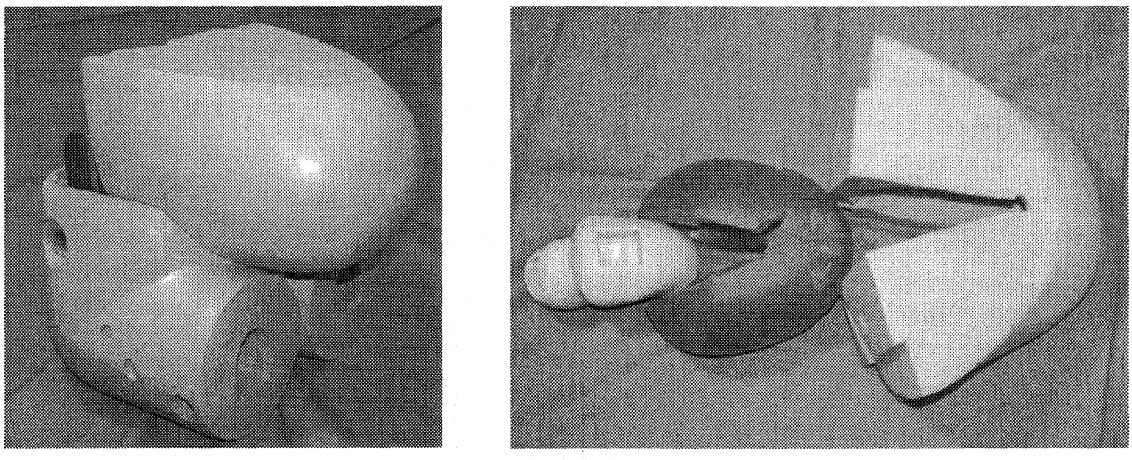

Figure 4. Original pregnant abdomen installed in pregnant dummy pelvis (right) and separated into fetal component, urethane casing, and urethane uterus (left).

3.5 Impact Response of the Abdomen

Numerous tests have been conducted to determine the response of the human abdomen to impact loading. Human cadaver tests have been used to develop response corridors that describe abdominal stiffness at different loading rates and with different impactor shapes. Also, abdominal response data from tests of living animals and animal cadavers have been used to develop scaling factors between the response of human cadavers and living humans.

3.5.1 Abdominal Response from Animal Tests

Stalnaker et al. (1985) summarized data from abdominal impacts on anesthetized primates in a seated posture performed by Beckman (1971), Stalnaker (1971), and Trollope (1973) using several rigid-bar and wedge-shaped impactors. Impact velocities and masses ranged from 8.4 to 17.0 m/s and 0.53 to 19.40 kg, respectively. Force-deflection data were described by a "rise-plateau-rise" response. Assuming linear velocity scaling, data were averaged to estimate human response. Differences between species, impact region, impact direction, and pendulum shape were ignored.

Rouhana et al. (1990) performed dynamic belt loading tests by driving a yoke fixture containing 50-mm wide belt webbing into the abdomens of swine cadavers. Loading rates were varied from 0.2 to 5.3 m/s. Actuator force, abdomen deflection, and belt stretch were measured. Rouhana et al. analyzed these tests, along with tests conducted by Miller et al. (1989) on anesthetized swine, to estimate scaling between living and cadaveric swine. This scaling was applied to abdominal response corridors developed for human cadavers (Cavanaugh et al., 1986) to estimate the response of a live human. The estimated human response was used to develop a frangible abdomen for use in the Hybrid III family of adult dummies.

3.5.2 Results from Human Cadaver Tests

3.5.2.1 Abdomen Response to Rigid Impactors

Cavanaugh et al. (1986) impacted the abdomens of twelve unembalmed human cadavers at the level of L3 using a 2.54 cm diameter rigid bar that was attached to one of two linear impactors weighing approximately 31.5 and 63.5 kg. Cadavers were positioned in a free-back seated posture. Prior to impact, the vascular system was pressurized. Impact velocities were either 6.1 or 10.4 m/s. Abdominal deflection and impactor force were measured. Equal-stress, equal-velocity scaling (Eppinger, 1976) was applied to the force and deflection data to account for the varying anthropometry of the test subjects. The force-deflection response during loading was found to be relatively linear, and abdominal stiffness was found to be proportional to impactor mass and velocity, implying that the abdominal response is somewhat rate sensitive. Data from this study were used to develop ±1 SD human response corridors for impact velocities of 6.1 and 10.4 m/s.

Nusholtz et al. (1994) impacted six unembalmed human cadavers using an angled semi-circular 18 kg rigid pendulum. Cadavers were positioned in a free-back seated posture. Prior to impact, the vascular system was pressurized. Impacts were performed at velocities between 4 and 11 m/s. Impactor force and abdominal deflection data were collected. No scaling techniques were applied and no rate sensitivity was observed. Results may have been influenced by the small sample size, the low pendulum mass, or contact between the impactor and ribcage at greater penetration depths.

Pendulum impacts were also conducted by Viano (1989). In this series of tests, a 23.4 kg, 152 mm diameter, flat-faced pendulum was used to impact pressurized, unembalmed human cadavers in a transverse plane at angles of ±30° from the midsagittal plane. Impacts were performed so that the direction of applied force was through the center of the subject's torso. Impact velocities were 4.5, 6.7, and 9.4 m/s. Impactor force and abdominal penetration data were measured and equal-stress, equal-velocity scaled.

Hardy et al. (2001) reprocessed data collected by Nusholtz, Rouhana, Stalnaker, and Viano to develop Cavanaugh-style equal-stress, equal-velocity responses. The Nusholtz data were separated into 10 m/s (high-speed) and 6 m/s (low-speed) ranges and equal-stress, equal-velocity scaling was applied. Upper abdomen impacts were removed from the Stalnaker data, and only data in the range of 10±1.5 m/s were considered for analysis. Velocity scaling was used to generate a 6 m/s response corridor from the 10 m/s Stalnaker data. The Viano cadaver data were averaged within the 6.7 and 9.4 m/s ranges to obtain responses that were comparable to the 6 and 10 m/s Cavanaugh corridors. Figure 5 shows the higher velocity reprocessed data compared to the Cavanaugh 10 m/s corridor. Figure 6 shows the 6 m/s reprocessed data plotted against the 6 m/s Cavanaugh corridor. Figure 6 also includes the response of Rouhana's frangible abdomen. Force-deflection data collected by Nusholtz, Stalnaker, and Viano, and plotted in Figure 5, generally fall within the 10 m/s Cavanaugh corridor. However, the data plotted in Figure 6 do not. Hardy postulated that these differences are due to the different impactor shapes and differences in the impactor-to-subject mass ratios.

To investigate differences in force-deflection response among previous test data, Hardy et al. (2001) performed nine rigid-bar impacts into nine pressurized cadavers using a 48 kg ballistic pendulum. The impactor was a 2.54 cm diameter, 45.7 cm long rod, similar to that used by Cavanaugh. Impact velocity levels of 3.4, 6.7, and 10.2 m/s were used to quantify rate sensitivity of the abdominal response. The effect of impact location was studied by impacting both the mid-and lower-abdomen. Both free- and fixed-back tests were performed. For the fixed-back tests, pendulum motion was arrested prior to contact with the lumbar spine using a series of deformable bars. Impactor force and pendulum penetration into the abdomen were measured and equal-stress, equal-velocity scaled to account for variations in subject mass. The rigid-bar force-deflection responses measured by Hardy et al. at 6 m/s and 10 m/s agree with those proposed by Cavanaugh and demonstrate rate sensitivity. Because only one subject was tested multiple times at the 3 m/s loading rate, Hardy was unable to generate a 3 m/s response corridor and instead generated a 3 m/s averaged response. Both the 10 m/s and the 6 m/s Cavanaugh corridors are plotted in Figure 7 along with the averaged Hardy 3 m/s response.

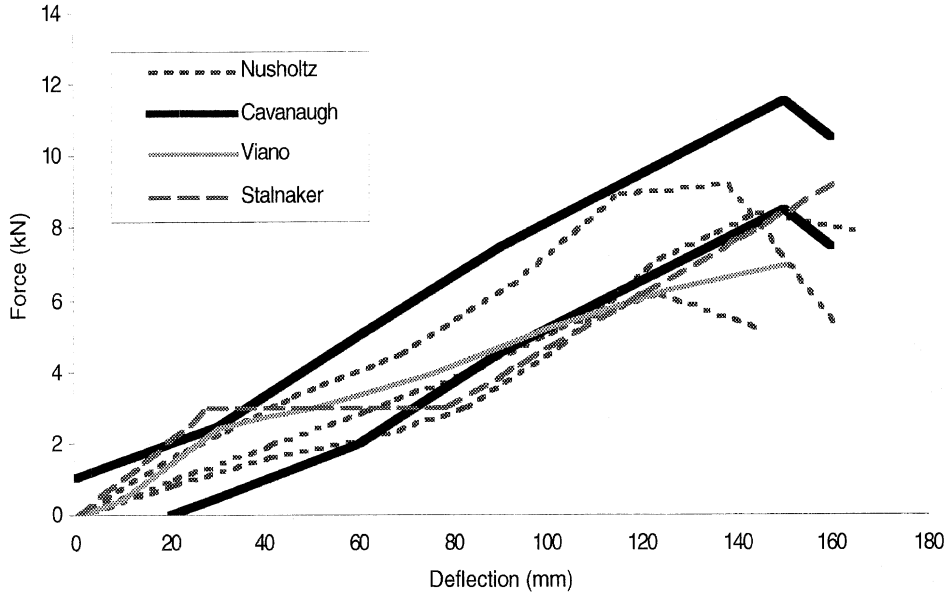

Figure 5. Comparison of the 10 m/s Cavanaugh rigid-bar corridor and reanalyzed Nusholtz, Viano, and Stalnaker data.

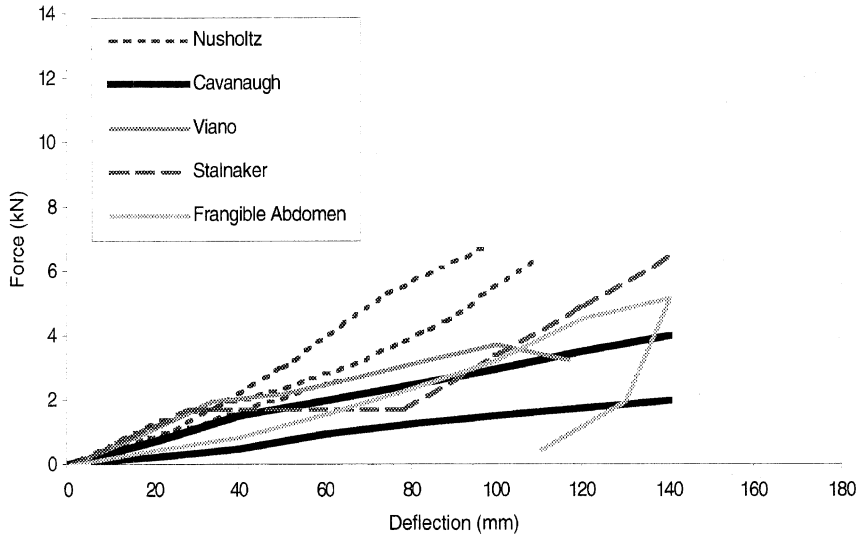

Figure 6. Comparison of the 6 m/s Cavanaugh rigid-bar corridor and reanalyzed Nusholtz, Viano, Stalnaker, and Rouhana data.

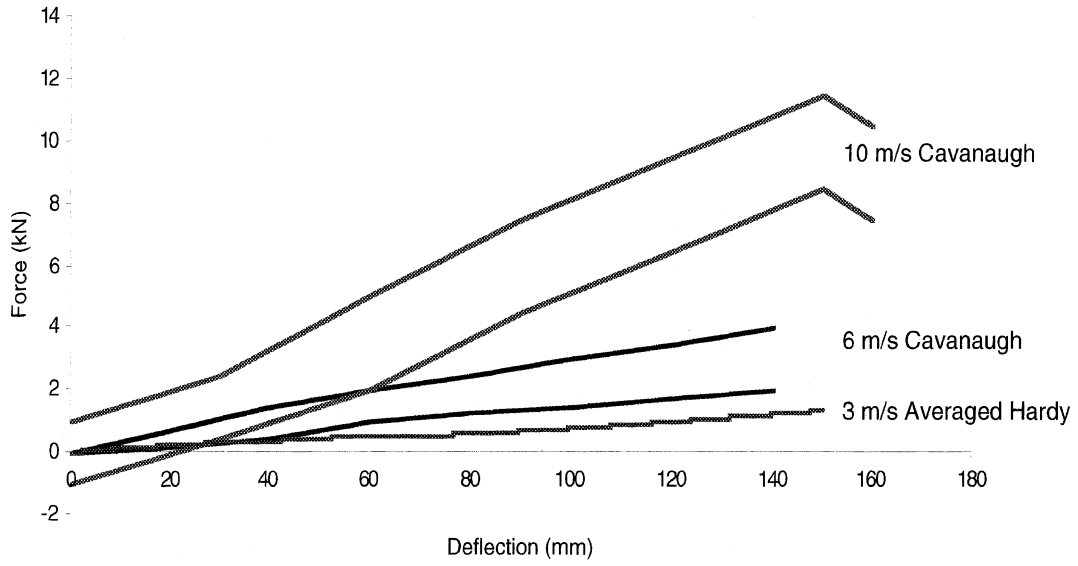

Figure 7. Comparison of the 10 and 6 m/s rigid-bar Cavanaugh Corridors to the 3 m/s averaged response developed by Hardy et al. (2001).

3.5.2.2 Abdominal Response to Belt Loading

Hardy also performed a series of belt loading tests on human cadavers utilizing a yoke-fixture similar to that used by Rouhana et al. on swine cadavers. The belt was positioned at mid-abdomen (umbilicus) level and curved around the abdomen. The yoke was pneumatically retracted at a nominal rate of 3 m/s. Belt penetration into the abdomen was calculated from the difference between belt displacement (measured using string potentiometers attached to the centerline of the belt) and lumbar spine displacement (measured with a laser range finder that tracked the difference in position between the yoke and the lumbar spine). Force was measured from two seat belt load cells positioned near the attachments to the yoke and was verified using the mass-corrected force measured by a load cell connected to the base of the yoke. Force and deflection data were equal-stress, equal-velocity scaled and used to develop the ±1 SD abdominal-response corridors for 3 m/s lap belt loading, shown in Figure 8.

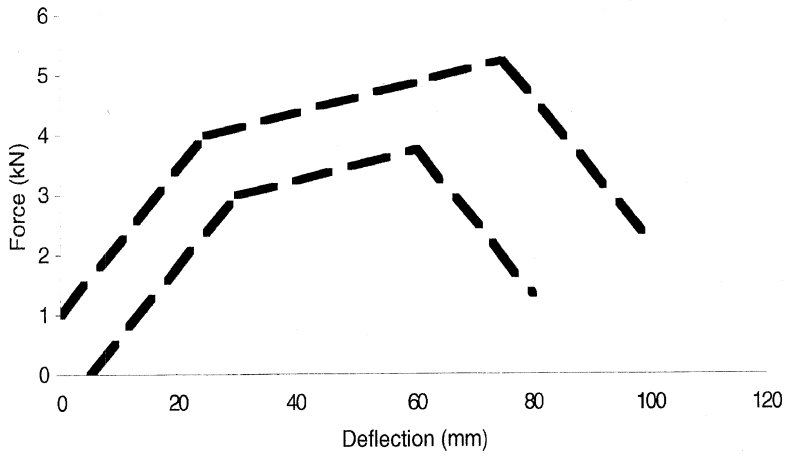

Figure 8. Belt-loading corridor developed by Hardy et al. (2001).

3.5.2.3 Out-of-Position Abdominal Response to Surrogate Airbag Loading

To simulate airbag loading of the abdomen when it is extremely close to or in contact with the airbag prior to deployment, or "out-of-position," Hardy et al. (2001) developed a surrogate airbag fixture. The impact surface is a 3-inch diameter, 8-inch long hollow cylinder. The cylinder is rigidly attached to a hollow shaft that is pneumatically accelerated along a single axis to a velocity between 12.5 and 13 m/s. The total mass of the cylinder and shaft is 1 kg. The cylinder is driven through the first three inches of its stroke and then allowed to continue moving until it is decelerated by contact with the abdomen. The motion of the cylinder is measured with a laser range finder and along with the time of abdomen contact, is used to determine penetration into the abdomen.

To validate the performance of the surrogate airbag impactor, Hardy et al. compared abdomen response from six tests into three cadaver abdomens, with results from three out-of-position deployments of passenger airbags into three cadaver abdomens. The force-deflection responses of the abdomens to the surrogate airbag loading agree well with the responses to deployments of the airbag positioned close to the abdomen. Using equal-stress, equal-velocity scaled data from surrogate airbag impacts into pressurized cadaver abdomens, Hardy et al. developed the out-of-position airbag-response corridor for the abdomen shown in Figure 9.

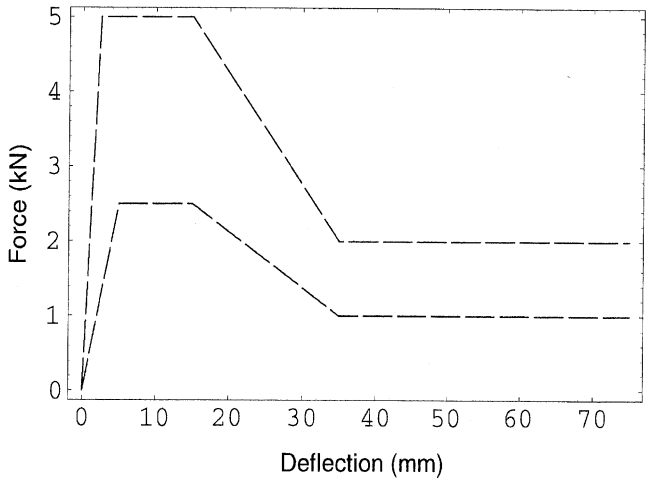

Figure 9. Out-of-position airbag-loading corridor developed by Hardy et al. (2001).

3.6 Fetal Injury Risk from Crash Investigations

Klinich et al. (1999) analyzed injury, restraint use, and vehicle damage data from crashes involving 43 pregnant occupants. The crashes span a range of crash severities and include injuries unique to pregnant occupants that have been described in the medical literature. The belt-restraint usage rate for the pregnant occupants in the database is representative of usage rates in the general occupant population. Data from variables including crash severity, maternal injury, maternal restraint usage, occupant seating location, maternal stature, gestational age, and impact direction were statistically analyzed to determine their significance with regard to fetal outcome. Crash severity was found to have the strongest effect on fetal outcome, with greater crash severities associated with poorer fetal outcomes. Maternal restraint use also had a significant effect on fetal outcome, with proper restraint use (three-point belt or three-point belt plus airbag) associated with improved fetal outcome. When comparing outcomes to mothers restrained by a three-point belt versus a three-point belt and airbag, it was found that airbags may have a positive effect on fetal outcome.

A risk analysis was performed using data from all 43 cases to quantify the relationships between crash severity and restraint usage, and the probability of adverse fetal outcome. Fetal outcome was divided into two categories: 1) good outcome or minor complication, and 2) major complications or fetal losses. Of thirty-one properly restrained occupants, eight (25.8%) experienced fetal loss or major complications. Of the twelve improperly restrained or unrestrained occupants, eight (66.7%) sustained fetal loss or major complications. Logistic regressions were performed to establish risk curves for adverse fetal outcome for the properly restrained occupants (three-point belts or three-point belts plus airbags) and improperly restrained occupants (unrestrained, airbag only, shoulder belt only, with and without airbag.) As shown in Figure 10, at crash severities below 50 kph delta V, unrestrained pregnant occupants have a much greater risk of adverse fetal

outcome than do properly restrained occupants. For example, at 20 kph delta V, the estimated risk of adverse fetal outcome for properly restrained pregnant occupants is less than 20%, while it is near 70% for unrestrained pregnant occupants. Removing data from side and rear impacts did not significantly alter the results of the regression. Results of this study clearly support the current recommendation that pregnant women properly wear the available three-point belt. They also provide useful information for establishing tolerance levels for adverse fetal outcome in the new pregnant crash dummy.

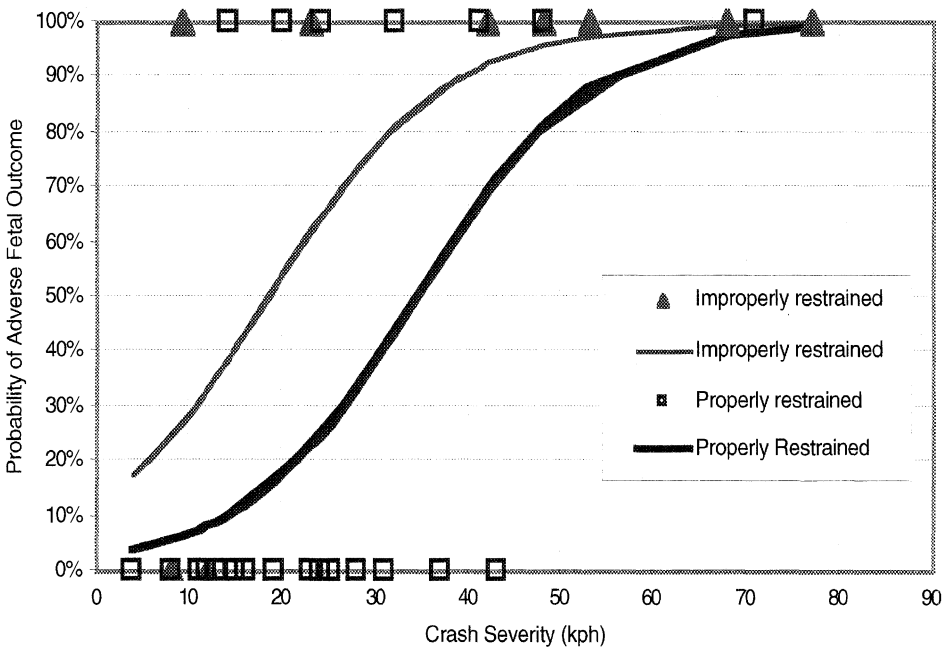

Figure 10. Logistic regressions for adverse fetal outcome as a function of crash severity, for properly restrained (i.e., three-point belt or airbag and three-point belt) and improperly restrained (unbelted, airbag only, or shoulder belt only). Based on data from Klinich et al. (1999).

4.0 HYPOTHESIZED MECHANISMS OF PLACENTAL ABRUPTION

4.1 Overview of Injury Types

Injuries sustained by the pregnant abdomen that can lead to fetal injury or loss in motor-vehicle crashes include placental abruption, uterine rupture, uterine laceration, and direct fetal injury. Of these injuries, placental abruption, which is the separation of the placenta from the uterine wall, is reported to be the most common, accounting for up to 70% of fetal losses resulting from motor-vehicle crashes (Pearlman, 1990). In crashes resulting in direct fetal or uterine injury, placental abruption usually also occurs. However, placental abruption frequently occurs without direct fetal or uterine injury. These observations, along with the high incidence of placental abruption, suggest that tolerance to placental abruption is lower than for either direct fetal injury or uterine rupture/laceration. It follows that, in designing a new abdomen that will assess for the risk of fetal loss, it would be most desirable to address the specific mechanisms that result in fetal loss. Consequently, it was decided to try to design and instrument the new pregnant abdomen to measure abdominal response parameters that are related directly to these mechanisms.

To do this, it was first necessary to establish the mechanisms that are most likely to cause traumatic fetal loss. In the absence of biomechanical studies of traumatic fetal-loss mechanisms, an effort was undertaken to explore the possible and likely mechanisms based on pregnant abdomen anatomy and basic principles of physics. This section of the report describes these exploratory efforts into the mechanisms of placental abruption, and the basis for determining which mechanisms should be considered in the abdomen design and instrumentation.

It is important to note that the decision to design the new pregnant abdomen to predict the risk of a specific injury, such as placental abruption, represents a departure from traditional dummy design and established injury criteria. Typically, crash dummies have been designed and instrumented to assess the general level of injury severity to a body region based on the Abbreviated Injury Scale or AIS. For example, measures of chest deflection, spine resultant acceleration, V*C, and TTI provide measures that can be related to the percentage risk of AIS 3 or 4 thoracic injuries in the general adult population, but not to the likelihood of lung contusion, rib fractures, aortic rupture, etc.

It should also be noted that the efforts in this study to instrument the new pregnant abdomen to assess for those mechanisms thought to be most likely to cause placental abruption in a motor-vehicle crash were not completely successful within the time and funding limitations of this project. However, the task of designing the new pregnant abdomen was considered an opportunity to advance the practice of dummy design, and it is expected that future efforts will be successful in resolving the remaining instrumentation problems. It is important to recognize that the mechanisms of placental abruption explored in this project, and those mechanisms considered most likely to cause placental abruption, are only best biomechanical guesses that may be proven wrong in future biomechanical studies. However, the efforts to study and evaluate these

mechanisms should prove valuable to future research and dummy design projects, and documentation of those efforts and their results is therefore considered important.

4.2 Tissue Testing to Determine Critical Strains for Placental Abruption

In an unpublished study, Ashton-Miller et al. quasi-statically tested sections of placenta, uterus, and intact utero-placental interface in an attempt to determine UPI failure criteria. Two different types of testing were conducted to measure potential failure modes of the UPI. As shown in Figure 11, a shear test was conducted to evaluate shear failure of the UPI. In this test, local strains were calculated from the digitized positions of retro-reflective markers attached to the each of the tissues. Because multiple markers were placed on both the uterus and placenta, multiple values of local strain were measured. These values were averaged in the area of the UPI to calculate strain across the UPI and the modulus of each tissue. Data from this test indicate that the UPI fails when a strain of approximately 60% is achieved in the uterus. As shown in Figure 12, a tensile test was conducted to evaluate the tensile failure of the UPI. Unfortunately, the specimen failed at the grip attachment so no UPI tensile failure data were obtained. Moduli calculated from average strain on each tissue in the area of the UPI fell within the respective ranges of 12-63 kPa for placenta and 20-280 kPa for uterus defined by Pearlman et al. (1999).

These results provide the only quantitative data on placental separation strains, and the only failure strain value for one sample that was tested to failure. As a check on this single data point for UPI failure strain, failure strains of other tissues were obtained from the literature and are listed in Table 1. Results of this comparison indicate that the UPI failure stain of 60% determined by Ashton-Miller is reasonable.

The tests performed by Aston-Miller were modeled using finite-element techniques to verify that material properties of the placenta and uterus used in other modeling efforts are appropriate. Results were checked by comparing force and strain data from Ashton-Miller's tests to force and strain data predicted by the FEM simulation of the test.

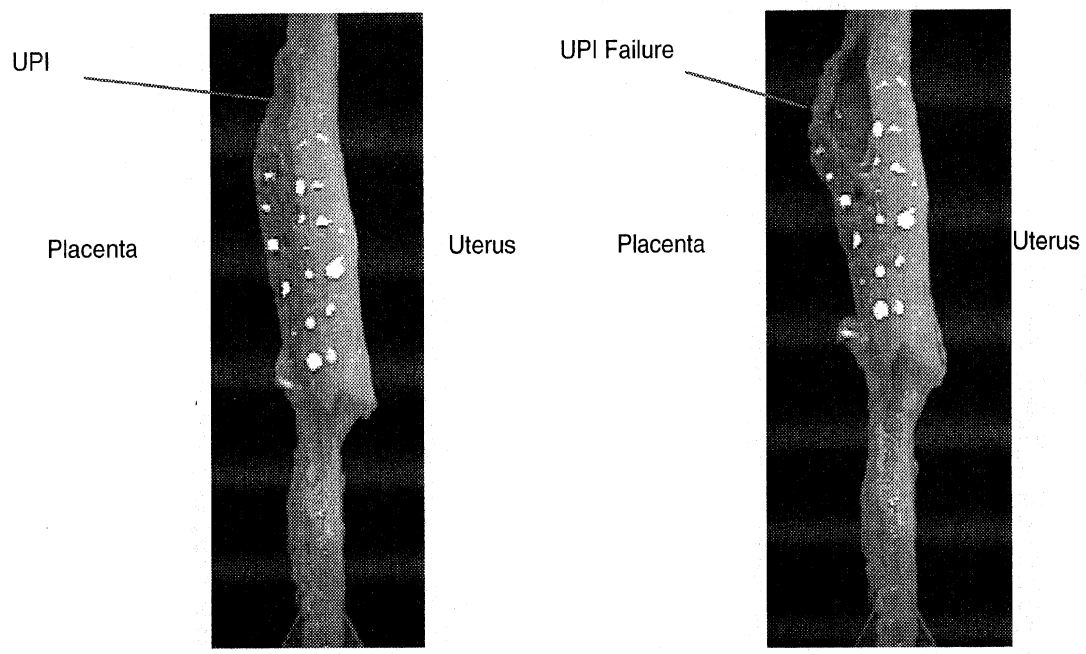

Figure 11. Shear testing of placenta, uterus, and UPI to determine UPI failure stresses and strains (from Ashton-Miller, unpublished).

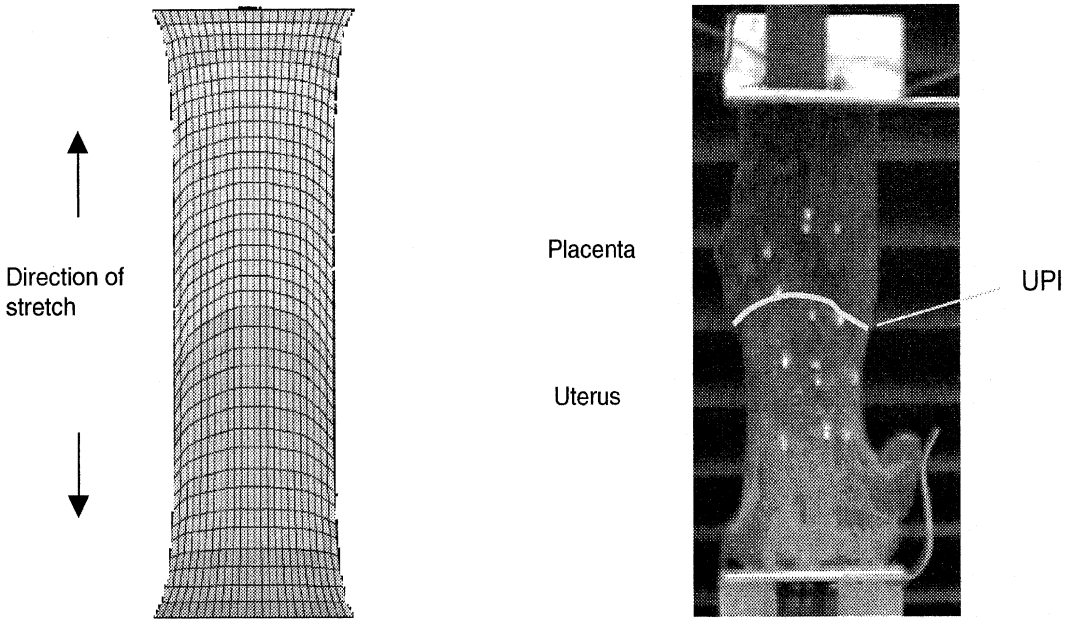

Figure 12. Deformed state of FEM simulation (left) and physical uniaxial tensile testing (right) of intact uterus, placenta, and uteroplacental interface (Ashton-Miller, unpublished).

Table 1.
Failure Conditions of Biological Tissues Used to Estimate UPI Failure Criteria

Source	Material	Test	Max stress (kPa)	Max strain	Failure
Ashton-Miller	UPI	shear		*0.58*[*1]	yes
Yamada	umbilical cord	tensile test failure force over placenta area	1.6-2.6		no
Ashton-Miller	UPI	tension	13.5	*0.572*	no
Pearlman et al.	uterus (2 specimens)	uniaxial tension 100 mm/min	13.1	*0.58*	no
Pearlman et al.	placenta (3 specimens)	uniaxial tension 100 mm/min	15.6	*0.622*	no
Pearlman et al.	uterus (2 specimens)	uniaxial tension 100 mm/min	78.6	*0.65*	no
McElhaney & Byars	bovine skeletal muscle	tension .001-1000	758-1965	.75	no
Wood	uterus	tension	483		yes
Pearsall & Roberts	uterus	tension .2 in/min	550-2069	0.3-0.95	yes
Kovanen et al.	rat skeletal muscle	tension	366-645	0.35-0.55	yes
Yamada	skeletal muscle	tension	108-157	*0.61*	yes
Best et al.	In vivo Rabbit skeletal muscle	tension 4-100 cm/s		*0.629* *0.608* *0.606*	yes
Ashton-Miller	UPI	modeling postpartum separation		0.70 circum. 4.5 radial	yes
Yamada	rabbit uterus	tension	177	1.5	yes

*Close to 60% estimated failure strain

4.3 Investigation of Mechanisms of Placental Abruption

Because the actual mechanisms of placental abruption are not known and have not been studied experimentally, it was necessary to hypothesize possible mechanisms based on an understanding of the anatomy of the pregnant abdomen and knowledge of occupant kinetics and kinematics under crash conditions. These hypothesized mechanisms were then explored using finite-element modeling techniques, clinical data collected in a separate study, physical modeling, and the limited data available on tissue properties and failure criteria described above, to establish which mechanisms of placental abruption are most appropriate to target in the design of the new pregnant abdomen.

Five possible mechanisms of placental abruption were hypothesized and explored. All of the mechanisms are based on the assumption that the interface between the placenta and uterus is weaker than either placental or uterine tissue. This assumption is supported by the prevalence of placental abruption relative to other traumatic injuries to the pregnant abdomen. The five hypothesized mechanisms of UPI failure are:

1) Fetus-placenta interaction,
2) Loading of the UPI from the inertia of the placenta,
3) Shear at the UPI from pressure-induced circumferential strains in the uterus,
4) Tensile loading at the UPI from pressure gradients generated by the inertia of the amniotic fluid, and

5) Shear strains in the UPI from local curvature changes in the uterus due to direct loading of the abdomen.

The following sections discuss each of the possible mechanisms in greater detail.

4.3.1 Fetus-Placenta Interaction

During an impact, the fetus may move within the uterus because of inertial or directly applied forces, causing it to push directly on the placenta and thereby begin to dislodge the placenta from the uterus. The feasibility of this mechanism causing UPI strains large enough to cause separation was investigated using FE models of a simplified human uterus and fetus to simulate direct loading of the uterus with fetus, placenta, and amniotic fluid. The first of these models represented a seven-month pregnant uterus with all parts represented by simplified geometric shapes. The fetus was represented by a rectangular block of fluid of a slightly higher density than the surrounding amniotic fluid. It was assumed that no fluid flow takes place during the impact event, and that the amniotic fluid and fetus can be characterized as incompressible elastic fluids. The viscous responses of the uterus and placenta were estimated using a short-term elastic modulus that was six times the long-term elastic modulus. Impact simulations involved dropping the filled uterus onto a rigid plate from a height of 0.5 m. The model proved to be stable, but the extreme amount of deformation was unrealistic, indicating that the fetus needed to be represented by a non-fluid element.

A second uterus model was constructed with the fetus represented by two ellipsoids made from solid elements. This model is shown in Figure 13 in the pre-impact and impact states. The second model also included fluid flow that would occur with large deformation of the uterus. Fluid flow was simulated by use of the LS-Dyna airbag material to give a sliding contact interface between the amniotic fluid and uterine wall. The amniotic fluid was represented as solid elements with a zero shear modulus. Vertical drops onto a rigid flat surface at angles of 0°, 30°, and 90° were simulated.

For the 30° and 90° contact angles, the fetus did not contact the placental area. For the 0° contact angle, the stress in the UPI showed two distinct peaks during the impact with the plate. The first peak occurred early in the event and was caused by local deformation of the uterine wall, which was strained due to changes in curvature as well as compressive strain as the uterus flattened against the plate. The second peak occurred at large uterine deformations when the fetus loaded the placenta and resulted in increased compressive stress and a small increase in shear stress at the UPI.

These results suggest that the contribution of the fetus to the stresses and strains generated in the UPI is probably small relative to the strain caused by deformation of the uterine wall. In addition, the placenta is located in the fundal region of the uterus in almost 80% of pregnancies (Freid, 1978). Consequently, an A-P compression, which would be commonly seen in a frontal impact, or inertial loading of the uterus, will not tend to cause fetal loading of the placenta.

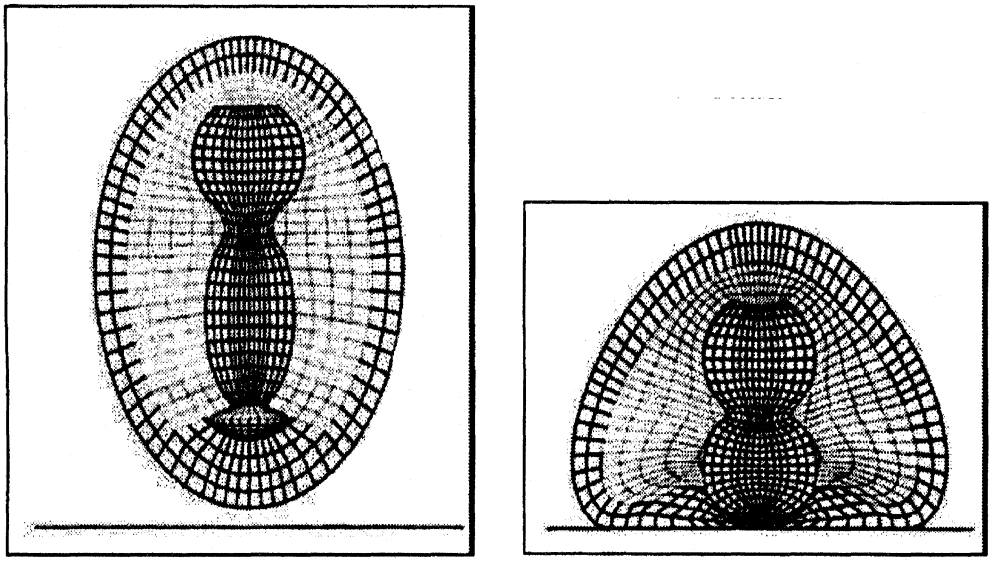

Figure 13. FE model of ellipsoid uterus with fetus comprised of solid elements in undeformed state (left) and deformed state during a simulated drop onto flat plate (right).

4.3.2 Inertial loading of the UPI by the Placenta

Modeling results from a series of simulations performed with a spherical uterus FEM, which were originally used to study how placental location affected stresses developed in the UPI under impact loading, were reanalyzed to explore how placental inertia affects stresses developed at the UPI. The model used in this series of tests is shown in Figure 14. The model consists of a spherical uterus that is posteriorly fixed to a rigid boundary to simulate the hypothesized viscous resistance to motion of the posterior uterus during dynamic loading. Impacts into a flat plate such that the rigid boundary condition was opposite the impact site (i.e., 180°) were studied. Only simulations with the placenta in a position such that impact-induced deformation of the placenta was small were considered for this analysis. To provide a consistent comparison between different simulations, the maximum shear stress at the UPI was recorded when the peak uterine wall strain resulting from impact with a flat plate was 60%. This value approximates the postpartum uterine strain of 58% at which placental separation occurred in the tissue tests conducted by Ashton-Miller (unpublished).

Table 2 lists the UPI shear stresses predicted by the model for placental locations of 0°, 30°, 60°, 90°, and 180° relative to the impact location. Deformation of the uterine wall due to contact with the simulated plate was found to be small enough so that stresses calculated with the placenta away from the contact location (i.e., in the 90° and 180° locations) was considered primarily due to placenta inertia. Shear stress data in Table 2 for all placental locations other than 90° and 180° are presented to illustrate that shear stress in the UPI due to deformation of the uterine wall is large relative to the shear stress produced by placental inertia.

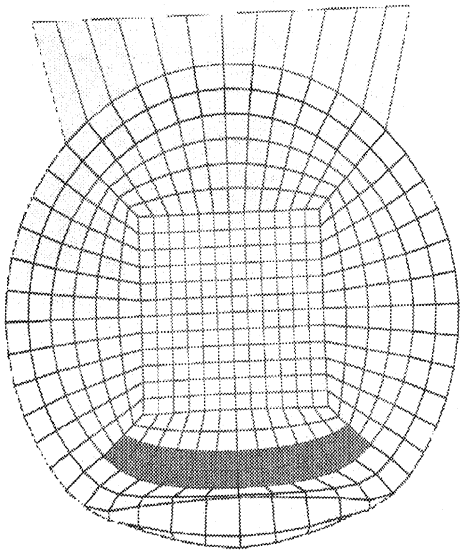

Figure 14. Spherical uterus model with placenta (shaded) used to study the effects of varying placental location on shear stress in the UPI under impact loading in an A-P direction.

Table 2.
UPI Shear Stress with Placenta Location Illustrating that Stresses Caused by Deformation are Much Higher than Those Caused by Placental Inertia

Placenta Location	Shear Stress[1] (kPa)
0° (at impact site)	18.7
30°	21.4
60°	22.4
90° (top of uterus)	6.1
180° (at constraint site)	1.0

[1] Measured when strain in the uterine wall reached 60%

4.3.3 Shear Strains at the UPI due to Pressure-Induced Circumferential Strains in the Uterus

Based on clinical impressions, it has been suggested in the medical literature (Pearlman et al., 1999) that the placenta is stiffer than the uterus because of its higher collagen content. If this is the case, the stiffer placenta will resist stretching more than the uterus, thereby creating shear strains at the UPI. If these strains exceed the UPI failure threshold, abruption will occur. This mechanism may be responsible for placenta detachment when the uterus contracts rapidly following delivery. Ultrasound measurements of the thickness of the placenta and uterine wall performed immediately following delivery have shown that the placenta detaches when uterine contractile strain reaches approximately 60% in the radial direction and 450% in the circumferential direction (Pearlman et al., 1999).

The FE model of a section of placenta attached to uterus shown in Figure 14 was used to explore how placental stiffness might affect strain generated at the UPI when the uterus

expands due to increased pressure from direct impact loading. Starting with the uterus and placenta having the same stiffness, the stiffness of placenta was increased until strains of 60% were achieved at the UPI under a 35 g deceleration, which is representative of a typical deceleration in a frontal impact. Results of this simulation indicate that for estimated abruption level strains to occur in the UPI by this mechanism, the placenta would have to be more than six times stiffer than the uterus.

Pearlman et al. (1999) performed tissue testing to determine the moduli of uterus and placenta tissue. In these tests, samples of uterus and placenta were cut in the plane of the uterine surface and quasi-statically stretched. Results of this testing are shown in Figure 15 and demonstrate a wide range of stiffnesses for both the uterus and the placenta. The modulus of the uterus is equal to and greater than that of the placenta. Thus, these data do not support the concept that high shear strains will develop in the UPI because the placenta is significantly stiffer than the uterus.

Even though the limited data available on the mechanical properties of the placenta and uterus do not support the medical view that the placenta is stiffer than the uterus, the potential for failure-level shear strains to develop at the UPI when the uterus is stretched from increased pressure still exists. As previously noted, tissue testing of intact uterus, placenta, and UPI indicates that the uterine strain required to cause abruption may lie between 50 and 60%, regardless of the difference or lack of difference in mechanical properties between the uterus and placenta.

A simple mathematical model of a spherical uterus was used to further investigate circumferential strain due to compression of the uterus. Calculations performed using this model indicate that if the bottom half of the uterus were compressed so that all fluid were displaced into the upper half of the uterus, the circumferential strain in the upper uterus would only be 26%, which is much less than the 60% uterine strain thought to be needed to initiate abruption. Thus, circumferential strain caused by fluid displacement is unlikely to result in placental separation.

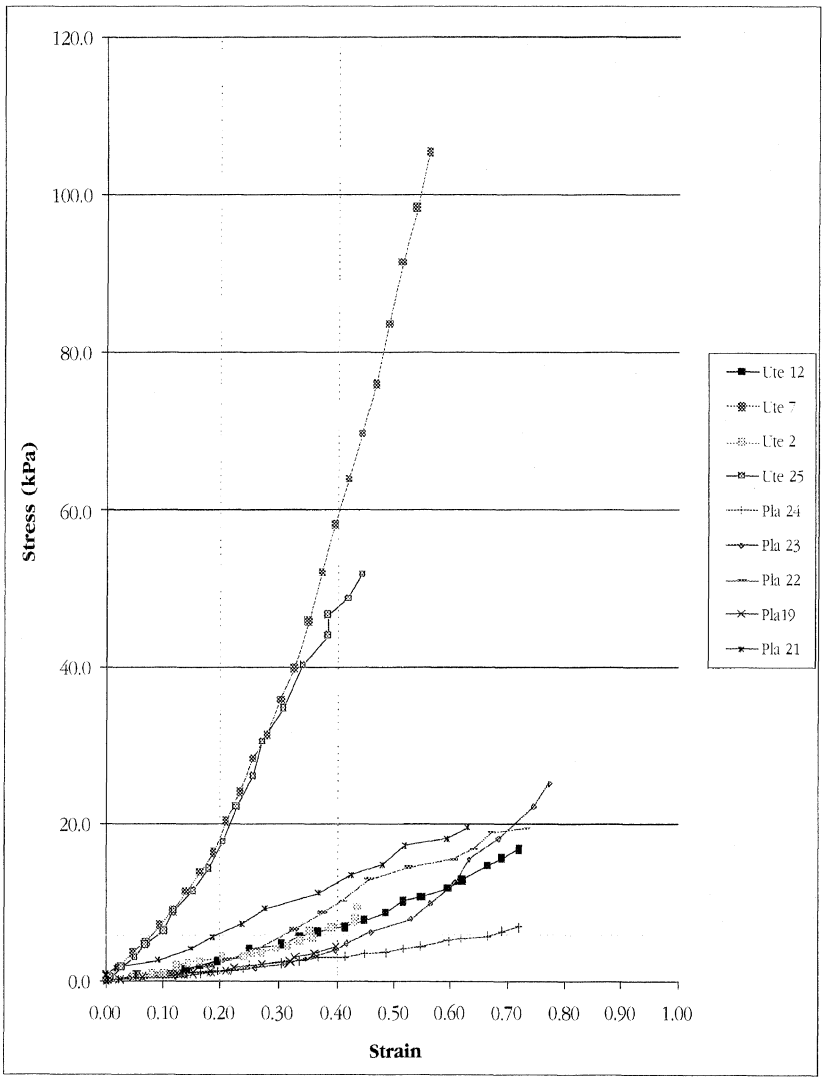

Figure 15. Result from tensile testing of uterus (denoted 'UTExx') and placenta samples (denoted 'PLAxx') performed by Pearlman et al. (1999).

4.3.4 Tensile Loading at the UPI due to Pressure Gradients Generated by the Inertia of the Amniotic Fluid

In a typical frontal impact, the seated pregnant occupant will move forward in the vehicle into the belt restraints, airbag, and knee bolster. If the pelvis is effectively restrained and decelerated through a properly positioned lap belt and/or a knee bolster, the uterus and its components will tend to keep moving forward relative to the maternal skeleton (i.e., pelvis and spine). It is hypothesized that forward movement of the posterior uterus would be constrained under these dynamic conditions by surrounding soft tissues that behave as incompressible viscous fluids. Any forward displacement of the uterus relative to the spine would require the viscous tissues that surround the uterus to flow in behind it. At the loading rates of high-speed impacts, viscous resistance to tissue motion would

likely be unable to fill the space rapidly, and "suction" will be created that will constrain the uterus at its posterior surface.

Under an anterior-to-posterior deceleration of the pelvis, these uterine boundary conditions and the inertia of the uterus will create an anterior-to-posterior pressure gradient in the uterus. This pressure gradient is characterized by negative pressures in the posterior uterus that might generate tensile strains on portions of the UPI located in this region. These negative pressures could develop early in the impact before belts or other vehicle components (e.g., steering wheel) load the abdomen. The behavior of the pressure gradient is similar to that found in contre-coup head injury, where negative pressures develop in the posterior brain following a blow to the front of the head due to anterior rebound movement of the brain and cerebrospinal fluid.

The spherical finite-element model of the pregnant uterus was modified as shown in Figure 16 to study the anterior-to-posterior pressure gradient generated by amniotic fluid inertia during deceleration of the pelvis. The utero-placental interface was modeled using a series of beam elements to connect the placenta to the uterus. The beam elements were oriented perpendicular to the interface surface to allow the tensile and shear stiffnesses to be varied independently. The uterus was constrained posteriorly by a rigid fixture, which was decelerated at a constant rate of 35 g. This level of deceleration is typical of the pelvic deceleration of a 30 mph barrier impact just after the knees contact the knee bolster.

As shown in Figure 16, at 3 ms after the application of the decelerative pulse, a pressure gradient develops throughout the uterus with a pressure of -34 kPa (approximately -5 psi relative to atmospheric pressure) near the posterior boundary and with minimal deformation of the whole uterus. The negative pressure rises to -40 kPa (-6 psi relative to atmospheric) at 10 ms into the deceleration pulse.

A pressure of -34 kPa, which FE modeling indicates can occur in a crash of moderate severity, would result in a net tensile stress that is within the plausible failure range on any portion of the UPI in the posterior uterus. This is based on UPI tensile properties measured by Pearlman et al., which indicate that the UPI can withstand tensile stresses up to 15.6 kPa without failure. This value is taken as a lower bound on the tensile failure of the UPI. An upper bound on UPI tissue failure of 177 kPa may be approximated from data provided by Yamada (1970) on rabbit uterus failure, and the assumption that the UPI is weaker than either the uterus or the placenta. Based on a UPI failure stress in shear of approximately 10 kPa, the UPI tensile failure stress is likely closer to the lower bound than the upper.

Because the placenta is most often attached to the fundal region of the uterus, it is possible that only a small portion of the UPI is located in the posterior region of the uterus, and thereby most susceptible to tensile failure due to negative pressures caused by fluid inertia. However, even a partial abruption can threaten the life of the fetus, and can propagate to other regions of the UPI.

Negative pressure in the posterior uterus is thought to be a likely mechanism of UPI failure. This hypothesis is based on intrauterine pressures from FE simulations of a human uterus under decelerations that are typical of a frontal crash. As shown in Figure 16, a negative pressure of 34 kPa is developed at the posterior UPI when a 30-g deceleration is applied. This stress is above the hypothesized lower bound for UPI failure of 15.6 kPa.

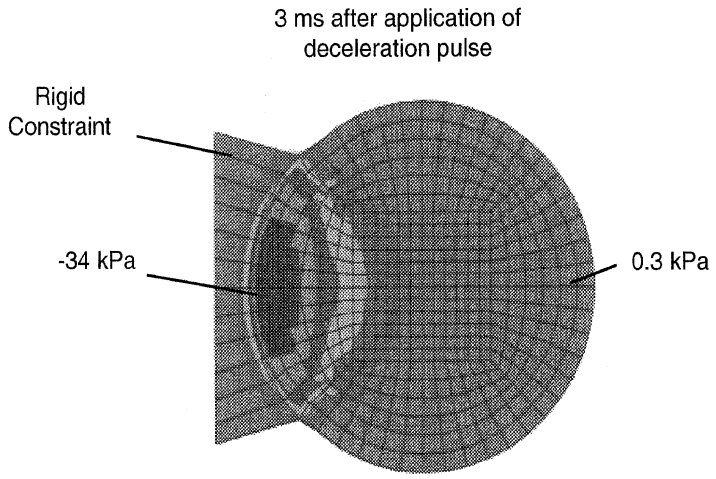

Figure 16. Stresses developed in FEM of human uterus under inertial loading conditions.

4.3.5 *Shear Strains in the UPI from Local Curvature Changes in the Uterus Due to Direct Loading of the Abdomen*

A FEM of the human uterus with a placental representation and hemispherical boundary constraint was used to study the effects of curvature changes in the uterus due to direct loading on shear strains at the UPI. This model is shown in an undeformed state in Figure 17. Material properties used for the uterus and placenta were obtained from tissue data collected by Pearlman et al. (1999). The rigid constraint shown in Figure 17 was used to simulate attachment of the uterus to the cervix and the hydrodynamic suction that is hypothesized to anchor the posterior uterus in place under inertial loading as described in the previous section. The uterus model was impacted by a 2.5 cm diameter hemispherical impactor. The resulting deformations and stresses calculated at the uteroplacental interface are shown in Figure 18. The circumferential strain in the uterus near the UPI was calculated and compared to uterine stretch at UPI failure estimated from tissue testing and from failure characteristics of similar tissues.

For this simulation, the peak uterine strains reached levels greater than 60%, which, as previously noted, may be sufficient to cause abruption at the UPI based on tissue failure measurements. Results of this simulation imply that curvature changes due to direct loading in the region of the placenta have the potential to cause abruption-level strains.

As shown in Figure 18, stresses and strains rapidly decrease away from the site of impact where the curvature of the uterus is greatest. Thus, this mechanism is only applicable to situations where the impact loading is close to the location of a portion of the placenta.

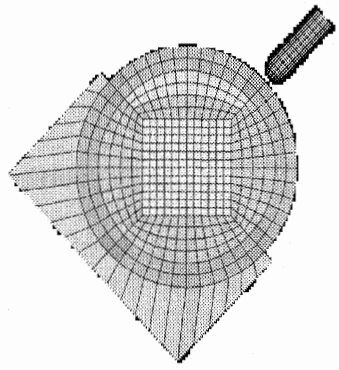

Figure 17. Direct loading of FEM uterus by 2.54 cm diameter hemispherical impactor.

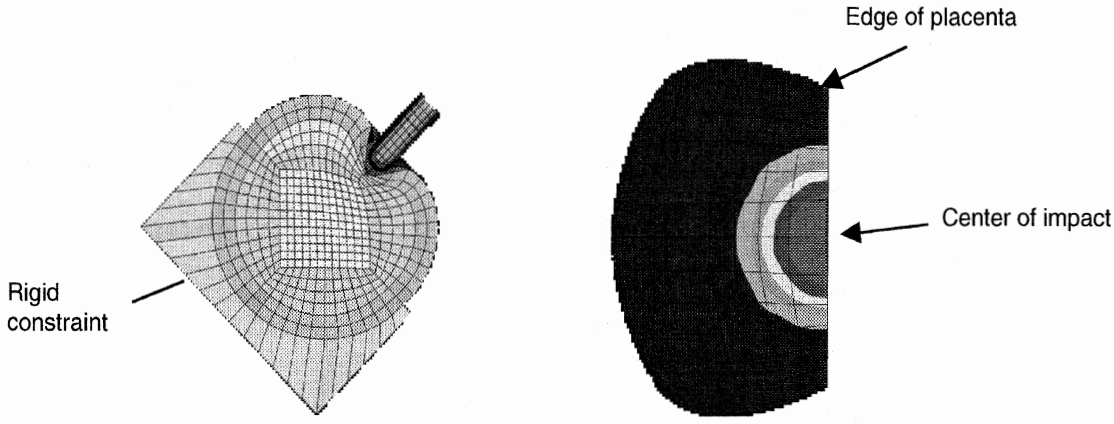

Figure 18. Stress distribution in FEM of uterus after impact with hemispherical impactor.

4.4 Likely Hypothesized Injury Mechanisms

It is likely that more than one of the hypothesized injury mechanisms described above work in combination to cause placental abruption in motor-vehicle crashes or other trauma-inducing events. However, based on the FE modeling, physical testing, and engineering judgment, it was concluded for the purposes of this project that fetal contact with the placenta, inertial loading by the placenta, and circumferential uterine strain due to increased uterine pressure are mechanisms that would be least likely to contribute to placental abruption in a motor-vehicle crash.

The remaining two hypothesized injury mechanisms were considered the most likely mechanisms responsible for UPI failure and placental abruption in motor-vehicle crashes. These mechanisms are:

1) negative pressure at the posterior boundary of the uterus due to fluid inertia generated in the absence of, or prior to, direct loading of the uterus, and

2) shear strain at the UPI due to local deformation of the uterine wall in an area where the placenta is attached.

As described in Sections 6, 7, and 8 of this report, these two mechanisms were targeted in the design of the new pregnant abdomen and, more importantly, in attempting to incorporate appropriate instrumentation to assess the risk of placental abruption in different ATD testing scenarios.

5.0 DESIGN SPECIFICATIONS

5.1 Design Goals and Constraints

As noted in the Introduction and Background sections, three main goals were identified for the design of the new pregnant abdomen: 1) more realistic anthropometry, 2) more humanlike force-deflection response in anticipated dynamic loading environments, and 3) the capability to assess the risk of fetal loss due to placental abruption. In addition to these primary design goals, the design effort involved the consideration of the following other design goals and constraints:

- *Packaging.* The new pregnant abdomen was targeted for use with the Hybrid III small-female dummy, which is the only adult "female" dummy currently available. However, because smaller females tend to have greater difficulty achieving a good fit of belt restraints and typically sit closer to the steering wheel and airbag module, the small female probably represents a worst-case risk assessment for fetal loss. As with the first pregnant dummy, the new pregnant abdomen should be incorporated into the standard small-female Hybrid III ATD with minimal modifications to standard components and with no significant changes in any of the response characteristics.

- *Durability.* The new pregnant abdomen should demonstrate high durability in repeated tests. In addition to durability of the physical components of the abdomen, robust instrumentation is needed to withstand abdomen loading by steering wheels, three-point belts, and airbags.

- *Repeatability and Reproducibility.* Repeatability and reproducibility were key design considerations. Measured response and injury assessment values should not vary more than ±10% for the same test conditions with the same or different dummies. This requires that the dummy shows no unreasonable changes in response and injury assessment for insignificant changes in ATD and restraint positioning.

- *Cost.* Abdomen components and instrumentation should be reasonable in cost, and in line with the cost of other dummy components and instrumentation.

- *Ease of Repair and Usability.* For the abdomen design and instrumentation to be acceptable to the automotive safety community, it should not present any unusual or unreasonable demands or problems for dummy users. This includes ease of repair and/or replacement of pregnant dummy components, and ease of processing instrumentation signals and computing injury criteria.

5.2 Anthropometry

The geometry of the pregnant abdomen is important for achieving representative belt fit, and for appropriate interactions of the ATD with restraint systems and steering wheels

during crash testing. Prior to the current series of GM-sponsored projects, the only information on pregnant anthropometry in the literature was contours that were estimated by scaling abdominal depth measurements from 5th percentile Japanese pregnant women to their larger 5th percentile American counterparts assuming that abdominal dimensions are proportional to maternal stature and weight (Culver and Viano 1990). This anthropometric scaling was used to determine the abdominal geometry of the original pregnant dummy. However, the assumption that the size of the pregnant abdomen scales directly with maternal anthropometry is not supported by findings of a recent study of pregnant anthropometry performed by Klinich et al. (1999). The anthropometry for the new pregnant abdomen was therefore based on data collected in this more recent study.

5.2.1 Summary of Seated Anthropometry During Pregnancy

Stature categories and sample sizes for the pregnant subjects tested by Klinich et al. are shown in Table 3. Several measures were taken on each subject to characterize the size of the pregnant abdomen during four test sessions that occurred at approximately 3, 5, 7, and 9 months of gestation. These include abdomen depth, abdomen circumference, and fundal height. As shown in Figures 19, 20, and 21, these measures do not show any correlation with maternal stature, but rather are dependent on the size of the uterus, which is highly dependent on the size of the fetus. Since most women deliver six to nine pound infants regardless of maternal stature, it is reasonable that the pregnant abdomen measurements are relatively independent of maternal stature.

Table 3.
Stature Group Ranges, Means, and Number of Subjects

Stature Group	Stature Range (mm)	Mean Stature at First Test Session (mm [in])	Number of Subjects
1	< 1549	1513 [59.6]	3
2	1549-1595	1579 [62.2]	4
3	1595-1638	1627 [64.0]	5
4	1638-1681	1656 [65.2]	5
5	>1681	1708 [67.2]	5

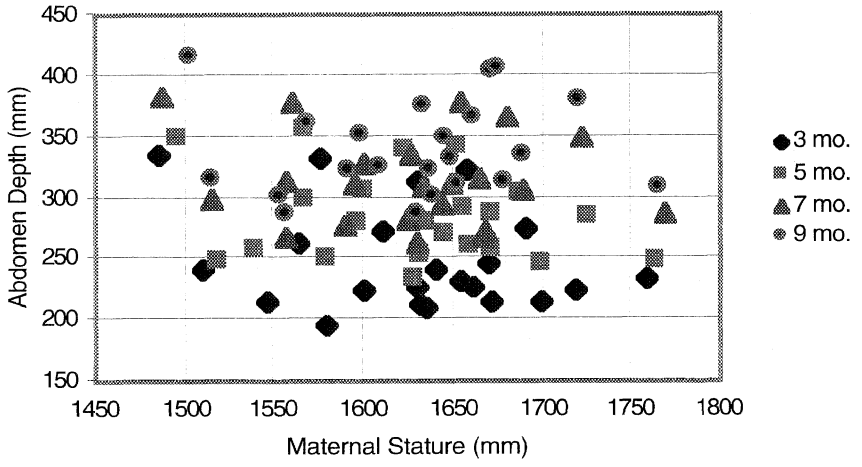

Figure 19. Abdomen depth vs. stature (r=0.126) from Klinich et al. (1999).

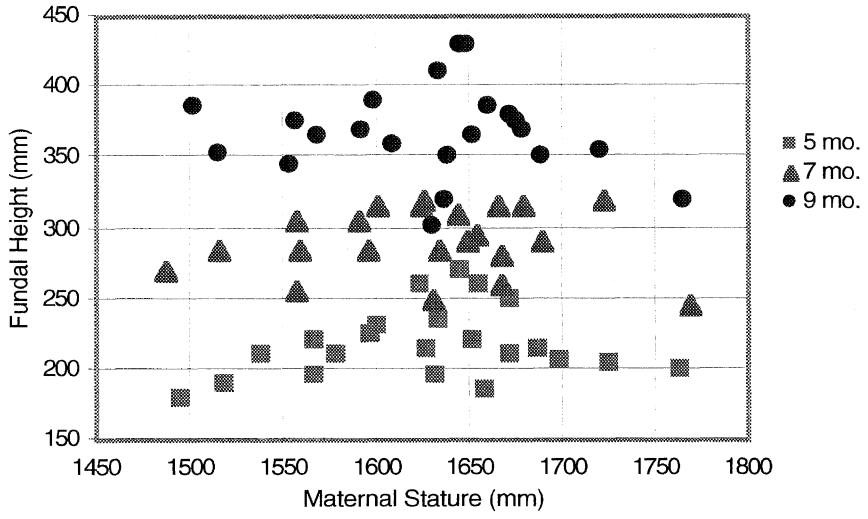

Figure 20. Fundal height vs. stature (r=0.000) from Klinich et al. (1999).

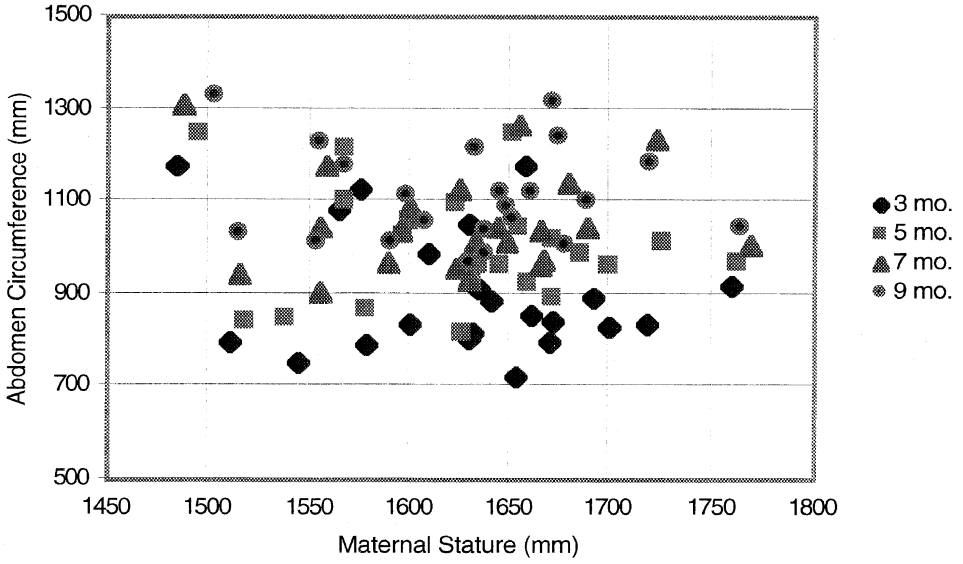

Figure 21. Abdomen circumference vs. stature (r = 0.114) from Klinich et al. (1999).

To quantify seated anthropometry, subjects were seated in a laboratory test buck that simulated different interior vehicle package configurations. A sonic digitizing system was used to measure the midsagittal abdominal profile, which included the palpated pubic symphysis, the bottom of the sternum, and eight points in between. To compare the abdomen shapes independent of occupant position and stature, the abdomen contour data for each subject were aligned at the pubic symphysis, and oriented so that the line connecting the pubic symphysis and the bottom of sternum was at an angle of 60° relative to horizontal.

Variations in abdominal contour with vehicle package geometry were small, suggesting that abdominal shape is not significantly affected by vehicle package and restraint geometry. Consequently, a single abdomen contour for each subject and test session was calculated by averaging the x and z coordinates of the abdomen contour points for all test configurations.

Average abdomen contours from the third test session (corresponding to a gestational age of about 30 weeks) are shown in Figure 22. These contours were analyzed to develop a contour for the new pregnant crash test dummy.

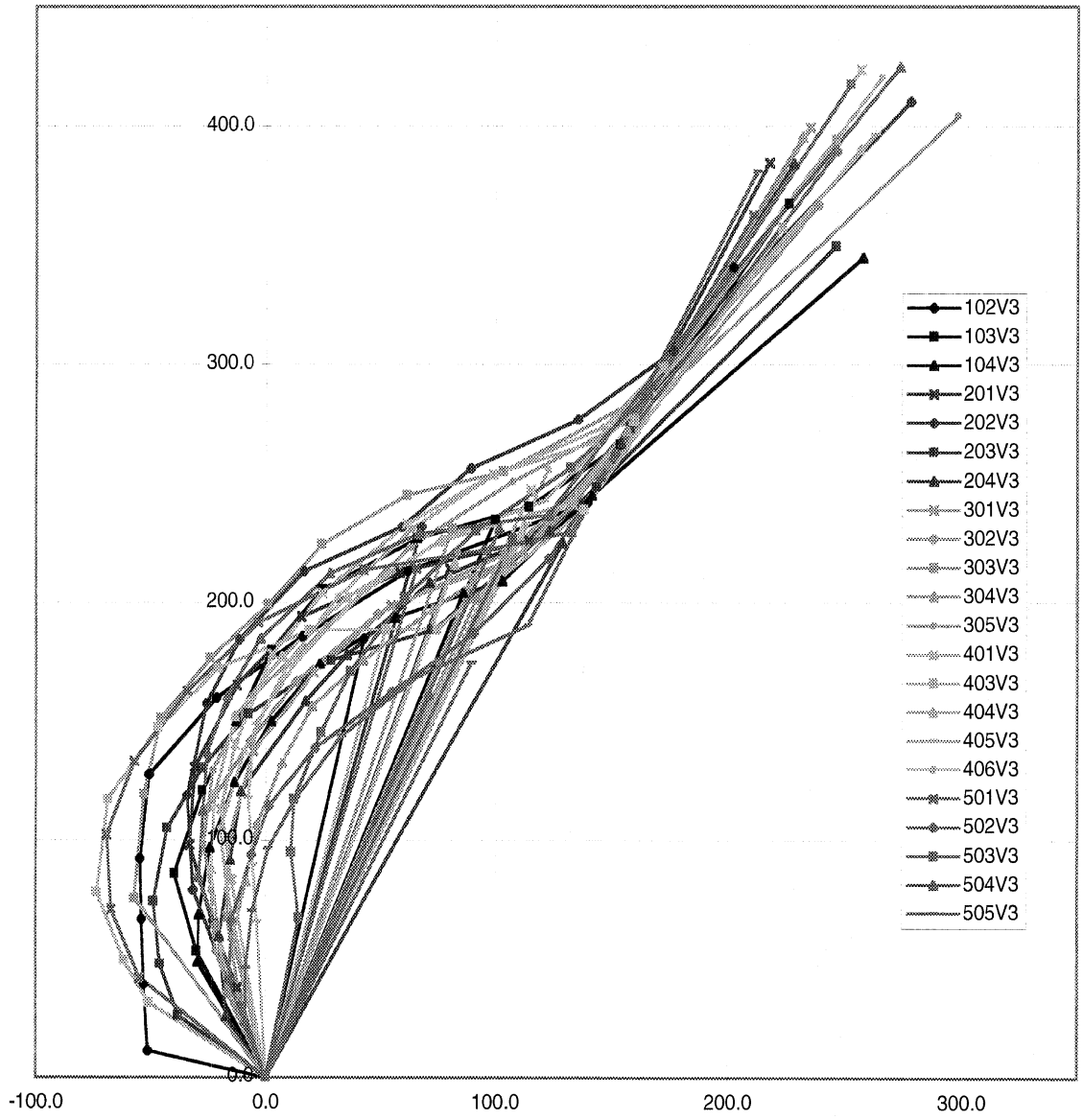

Figure 22. Composite plot of average abdomen contours from the third test session. Lines connect points along the mid-sagittal contour of the abdomen from supersternale to pubic symphysis as well as from pubic symphysis to fundus. From Klinich et al. (1999).

5.2.2 *Selection of MAMA-2B External Contour from Anthropometric Data*

Four different analyses of the abdominal contour data shown in Figure 22 were performed to determine the midsagittal contour for the new pregnant abdomen. These include:

- averaging the midsagittal contour data from all subjects,
- averaging the midsagittal contours after deleting visually selected outlier contours,
- averaging midsagittal contours from women whose abdominal depth was within 1 SD of the mean abdominal depth at 30 weeks gestation, and
- averaging midsagittal contours from women who were considered thin based on initial body mass index and weight gain during pregnancy

Since the anthropometric measurements of pregnant abdomen depth, abdomen circumference, and fundal height do not correlate with stature, all stature groups were included in each analysis.

Figure 23 shows the midsagittal contour obtained from each of these methods. Because the differences are small, the average of all subject contours was used to define the shape of the new pregnant abdomen. Figure 24 compares this contour with that of the first pregnant abdomen, which protrudes much too far forward.

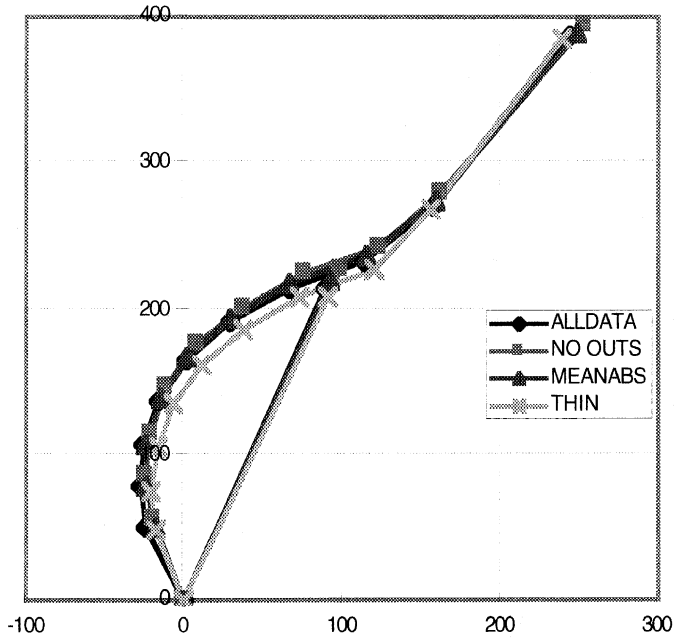

Figure 23. Comparison of mean abdomen contours for the four analysis methods from Klinich et al. (1999).

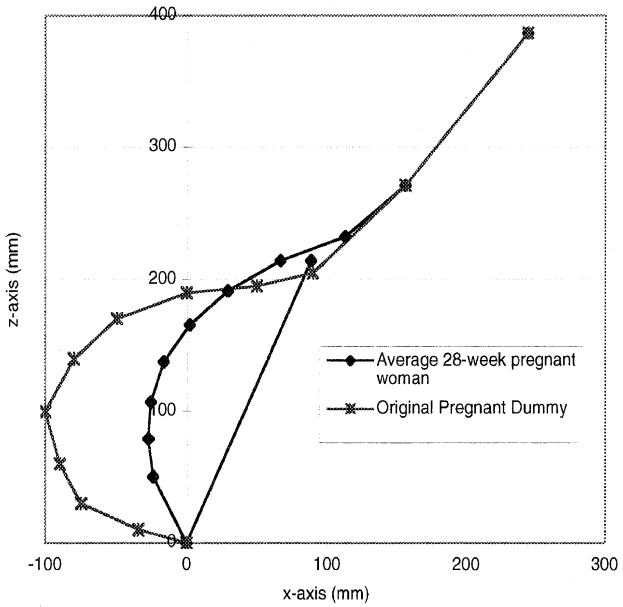

Figure 24. Comparison of the midline abdomen contour for the new abdomen to that of the first pregnant dummy. From Klinich et al. (1999).

5.2.3 Dummy Mass

The target weight for the new pregnant dummy was based on the weight of the standard small adult female dummy with instrumentation (108 lb or 49 kg) plus the recommended weight gain at 30 weeks gestation. A suggested target schedule for weight gain is roughly 0.23 kg (1/2 pound) per week for the first half of pregnancy and 0.45 kg (one pound) per week for the second half of pregnancy (Institute of Medicine, 1990). Following this schedule, a 30-week pregnant woman should have gained approximately 9.1 kg (20 pounds). The target weight for the new pregnant dummy was therefore selected to be approximately 58 kg (49 kg plus 9.1 kg). This is identical to the mass selected by Viano et al. (1996) for the original pregnant dummy. Since only about 40% of the weight gain results from volume increases of the uterus and the components that it contains (fetus, placenta, and amniotic fluid) approximately 3.6 kg (8 lb) of the additional mass should be placed in the pregnant abdomen. The remaining 5.5 kg (12 lb) of weight gain is distributed among blood (other than the volume contained in the placenta), fluid, breasts, and maternal fat reserves, and should therefore be placed in body regions other than the abdomen.

The desired location for the seated center of gravity (CG) of the new pregnant dummy was based on a study of the changes in segment masses of pregnant women throughout pregnancy (Jensen et al., 1996). These researchers estimated a percent weight gain per week for each body segment that was linearly proportional to gestational age. The calculated weight gain factors were applied to the segment masses of the Hybrid III small female dummy to determine a seated CG location with weight gain of 9.1 kg (20 lb) distributed appropriately. Using this approach, the seated whole-body CG of the new

pregnant dummy is 227 mm above and 169 mm forward of the H-point. This location is 8 mm forward and 10 mm down from the standard Hybrid III small female seated CG location.

5.3 Response Corridors for the New Pregnant Abdomen

The mechanical response of a dummy component is typically based on force-deflection data collected during dynamic testing of unembalmed cadavers. Since such data are not available for pregnant women, it was necessary to use FE modeling and quasi-static testing to estimate how the unknown dynamic response of the pregnant abdomen relates to the known dynamic response of the non-pregnant human cadaver abdomen.

One of the factors that was thought to be capable of influencing the dynamic response of the pregnant abdomen relative to the non-pregnant abdomen was resting pressure. For non-pregnant abdomens, the resting abdominal pressure is 8 mm Hg, while it is 15 mm Hg inside the pregnant uterus. To investigate the potential effects of these pressure differences on the dynamic response of the abdomen, a simple finite element model of a fluid-filled ovoid was constructed and exercised with the initial pressure in the fluid set to each of these values. Dynamic loading tests were simulated, but showed no significant differences in response for the two initial pressure conditions. The differences in initial pressure were small compared to the pressures predicted to result from loading. Results of these simulations indicate that changes in abdominal pressure do not lead to important differences in dynamic response between pregnant and non-pregnant abdomens.

To further investigate differences in the dynamic response of the pregnant abdomen, quasi-static testing of pregnant and non-pregnant abdomens was used to estimate how the dynamic response of the pregnant abdomen might relate to that of the non-pregnant abdomen*. Quasi-static loading was applied to the abdomens of five pregnant women and ten non-pregnant volunteers using a 2.54 cm diameter bar and a 7.6 cm diameter disc. Results of these tests indicated that the quasi-static stiffness of the pregnant abdomen is not significantly different from that of the non-pregnant abdomen. The results of these tests may have been compromised by the need to limit applied forces to 45 N or less and abdominal penetration to 5 cm or less.

Because the results from simple modeling and quasi-static subject testing do not suggest that the response of the pregnant abdomen is different from that of the non-pregnant abdomen, it was decided that there was no basis for using different dynamic response corridors for the pregnant and non-pregnant abdomens. Consequently, response corridors for the non-pregnant abdomen were assumed to be valid for the pregnant abdomen. Data from the literature on the dynamic response of human abdomens collected from cadaver testing are summarized in Section 3.4.

---

* The rights, welfare, and informed consent of the volunteer subjects who participated in this study were observed under guidelines established by the U.S. Department of Heath and Human Services on Protection of Human Subjects and accomplished under medical research design protocol standards approved by the Committee to Review Grants for Clinical Research and Investigation Involving Human Beings, Medical School, The University of Michigan.

Target response corridors for the new pregnant abdomen for rigid-bar, belt, and out-of-position airbag loading are shown in Figures 7, 8 and 9. Corridors developed for the rigid-bar and belt tests were equal-stress, equal-velocity scaled (Eppinger, 1976) from the reference mass of 76 kg to the pregnant dummy mass of 58 kg. This allowed unscaled abdominal response data to be compared to rigid-bar and belt corridors. Equal-stress, equal-velocity scaling is discussed in greater depth in Appendix A.

The scaled bar and belt corridors are shown in Figures 25 and 26, respectively. Out-of-position airbag loading corridors were not equal-stress, equal-velocity scaled because the airbag loading event described by the corridors was complete before the test subject began to move and, consequently, equal-stress, equal-velocity scaling was not appropriate. Two belt-loading corridors are shown in Figure 26. The preliminary, trapezoidal corridor was used for development and validation of the pregnant dummy belt-loading response. Based on additional analyses of the cadaveric response data, a final, more restrictive corridor was later proposed by Hardy.

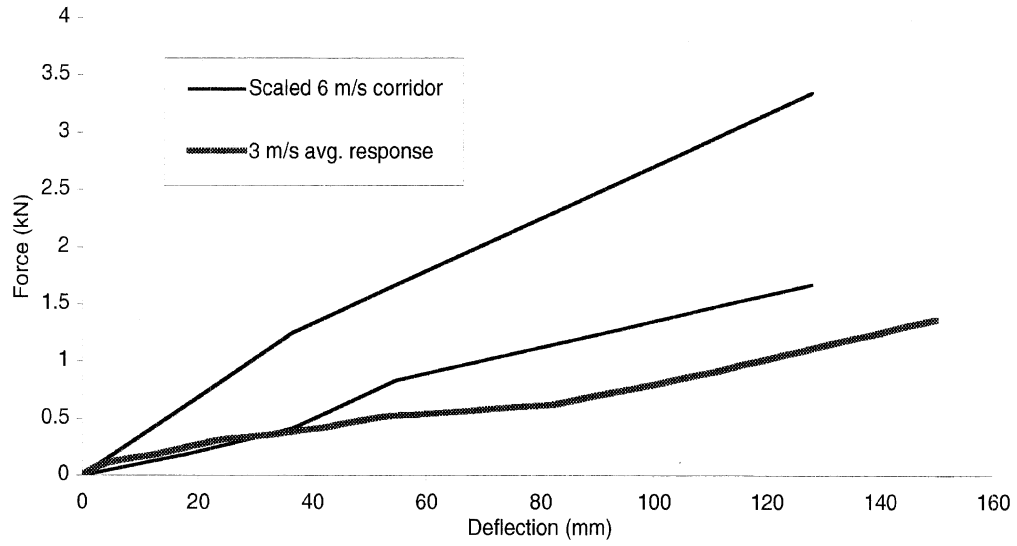

Figure 25. 6 m/s rigid bar loading corridor and 3 m/s averaged response scaled to the pregnant dummy mass using equal-stress, equal-velocity scaling.

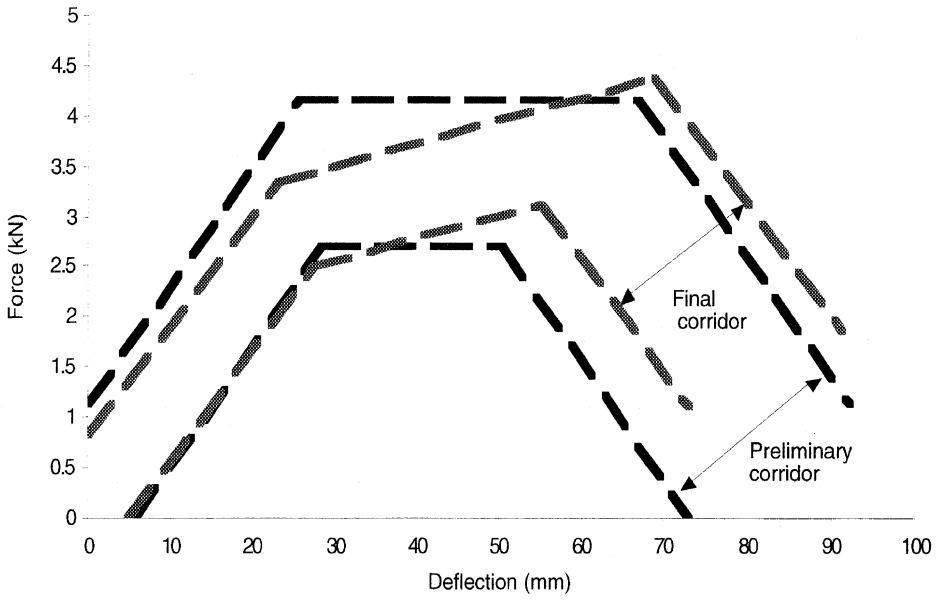

Figure 26. Initial and modified belt-loading corridors developed by Hardy et al. (2001). Both corridors are scaled to the pregnant dummy mass of 58 kg from the reference mass used to develop the corridors (76 kg) using equal-stress, equal-velocity scaling (Eppinger, 1976). This allowed force-deflection responses of the new pregnant abdomen to be plotted in unscaled format.

6.0 ABDOMEN DESIGN AND DEVELOPMENT

6.1 Design Approach

In the past, the design of crash dummy abdomens has included the use of elastic urethane foams, damped metal ribs, air-filled bladders, and frangible floatation foams. Melvin et al. (1985) proposed the use of fluid-filled bladders for the design of both thoracic and abdomen components of an advanced multi-directional crash dummy. Schneider et al. (1992) explored this concept of inextensible fluid-filled bladders further in the development of a thorax for the NHTSA's advanced frontal-impact dummy. Several concepts were tested to obtain a more biofidelic viscoelastic response, improved inertial characteristics, improved regional response, and omnidirectional sensitivity. These concepts included fluid-filled and fluid- and gas-filled bladders, with controlled and variable orifice venting. Elastomeric bladder materials were researched along with various bladder-wrapping materials to obtain a rate-sensitive (i.e., viscoelastic) response. Due to time constraints, this development effort did not result in a usable fluid-filled thorax. However, many of the design approaches researched in this program have potential applications to the design of a pregnant abdomen.

More recently, Rouhana et al. (unpublished) expanded on the fluid-filled bladder concept in the development of a reusable, rate-sensitive abdomen for the Hybrid III midsize-male dummy. This abdomen consists of a silicone rubber bladder that has a dynamic force-deflection response within the cadaver response corridors developed by Cavanaugh and Hardy. The rate sensitivity observed in the bladder response is obtained from the viscoelastic characteristics of the bladder material and the viscosity of the fluid within the bladder. The bladder is manufactured using a mandrel dipping process that was adapted for dummy component development. The silicone rubber bladder material has several advantages over elastomeric materials commonly used in dummy components (e.g., vinyl and urethane). These include its high durability, the ability to bond components to the bladder, and the option to cut into and reseal the bladder using silicone-based glues.

Based on previous research performed by Schneider (1992), Viano (1996), and Rouhana (unpublished), two basic design options were considered for the uterine component of the pregnant abdomen: a solid mechanical insert, and a fluid-filled bladder insert. The fluid-filled bladder concept was ultimately selected for three reasons. First is its potential to provide greater rate sensitivity to impact loading with minimal temperature dependency. Second, it was believed that this design approach offered the most potential for instrumentation and measurements that would be relevant to the hypothesized injury mechanisms (see Section 4.4). Third, the success of the concurrent project by Rouhana to develop a rate-sensitive fluid-filled bladder representation for the non-pregnant abdomen for the Hybrid III midsize male ATD provided confidence that this approach was feasible and resolved several design and fabrication problems.

From the beginning, consideration was given to including physical representations of the fetus as was done in the first pregnant abdomen, as well as to including a placenta that attaches to a uterus. Such components are visually appealing, but are believed to be

unnecessary, and possibly problematic, in obtaining the desired response biofidelity and repeatability, as well as to measuring response variables that best relate to the risk of fetal injury and loss. It was therefore decided to design the new pregnant abdomen without including a fetus or placenta, and only to add these at a later date, if the results of design and testing showed a clear need and purpose for including them.

6.2 Fitting the Pregnant Abdomen into the Small-Female Hybrid III ATD

To locate the proposed 30-week abdominal contour (Figures 23 and 24) on the Hybrid III ATD, an appropriately scaled abdominal contour was superimposed on a sagittal-plane drawing of a small female Hybrid III ATD. This exercise demonstrated that the top of the uterus would be positioned at the level of the fourth rib and that the anterior portions of the lower ribs would interfere with proper position of the uterus. To resolve this problem, half of the sternum plate and varying amounts of rib material were removed from the 4th through the 6th ribs to create an inverted "v"-shaped opening. When viewed from the front, this opening appears as illustrated in the finite element model (FEM) representation of the redesigned ribcage in Figure 27.

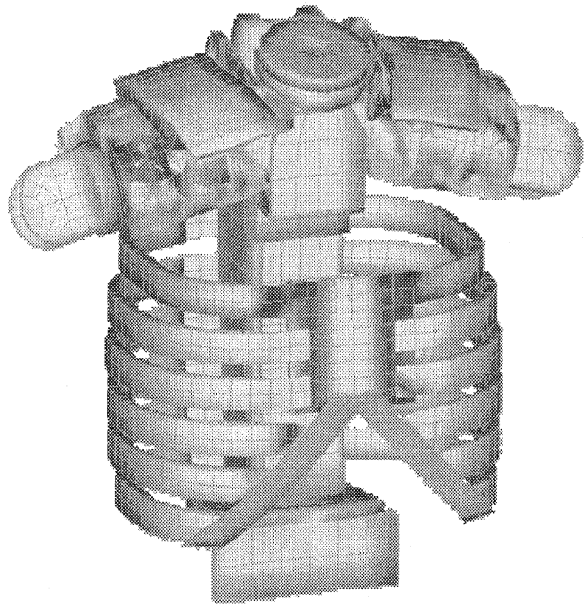

Figure 27. FEM showing geometry of modified Hybrid III ribcage. Stiffener plate runs from the sternum plate along the anterior and medial edges of the ribs.

Before proceeding with the rib redesign, computer simulations of 6.7 m/s pendulum impacts were performed using the FEM shown in Figure 27 to determine the force-deflection characteristics of the modified ribcage. The calculated response is shown in Figure 28, with the response of a standard ribcage included for comparison. To stabilize the ends of ribs 4 to 6 and to stiffen the rib response, spring steel stiffeners were added to each side of the rib cage as shown in Figure 29. The performance of the redesigned rib set, with the spring steel stiffeners, was determined through both pendulum testing and

computer modeling to be within the performance specification for the small female Hybrid III dummy. The measured impact response of the redesigned ribcage is shown in Figure 30 along with the thoracic response for an unmodified small-female thorax that meets the specification.

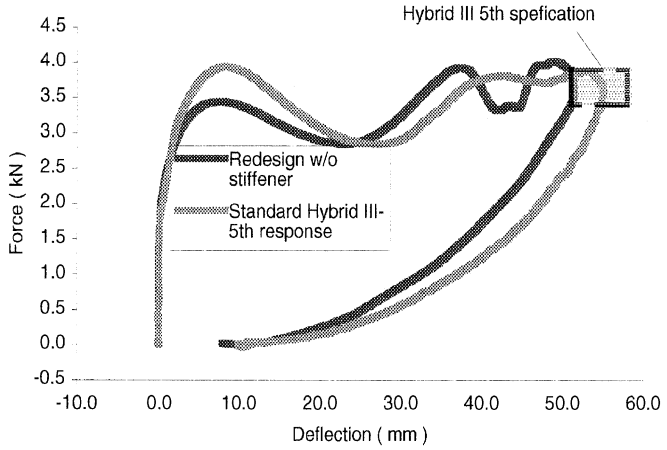

Figure 28. Comparison of FEM simulated responses to the 6.7 m/s pendulum calibration tests of the standard and modified small female ribcages.

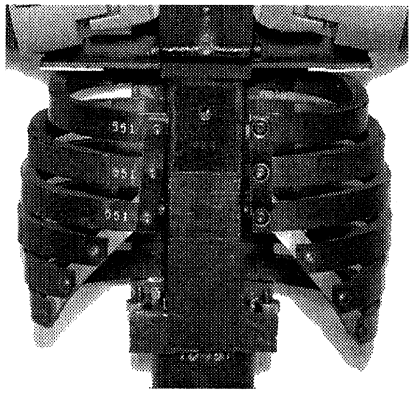

Figure 29. Modified Hybrid III ribcage with spring-steel stiffeners connecting the ends of ribs 4 through 6 on each side (redesigned sternum plate not shown).

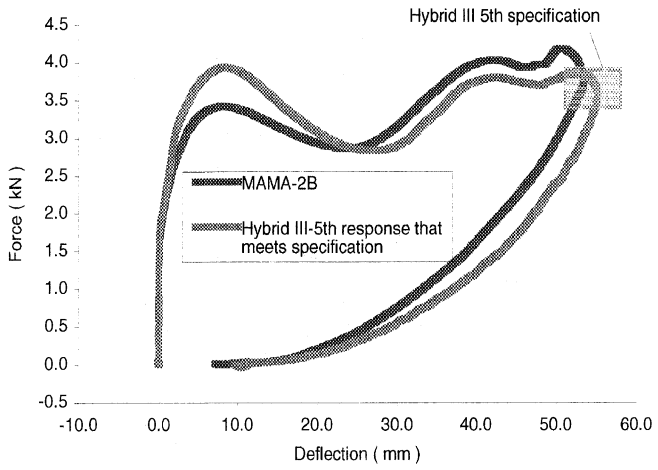

Figure 30. Force-deflection response for the modified and standard small-female ribcage to 6.7 m/s pendulum calibration tests.

6.3 Early Development of the Uterine Component

To develop the first prototype of the new pregnant abdomen, a clay model of a 30-week uterus was constructed based on anthropometric data previously described. As shown in Figure 31, the model was constructed inside the small female ATD with the modified pelvis used for the first pregnant dummy and with the three bottom ribs removed. As shown in Figure 32, the pelvis from the first pregnant dummy is a standard Hybrid III small female pelvis with a crescent-shaped block of material removed from the pelvic cavity to accommodate the lower portion of the pregnant abdomen. The completed clay uterus model was removed and used to make a mold from which the first prototype uterus or bladder was fabricated.

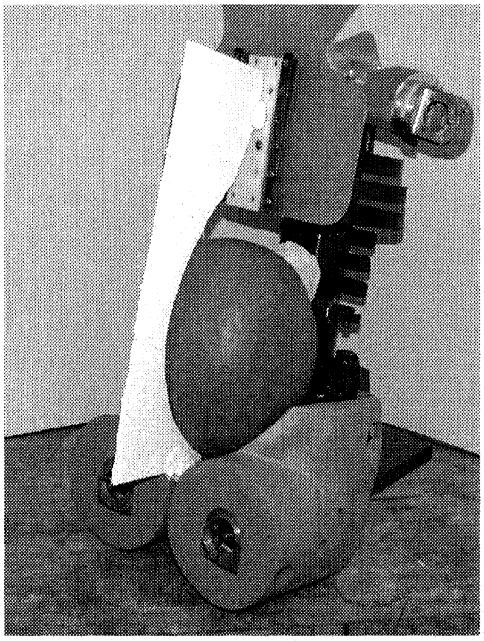

Figure 31. Clay model of a 30-week uterus in small-female dummy with ribs 4 to 6 removed. Cardboard cutout provides abdomen midline contour based on results from Klinich et al. (1999).

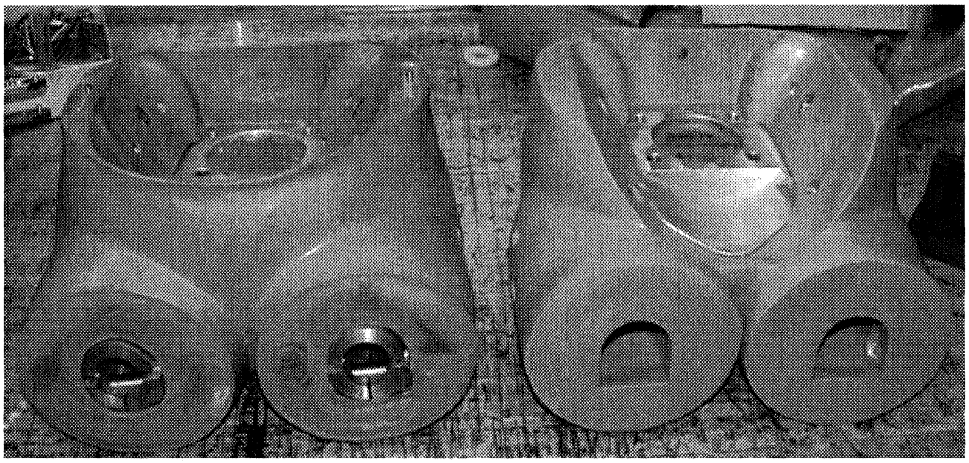

Figure 32. Standard Hybrid III small-female pelvis (left) and first pregnant dummy pelvis (right).

To attach the uterus to the ATD, the bladder was glued to attachment "cradles" as illustrated in Figure 33. The lower cradle is bolted to the pelvis and represents the anatomical connection between the base of the uterus and the cervix. The upper cradle is attached to the inferior spine box and represents viscous resistance to forward motion described in Section 4.3.4 of this report. Figure 34 illustrates the position of the uterus within the small-female dummy with modified ribs and cradle attachments. Installation of the prototype abdomen components required removal of the Hybrid III lumbar load cell and the fetal-force-measurement load cell that were installed on the pelvis and lumbar spine of the first pregnant dummy.

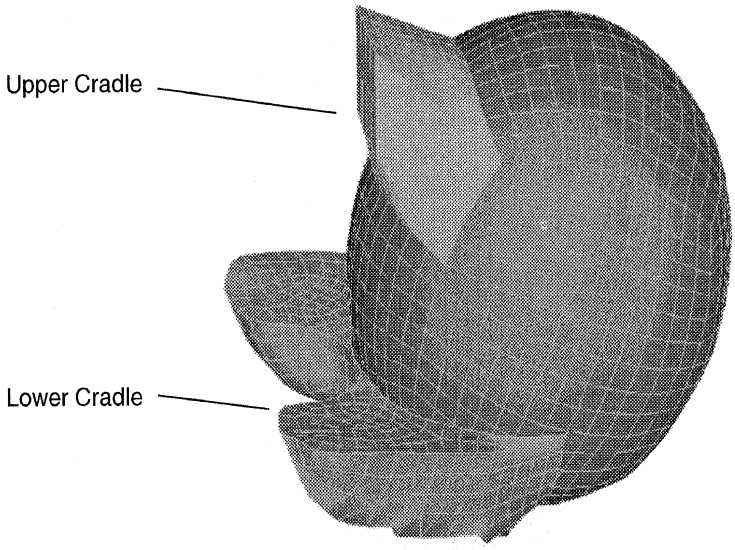

Figure 33. Computer model of first prototype bladder and attachment cradles.

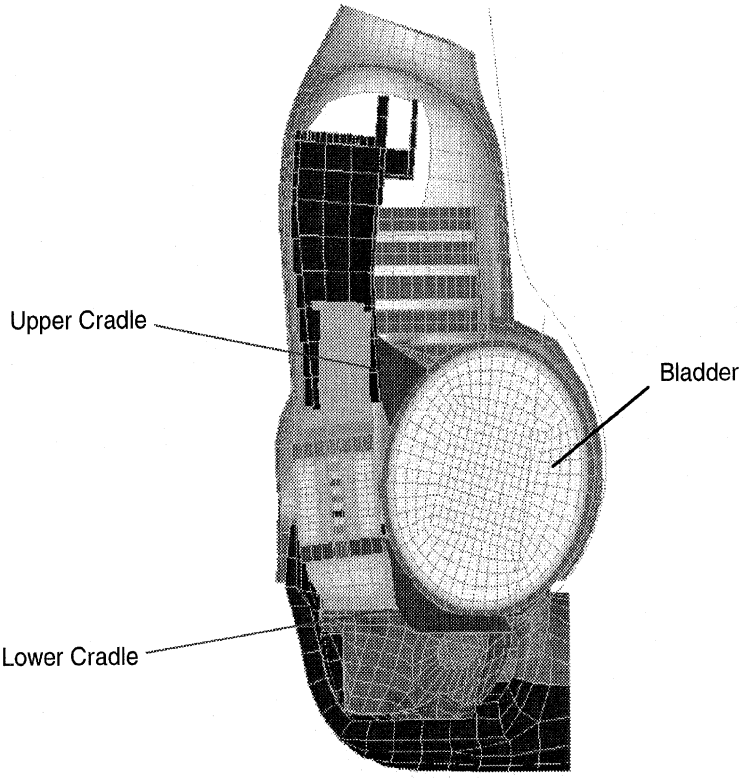

Figure 34. FEM of prototype uterus installed in dummy showing upper and lower mounting "cradles."

6.4 Dummy Mass

As previously noted, the target mass for the new pregnant dummy is approximately 58 kg (128 lb), which is the same as the mass of the original pregnant dummy. The desired location for the center of gravity of the seated MAMA-2B is 227 mm above and 169 mm forward of the hip joint center. To obtain the desired CG location while minimizing differences between the Hybrid III small female and the new pregnant dummy, 5.3 kg (11.7 lb) of ballast were added to the pelvis and 2.5 kg of mass (5.6 lb) were distributed along the posterior spine box. The remainder of the additional mass was included in the bladder and its attachment hardware. The added ballast brought the total weight of the pregnant dummy to 58 kg (128 lb) and therefore compensated for mass removed in the redesigns of the pelvis and ribs.

Locating ballast in the pelvis and the posterior spine box provides a significant improvement over the ballast mass added to the first pregnant dummy in which metal ballast is located in pockets in the posterior chest jacket. This ballast tends to decouple from the dummy during rebound after a frontal impact, which changes the effective mass of the dummy thorax. Also, when the decoupled mass returns to its original position, contact with the spine box results in spikes in the output of the chest spine accelerometers.

6.5 Chest Jacket and Breast Design

Like the original pregnant dummy's chest jacket, the MAMA-2B chest jacket is made from neoprene wetsuit material that covers the dummy's torso. The MAMA-2B and the original pregnant dummy chest jacket both include a crotch strap to better secure the anterior surface of the jacket. However, the MAMA-2B jacket does not include pockets for ballast material because all ballast in the MAMA-2B has been distributed over the pelvis and torso to obtain the appropriate seated CG.

Because the contour of chest skin used with the original pregnant dummy differs from the contour of the MAMA-2B abdomen, the molded chest skin was replaced with silicone breast prostheses, which are more likely to allow appropriate belt routing. To accommodate the prostheses, pockets were added to the front of the chest jacket. The prosthetic breasts have proved to be durable in sled tests and pendulum impacts to the dummy chest. Figure 35 shows the first assembled prototype of the new pregnant dummy with the redesigned chest jacket.

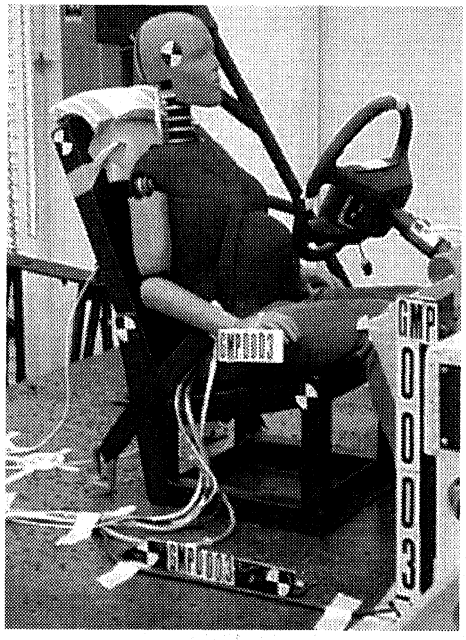

Figure 35. Photo of new pregnant dummy with neoprene jacket.

6.6 Testing and Development of the New Pregnant Abdomen

6.6.1 Test Methods

The dynamic response of the first prototype of the new pregnant abdomen installed in the modified small-female Hybrid III ATD was determined using rigid-bar impacts, dynamic-belt loading, and physically-simulated-airbag (i.e., surrogate airbag) loading of the abdomen when it is extremely close to, or in contact with, an airbag module prior to deployment (i.e., out-of-position). Force-deflection responses were compared to rescaled human cadaver response corridors developed by Cavanaugh and Hardy. Descriptions of these test methodologies are contained in the following subsections, while test results are contained in Section 6.6.2.

6.6.1.1 Rigid-Bar Impact

The majority of impact testing was conducted using a ballistic pendulum with a rigid-bar impactor in the test setup shown in Figure 36. This is the same test fixture used by Hardy to verify the 6.7 m/s Cavanaugh corridor and to develop the 3 m/s abdominal response corridor described in Section 3.5.2.1. A six-axis load cell is positioned between the ballistic mass and the impactor. A single accelerometer is positioned to measure x-axis acceleration at the pendulum CG during impact. Additional accelerometers are placed on the forward face of the load cell to measure x- and y-axis accelerations. Data from one of the x-axis accelerometers, typically the one located on the pendulum face, were used to mass correct the force data measured by the load cell. Acceleration data, along with the mass of the impactor, were also used to verify peak forces measured by the load cell. For most tests, impactor motion was arrested by a set of cables connected to the impactor CG

on one end and a series of deformable bars on the other end. The fore-aft positioning of the dummy was set so that arresting of the impactor motion began at 75 to 85 mm of the abdominal penetration, which corresponds to approximately half of the abdominal depth. Limits on impactor penetration into the abdomen were applied to prevent damage to the instrumentation contained within the bladder and prevent overloading of the impactor load cell due to contact with the lumbar spine.

During a typical test, the dummy was positioned on a Teflon skid-plate. The height of the plate was adjusted so that the impactor was located at the level of the anterior-most point of the abdomen. A pneumatic accelerator drove the impactor to the desired pre-impact speed by applying a force through a fork-like fixture attached to the CG of the ballistic mass. The arc of the ballistic pendulum was such that the impactor motion was horizontal when it contacted the dummy abdomen.

Force data were collected from the six-axis load cell attached to the posterior surface of the impactor. These data were sampled at 10 kHz, mass corrected, and filtered at SAE channel class 1000. Abdominal deflection was calculated by digitizing targets on the lumbar spine and pendulum using high-speed video or film data collected at 1000 frames/s. Digitized deflection data were filtered at SAE channel class 180. Results of these tests are discussed in Section 6.6.2.

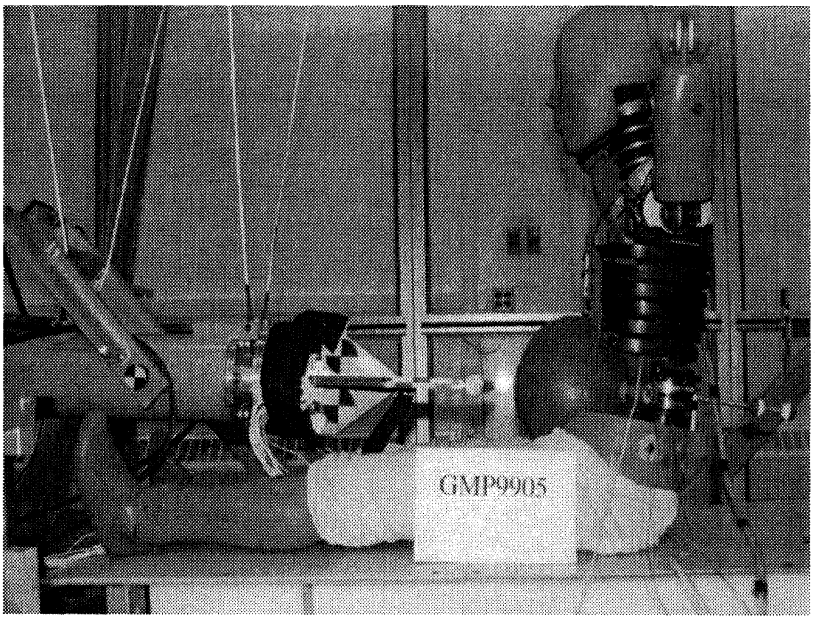

Figure 36. Ballistic pendulum impact test setup.

6.6.1.2 Dynamic Belt-Loading

Dynamic belt-loading tests were conducted using the apparatus shown in Figure 37. This device applies a horizontal load to the dummy abdomen through belt webbing connected to a yoke-fixture, which is pneumatically driven rearward relative to the dummy. Force applied to the dummy abdomen was measured by belt load cells attached to the ends of

the belt near their attachment to the yoke fixture. The force measurement was verified using a load cell attached between the yoke and the linear accelerator. Data from the yoke load cell were mass corrected using data from an accelerometer mounted on the face of the load cell. Belt motion was measured using a string potentiometer mounted to a stationary fixture and connected to the center of the belt webbing. The height of the potentiometer was adjusted so that the motion of the string was horizontal. Prior to the test, the belt was in contact with, but was not loading, the abdomen. The motion of the dummy was measured using a laser-based displacement transducer mounted in the yoke, with the laser beam focused on the lumbar spine. The displacement of the yoke was measured using an LVDT. Belt penetration was calculated by determining the motion of the belt relative to the position of the lumbar spine, which was measured relative to the yoke. All measurements were independent of the stretch of the belt webbing, and consequently, belt stretch was not included in any analyses.

All data were sampled at 10 kHz and filtered using SAE channel class 1000. For all tests, the loading velocity pulse was approximately sinusoidal with a peak loading velocity between 3 and 4 m/s. This was comparable to the pulse used by Hardy to develop the 3 m/s belt loading corridors discussed in Section 3.5.2.2. Results of these tests are discussed in Section 6.6.2.

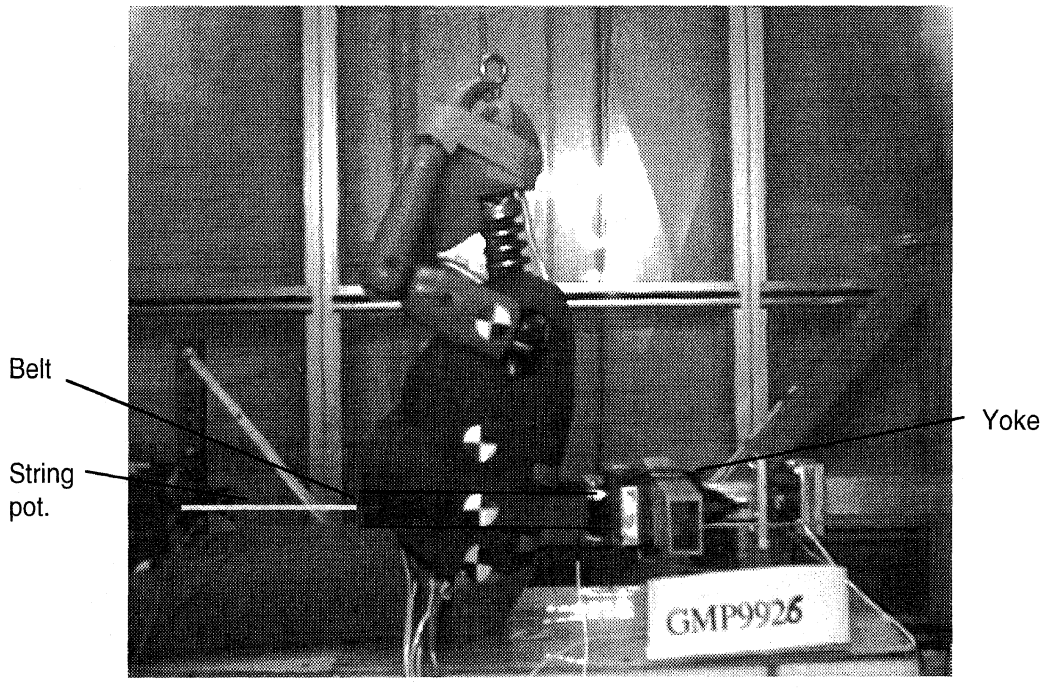

Figure 37. Setup for dynamic belt-loading tests. Lines added to illustrate string pot and belt outline.

6.6.1.3 Inertial Loading

All quantitative evaluations of the dynamic response of the pregnant abdomen used either rigid-bar or belt loading as described above. However, in situations where the pelvis is decelerated without direct loading of the abdomen, the pregnant abdomen will experience

forward distension due to fluid inertia. To qualitatively evaluate the general response of the prototype abdomen under these conditions, sled tests were conducted on the isolated pregnant abdomen. These tests were conducted with and without jacket material surrounding the abdomen. When jacket material was used, it was rigidly anchored to the bladder mounting fixture to create a boundary condition that is representative of the pregnant dummy chest jacket, which effectively restrains only the anterior bladder surface. The setup for these tests is shown in Figure 38. The bladder assembly (including cradles) was attached to a rigid fixture that simulates the bladder mounting geometry used in the dummy. This fixture was rigidly bolted to the sled platform, which was used to apply decelerative pulses to the bladder-mounting fixture. The lack of a pelvic representation to support the inferior bladder was not expected to affect the resulting distention (recall that the dummy skin on the front of the standard Hybrid III 5th is removed on the pregnant dummy). Results of these tests are discussed in Section 6.6.2.

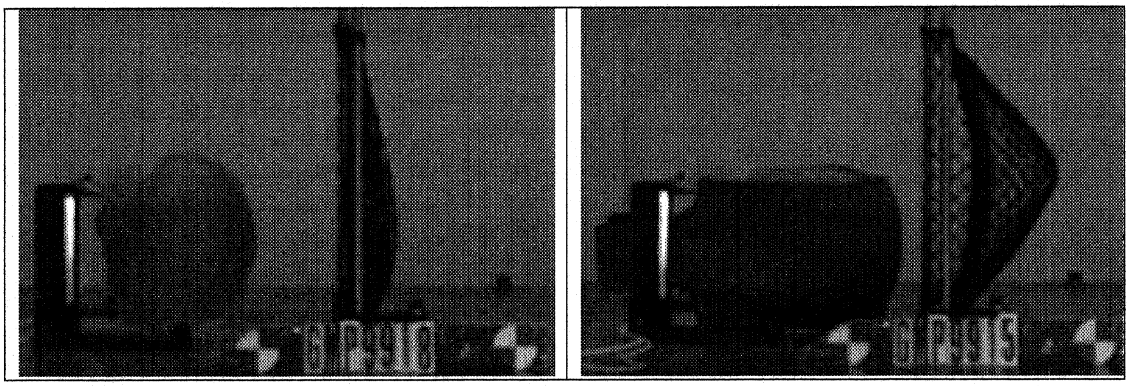

Figure 38. Sled test setup for inertial loading of prototype abdomen showing bladder prior to impact (left) and bladder with jacket material at maximum distention (right).

6.6.1.4 Out-of-Position Airbag Loading

The response of the new pregnant abdomen to simulated out-of-position airbag loading was measured using the surrogate-airbag device shown in Figure 39 and described in Section 3.5.2.3. For these tests, the dummy's lumbar spine was anchored to a rigid seat back. A low-mass cylinder was pneumatically actuated to a velocity of about 13 m/s prior to contact with the abdomen. Force continued to be applied following initial contact by air pressure in a tube connected to the impactor cylinder. Force applied to the impactor was measured using an acceleration-insensitive pressure transducer inside the tube and deceleration of the cylinder. Acceleration of the cylinder was also used to mass correct the calculated force applied to the impactor to obtain force applied to the abdomen. Penetration into the abdomen was measured using a laser-based displacement transducer. All data were collected at a rate of 20 kHz and filtered at SAE channel class 1000.

Equal-stress, equal-velocity scaling is not typically applied to fixed-back tests because the mass of the test subject is essentially infinite. However, free-back cadaver tests with the surrogate airbag showed no motion of the lumber spine in response to the low-mass impact. Consequently, the fixed-back condition served primarily to stabilize the dummy,

and equal-stress, equal-velocity scaling procedures were considered appropriate. Results of these tests are discussed in Section 6.6.2.

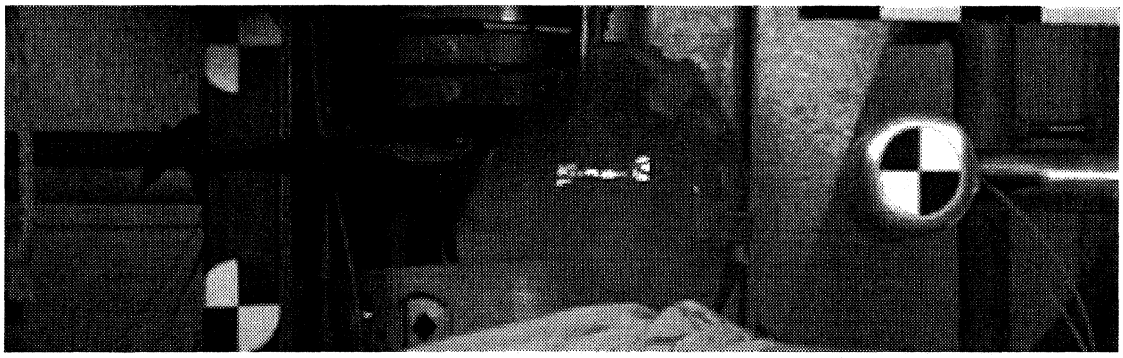

Figure 39. Test setup for surrogate airbag tests showing a side view of the cylindrical impactor (right) and the new pregnant abdomen (center).

6.6.1.5 Sled Tests

Full dummy sled tests were conducted to evaluate the performance of the MAMA-2B under loading conditions that are more representative of impact loading occurring in a motor-vehicle crash. Sled tests were performed using a rebound sled. Sled acceleration and all other dummy instrumentation measurements were processed according to SAE J211 (SAE, 1995). When processing data from sled tests, t_{zero} was taken to be the time where the sled acceleration first exceeded 0.5 g. Results of these tests are discussed in Section 6.6.2.

6.6.2 Evaluation and Further Development of the Pregnant Abdomen

Table 4 lists all of the tests performed throughout the development of the new pregnant abdomen. Appendix B contains all relevant signals from these tests. Figure 40 is a flow chart detailing the process of design, fabrication, testing, evaluation, and design modification. Twenty-nine rigid-bar impacts, nine belt-loading tests, two surrogate-airbag impacts, and thirty-four sled tests were conducted on eight different prototype bladders. All bladders were approximately ellipsoidal in shape and contained a port for filling the bladder with water and for installing instrumentation within the bladder. Bladders were filled with water because it closely resembles the density of uterine contents (amniotic fluid, fetus, and placenta), and because a realistic pressure response was desired under impact and inertial loading. Fluids other than water, e.g., silicone, were considered, however, concerns about fluid viscosity altering the pressure response within the bladder, and potential issues with cleanup of any fluid spills precluded the use of any fluid but water.

Table 4.
Dummy Development and Testing History

Test ID	Test Type	Rate	Comments
PROTOTYPE 1 25-Durometer Skin Flex Urethane. Full rigid upper and lower cradles			
GMP9901	Rigid Bar	6.0 m/s	
GMP9902	Rigid Bar	6.2 m/s	No data collected. Bladder failure due to compression against rigid upper cradle.
PROTOTYPE 2 30-durometer bladder, soft upper, full rigid lower cradle			
GMP9903	Rigid Bar	3 m/s	
GMP9904	Rigid Bar	6 m/s	Bladder failure due to shear over rigid lower cradle.
PROTOTYPE 3 25-durometer soft upper cradle, reduced profile rigid lower cradle			
GMP9905	Rigid Bar	2.2 m/s	
GMP9906	Rigid Bar	2.3 m/s	
GMP9907	Rigid Bar	3.3 m/s	
GMP9908	Rigid Bar	4.2 m/s	
GMP9909	Rigid Bar	5.2 m/s	
GMP9910	Rigid Bar	6.2 m/s	Bladder response too soft
PROTOTYPE 4 30-durometer bladder, soft upper cradle, reduced profile rigid lower cradle			
GMP9911	Belt Loading Belt	5.6 m/s	
GMP9912	Belt Loading Belt	5.6 m/s	Bladder failed due to shear over lower cradle
PROTOTYPE 5 35-durometer soft upper, soft upper cradle, reduced profile rigid lower cradle			
GMP9913	Bladder Only Sled Test	10g	
GMP9914	Bladder Only Sled Test	10g	
GMP9915	Bladder Only Sled Test	15g	
GMP9916	Bladder Only Sled Test	20g	
GMP9917	Bladder Only Sled Test	20g	
GMP9918	Bladder Only Sled Test	15g	Unrealistic distension. Concerns over urethane durability.
PROTOTYPE 6 40-durometer silicone rubber, soft upper cradle, reduced profile rigid lower cradle			
GMP9919	Belt Loading	5.0 m/s	Loading rate too high
GMP9920	Belt Loading	5.0 m/s	Loading rate too high
GMP9921	Rigid Bar	3 m/s	
GMP9922	Rigid Bar	6 m/s	
GMP9923	Rigid Bar	5 m/s	
GMP9924	Rigid Bar	4 m/s	Response too soft
GMP9925	Belt Loading	3.0 m/s	
GMP9926	Belt Loading	4.7 m/s	
GMP9927	6.2 kg Head form impact using drop tower. For FE validation.	3 m/s	

Test ID	Test Type	Rate	Comments
GMP9928	Same as 0027	6 m/s	
GMP9929	Rigid Bar. Bladder w/ inextensible wrap	4.0 m/s	Response within 6 m/s corridor
GMP9930	Rigid Bar. Bladder w/ inextensible wrap.	6.7 m/s	Response less stiff than 0029 due to loosening of wrap
PROTOTYPE 7 0.3" thick silicone rubber bladder, soft upper cradle, reduced profile rigid lower cradle			
GMP9931	Rigid Bar	3.8 m/s	Bladder rupture and was repaired for subsequent tests
GMP9932	Rigid Bar	3.7 m/s	
GMP9933	Rigid Bar	6.7 m/s	
GMP9934	Rigid Bar	6.4 m/s	Response within Cavanaugh/Hardy Corridors
GMP0001	Whole Dummy Sled. Knee bolster spacing = 70 mm. H30 = 320 mm. Wheel-to-abdomen=30 mm. Three-point belt.	20mph/ 15 g	
GMP0002	Whole Dummy Sled. Same config as 0001.	30 mph/20g	
GMP0003	Whole Dummy Sled. Airbag @ 15ms post tzero†. Rest of setup same as 0001 and 0002	20 mph/15 g	
GMP0004	Whole Dummy Sled. Unrestr. Airbag, knee bolster, seat, same as 0001 and 0002	20 mph/15 g	
GMP0005	Sled. Repeat of GMP001.	20 mph/15 g	
GMP0006	Sled. European-style Passenger 3-point belt.	20 mph/15 g	
GMP0007	Sled. Same config as 0005.	30 mph/ 15 g	
GMP0008	Sled. Repeat of 0006.	20 mph/ 15 g	
GMP0009	Bladder-Only Sled w/Jacket Material	21 mph/16g	
GMP0010	Bladder-Only Sled w/o Jacket Material	20 mph/15g	
PROTOTYPE 8 50-durometer silicone abdomen soft upper cradle, reduced profile rigid lower cradle			
GMP0011	Rigid Bar. With chest jacket.	4.34 m/s	No data collected. Data Acquisition did not trigger.
GMP0012	Rigid Bar. With chest jacket.	4.31 m/s	
GMP0013	Rigid Bar. With chest jacket.	6.64 m/s	Validation rigid-bar test
GMP0014	Rigid Bar. No jacket.	6.51 m/s	Appropriate response. No change in response w/ jacket
GMP0015	Rigid Bar. No jacket	4.73 m/s	
GMP0016	Rigid Bar-knee impact. No jacket.	2.8 m/s	Conducted to verify that pelvic x accel can cause negative pressure in bladder
GMP0017	Belt Loading. No jacket	4.5 m/s	
GMP0018	Belt Loading . W/jacket.	3.0 m/s	Validation belt loading test
GMP0019	Belt Loading . W/o jacket.	3.0 m/s	
GMP0020	6.2 kg Head form impact using drop tower. For FE validation.	3 m/s nominal	

† t_{zero} is defined as the moment where sled acceleration first rises above 0.5 g.

Test ID	Test Type	Rate	Comments
GMP0021	Same as 0020	3 m/s nominal	
GMP0022	Same as 0020,21	3 m/s nominal	
GMP0023	Same as 0020-0022	3 m/s nominal	
GMP0024	Same as 0020-0023		Failed instrumentation. No data collected.
GMP0025	Same as 0020-0024		Failed instrumentation. No data collected.
GMP0026	Whole Dummy Sled w/ Airbag	20 mph/15g	
GMP0027	Instron Shape tape test		
GMP0028	Rigid Bar. Shape tape test	5.84 m/s	
GMP0029	Rigid Bar. Shape tape test	5.94 m/s	
GMP0030	Rigid Bar. Shape tape test	6.02 m/s	
GMP0031	Whole Dummy Sled. Unrestrained driver 36% risk of injury.	14.6 kph/3.2 g	
GMP0032	Whole Dummy Sled. 3-pt belt restrained driver. 9% risk	14.8 kph/3.7g	
GMP0033	Whole Dummy Sled. 3-pt belt restrained driver. 26% risk	23 kph/8.6g	
GMP0034	Whole Dummy Sled. 3-pt belt + airbag (deployed 15 ms after tzero) 26% risk.	23 kph/8.6g	
GMP0035	Whole Dummy Sled. 3-pt belt + airbag (deployed 15 ms after start of impact) Repeat of 0034 with wheel pinned. 26% risk.	23 kph/8.6 g	
GMP0036	Whole Dummy Sled. Unrestrained driver. 54% risk	19.4 kph /5.6 g	
GMP0037	Whole Dummy Sled. 3-pt belt restrained passenger. 9% risk.	15.0 kph//3.3g	
GMP0038	Whole Dummy Sled. 3-pt belt passenger 51% risk.	34.3 kph/12 g	
GMP0039	Whole Dummy Sled. 3-pt belt driver 51% risk. Repeat of 0039.	34.4 kph/12 g	
GMP0040	Whole Dummy Sled. 3-pt belt driver 51% risk.	34.5 kph/12 g	
GMP0041	Whole Dummy Sled. Unrestrained driver 86% risk.	34.1 kph/12.2 g	
GMP0042	Whole Dummy Sled. 3-pt belt driver 86% risk.	46.8 kph/15.7 g	
GMP0043	Whole Dummy Sled. 3-pt belt driver + airbag 86% risk.	46.8 kph/15.7 g	
GMP0044	Whole Dummy Sled. 3-pt belt driver. 90% risk.	52.3 kpg/17.4 g	
GMP0045	Whole Dummy Sled. 3-pt belt passenger. 90% risk.	52.6 kpg/17.5 g	
GMP0046	Bladder Only Sled. Bladder Only Sled with Shape Tape.	15 mph/ 20g	
GMP0047	Bladder Only Sled. Bladder Only Sled without Shape Tape.	15 mph/ 20g	
GMP0048	Surrogate Airbag. Fixed back pregnant dummy without jacket.	12.5 m/s	
GMP0049	Surrogate Airbag. Fixed back pregnant dummy with jacket.	12.5 m/s	Response is within the Cavanaugh/Hardy corridors

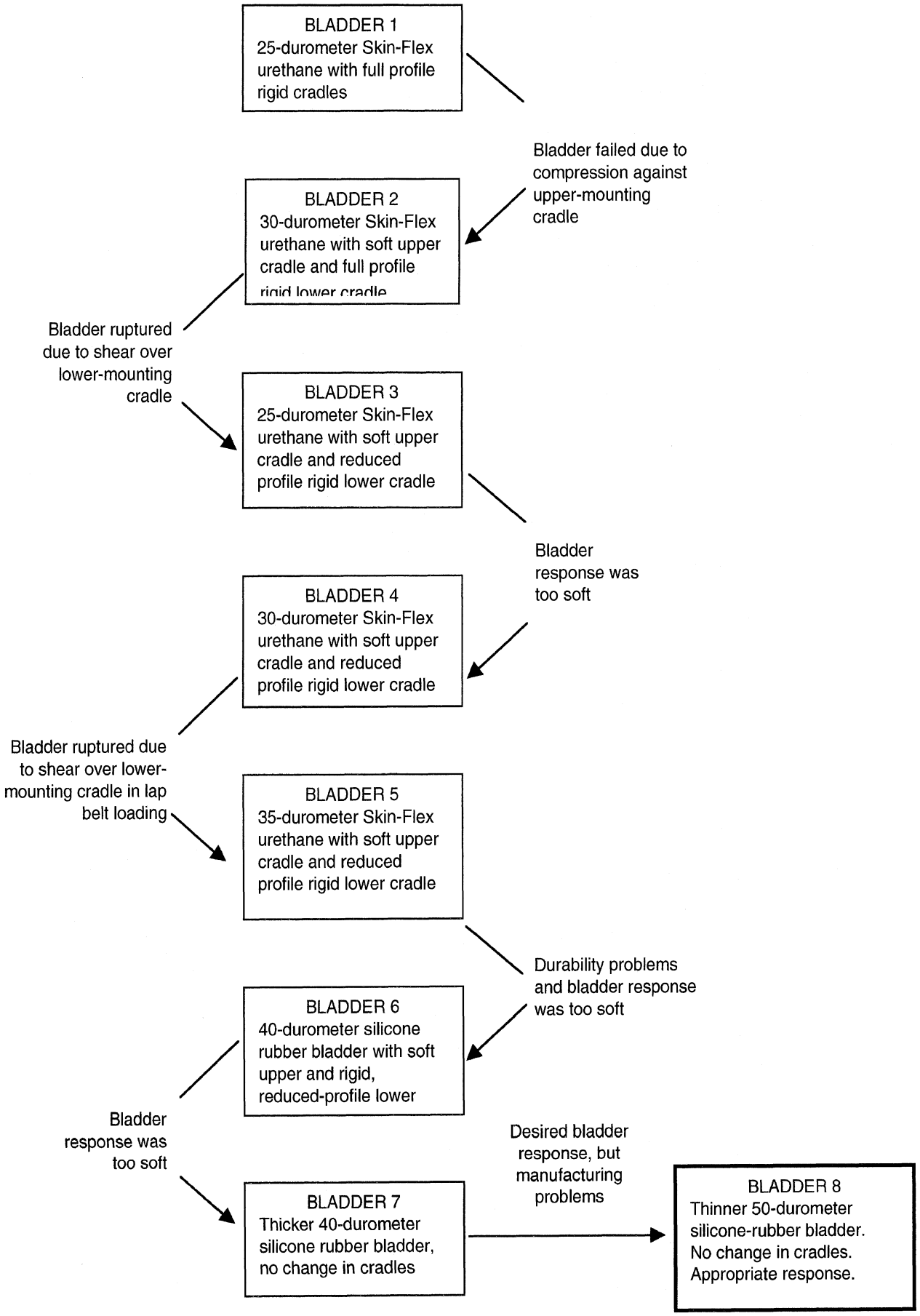

Figure 40. Flow chart of bladder development process.

Bladder 1. The first prototype pregnant abdomen was made of 25-durometer (Shore A scale) skin-flex urethane using a lost wax molding process. For reference, this bladder is referred to as Bladder 1 or Prototype 1. It was attached to the dummy at the top and bottom of the lumbar spine using two rigid urethane-mounting cradles. The attachment of these cradles to the bladder is shown in Figure 41. Figure 42 shows a FEM of the dummy with the larger mounting cradles used with Bladder 1.

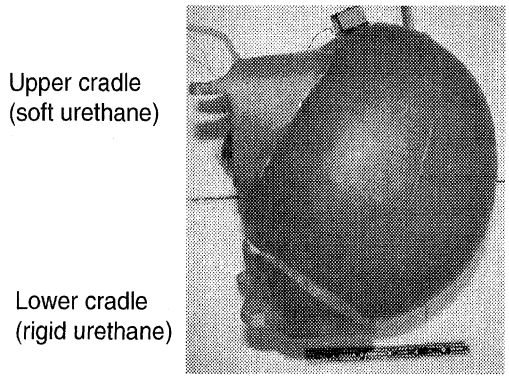

Figure 41. Side view of urethane bladder showing attachment of upper and lower cradles.

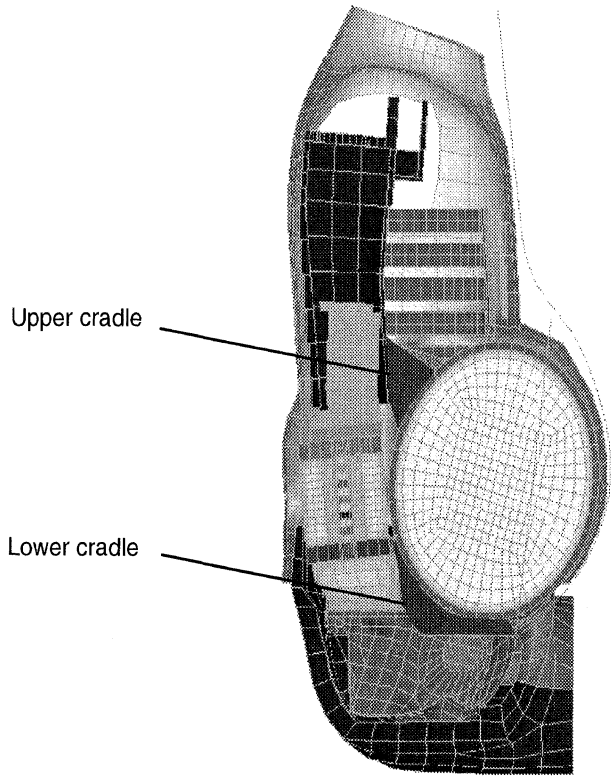

Figure 42. FEM showing side view of pregnant dummy with first prototype attachment cradles.

Two rigid-bar impacts were performed on Bladder 1 at a velocity of approximately 6 m/s (GMP9901 and 9902 in Table 2). Figure 43 shows the force-deflection response calculated from the first of these impacts relative to the 6 m/s pregnant dummy response corridor (i.e., the Cavanaugh 6 m/s corridor with equal-stress, equal-velocity scaling used to scale the corridors from a 76 kg reference mass to the mass of the pregnant dummy a described in Appendix A). While the response of the bladder was within the 6 m/s corridor, the bladder tore in a subsequent test due to shear forces at the edges of the rigid upper-mounting cradle.

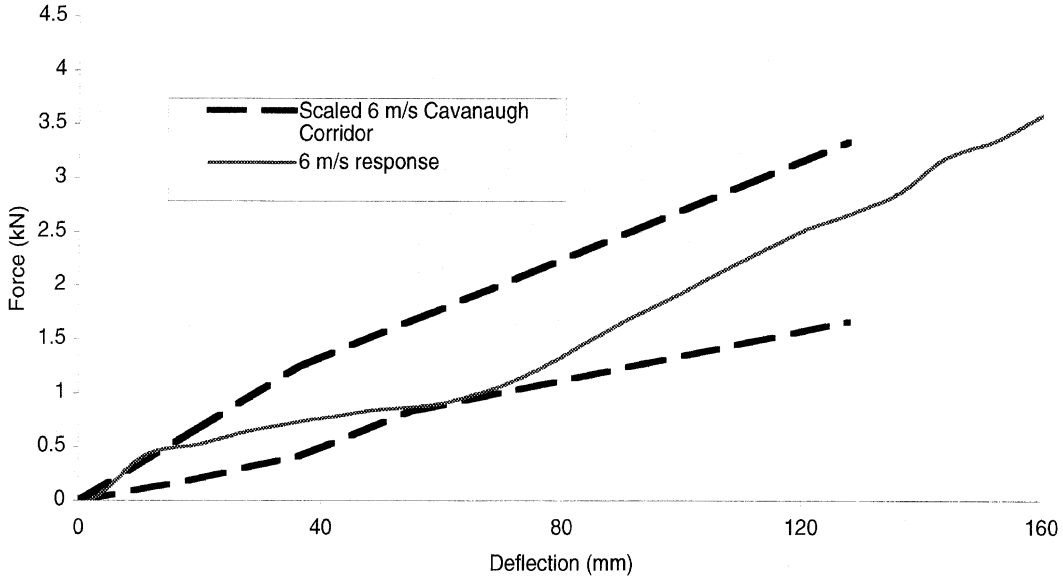

Figure 43. Force-deflection response to rigid-bar impact of Bladder 1 (25-durometer urethane bladder with rigid upper and full-profile lower-mounting cradles) at 6 m/s relative to scaled 6 m/s Cavanaugh corridor.

Bladder 2. The bladder assembly was subsequently redesigned with a softer, 30-durometer urethane upper-mounting cradle (Bladder 2). In addition, the hardness of the new bladder was increased to 30 durometer to compensate for the reduction in overall bladder stiffness due to the softer upper-mounting cradle. The rigid-bar impact response at 3 m/s (test GMP9903) of Bladder 2 with soft upper- and rigid lower-mounting cradles is shown in Figure 44. The bladder response is near the 3 m/s average response curve developed by Hardy from repeated tests on a single cadaver (see Section 3.5.2.1). If the responses in Figures 43 and 44 are considered together, the bladder appears to demonstrate the desired rate sensitivity, although subsequent tests indicated that this is not the case. Bladder 2 failed at an impact velocity of 6 m/s in test GMP9904 due to shear over the lower-mounting cradle. Figure 45 shows the failed bladder after impact.

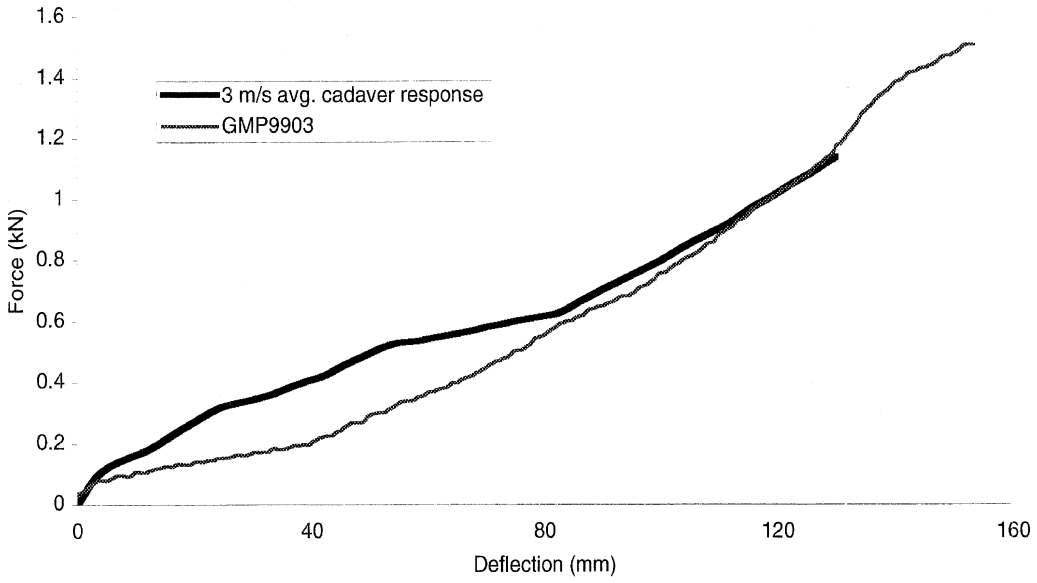

Figure 44. Force-deflection response to rigid-bar impact of Bladder 2 (30-durometer urethane bladder with soft upper and full-profile lower-mounting cradles) at 3 m/s relative to 3 m/s averaged cadaver response.

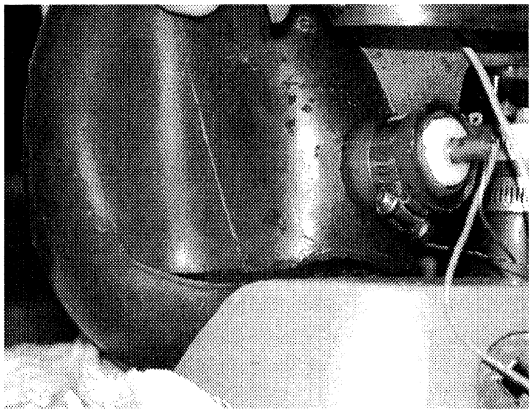

Figure 45. Bladder 2 failure due to shear at lower-mounting cradle during 6-m/s rigid-bar impact.

Bladder 3. To decrease the possibility of shear failure at the lower-mounting cradle, Bladder 3 was designed with a smaller rigid lower-mounting cradle. The upper-mounting cradle was again fabricated from 30-durometer urethane, while Bladder 3 was fabricated from 25-durometer skin-flex urethane because 30-durometer urethane was not available within a reasonable timeframe. Figure 46 shows the rigid-bar impact response of Bladder 3 over impact velocities ranging from 2.2 to 6.2 m/s (tests GMP9905-9910). To prevent damage to instrumentation within the bladder and to prevent catastrophic failure of the bladder, pendulum motion was arrested prior to 130-150 mm of penetration, which is greater than the maximum penetration that is estimated to occur in vehicle-impact testing. While the force-deflection responses from these tests at loading rates were close to the respective specifications at loading rates of 3 and 6 m/s for the first 40-mm of deflection, the general response of the abdomen was too soft, and rate-sensitivity was not as

pronounced as the previous rigid-bar impacts indicated. The soft response was attributed to the 25-durometer urethane bladder material.

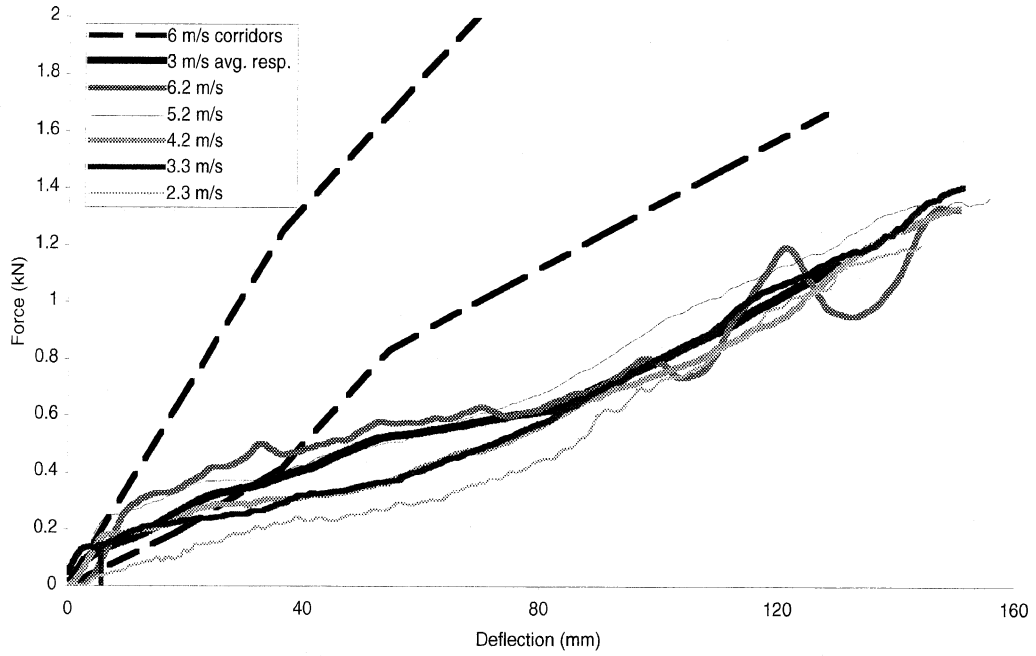

Figure 46. Force-deflection response of Bladder 3 (25-durometer urethane bladder with soft upper and partially reduced-profile lower-mounting cradles). All tests were conducted with the chest jacket except the 2.2 m/s impact.

Bladder 4. For the next prototype, Bladder 4, the stiffness of the bladder was increased by again using 30-durometer urethane as the bladder material. Two belt-loading tests were performed on Bladder 4 with soft upper and rigid lower cradles. The force-deflection response from the first of these tests (GMP9912) lies below the belt-loading corridor in Figure 47. The response of the bladder in the second test could not be measured because the bladder failed due to excessive stretch near the lower cradles. Figure 48 shows the failed bladder.

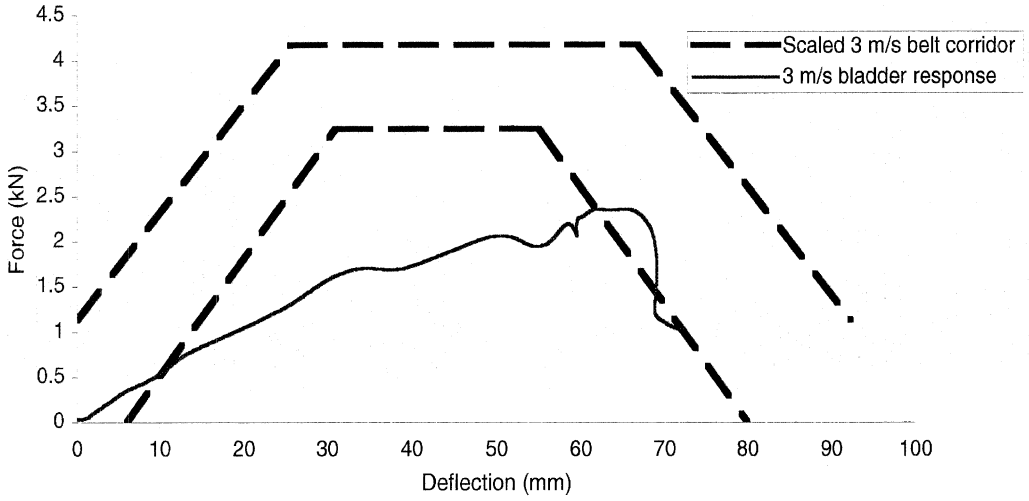

Figure 47. Belt loading response of Bladder 4 (30-durometer urethane bladder) with soft upper and reduced-profile lower-mounting cradles relative to scaled 3 m/s cadaver belt loading corridors (from Hardy, 2000).

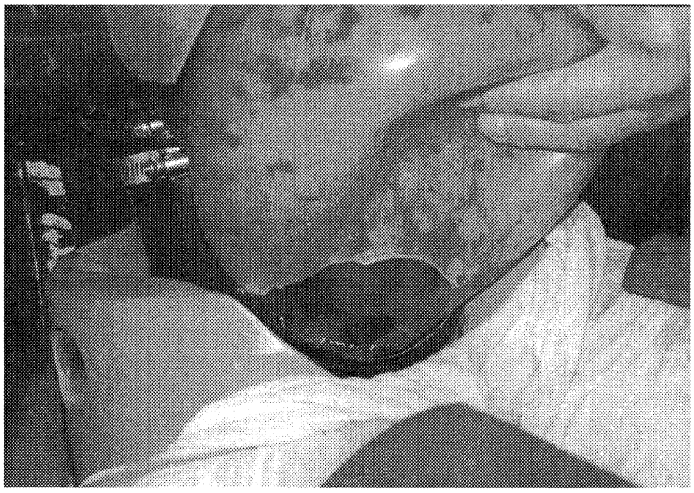

Figure 48. Failure of Bladder 4 due to high strains near lower-mounting cradles during rigid-bar impact.

Bladder 5. To stiffen the force deflection response, Bladder 5 was fabricated from 35-durometer urethane. Soft upper and reduced profile lower-mounting cradles were used. The inertial response of Bladder 5 was evaluated by rigidly mounting it to the sled platform as previously described. Ten, 15, and 20 g decelerative pulses were applied with and without jacket material surrounding the bladder. Figure 49 shows that the distention of the bladder was at least two to three times larger than was expected. A separate test conducted without the chest jacket material covering the anterior bladder indicated that the jacket material slightly reduces bladder distention.

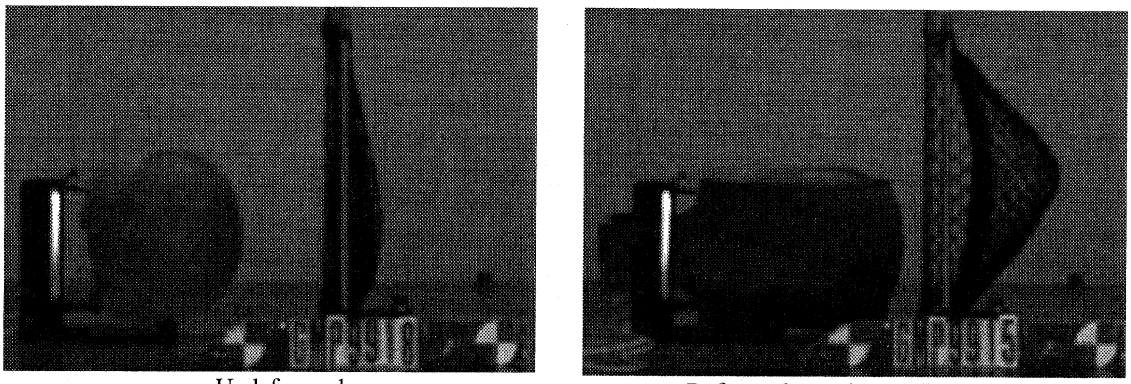

Undeformed

Deformed (maximum distention)

Figure 49. Inertial loading of Bladder 5 (35-Durometer urethane) showing gross distention of the bladder under a 20-g deceleration.

Bladder 6. Due to repeated bladder ruptures under loading conditions that could reasonably occur in impact testing, the bladder material was changed from urethane to a tough silicone rubber. Silicone rubber was selected as a bladder material after tests by Rouhana (unpublished) demonstrated its high strength, toughness, and ability to withstand large tensile strains. Bladder 6 was fabricated from 40-durometer silicone rubber to stiffen the bladder response and decrease its distension under inertial loading conditions. Cradle material and geometry were not changed. However, to improve the durability of the upper cradle attachment to the lumbar spine, urethane attachment points were replaced with metal plates that were bolted to a rod inserted through the upper cradle.

Belt loading tests and rigid-bar impacts were conducted to determine the force-deflection response of Bladder 6 over a range of loading conditions. Results of the belt and rigid-bar tests (GMP9919-26) are shown in Figures 50 and 51, and demonstrate that the response of the bladder was still too soft, although some rate sensitivity was observed.

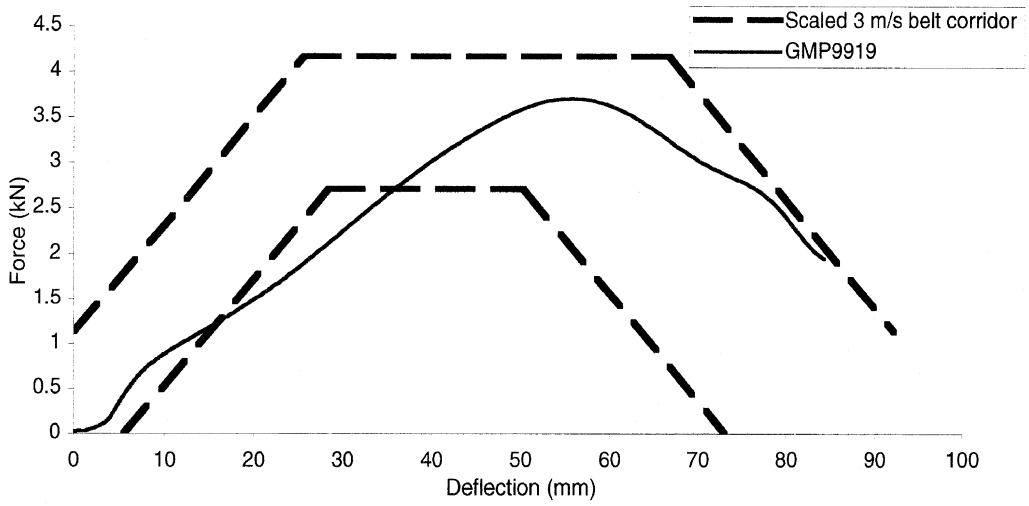

Figure 50. Force-deflection response of Bladder 6 (40-durometer silicone rubber) to belt loading in test GMP9919 relative to scaled 3 m/s belt loading corridor.

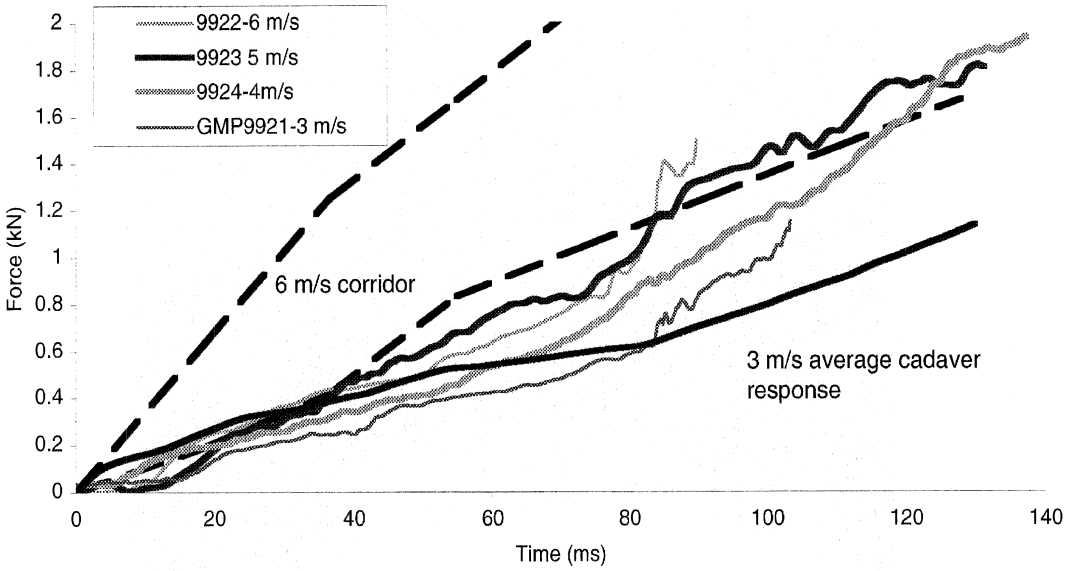

Figure 51. Force-deflection response of Bladder 6 (40-durometer silicone rubber) to rigid-bar loading from tests GMP9921-24 shown relative to scaled 6 m/s Cavanaugh Corridors and average 3 m/s average cadaver response.

To obtain a stiffer response, the wrapping concept proposed by Schneider et al. in the advanced dummy development (summarized in Section 6.1) was applied to Bladder 6. Figure 52 shows Bladder 6 installed in the pregnant dummy and surrounded by an inextensible wrap. The wrap was positioned so that it constrained the front and sides of the bladder. Because the bottom and back of the bladder were constrained by the pelvis and lumbar spine, respectively, the constrained bladder could only expand upward into the chest cavity.

Figure 53 shows the results of rigid-bar impacts into the bladder with and without the wrap. The addition of the inextensible wrap stiffened the bladder response so that it fell within the 6 m/s corridor. However, consecutive testing at 4 and 6 m/s impact velocities demonstrated that the tightness of the wrap had a large effect on bladder force-deflection response. That is, the 4 m/s test was conducted before the 6 m/s test and demonstrated a stiffer response due to loosening of the strings that connect the ends of the wrap between tests. Although the inextensible wrap stiffened the bladder to the desired response, repeatability issues resulting from the wrap attachment methods rendered it an unacceptable solution, and the wrapping concept was abandoned.

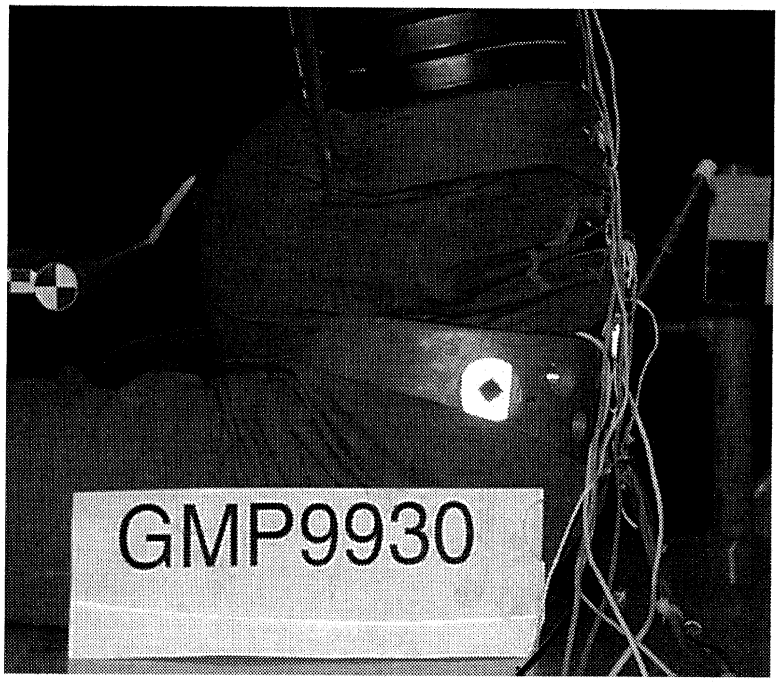

Figure 52. Bladder 6 (40-durometer silicone rubber) with inextensible wrap.

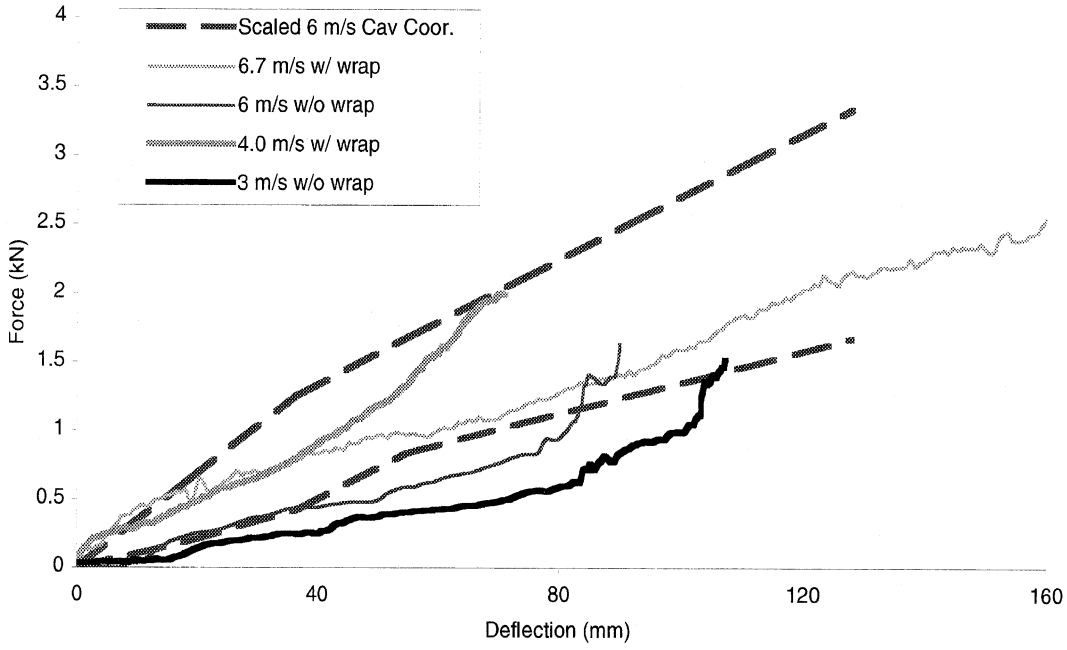

Figure 53. Bladder 6 (40-durometer silicone rubber) response to rigid-bar impacts with and without inextensible wrap relative to scaled 6 m/s Cavanaugh Corridor.

Bladder 7. Bladder 7 was constructed of a thicker 40-durometer silicone. Figure 54 shows that the rigid-bar impact responses of Bladder 7 fall within both the 6 and 3 m/s corridors defined for the pregnant dummy and that the bladder demonstrates reasonable

rate sensitivity. Bladder 7 would have been used for the final abdomen design except for manufacturing problems that prevented rapid fabrication. Because of its thickness, Bladder 7 required almost a month of cure time following the conclusion of the fabrication process. Faster cures at higher temperatures were attempted, but resulted in large surface defects in the cured bladder material.

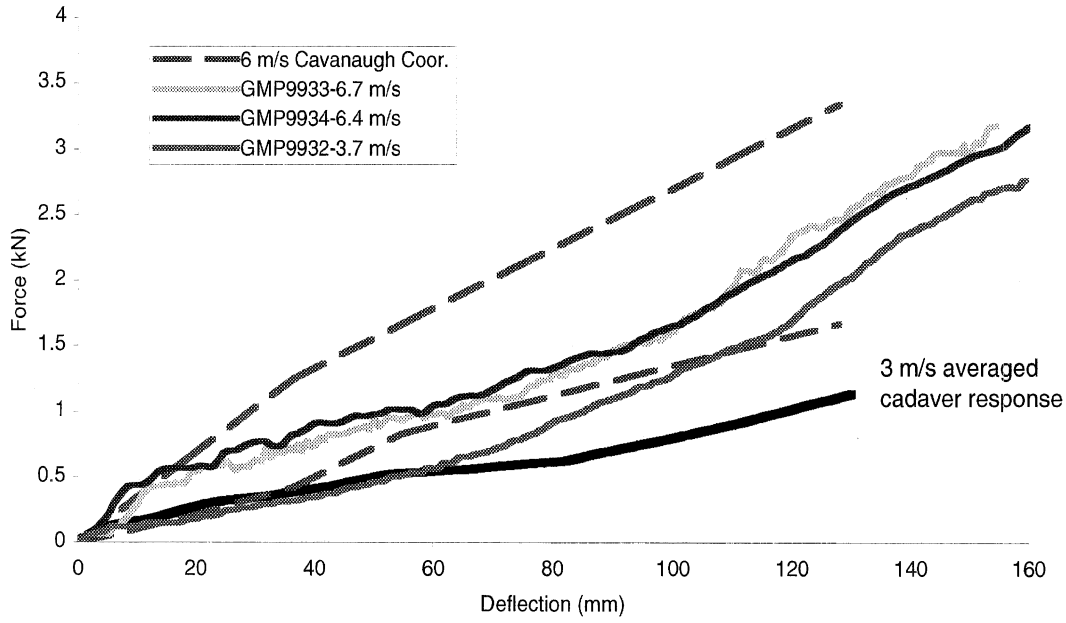

Figure 54. Force-deflection responses to rigid-bar impacts of Bladder 7 (thicker 40-durometer silicone rubber) in tests GMP9932-34 relative to scaled 6 m/s Cavanaugh Corridor and 3 m/s averaged cadaver response.

Bladder 8 (Final Prototype). Bladder 8 was fabricated to address the manufacturing problems that occurred with Bladder 7. To decrease the cure time, bladder thickness was decreased. To account for the loss of stiffness due to the decreased wall thickness, the stiffness of the silicone rubber bladder material was increased from 40 to 50 durometer. The responses of Bladder 8 to rigid-bar impacts and belt loading are shown in Figures 55 and 56, respectively. While the rigid-bar response is slightly less stiff than that of Bladder 7, it still is close to the 3 m/s average response and within the 6 m/s rigid-bar response corridor and the 3 m/s belt loading corridor. Bladder 8 is not as rate-sensitive as the human abdomen. Although its response is close to the 3 m/s average response and within the 6 m/s rigid-bar corridor, it is at the soft end of the 6 m/s corridor and stiffer than the 3 m/s average response. The belt loading response also leaves the 3 m/s belt corridor at 20 mm of penetration and reenters it at 40 mm of penetration. Because of project time constraints and because its response was near the desired corridors, Bladder 8 was selected for use in the final MAMA-2B abdomen.

Figure 56 also shows the belt-loading response of Bladder 8 relative to the more restrictive, final belt-loading corridor developed by Hardy et al. (2001) after reanalysis of

the data used to generate the original corridor. The belt-loading response data are observed to fall within the final corridors, except for the period between 20 and 40 mm of penetration, where they fall below the final corridors.

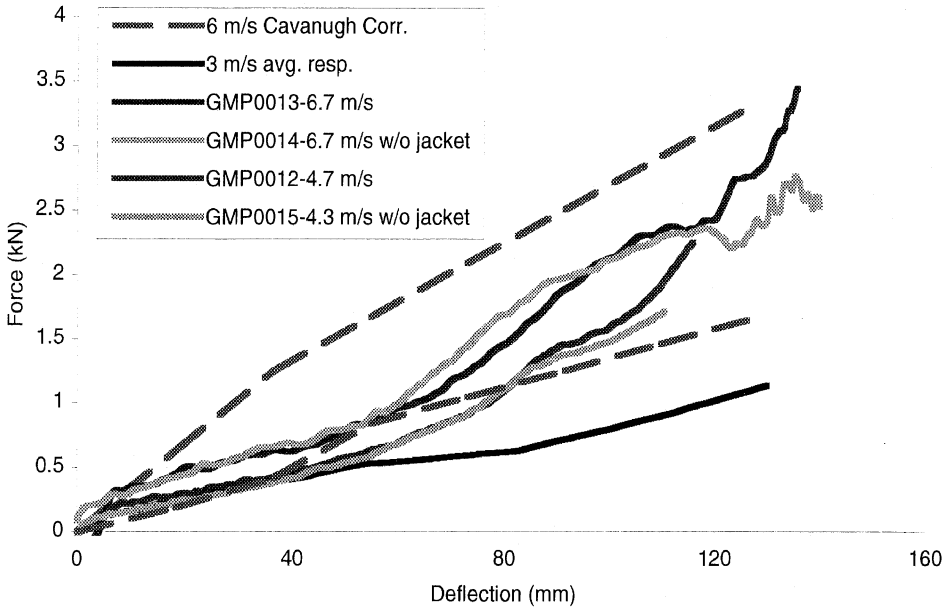

Figure 55. Force-deflection responses of Bladder 8 (final MAMA-2B 50-durometer silicone rubber bladder) to rigid-bar impacts in tests GMP0012-15 relative to scaled 6 m/s Cavanaugh Corridor and 3 m/s averaged response.

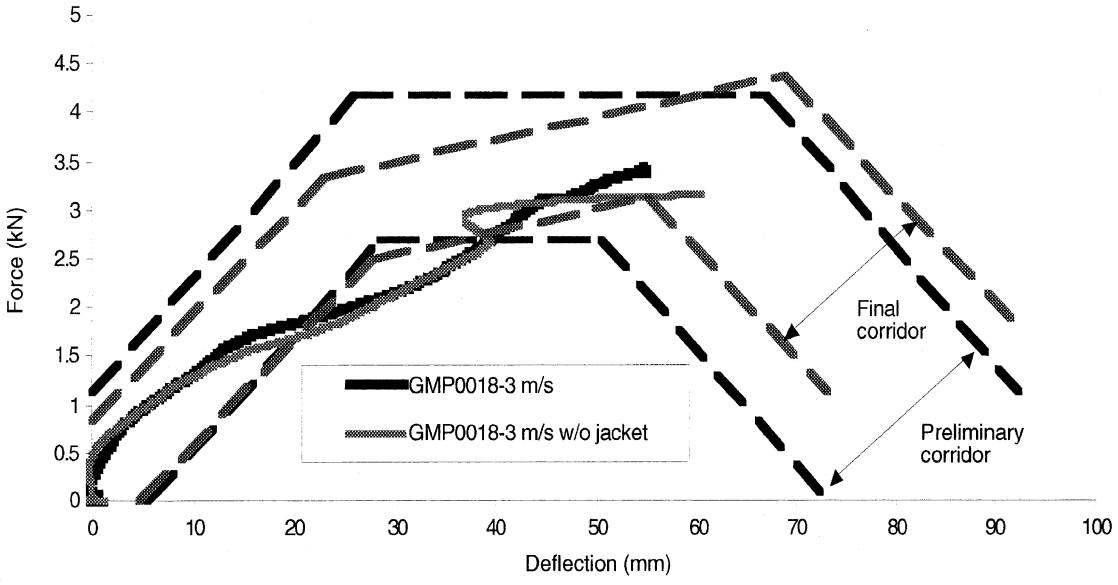

Figure 56. Force-deflection responses of Bladder 8 (final MAMA-2B 50-durometer silicone rubber bladder) to belt loading in tests GMP0017-19 compared to preliminary and final belt-loading corridors.

Bladder 8 was also tested with the surrogate airbag device. Figure 57 shows the force-deflection response from tests with and without the chest jacket, which correspond to tests GMP0049 and GMP0048, respectively. The bladder response without the chest jacket is slightly less stiff during initial loading than the surrogate airbag corridor, but after approximately 5 mm of penetration, the MAMA-2B response falls within the corridor. The bladder response with the chest jacket is less stiff than the corridors until the surrogate airbag has penetrated to a depth greater than the thickness of the chest jacket, at which time the response falls within the corridors. The decrease in initial stiffness with the chest jacket was expected because the neoprene chest jacket is significantly softer than the silicon rubber bladder that it encloses. As the penetration into the jacketed MAMA-2B abdomen increases, the chest jacket is completely compressed and the deflection shift caused by the chest jacket disappears.

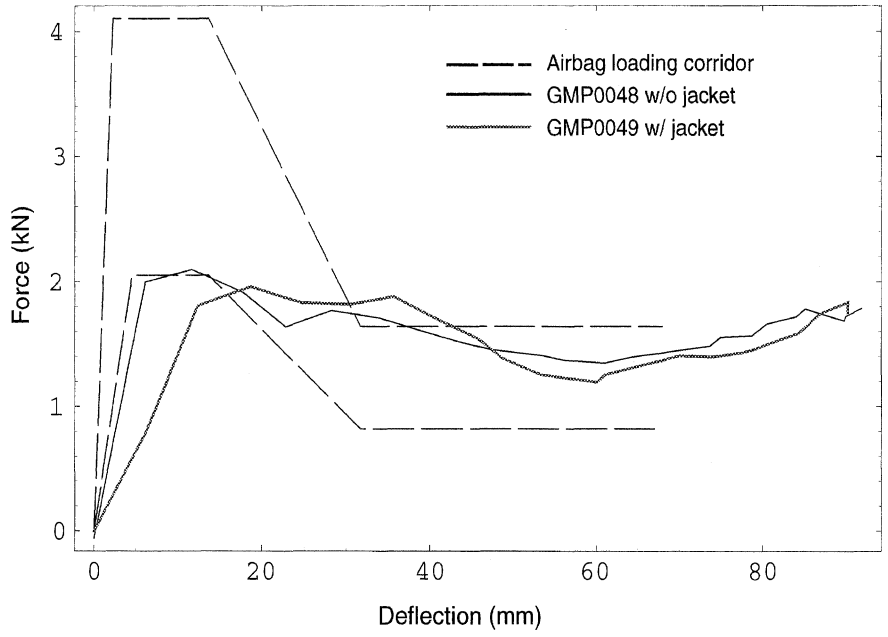

Figure 57. Responses of MAMA-2B to out-of-position surrogate airbag loading response with and without chest jacket from tests GMP0048 and 0049 compared to out-of-position airbag loading corridor developed by Hardy et al. (2001).

6.7 Summary of MAMA-2B Abdominal Component Response

Plots of the response of the improved abdomen component are found in Figures 56, 57, and 58 for rigid-bar, belt, and surrogate-airbag loading. The response of the MAMA-2B abdomen was generally within corridors defined for each type of loading tested. Rigid-bar response was within the 6-m/s Cavanaugh corridor and was close to the 3-m/s average response for deflections less than approximately 50 mm. Rigid-bar tests also

indicated that the MAMA-2B abdomen demonstrated some rate sensitivity but not as much as was observed in rigid-bar cadaver impacts conducted by Hardy et al. (2001).

Belt-loading response was generally within the defined 3 m/s corridor, except for a window between 20 and 40 mm of penetration where the response was too soft and dropped below the corridor. Simulated out-of-position airbag loading demonstrated that the abdomen component response without the chest jacket was close to the surrogate airbag corridor. With the chest jacket, the MAMA-2B abdomen response to surrogate airbag loading was less stiff than the corridor at penetrations less than 20 mm. The majority of this difference is attributed to the jacket, which is approximately 10 mm thick and is much softer than the abdomen component that it encases.

Since one of the primary objectives of this project was to improve upon the response biofidelity of the first pregnant abdomen, it is useful to compare the response characteristics of the first-generation pregnant dummy abdomen to the targeted responses for the MAMA-2B abdomen under different loading conditions. Quasi-static A-P rigid-bar loading of the original pregnant abdomen installed in the small-female dummy was conducted first using the test facility developed for measuring the quasi-static stiffness of pregnant and non-pregnant volunteers. The results showed that the quasi-static stiffness of the first pregnant abdomen is 10 N/mm, which is approximately ten times stiffer than the average stiffness measured for human volunteers.

The first pregnant abdomen was also tested dynamically using a ballistic pendulum and rigid-bar impact test setup similar to that used by Cavanaugh et al. (1986) and Hardy et al. (2001). Figure 58 shows the response for a loading rate of 6 m/s compared to the 6 m/s Cavanaugh corridor. As suggested by the quasi-static response, the dynamic force-deflection response of the original pregnant abdomen is more than twice as stiff as that specified by the 6 m/s Cavanaugh corridor. The single rigid-bar impact shown in Figure 58 damaged the abdomen and consequently prevented belt-loading and out-of-position airbag tests from being conducted on the first-generation pregnant abdomen. However, it is expected that the belt loading response of the first-generation pregnant abdomen would significantly differ from the belt-loading response corridors due to the shape, which tends to allow the belt to slide under the abdomen, and stiffness of the abdomen. Surrogate airbag loading response of the original pregnant abdomen is also expected to be significantly stiffer than the out-of-position response corridor.

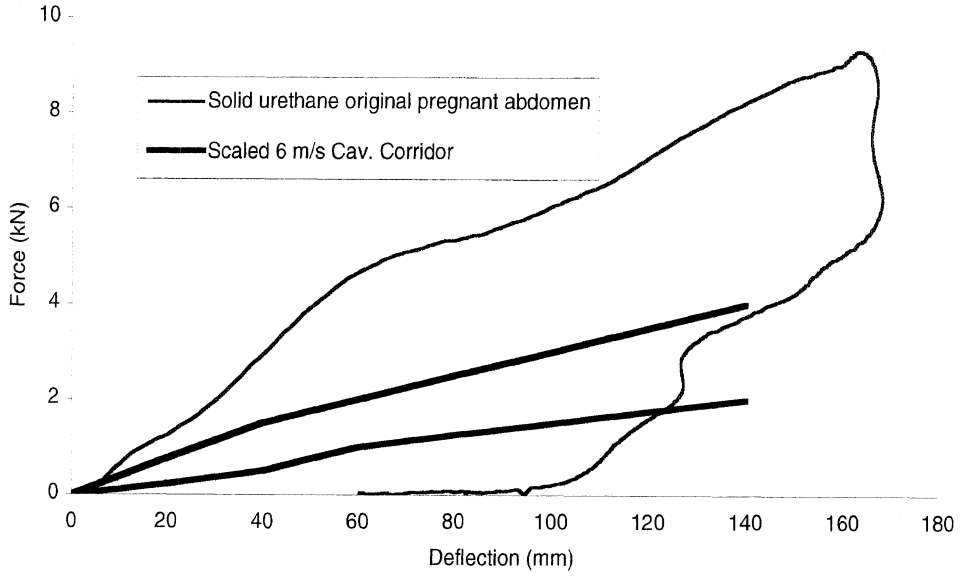

Figure 58. Dynamic response of the first pregnant abdomen compared to scaled 6 m/s abdominal response corridor derived from Cavanaugh (1986).

7.0 INSTRUMENTATION DEVELOPMENT

7.1 Instrumentation Overview

Based on the analyses and modeling described in Section 4.3, the injury mechanisms of tensile strain at the UPI due to inertially generated negative pressures and shear strains at the UPI were considered to be the most likely causes of placental abruption in motor-vehicle crashes. It was therefore desired to include instrumentation in the MAMA-2B abdomen to measure variables that can be directly related to these two injury mechanisms–that is, instrumentation to measure anterior-posterior pressure gradients within the fluid-filled bladder and circumferential strains in the bladder wall.

Because instrumentation development was initiated before the exploration of injury mechanisms was completed, instrumentation was initially developed to measure circumferential strains in the fundal (top) region of the bladder due to increased pressure caused by direct anterior loading, which was originally thought to be one of the main causes of placental abruption. As exploration of injury mechanism progressed, emphasis was placed on measuring circumferential strains due to curvature changes in the regions of direct loading and, following that, to measuring changes in curvature along the midsagittal contour of the bladder. However, development of curvature measurement instrumentation could not be completed within the time and funding constraints of the this project. Consequently, the development of curvature measurement is documented to provide guidance for future instrumentation development efforts.

Initial attempts to measure circumferential bladder strains away from the area of direct loading involved the use of strain-gaged "top hats" as shown in Figure 59. Foil-type gages are bonded to a strip of metal that is bent in the shape of a top hat, and the bottom of the hat is bonded to the inner or outer surface of the bladder. As the bladder stretches or shrinks, the feet of the top hat spread apart or move together, which results in bending and strain in the top of the hat that can be measured by the foil gages. Testing of bladders was conducted with these uniaxial top-hat transducers bonded to both the inside and outside surfaces and with the top hats oriented in different directions relative to the impact loading. The use of top-hat instrumentation to measure circumferential strains in the bladder was abandoned for several reasons. The most important reason was that exploration of injury mechanisms indicated that circumferential strain in the uterus due to increased uterine pressure away from the placenta is not a likely source of UPI failure and fetal loss. This conclusion is supported by top-hat strain measurements obtained in quasi-static rigid-bar bladder indentation. For reference, the setup for these tests is shown in Figure 60. Results from tests with top-hat transducers are shown in Figure 61.

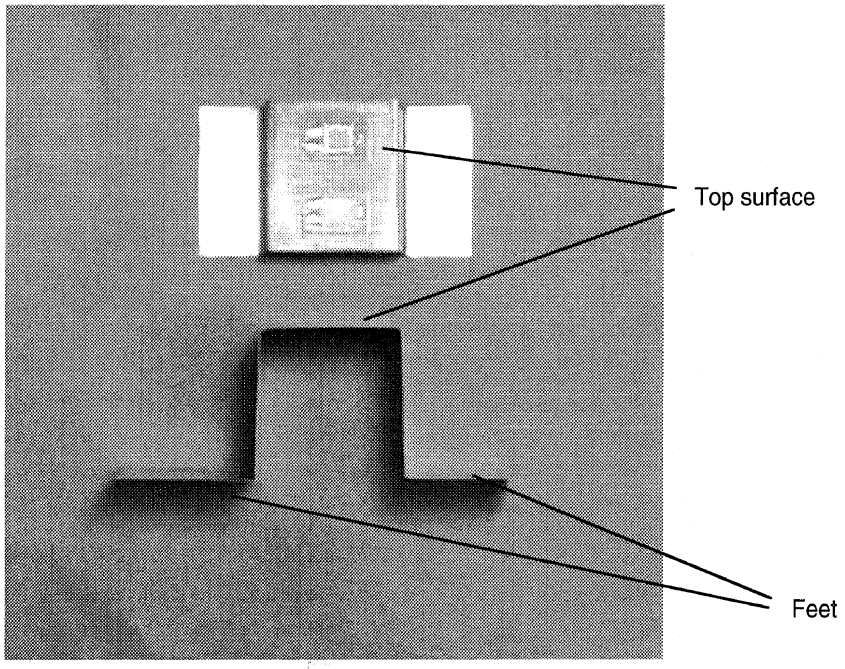

Figure 59. "Top-hat" transducers.

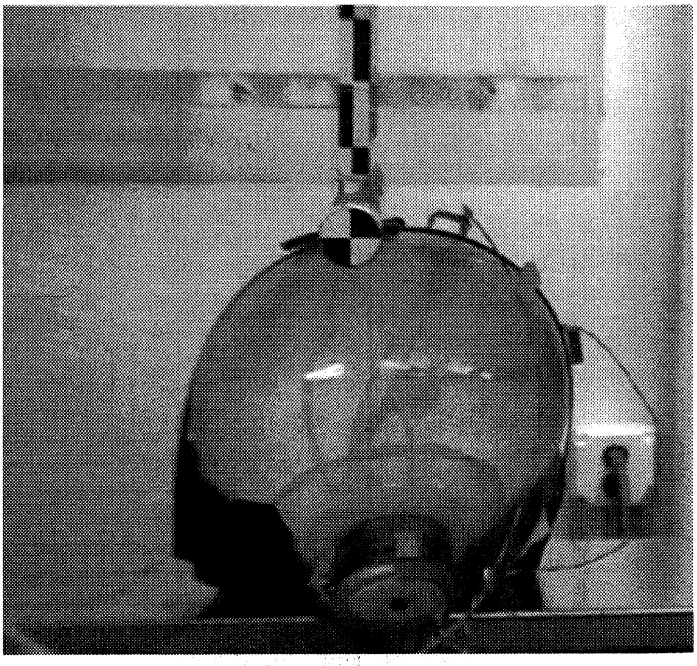

Figure 60. Side view of test setup for quasi-static rigid-bar loading of the MAMA-2B bladder to evaluate top-hat transducer performance. Loading of the abdomen occurs when the rod-shaped indentor (the object covered with target tape) is uniaxially displaced into the bladder.

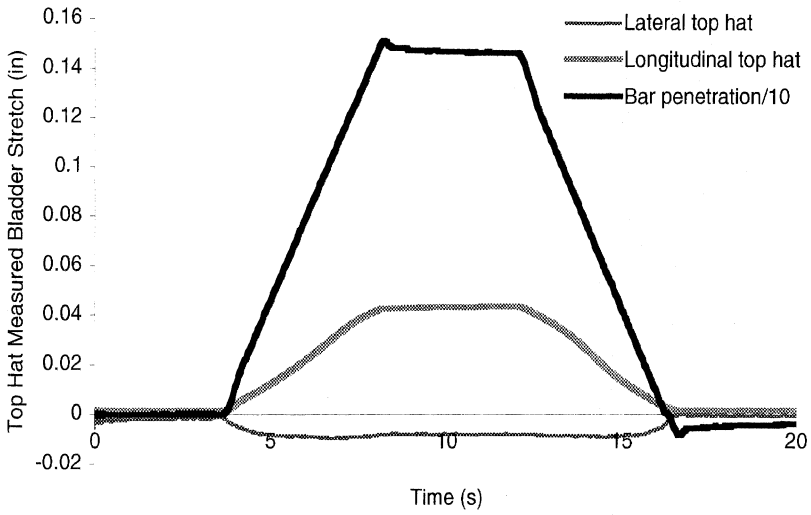

Figure 61. Laterally- and longitudinally- oriented top hat stretch measured during quasi-static indentation of the bladder away from the top-hat location, indicating that circumferential stretch caused by increased pressure in the bladder is small (approx. 0.04 in the figure above).

An attempt was made to use the top-hat transducers to measure strains due to curvature changes in the bladder, but the size of the top hats and their unidirectional capabilities precluded their successful application to achieving the desired measures. As a result, measurement of circumferential strains in the bladder was abandoned in favor of finding a direct method for measuring changes in curvature due to impact loading.

Development of instrumentation to measure A-P pressure gradients was more straightforward than measurement of bladder strains and curvature, and involved attaching pressure transducers on the inside surface of the bladder. However, as discussed below, measuring reliable dynamic pressure changes within a water-filled bladder under loading conditions that can be expected in a crash test is not without significant problems and challenges.

7.2 Measurement of Bladder Curvature

Once it was determined that a likely mechanism of placental abruption was curvature change in the area of the placenta, a search for possible curvature-measuring instrumentation was initiated. This search led ultimately to exploring the use of a fiber optic "Shape Tape" made by Measurand Inc. As documented below, the results of this exploration effort are encouraging, although some problems remain before the Shape Tape can be reliably used for this rather demanding application.

7.2.1 Shape Tape Theory

Figure 62 shows the Shape Tape connected to the interface box that was used in preliminary testing with the uterine bladder. The tape consists of 16 glass-fiber sensors equally spaced over a 42 cm section of curvature-sensitive tape. These sensors are connected to an interface box through a 3 m long curvature-insensitive length of tape. The interface box houses 16 LEDs that provide independent light sources for each sensor in the tape. Each sensor consists of a loop of glass fiber that is specially treated so that changes in curvature over the length of the sensor result in a change in the amount of light passing through the fiber loop, which is converted into analog voltage by the interface box. The shape of a surface that contacts the tape is determined by integrating curvature measurements of all the sensors from one end of the sensitive zone of the tape to the other. Similar to the chest band, this integration is performed by customized algorithms that are used during post processing.

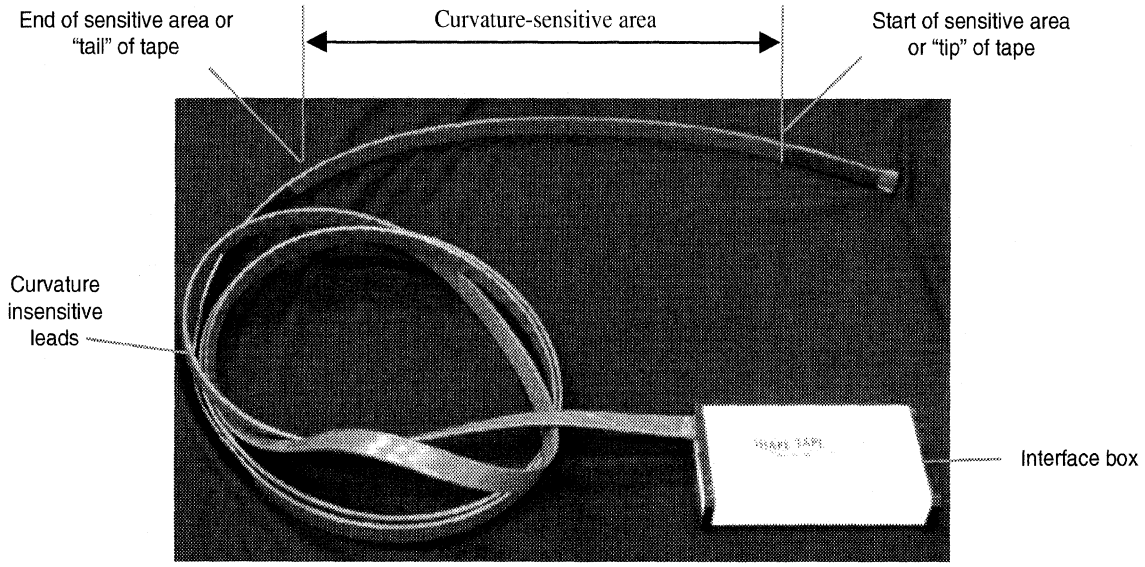

Figure 62. Shape Tape by Measurand, showing the curvature-sensitive section along with the curvature-insensitive lead length and the interface box.

Early versions of Shape Tape were not suitable for applications where the tape was directly loaded because pressures applied to the tape caused changes in sensor response that mimicked changes in curvature. However, the Shape Tape was modified by Measurand to reduce pressure sensitivity by sandwiching the sensitive areas of the tape between flexible steel bands. Glass fibers of a diameter greater than the thickness of the sensitive area were used to separate the steel bands so that direct loading does not apply pressure to the sensitive area.

Because the Shape Tape measures curvature, which it integrates from the base to the tip of the tape to determine total shape, it theoretically can be used to measure penetration (and rate of penetration) into the MAMA-2B abdomen by objects of almost any geometry. However, the measurement resolution of the Shape Tape is limited by the length and spacing of the fiber optic loops within the tape. For the tape used in prototype

testing, 16 sensors were used and each sensor loop was approximately 26 mm long. Because at least one sensor loop is required to resolve each monotonic change in curvature, the minimum radius of curvature that the tape can measure is approximately 9 mm. Figure 63 illustrates the concept.

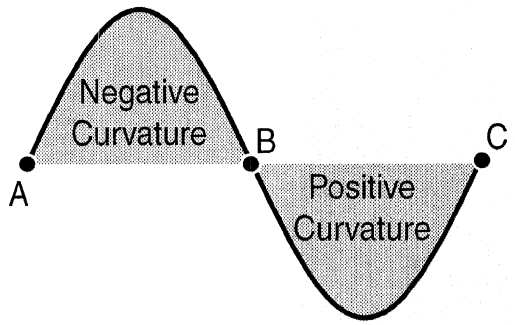

Figure 63. "Nyquist Theorem" of curvature measurement. If the sensor length is ABC or greater, the sensor measures equal amounts of upwards and downwards curvature and consequently its averaged output is zero. If one sensor per monotonic curve is used (i.e., two sensors of length AB and BC, respectively) the correct curvature is measured.

7.2.2 Performance of Shape Tape in Quasi-Static Testing

To evaluate the Shape Tape performance, it was positioned on the pregnant abdomen as shown in Figure 64. The tip of the tape was loosely attached to the upper-mounting cradle. The tape was routed through silicone-rubber anchoring straps to hold it in place along the midline of the bladder, passed through the lower-mounting cradle, and then routed along the back of the bladder. Friction against the bladder and lower-mounting cradle prevented the tape from sliding through the lower-mounting cradle during a test. When the abdomen was installed in the dummy, the tape was lightly pressed against the lumbar spine near the upper-mounting cradle and the tape was routed so it ran through the ribcage and exited the dummy at the posterior neck. The 42 cm sensitive area of the tape ran along the midline of the abdomen from the upper-mounting cradle to just inside the lower-mounting cradle. This configuration ensured that the base of the tape would be stationary with respect to the bladder during a test. However, to prevent damage to the tape from stretching, the tip of the tape was allowed to move when the bladder experienced large deformations.

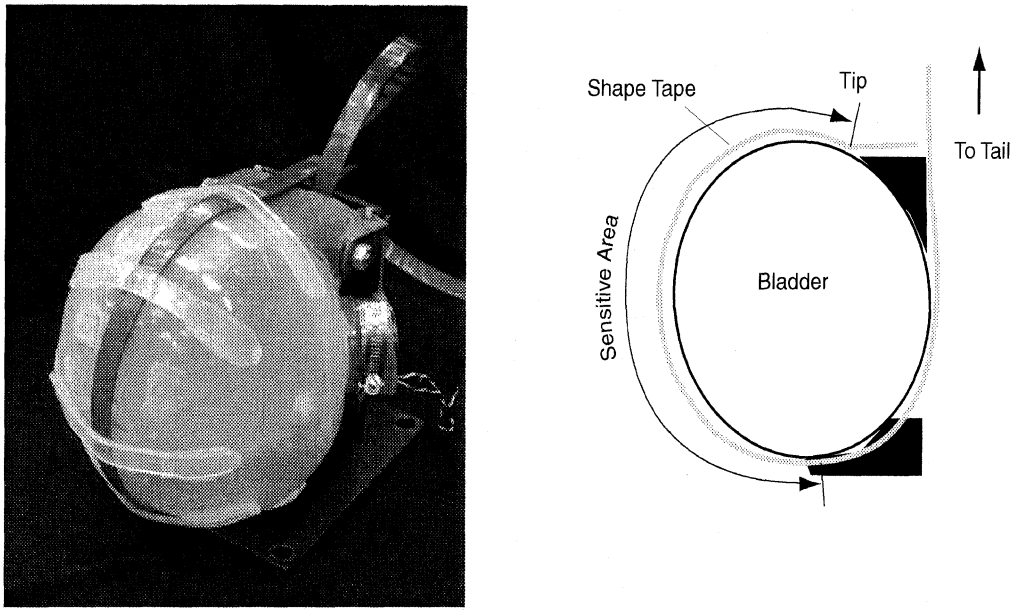

Figure 64. Shape Tape installed on prototype bladder (left) and schematic of Shape Tape routing (right).

Quasi-static penetration tests of the bladder with the Shape Tape installed were performed using the 2.54 cm diameter, 45.7 cm long indentor, shown in Figure 65, to determine if the Shape Tape is capable of measuring curvatures near its resolution limits and to study the effect of pressure on curvature measures. These tests were performed using an Instron material test device to drive the indentor into the bladder. The ability of the Shape Tape to resolve curvature was evaluated by comparing indentor penetration (i.e., displacement of the Instron cross head) to penetration measured by the Shape Tape at discrete depths of penetration. Plots of the abdomen contour based on the Shape Tape were visually compared to observations of the bladder shape during the test. Figures 66a and 66b show this comparison. Because penetration into the bladder was less than 50 mm, no stretch of the bladder was expected and, consequently, the positions of the ends of the sensitive zone of the tape did not move during testing. However, if penetration to a greater depth were applied, the tip of the tape, which is only loosely attached to the bladder, would have likely moved because of stretch of the bladder.

As shown in Figure 66b, the position of the tip deviates from its initial value. Because the indented shape closely matches the undeformed shape up to the indented region, the deviation of the position of the tip probably results from an error in curvature measurement from a single sensor near the indented area. This error could have resulted from either the inability of the Shape Tape to resolve the curvature of the indentor or from pressure sensitivity.

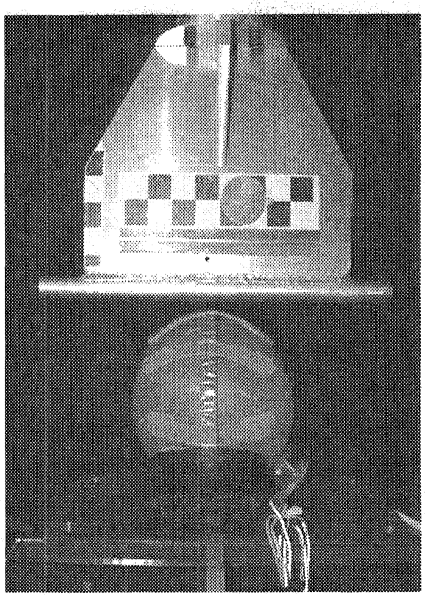

Figure 65. Quasi-static testing of Shape Tape installed in bladder.

The standard "base-to-tip" algorithm used by the Shape Tape is particularly vulnerable to errors in curvature measurement because the position of any segment of the tape is determined by integrating the curvature information from all sensors closer to the base of the tape. Because sensor position is determined by integrating curvature from the base of the tape to its tip, errors in curvature measurement near the base of the tape will result in large errors in the calculated position of the tip of the tape. However, errors in curvature near the tip of the tape will only result in small errors in the calculated tip position. This behavior can be observed in Figure 66b in the calculated shape labeled "base-to-tip," where the position of tape near the base is close to the curve defining the undeformed shape and deviates from the undeformed shape near the tip.

Along with the standard shape interpretation algorithm, two other algorithms were used to adjust for curvature error and improve shape measurements. The first of these algorithms determined shape by integrating curvature from the tip to the base of the tape. Figure 66c shows the shape calculated using tip-to-base curvature integration. This algorithm is best suited to cases where the error in curvature measurement occurs near the base of the tape and requires that the tip of the tape remains stationary during a test. For curvature measurement errors that occurred near the center of the tape, a third algorithm was developed. This algorithm averaged the position data of each of the sensors in the Shape Tape calculated from tip-to-base and base-to-tip integration. Figure 66d shows shape data calculated using this algorithm. Because the third algorithm is an average of the first two, it also requires that the ends of the tape remain stationary during a test. If the ends of the tape do not remain stationary, the calculated length of the tape may change, resulting in a physically unrealistic shape. To correct for this, a scaling factor was applied to the data as necessary to ensure that the length of the tape remained constant.

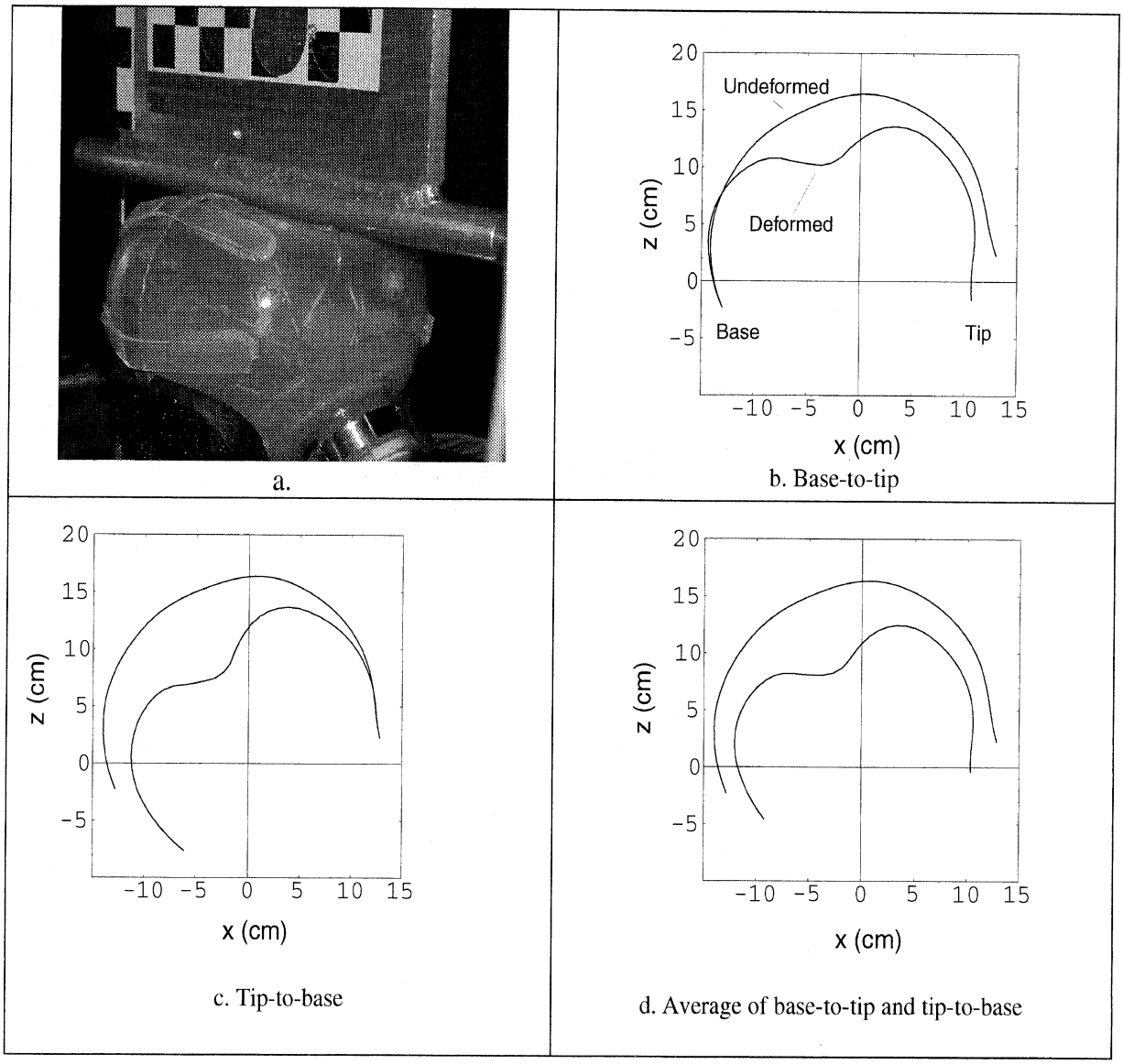

Figure 66. Peak penetration of bladder during quasi-static indentation of MAMA-2B abdomen and associated deformed and undeformed Shape Tape results. (a) Picture of indentation. (b) Shape calculated using base-to-tip integration. (c) Shape calculated using tip-to-base integration. (d) Shape calculated by averaging base-to-tip and tip-to-base integrations.

As an additional check on the accuracy of the three algorithms, the penetration of the indentor in the bladder was calculated from the measured shapes. The results of this calculation for each of the three algorithms are shown in Figure 67 along with the actual penetrations (i.e., the movement of the Instron crosshead). As indicated, penetration measurements obtained from the shape contours measured by the Shape Tape are close to the actual values. This indicates that curvature integration up to the indented area is probably correct and that the errors in predicted shape observed in Figure 66 are likely due to errors in the curvature measurement from a single sensor in the indented area. These errors may result from pressure sensitivity or from the inability of the Shape Tape to resolve curvatures near its theoretical limits.

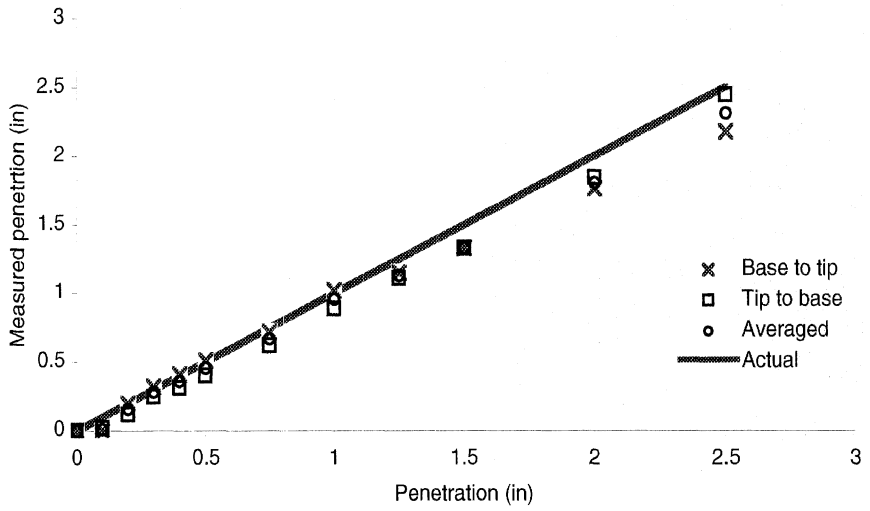

Figure 67. Comparison of penetration calculated from static indentation of MAMA-2B bladder using base-to-tip, tip-to-base, and average of tip-to-base and base-to-tip algorithms to actual penetration measured from displacement of the indentor.

7.2.3 Performance of Shape Tape in Rigid-Bar Impacts

To determine if penetration and curvature can be measured under anticipated abdominal loading conditions with higher loading rates, higher contact pressures, and greater penetrations, rigid-bar impacts were conducted in the manner described in Section 6.6.1.1 using a nominal loading rate of 6 m/s. The setup for these tests is shown in Figure 68 along with the shapes calculated using each of the three algorithms. If it is assumed that the tip of the tape remains stationary during the test, none of the measured shapes appear to be realistic. However, because of the large stretch of the upper portion of the bladder, the tip of the tape probably moved from its initial position since it was loosely attached to the upper-mounting cradle to prevent damage if the bladder below the tape stretched. Taking this into consideration, the shape shown in Figure 68b using base-to-tip integration appears to be realistic, while the shapes shown in Figure 68c and 68d do not appear to be realistic. Actual penetration depth could not be calculated from film data due to an error in camera positioning that resulted in the camera filming a slightly oblique view. However, the peak penetrations measured by the Shape Tape were 170, 160, and 120 mm for base-to-tip, tip-to-base, and average methods of shape calculation. Of these penetrations, 120 mm is considered to be the most accurate measure. This is based on the overall depth of the filled bladder of 185 mm and the picture at peak penetration shown in Figure 68a showing approximately 50 mm between the tip of the pendulum and the front of the lumbar spine.

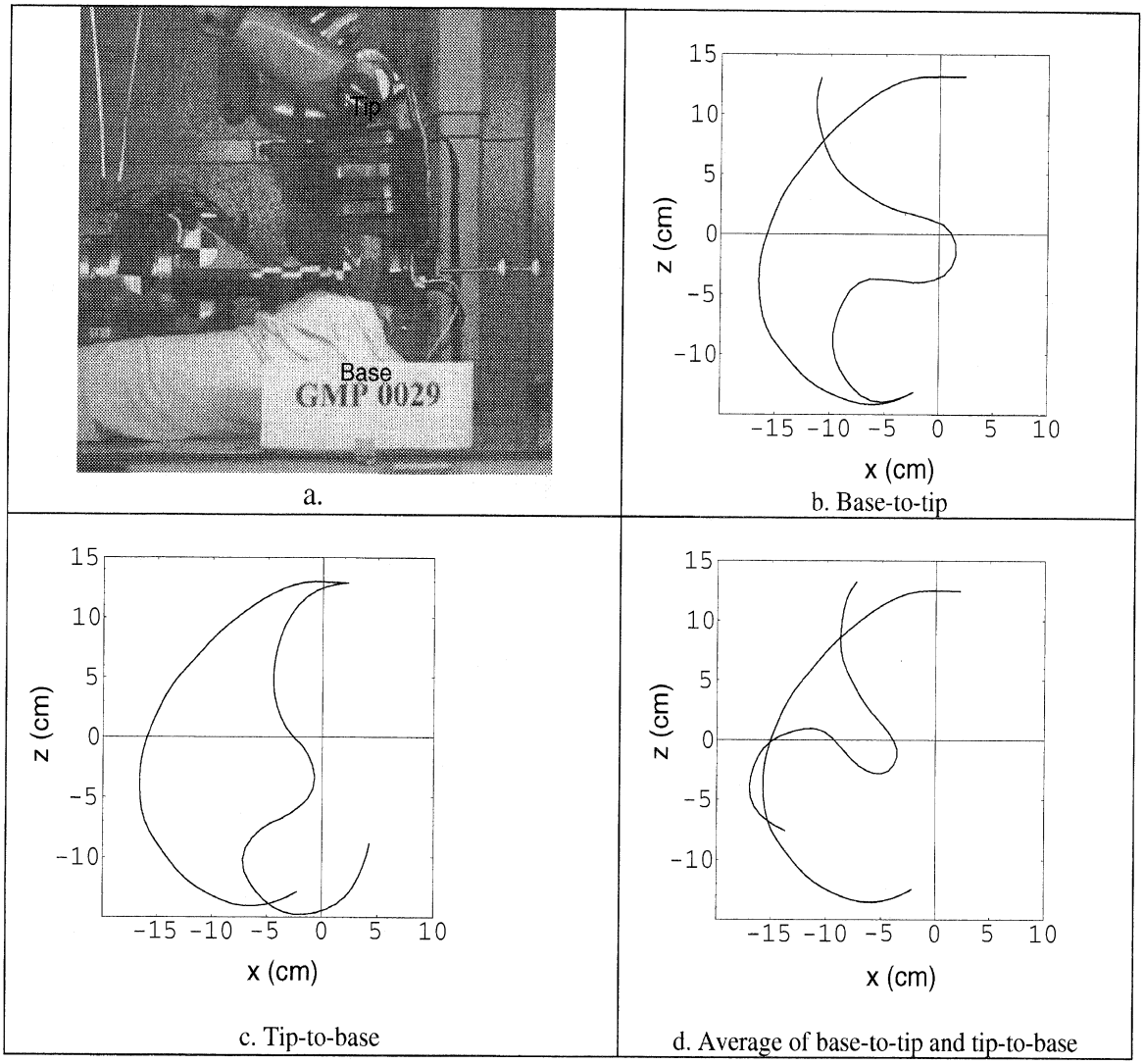

Figure 68. Peak penetration into bladder during pendulum impact of MAMA-2B with Shape Tape in test GMP0029. Deformed (right) and undeformed (left) shapes are shown at a time corresponding to maximum penetration. (a) Bladder deformation. (b) Shape calculated using base-to-tip integration. (c) Shape calculated using tip-to-base integration. (d) Shape calculated by averaging base-to-tip and tip-to-base integrations.

7.2.4 Performance of Shape Tape for Out-of-Position Airbag Loading

Instead of repeating pendulum tests to obtain better film data for penetration measurements, simulated out-of-position airbag tests were conducted using the surrogate airbag test methodology described in Section 6.6.1.3, which includes a laser device for direct and more accurate penetration measurement. The setup for these tests is shown in Figure 69a. The shapes calculated using each of the three algorithms are shown in Figures 69b through 69d. The shape calculated using base-to-tip integration (Figure 69b) appears to be the most realistic for this type of distributed loading, while shapes from the tip-to-base (Figure 69c) and average algorithms (Figure 69d) are not realistic. The problems with the tip-to-base integration, and consequently the average integration, are probably due to motion of the tip of the tape due to bladder stretch, although pressure sensitivity of the Shape Tape may also affect measurements.

Figure 70 shows penetration-time histories from the base-to-tip, tip-to-base, and averaged shape calculation methods relative to the measured penetration values. All of the curves closely resemble the penetration measured by the laser. Peak penetration measured by the laser at the end of the loading phase, which corresponds to a time of 12 ms in Figure 70, was 100 mm, while the values calculated by the base-to-tip, tip-to-base, and average methods of shape integration gave penetrations of 99, 101, and 100 mm at the same time.

Penetrations measured by the Shape Tape during simulated out-of-position airbag loading are closer to the actual values than penetrations measured during rigid-bar testing for several reasons. The diameter of the surrogate airbag impactor is larger than that of the pendulum. Consequently, the Shape Tape experiences larger curvatures, which are easier to resolve. Also, the larger bladder deformations resulting from rigid-bar impacts likely result in more bladder stretch, which leads to more movement of the tip of the tape, which causes problems with both the tip-to-base and average curvature calculations. In addition, the contact pressure experienced by the Shape Tape during surrogate airbag loading is likely less than that experienced by the tape in rigid-bar impacts.

Shape Tape measurements from out-of-position airbag loading are encouraging. In particular, the base-to-tip integration produces realistic shapes and accurate peak penetrations. Neither of the other two integration methods produces reasonable shapes nor calculates realistic penetrations. The base-to-tip integration likely gives better results than either the tip-to-base or average integrations because the base-to-tip integration makes the physically realistic assumption that the base of the tape is stationary with respect to the rest of the tape. The other two integration methods are likely unrealistic because they are affected by the assumption in the tip-to-base algorithm that the tip of the tape is stationary, when it is likely not.

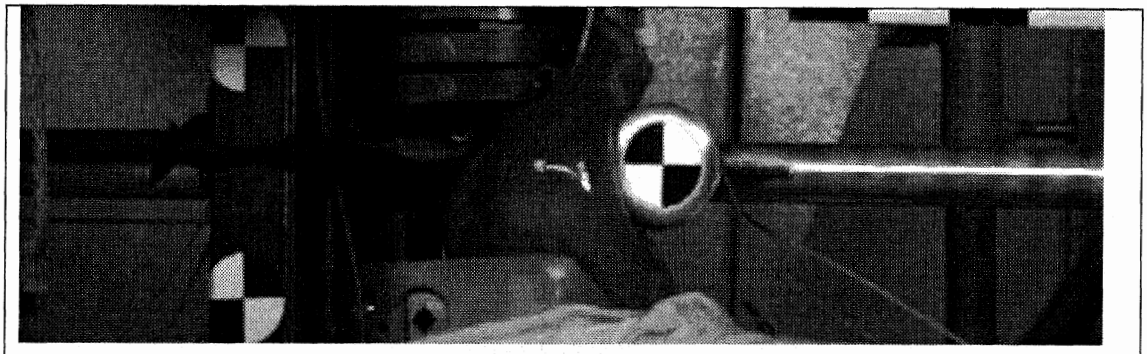

a.

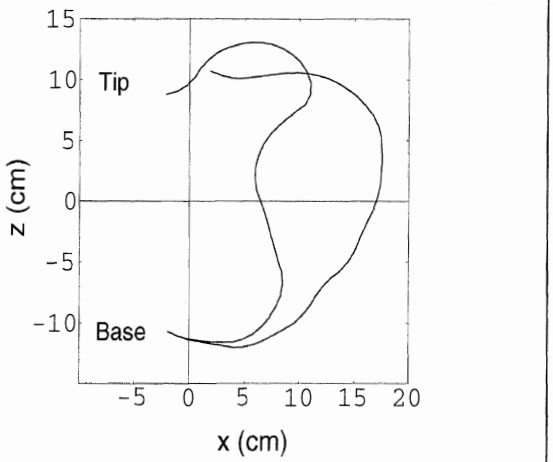

b. Base-to-tip

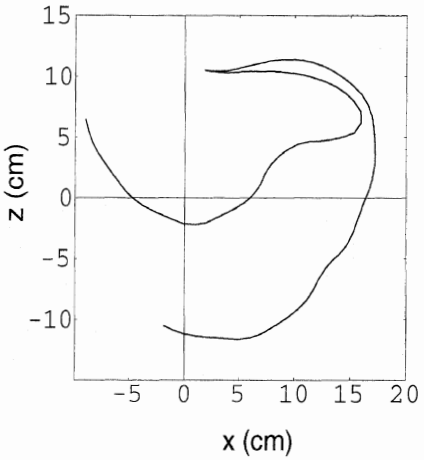

c. Tip-to-base

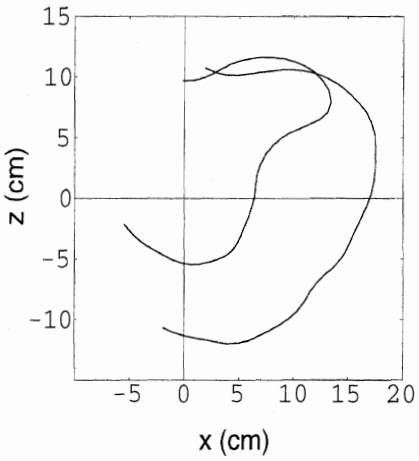

d. Average of base-to-tip and tip-to-base

Figure 69. Peak deflection from out-of-position airbag loading of the MAMA-2B abdomen. Deformed (left) and undeformed (right) bladder shapes were taken at a test time that corresponds to maximum observed penetration. (a) Indentation shape. (b) Shape calculated using base-to-tip integration. (c) Shape calculated using tip-to-base integration. (d) Shape calculated by averaging base-to-tip and tip-to-base integrations.

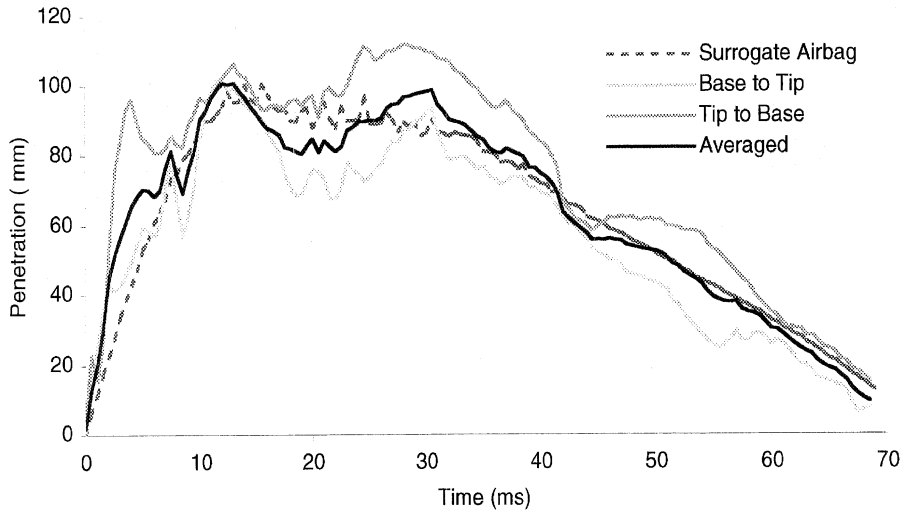

Figure 70. Surrogate airbag penetration measured from Shape Tape using each of the three processing algorithms compared to the direct displacement measurement from the surrogate airbag device.

7.2.5 Performance of Shape Tape in Full-Dummy Testing

Fifteen sled tests were conducted to determine the performance of the Shape Tape under loading from vehicle and restraint components such as three-point belts, airbags, and steering wheels. The setup for these tests is shown in Figure 71. The dummy was placed on a rigid seat with a seat back angle of 35° from vertical and a seat pan angle of 15° from horizontal. All values for dummy positioning were based on the positions of pregnant small females measured in a study of seated anthropometry during pregnancy (Klinich et al., 1999). The position of the seat was set so that there was 70 mm of clearance between each dummy knee and the front surface of the knee bolster. The steering wheel was positioned so that its lower rim was approximately 30 mm from the dummy abdomen. The steering wheel angle was set to 30° from vertical. The lap belt was rigidly anchored to a sled platform. The upper end of the shoulder belt was connected to a D-ring located 305 mm behind and 178 mm above the seated dummy's shoulder at a lateral distance of 305 mm from the midsagittal plane of the dummy. To simulate retractor spool out, approximately 70 mm of slack was left in the shoulder belt and the lap belt was pulled to a snug fit. Abdominal contours calculated at peak penetration are contained in Appendix B, along with signals from all dummy instrumentation.

Qualitatively, the abdomen bladder midline contours resulting from Shape Tape are realistic for loading by a single object, such as a steering wheel or a lap belt. Whether the tape accurately measured penetration of a single object is unknown, since there was no way to calculate the belt and steering wheel penetration in the tests. However, as illustrated in Figures 72a and 72c, the Shape Tape does not produce realistic shapes when the abdomen was loaded by more than one object (i.e., in two of these figures the penetration of the steering wheel is observed to be greater than the original abdominal

depth). Penetration by the steering wheel in Figure 72b is more reasonable; however, in the area where the lap belt would compress the bladder, distention is observed. For both Figures 72a and 72b, the portion of the curve closest to the point where integration starts gives the best prediction of shape. Problems in the shape calculations appear to result from errors in the curvature measurement from several sensors. These include the sensor near the base of the tape where the lap belt contacts the abdomen, the sensor at the tip of the tape, and possibly the sensor beneath steering wheel contact. Problems with the measurement at the tip of the tape are probably due to motion of the tip due to bladder stretch. Problems with the sensors below the lap belt and the steering wheel contacts are likely due to either pressure sensitivity or to the inability of the Shape Tape to resolve small curvatures.

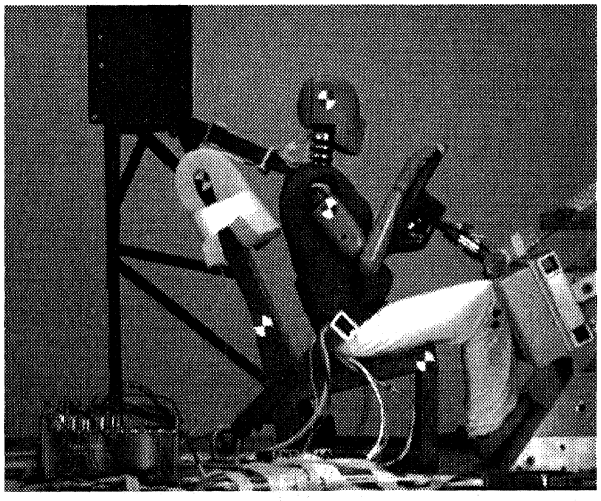

Figure 71. Side-view photo showing peak penetration of steering wheel and lap belt into upper and lower regions of the new pregnant abdomen in frontal sled test GMP0042.

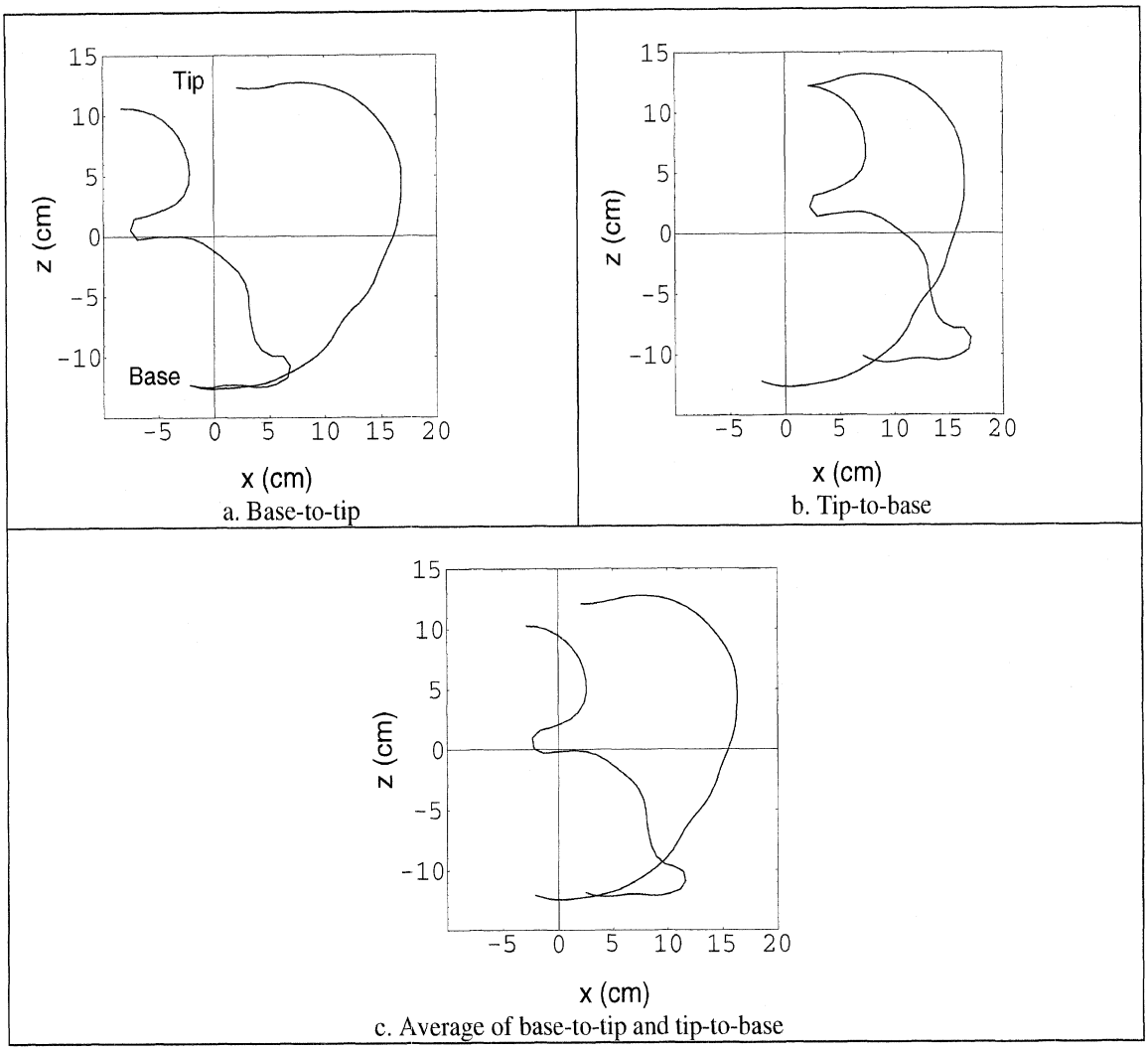

Figure 72. Deformed and undeformed shapes calculated at peak deformation from steering wheel and lap belt contact in test GMP0042. (a) Shape calculated using base-to-tip integration. (b) Shape calculated using tip-to-base integration. (c) Shape calculated by averaging base-to-tip and tip-to-base integrations.

7.2.6 Further Development of Shape Tape Transducer

The Shape Tape testing described above indicates that the Shape Tape can measure penetration and shape when the bladder is indented quasi-statically with small-diameter objects at low penetration and low contact pressures, and dynamically with large-diameter objects that likely produce relatively low contact pressures. Testing also indicates that the Shape Tape has problems measuring dynamic penetrations with small-diameter objects that produce high contact pressures. However, based on the results described above, it cannot be determined whether the errors in measured shape during dynamic testing at large penetrations with small-diameter objects result from pressure sensitivity or the inability of the tape to resolve small curvatures at large penetrations.

Further improvements in the Shape Tape require knowing whether the erroneous shapes calculated from curvature data result from pressure effects or from the inability of the tape to resolve small curvatures, or both. If problems in shape measurement result from of pressure sensitivity, the tape can be redesigned with thicker supporting fibers or with thicker metal plating. Moving the tape to the inner surface of the bladder would also eliminate pressure sensitivity, although this could result in shapes that are not completely accurate unless a reliable method for attaching the full length of the tape to the inner surface of the bladder can be found. If errors in curvature measurement result from the spatial resolution of the tape, a new tape could possibly be fabricated with more sensors. Alternatively, a combination of two shorter tapes could be used, with one starting at the upper-mounting cradle and running to the bladder midline, and the other starting at the lower-mounting cradle and running to the bladder midline.

To determine if errors in quasi-static shape-tape curvatures resulted from pressure sensitivity or the inability of the tape to resolve the curvature of the indentor at large penetrations, additional quasi-static tests were conducted with the Shape Tape located on the inner surface of the bladder to minimize contact pressures. In these tests, the radius of the curvature of the indentor was 12.6 mm, which is identical to that of the pendulum and close to that of the steering wheel used in sled testing. Figure 73 shows this test setup. The Shape Tape was routed through slits in an unfilled bladder near where the cradles would normally be mounted. The ends of the tape were rigidly anchored to each other and did not move over the duration of the test.

Results from this testing are shown in Figures 74a to 74d, and indicate that even under test conditions where pressure is probably not a factor and the ends of the tape are rigidly anchored, errors in shape measurement still occur. This suggests that some of the error in the Shape Tape measurements results from the inability of the tape to resolve the applied curvatures, even though those applied curvatures are within the theoretical resolution limits of the tape. Therefore, any redesign of the tape should focus on improving resolution by either adding more sensors to a single tape or by using a dual tape approach, where the two tapes measure penetrations to the upper and lower halves of the bladder, respectively.

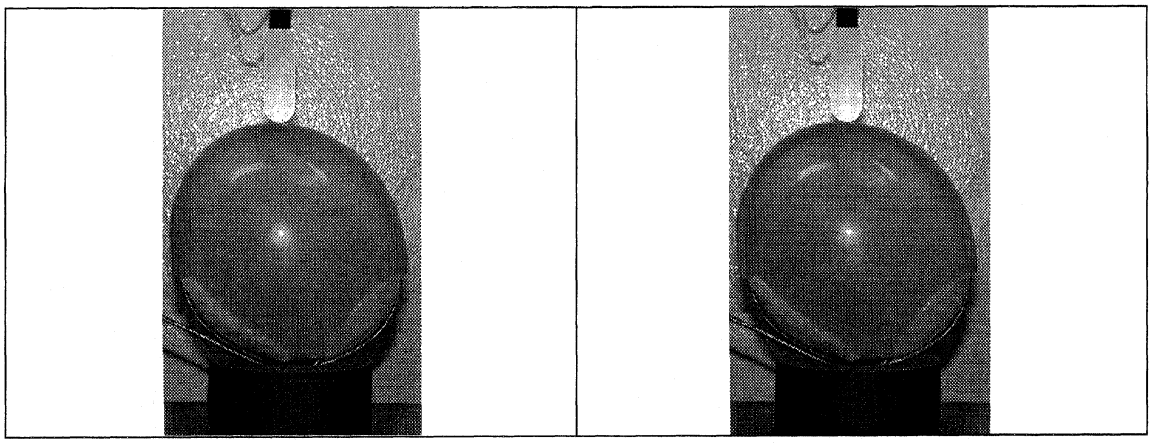

Figure 73. Quasi-static loading with tape routed inside the bladder to eliminate pressure sensitivity.

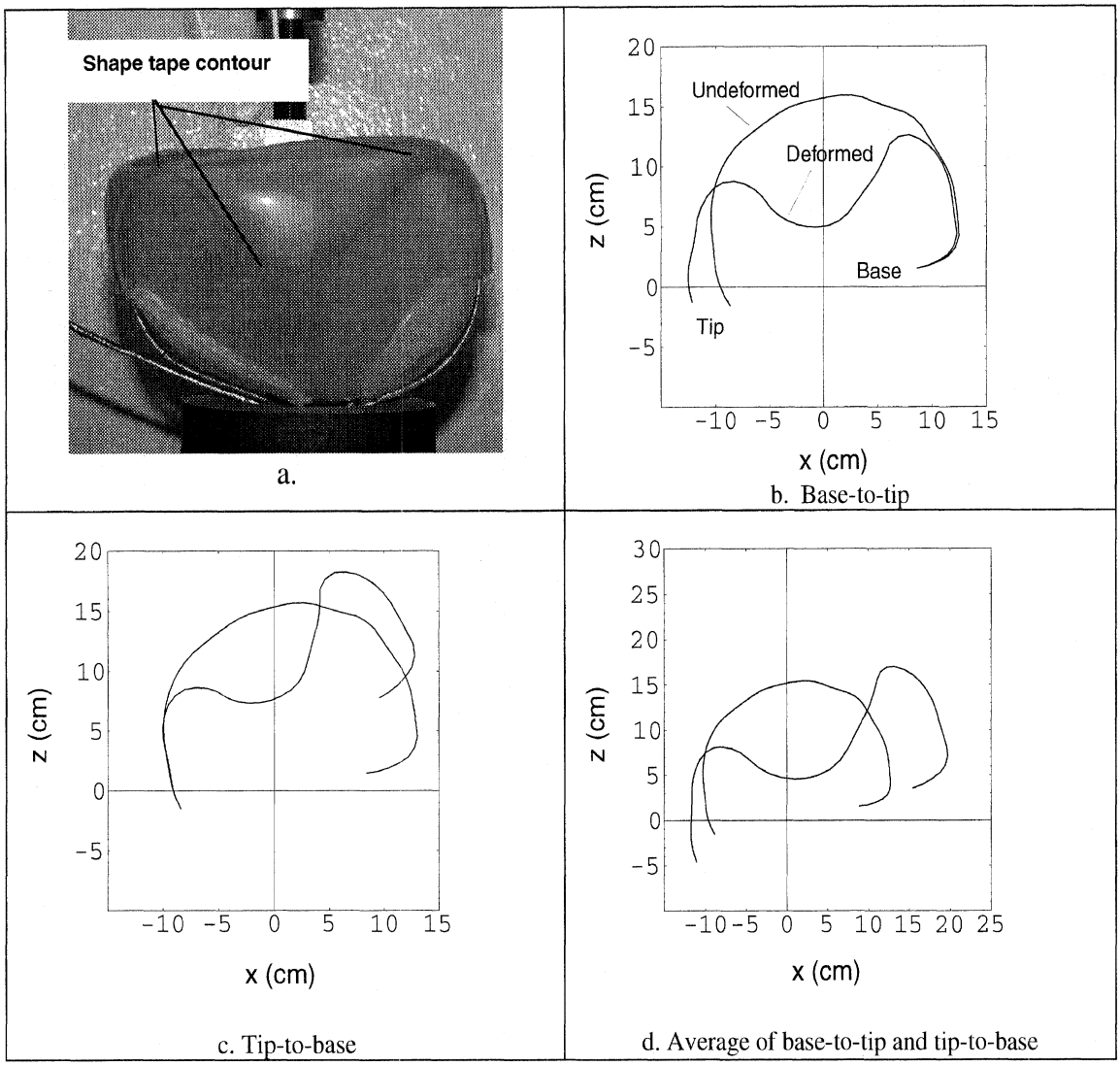

Figure 74. Quasi-static indentation of Shape Tape inside an unfilled bladder to eliminate pressure sensitivity. Tests were performed using 2.54 cm wide bar with rounded 2.54 cm diameter tip. (a) Deformed shape. (b) Shape calculated using base-to-tip integration. (c) Shape calculated using tip-to-base integration. (d) Shape calculated by averaging base-to-tip and tip-to-base integrations.

7.2.7 Conclusions from Shape Tape Testing

In summary, the Shape Tape is not currently usable for the pregnant dummy application. However, further investigation of Shape Tapes with increased numbers of sensors or different processing algorithms holds promise for curvature and penetration measurement in future pregnant dummy development.

7.3 Measurement of Internal Bladder Pressures

To measure negative pressure in the posterior bladder along with the anterior-to-posterior pressure differential across the bladder, pressure transducers were attached at the anterior and posterior inner surfaces, as shown in Figure 75. The performance of these transducers was evaluated using quasi-static and dynamic tests, including whole-dummy impact and sled testing.

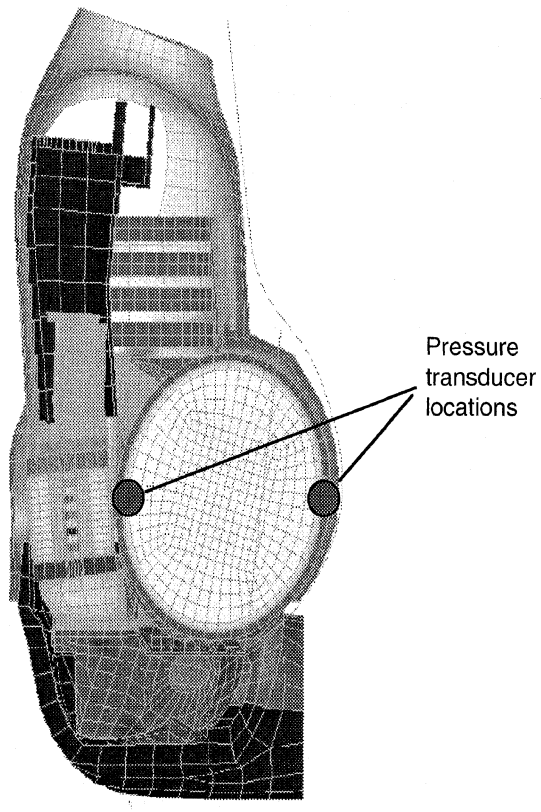

Figure 75. FEM of dummy with pressure transducer locations highlighted.

Miniature pressure transducers manufactured by Precision Measurement Co. were selected for the pregnant dummy application because they are submersible in water for extended periods of time. These transducers consist of a single strain gage bonded to a brass diaphragm that is attached to a brass casing. Because the brass casing would not bond to the silicone bladder, pressure transducers were first bonded to a thin aluminum plate using cyanoacrilate. The aluminum plate was then bonded to the silicone bladder using a silicone-based adhesive.

7.3.1 *Pressure Measurements from Rigid-Bar, Belt-Loading, and Bladder-Only Sled Tests*

Pressure transducer performance was evaluated during belt loading and rigid-bar impacts. Because both types of tests involve a single object compressing the anterior surface of the bladder, the shape and general character of the pressure histories for these two types of tests are comparable. Figures 76 (rigid-bar impact) and 77 (belt loading) illustrate these similarities for anterior and posterior pressures, and are representative of pressure transducer responses for pendulum and belt-loading tests contained in Appendix B. Pressure data were sampled at 10 kHz and digitally filtered at a cutoff frequency that was at least two times greater than the highest frequency associated with a meaningful amount of signal content (i.e., power). Typically, this resulted in filtering at a cutoff frequency of 25 Hz for the anterior pressure transducer and 40 Hz for the posterior transducer. As expected, the pressure response from both transducers is generally sinusoidal with similar pressures measured in both the front and back of the bladder. The initial spike in anterior pressure for rigid-bar loading is thought to result from impact of the pendulum on the outer surface of the bladder over the area where the transducer was mounted.

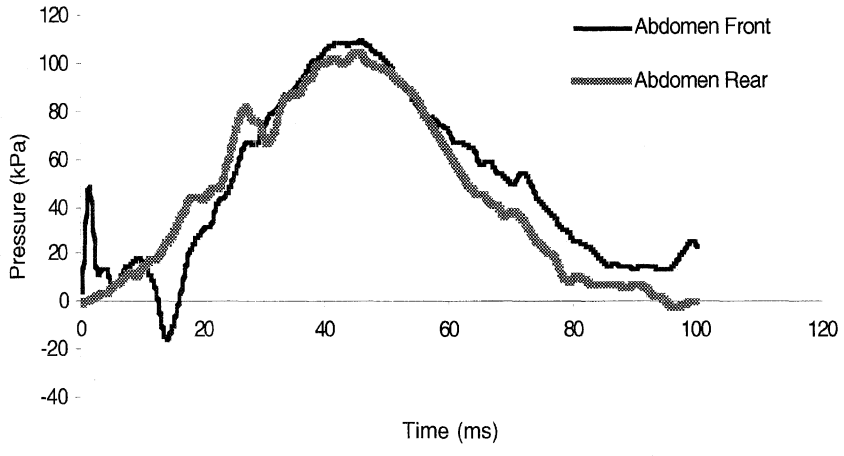

Figure 76. Pressure histories from rigid-bar loading at 4.3 m/s in test GMP0012.

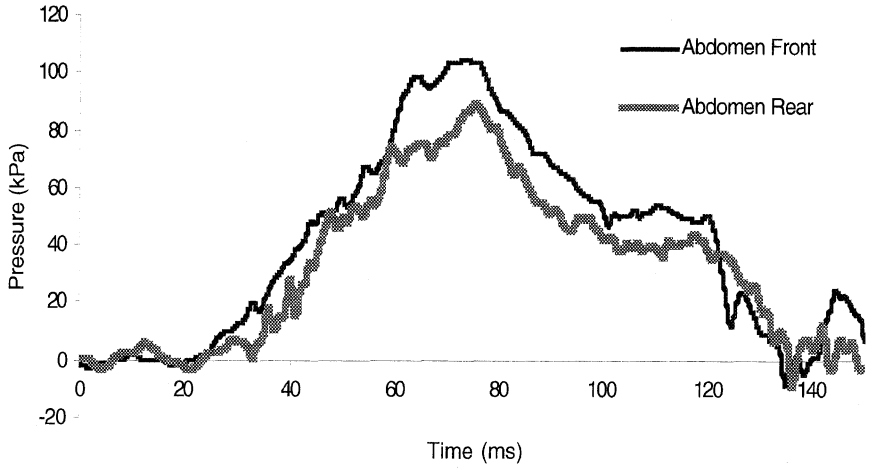

Figure 77. Pressure-time histories from belt loading at 3 m/s in test GMP0019.

Sled tests of an isolated bladder and mounting fixture were conducted to examine the performance of the pressure transducers in the absence of any direct loading on the bladder. It was expected that the pressure response of the bladder would be similar to that predicted by the FE models of the isolated bladder discussed in Section 4 that were used to explore mechanisms of placental abruption. That is, due to fluid inertia and the attachment of the bladder to the sled through the mounting cradles, the pressure in the posterior bladder was expected to be negative and pressure in the anterior bladder was expected to be positive. The expected responses were observed during physical testing of Bladder 6 in test GMP009, shown in Figure 78. However, the expected behavior was not observed in the posterior pressure response during validation sled testing of the isolated final bladder, as shown in Figure 79. Deviation from the expected posterior pressure response was attributed to a faulty posterior pressure transducer during validation testing, although physical inspection of the transducer and static calibration performed following the validation testing indicated that the transducer was functioning normally. Because post-test pressure transducer calibration was performed using dry gas, is possible that the errors in pressure transducer measurement were due to a partial electrical short caused by intermittent contact between water and the transducer leads.

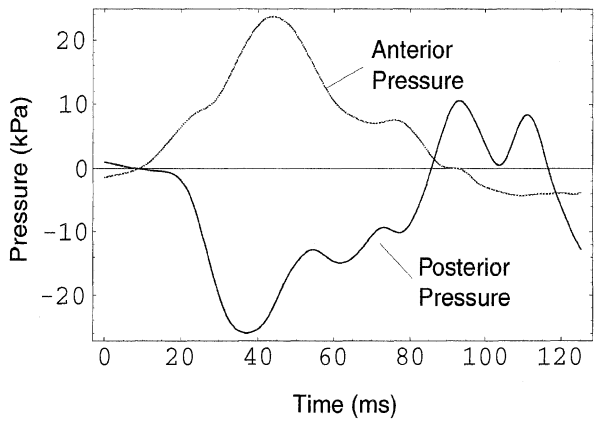

Figure 78. Anterior and posterior pressure transducer response from bladder-only sled test (GMP0009) using Bladder 6.

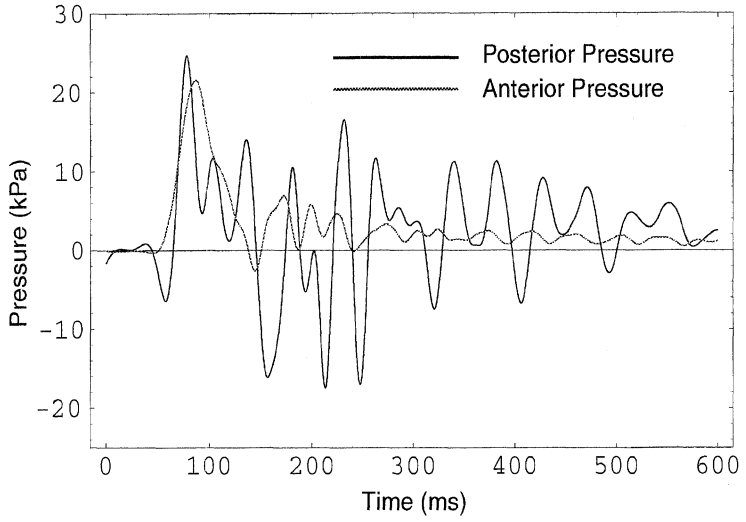

Figure 79. Anterior and posterior pressure transducer responses from bladder-only sled test (GMP0046) using Bladder 8 (final prototype).

7.3.2 Pressure Measurements in Full Dummy Sled Tests

A typical pressure response from a full dummy sled test of the final MAMA-2B restrained by a three-point belt in a driver configuration is shown in Figure 80. Pressure data were sampled at 10 kHz and digitally filtered at a cutoff frequency that was at least two times greater than the highest frequency associated with a meaningful amount of signal content (i.e., power). Typically, this resulted in filtering at a cutoff frequency of 25 Hz for the anterior pressure transducer and 40 Hz for the posterior transducer. As expected, the pressures measured by the anterior pressure transducer were positive throughout the test. This is expected because all loading of the bladder is compressive and the inertia of the fluid causes positive pressures in the anterior region of the bladder. Anterior bladder pressure tended to peak at times close to the peaks in belt loading, which reflects penetration of the lap belt into the abdomen, and chest deceleration, which reflects loading of the abdomen by the steering wheel and shoulder belt.

Response of the posterior pressure transducer is, however, very erratic and is not as expected. Prior to about 25 ms, the pressure response is negative as expected. From 25-50 ms, the pressure response becomes positive, possibly because of compressive loading on the bladder from the restraint system and steering wheel. However, after 50 to 100 ms, the pressure signal shows large oscillations that are unexpected and unrepresentative of the loading conditions.

It was therefore concluded that the posterior pressure transducer produced faulty output under these loading conditions. This response was observed in all full-dummy sled tests performed with the final prototype MAMA-2B abdomen. Because of this problem with the posterior pressure measurements, further development of injury criteria and injury tolerance measures based on the negative-pressure mechanism could not be completed.

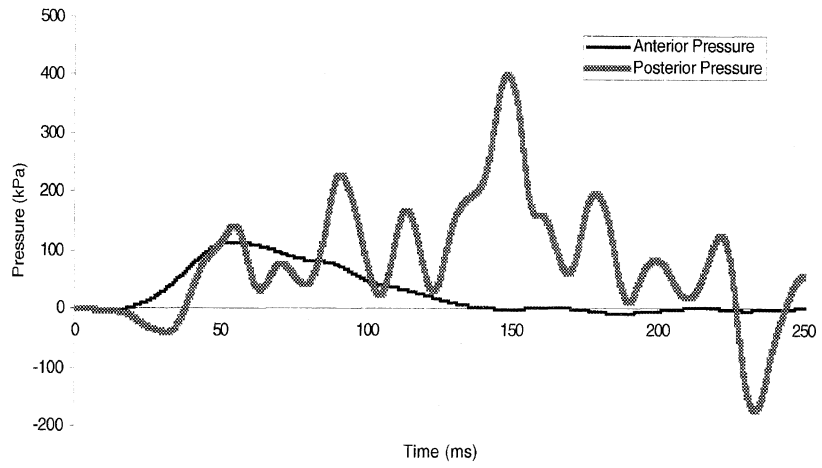

Figure 80. Pressure response from a whole-dummy sled test conducted at 47 kph/16 g with final MAMA-2B abdomen (GMP0042).

7.4 Final MAMA-2B Instrumentation

The completed MAMA-2B includes instrumentation to measure anterior and posterior pressure in the bladder. Shape Tape is not included with the completed MAMA-2B because of problems described in Section 8.2. The cradles included with the MAMA-2B abdomen have been designed to accommodate the Shape Tape, since future modifications may resolve its existing problems.

The MAMA-2B does not provide a means of measuring chest deflection because ribcage modifications resulted in shortening of the sternum connection for the chest potentiometer. Consequently, the standard Hybrid III chest potentiometer could not be used. While space constraints prevent a rotary chest potentiometer from being used, a linear deflection measurement system such as the IR-TRACC could be implemented in future versions of the MAMA-2B.

8.0 INJURY CRITERIA

8.1 Overview of Injury Criteria Development

The initial goals of the project called for development of injury criteria that predicted the likelihood of placental abruption. To this end, instrumentation was selected to attempt to measure quantities (i.e., pressure and changes in bladder curvature) that relate to the mechanisms considered the most likely causes of placental abruption. However, problems with instrumentation that could not be resolved within the funding and time constraints of this project prevented the development of fully functional pressure and bladder curvature measuring devices. Consequently, injury criteria that relate the probability of placental abruption to pressure gradient and local strains were not included in the MAMA-2B. However, it is considered important for future development efforts to document the procedure intended for developing injury criteria based on hypothesized placental abruption mechanisms had functional instrumentation been available. Section 8.2 contains this documentation.

An alternative method for assessing fetal injury risk using a simple measure of internal bladder pressure has been implemented as an interim solution. Development of this method is described in Section 8.3.

8.2 Preliminary Development of Placental Abruption Thresholds for the MAMA-2B

Figure 81 outlines the proposed steps in placental abruption-based injury criteria development. In this process, loading scenarios selected to be representative of inertial and direct-contact loading would be applied to both FE models of the human and dummy uterus. The human uterus model is discussed in Section 4.3.4 while the dummy FEM is discussed in Section 4.3.5 and is validated and tuned using physical results from dummy component tests. Assuming that the dummy and human uterus models are representative of their physical counterparts, pressure and strain measurements from these models under identical loading conditions would be used to develop a scaling factor that relates pressures and strains at specific sites on the dummy uterus to pressures and strains at corresponding sites on the human uterus. For example, under the same loading conditions, a 30% shear strain at the anterior pressure transducer location in the dummy bladder may correspond to a 60% strain at the human UPI. Applying UPI failure strains from testing performed by Ashton-Miller to the scaling factor would be used to determine threshold abruption strains and pressures in the physical MAMA-2B abdomen. For this method of injury criteria development, it is assumed that the FE model of the dummy is representative of the physical dummy and that strain and pressures predicted by the FE model are the same as those that would be measured on the dummy under identical loading scenarios. Validation of injury criteria would have been performed by

conducting sled tests at a range of crash severities that Klinich et al. (1999) correlated to risk of placental abruption in real-world motor-vehicle crashes.

Development of injury criteria using a scaling factor that relates tissue-level failure in the human uterus to strains and pressures measured in the dummy uterus requires knowledge of tissue properties and dummy instrumentation that can take measurements for use with the scaling factor. Consequently, for this method of injury criteria development to become feasible, improved data on tissue properties must be obtained and pressure and curvature measurement instrumentation must be developed. However, until these measurements can be made in the dummy, alternative injury criteria must be used.

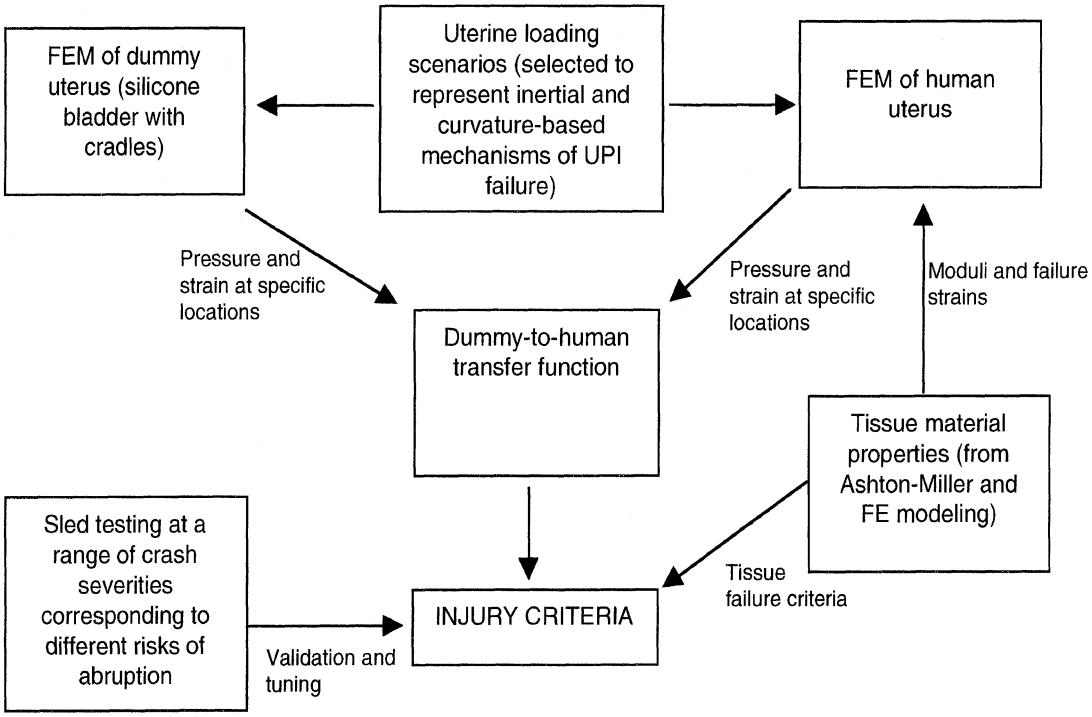

Figure 81. Process to develop injury criteria based on FE modeling and crash reconstructions.

8.3 Alternative Method of Injury Prediction Based on the Risk of Fetal Loss in MVC

Because of the problems and limitations with instrumentation described in Sections 7.2 and 6.3, and time limitations on the project, an alternative injury criterion was developed based on the injury risk curves from Project D.9 Investigation of Pregnancy Loss Resulting from Motor-Vehicle Crashes (Klinich et al., 1999). This alternative injury criterion was originally developed to validate the placental abruption-based injury criteria discussed in Section 8.2. Injury risk curves were used to develop a sled test matrix that spanned a range of crash severities and restraint conditions.

Figure 82 shows logistic regression curves relating the probability of an adverse fetal outcome to crash severity for properly restrained and improperly restrained pregnant occupants. These curves show that the probability of adverse fetal outcome, which includes placental abruption and other injuries resulting in fetal loss or long-term impairment, increases with increasing crash severity and is significantly lower at a given crash severity for properly restrained pregnant occupants. The relationship between crash severity (i.e., ΔV), restraint, and the probability of adverse fetal outcome was used to develop the sled test matrix shown in Table 5.

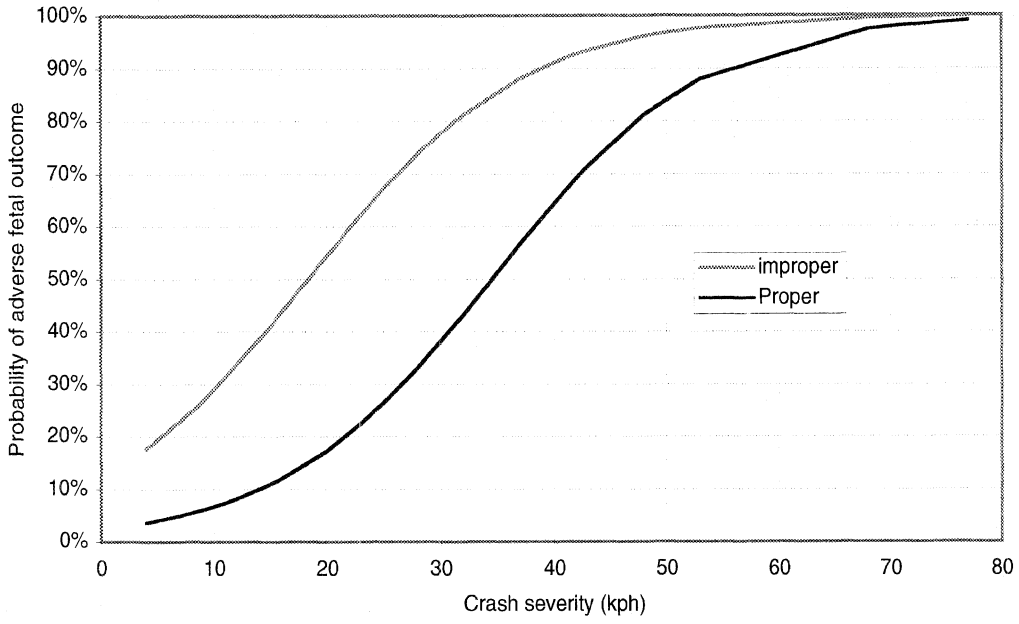

Figure 82. Fetal outcome as a function of crash severity, controlling for proper (i.e., three-point belt or airbag and three-point belt) restraint use. From Klinich et al. (1999).

Table 5.
Test Matrix for Developing Risk-Based Injury Criteria and Tolerance Thresholds

Test	Delta V (target/actual) kph	Position	Restraint	Risk (target/actual) %
GMP0031	13/14.8	driver	none	36/40.5
GMP0032	13/14.8	driver	three-point belt	9/10.7
GMP0033	25/23	driver	three-point belt	26/22.5
GMP0034	25/23	driver	three-point belt + airbag	26/22.5
GMP0035*	25/23	driver	three-point belt + airbag	26/22.5
GMP0036	20/19.4	driver	none	54/52.8
GMP0037	13/15.0	passenger	three-point belt	9/10.7
GMP0038	35/34.3	passenger	three-point belt	51/50
GMP0039	35/34.4	driver	three-point belt	51/50
GMP0040	35/34.5	driver	three-point belt	51/50
GMP0041	35/34.1	driver	none	86/84.5
GMP0042	45/46.8	driver	three-point belt	76/79
GMP0043	45/46.8	driver	three-point belt + airbag	76/79
GMP0044	55/52.3	driver	three-point belt	90/87.5
GMP0045	55/52.6	passenger	three-point belt	90/87.5

*Repeat of test GMP0034 to account for unexpected steering wheel rotation.

Crash severities for these tests were selected so that test conditions correlated to a range of 9 to 90% likelihood of adverse fetal outcome. Test conditions were selected to provide a range of adverse outcome risks and restraint conditions. Three unrestrained driver tests (test GMP0031, 0036, and 0041) were conducted at nominal delta V's of 13, 20, and 35 kph to approximate conditions of 36, 54, and 86% risk on the improperly restrained curve. Five three-point-belt-restrained driver tests were run to approximate crash severities of 13, 25, 35, 45, and 55 kph (tests GMP0032, 0033, 0039, 0042, and 0044, respectively) on the properly restrained curve. Test GMP0040 was identical to test GMP0039 (35 kph, three-point-belt-restrained driver) as a check for repeatability. This matrix of tests includes inertial and direct loading scenarios, although no tests contained purely inertial or purely contact loading. The tests that were closest to producing purely inertial loading were those that involved a three-point-belt restrained passenger where the only object loading the abdomen was the lap belt. The tests that were closest to producing purely contact loading were those with an unrestrained driver, where the steering wheel was the only object loading the abdomen.

The risk curves for the properly restrained pregnant occupants are based on both drivers and passengers who wore three-point belts, with or without an airbag. To explore how different restraint and occupant positions would affect results, tests in conditions other than the three-point-belted driver were performed. Tests GMP0035 and GMP0043 were conducted at nominal impact velocities of 25 kph and 45 kph, respectively, with the MAMA-2B in a driver configuration and restrained by a three-point belt and airbag. Comparisons with tests GMP0033 and GMP0042, which are at the same level of risk based on the properly restrained curve, were used to determine if the MAMA-2B can distinguish between restraint type. Tests GMP0037, 0038, and 0045, were conducted in the passenger position (i.e., no steering wheel) at impact velocities matching tests 0032, 0039, 0044 to explore the effect of steering wheel loading.

Several response measures of the MAMA-2B abdomen were considered in searching for response parameters that best correlate with the probability of adverse fetal outcome across the test conditions. However, due to problems with the Shape Tape and problems with the posterior pressure transducer noted above, anterior pressure became the only acceptable measure for this analysis.

Figure 83 shows the relationship between peak anterior pressure and the risk of adverse fetal outcome across all restraint conditions. Figure 84 shows that impacts associated with a greater likelihood of adverse fetal outcome resulted in higher positive anterior pressures. Using a power-law relationship ($r^2 = .66$) 20, 50 and 80% risks of adverse fetal outcome were found to correspond to anterior pressure of 59, 88, and 109 kPa, respectively. The form of the power-law relationship between the peak anterior pressure and the risk of adverse fetal outcome is shown in Equation 1, where P is peak anterior pressure and θ is the risk of adverse fetal outcome.

$$\theta = 15.552P^{0.4442}$$

where, [1]
θ is risk of adverse fetal outcome, and P is peak anterior pressure (in kPa)

Figure 85 shows the relationship between crash severity and peak anterior pressure across restraint conditions. For each restraint type, peak anterior pressure increased with increasing crash severity. Consistent with results from Klinich et al., restraint by a three-point belt resulted in lower pressures than for unrestrained conditions, and adding an airbag further decreased pressure. In addition, it has been hypothesized that under similar impact conditions, occupants in a passenger position would have less risk of adverse fetal outcome than occupants in a driver position because steering-wheel loading is avoided. These preliminary results are consistent with this hypothesis.

In addition to its correlation with crash severity and the ability to distinguish between restraint systems, peak anterior bladder pressure has a major advantage as a predictor of fetal injury because it relates directly to loading of the pregnant abdomen. That is, as more fluid is displaced by compression of the anterior abdomen, peak anterior pressure increases. In addition, peak anterior pressure is also moderately related to the deceleration of the abdomen because fluid inertia tends to create positive pressures in the anterior bladder as the bladder is decelerated through its connection to the lumbar spine. The major disadvantage to using peak positive anterior bladder pressure as a predictor of the probability of adverse fetal outcome is that it is a function of loading area, as well as depth of penetration. Thus, it cannot predict placental abruption and fetal loss that result from abdomen loading by small objects that produce high local strains in the UPI. This limitation may, however, not be a significant disadvantage in most crash test environments, and is not unlike the limitations of most other injury predictors, such as HIC, resultant chest acceleration, or V*C currently used for injury assessment in non-pregnant dummies.

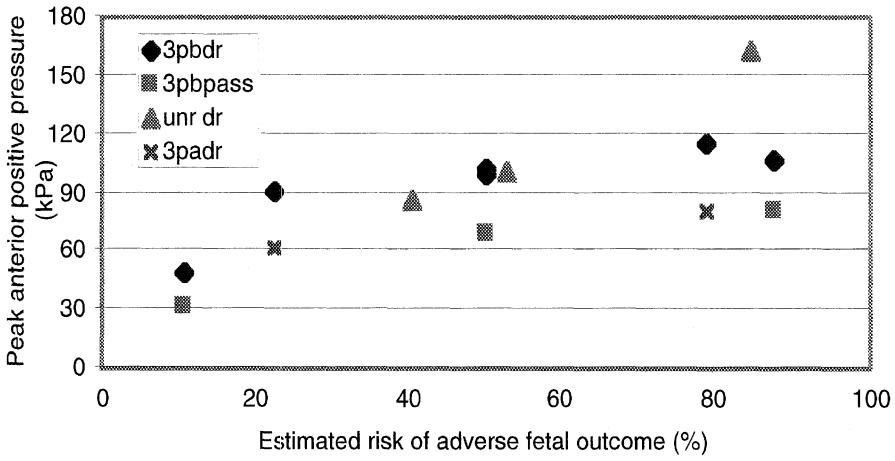

Figure 83. Relationship between peak anterior positive pressure and risk of adverse fetal outcome for three-point belted drivers (3pbdr), three-point belted passengers (3pbpass), three point belted and airbag-restrained drivers (3padr), and unrestrained drivers (unr dr).

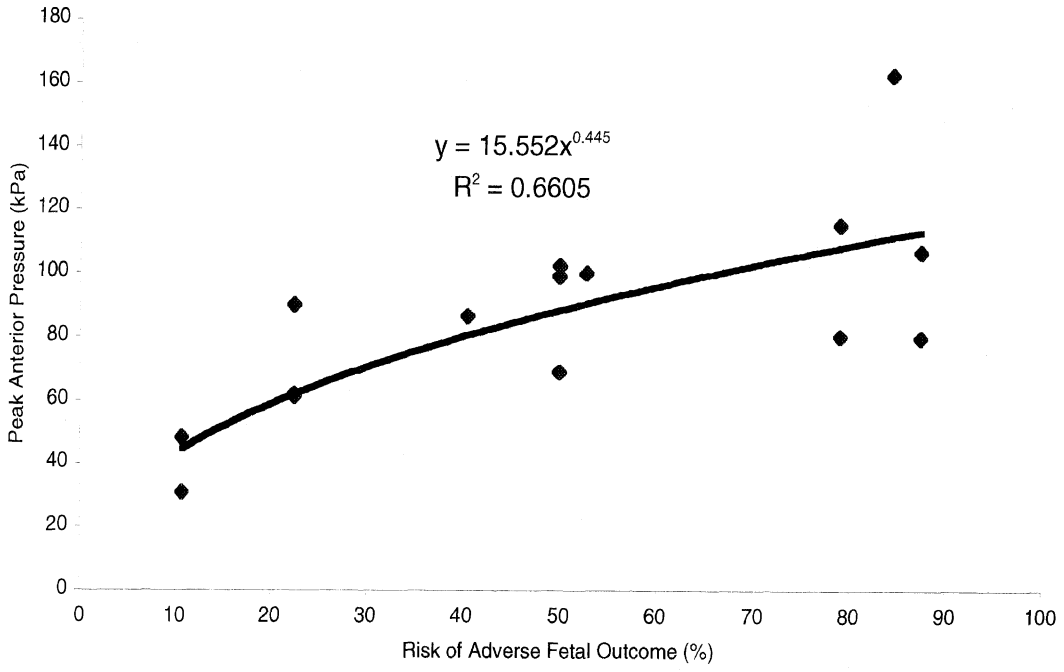

Figure 84. Correlation between peak anterior positive pressure and risk of adverse fetal outcome for tests GMP0031-GMP0045.

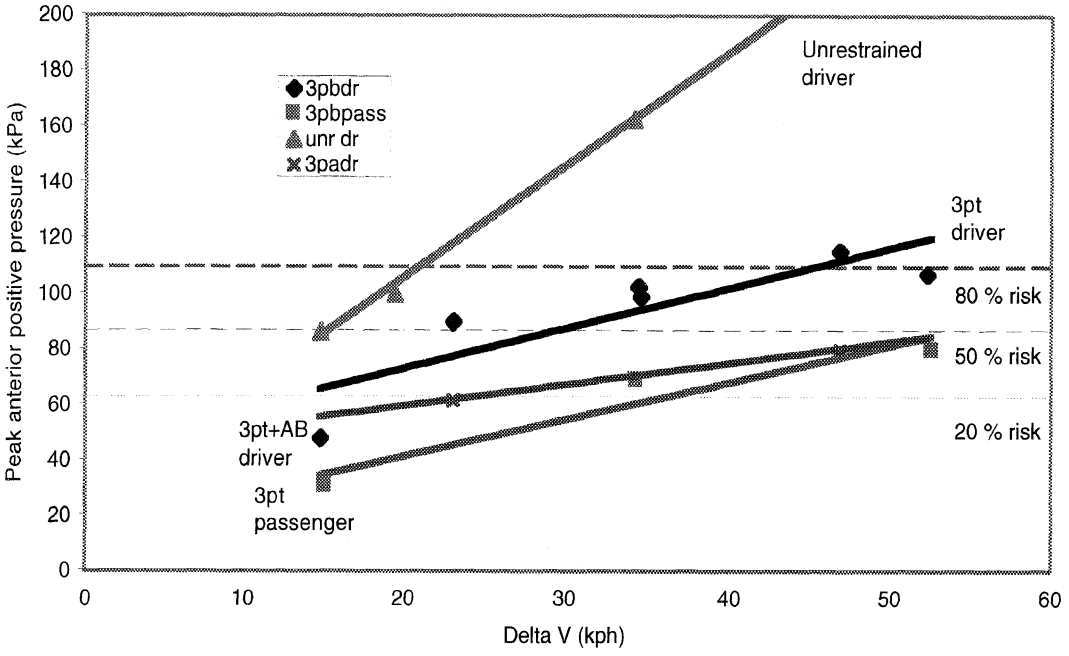

Figure 85. Relationship between peak anterior positive pressure and crash severity for three-point-belted drivers (3pbdr), three-point-belted passengers (3pbpass), three-point-belted and airbag-restrained drivers (3padr), and unrestrained drivers (unr dr).

8.4 Repeatability of Injury Prediction

Tests GMP0039 and GMP0040 were used to test the repeatability of the MAMA-2B's injury prediction capability based on the approach described in Section 8.3. Figure 86 shows the results of these comparisons for anterior pressure. The anterior pressure responses in tests GMP0039 and 0040 differ by at most 4% at any point in time, although peak pressures measured from these curves differ by less than 1%.

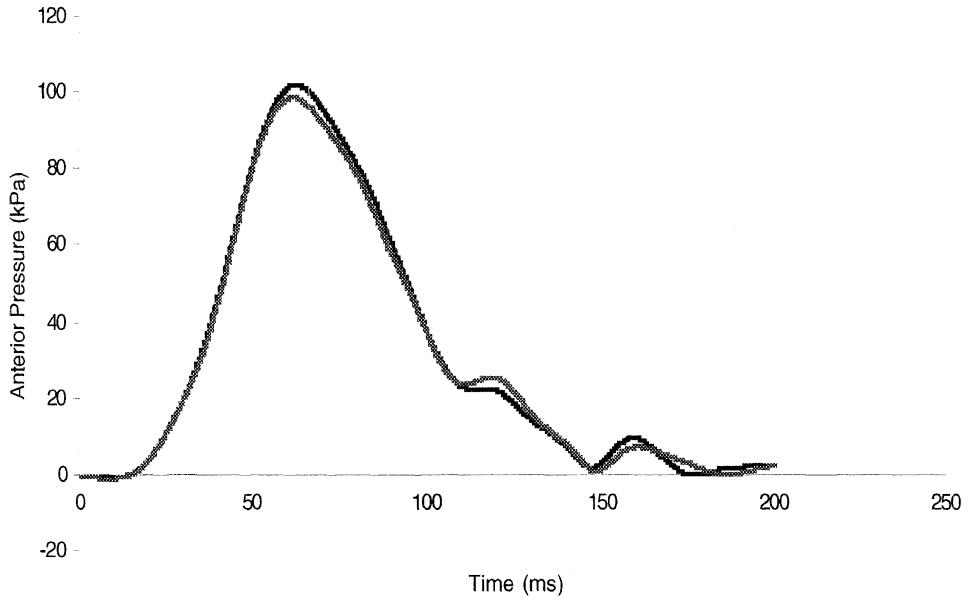

Figure 86. Anterior pressure transducer signals from tests GMP0039 and GMP0040 (three point belted driver).

Repeatability of anterior pressure measurements was also checked using pressure histories from rigid-bar impacts, belt loading, and surrogate airbag tests, even though these tests were not designed for this purpose and are therefore not identical in all respects. Figures 87 through 89 show these comparisons. For the 4.3 m/s rigid-bar impacts shown in Figure 87, the difference between the positive peaks of the anterior pressure curve is 13%. Much of this difference may be due to a change in the coupling of ballast weights to the dummy between tests. In both of these tests, ballast weights were attached to the MAMA-2B's legs (in these tests, ballast had not yet been relocated to the pelvis and spine box). Films of test GMP0012 showed some decoupling of ballast from the legs. This would decrease the effective mass of the dummy and consequently decrease the amount of force that the rigid bar impactor would have to apply to the dummy, which would decrease the pressure developed in the bladder.

The anterior pressure measurement in two 3.0 m/s belt-loading tests is shown in Figure 88. In these tests, the difference between the peak anterior pressure measurements is 11%. Part of this difference may again be due to decoupling of ballast weights from the

dummy legs. Part of the difference may also be due to removal of the chest jacket in the second test.

The repeatability of the anterior pressure measurement under surrogate airbag loading was very good. The difference between pressure peaks between the two tests shown in Figure 89 is 4%. Some of the difference may be due to the removal of chest jacket for the second test.

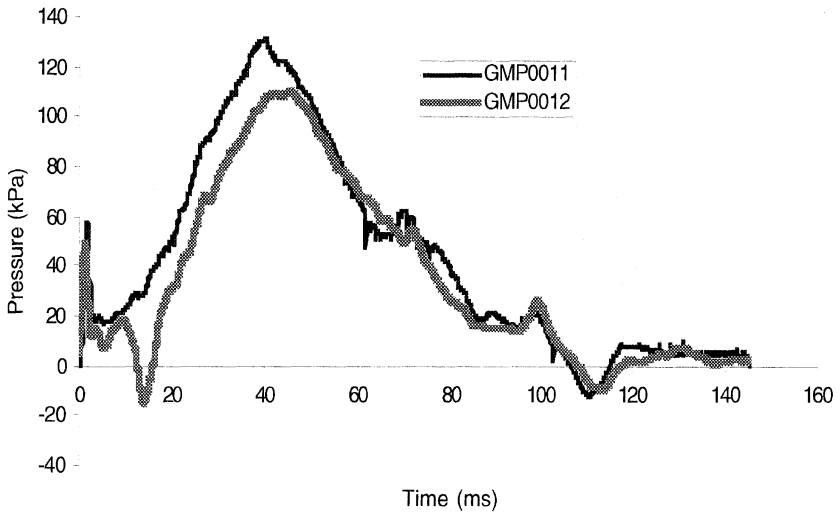

Figure 87. Anterior pressure transducer signals from 4.3 m/s pendulum impacts in tests GMP0011 and GMP0012.

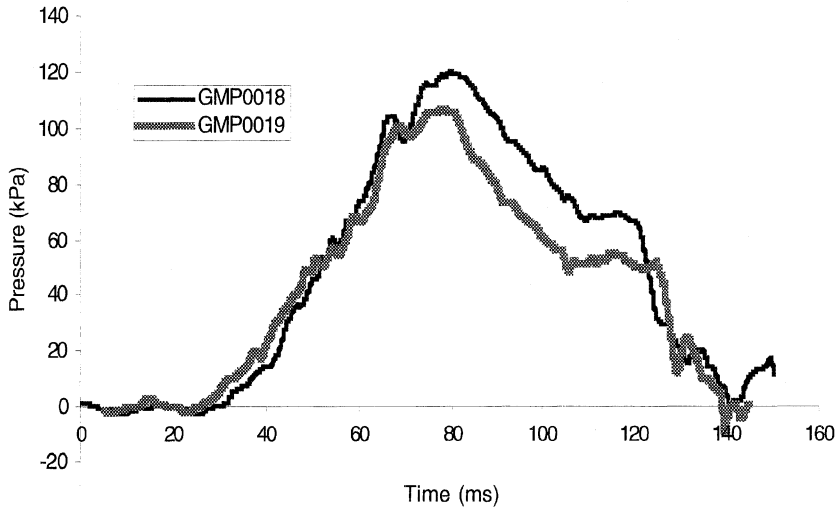

Figure 88. Anterior pressure responses from 3 m/s lap belt loading tests (GMP0018 and GMP0019). Test GMP0018 was conducted with the chest jacket, while test GMP0019 was conducted without the jacket.

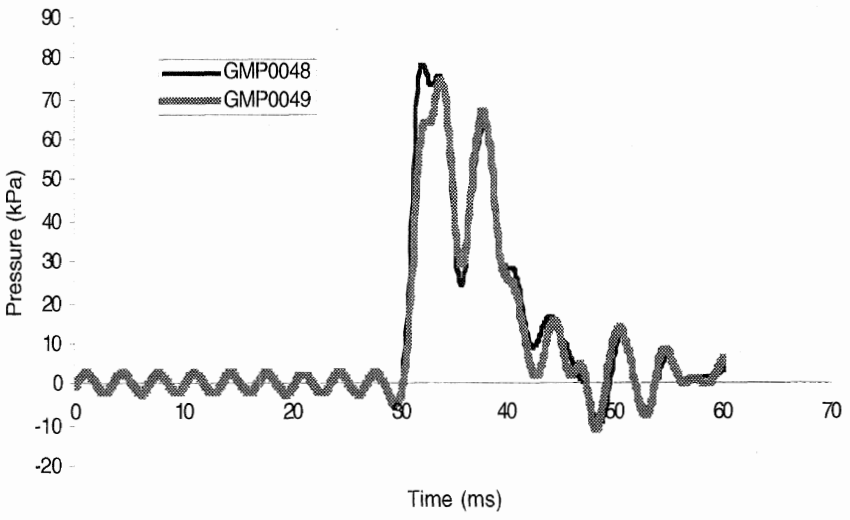

Figure 89. Anterior pressure transducer responses from surrogate-airbag loading tests (GMP0048 and GMP0049). Test GMP0048 was conducted without the chest jacket, while test GMP0049 was conducted with the jacket.

9.0 SUMMARY AND DISCUSSION

The goal of this project was to develop and test a new and improved pregnant version of the small-female Hybrid III ATD. The project was conducted in conjunction with several other projects funded through the GM/DOT Settlement Agreement, including: D.10 Seated Anthropometry During Pregnancy (Klinich et al., 1999), D.8 Investigation of Pregnancy Loss Resulting from Motor Vehicle Crashes (Klinich et al, 2000), D.8 Data Acquisition for Development of a Uteroplacental Interface for the Second-Generation Pregnant Crash Test Dummy (Pearlman et al., 1999), and D.2a Development/Refinement of Abdominal Response Corridors and Tissue Properties (Hardy et al. 2001) and D.2b Development of a Reusable, Rate-Sensitive Abdomen (Rouhana, unpublished).

Based on data from these other projects, previous medical research on fetal injury and loss in motor-vehicle crashes (Pearlman, et al. 1990), and recognized limitations and deficiencies with the first pregnant dummy (Viano and Pearlman, 1996), three primary objectives for the design and performance of the new pregnant dummy were established early in the project. These include:

1. improving the anthropometry of the pregnant abdomen to achieve more humanlike interaction with restraint systems and vehicle interiors,
2. enhancing the biofidelic response of the pregnant abdomen, and
3. implementing design features and instrumentation that will assess the likelihood of placental abruption in crash environments.

The project has resulted in a new prototype pregnant crash test dummy known as MAMA-2B for Maternal Anthropomorphic Measurement Apparatus, version 2B. Unlike the solid urethane abdomen of the first pregnant dummy, the design of the new pregnant abdomen uses a fluid-filled silicon bladder representing the human uterus at 30 weeks. This approach to abdomen design is similar to the advanced abdomen design resulting from project D.2b for standard Hybrid III ATDs. The shape and size of the MAMA-2B abdomen closely approximates the average size and shape of pregnant women at 30 weeks, based on data collected in project D.10. This size and shape is greatly improved from the first pregnant dummy, for which the abdomen protrudes much too far forward and does not extend upward to interact with the ribcage in an appropriate manner.

Incorporating the pregnant uterine-like bladder into the small-female Hybrid III dummy required trimming the 4th through 6th ribs at the front, which is accomplished in a manner that keeps the force-deflection response of the dummy's chest within the performance specification. The weight of the MAMA-2B is 9.1 kg greater than that of the small-female Hybrid III to account for typical weight gain during pregnancy. Ballast was added to the dummy in a manner that does not result in the mass decoupling that could occur in dynamic testing with the first pregnant dummy. Also, the weight distribution was adjusted to so that the seated CG is located appropriately for a seated pregnant woman (about 8 mm forward and 10 mm above the seated non-pregnant whole-body CG).

The dynamic force-deflection response of the MAMA-2B abdomen is significantly improved from that of the first pregnant dummy. The new abdomen has been designed and tested for rigid-bar, belt, and out-of-position airbag loading, and the response of the MAMA-2B abdomen falls within force-deflection corridors established for each type of test. The abdomen also demonstrates rate sensitivity in its force-deflection response, although additional rate sensitivity would be desirable to better match the response of the human abdomen.

In attempting to design and instrument the abdomen to assess for the risk of adverse fetal outcome due to placental abruption, two approaches were considered. The first approach was extremely ambitious, and involved an attempt to instrument the abdomen to measure response parameters needed for injury criteria that relate directly to hypothesized mechanisms of traumatic placental abruption. The second approach is more typical of injury criteria development, and involved searching for relationships between regional response measures to general levels of fetal outcome, without concern for the specific mechanisms of injury or specific tissues injured.

Because the tissue-level mechanisms of placental abruption hypothesized for the first of these approaches cannot be easily verified experimentally, potential injury mechanisms were examined using FE and physical modeling. This resulted in two mechanisms that are thought to be most responsible for placental abruption in motor-vehicle crashes: 1) tensile strain at the Uterine Placental Interface (UPI) due to an anterior-posterior fluid pressure gradient developed from inertial forces, and 2) shear strain or stress at the UPI due to uterus curvature changes caused by direct abdomen loading. A significant effort was made to successfully instrument the MAMA-2B with pressure transducers to measure anterior-posterior pressure gradients, and with Shape Tape to measure circumferential bladder strains and changes in curvature. However, results of numerous whole-dummy and isolated abdomen dynamic tests revealed problems that could not be resolved within the time and funding limitations of this study. While these instrumentation approaches offer promise for future improvements in instrumentation that appear feasible, it was necessary to abandon this specific-injury approach in the current effort.

The measure of fetal outcome developed using the second approach is based on pressure measured in the anterior region of the uterine-like MAMA-2B bladder. This pressure was measured in a matrix of sled tests designed to span the range of occupant-restraint and crash-severity conditions used in probability curves of adverse fetal outcome developed in project D.8 from real-world crashes and injuries. The peak anterior pressures in these tests correlated well to the expected risk of adverse fetal outcome. Therefore, a relationship was established between peak anterior pressure and the probability of adverse fetal outcome.

One possible limitation to using anterior bladder pressure as the sole predictor of fetal injury is that this measure is directly related to the volume of fluid displaced by an object penetrating the bladder. Consequently, a small object penetrating deep into the bladder

can produce the same peak pressure as a large surface penetrating a small distance, and thereby predict the same risk of adverse fetal outcome for two significantly different loading conditions, which may not be appropriate.

Although the MAMA-2B is considered to be in a prototype (rather than production) stage of development, whole-dummy testing under various restraint and crash-severity conditions indicate that the new design is relatively durable, repeatable, and easy to use. Future work to improve MAMA-2B should focus on instrumentation issues. The rear pressure transducer should also be replaced and sled tests conducted to determine if posterior pressure, or a combination of anterior and posterior pressure (e.g., pressure differential), better correlates to injury risk than peak anterior pressure. Proposed improvements to the Shape Tape should also be investigated to allow estimation of localized strain. Successful implementation of both the Shape Tape and dual pressure measures for expected abdomen loading scenarios along with additional tissue response data would allow the development and use of injury criteria that relate more directly to the hypothesized mechanisms of placental abruption.

Additional validation sled tests should also be conducted to determine how the MAMA-2B performs in a greater range of impact conditions, particularly in restraint misuse conditions, such as an improperly placed lap belt and out-of-position airbag loading. A second MAMA-2B should also be developed and tested to confirm and improve the fabrication process, and to verify that the MAMA-2B design is reproducible.

10.0 REFERENCES

Ashton-Miller, J. A., Cowan, L. *Investigation of the mechanical failure characteristic of the uteroplacental interface*. Unpublished.

Beckman, D. L., McElhaney, J. H., Roberts, V. L., Stalnaker, R. L. (1971). *Impact tolerance - abdominal injury. Final report.* Highway Safety Research Institute, Ann Arbor, MI. 311 p. Sponsor: National Highway Traffic Safety Administration, Washington, D.C. Report No. HSRI-71-102/ DOT HS 800 549.

Best, T. M., McElhaney, J. H., Garrett, W. E., Jr, Myers, B. S. (1995). Axial strain measurements in skeletal muscle at various strain rates, *Journal of Biomechanical Engineering*, 117: 262-265.

Cavanaugh, J.M., Nyquist, G.W, Goldberg, S.J., and King, A.I. (1986). Lower abdominal tolerance and response. *Proceedings of the 30th Annual Stapp Car Crash Conference*. Society of Automotive Engineers, Warrendale, PA. 406 p. Report No. SAE-P-189.

Crosby, W. M., Snyder, R. G., Snow, C. C., Hanson, P. G. (1968). *Impact injuries in pregnancy I: experimental studies.* Department of Transportation, #AM 68-6.

Crosby, W. M., King, A. I. (1971). *Lap and shoulder restraints for pregnant women*. U. S. Department of Transportation, #DOT HS-800 533.

Crosby, W. M., King, A. I., Stout, L. C. (1972). Fetal survival following impact: improvement with shoulder harness restraint. *American Journal of Obstetrics and Gynecology*, 112(8):1101-1106.

Culver, C. C., Viano, D. C. (1990). Anthropometry of seated women during pregnancy: defining a fetal region for crash protection research. *Human Factors*, 32(6):625-636.

Eppinger, R.H. (1976). Prediction of thoracic injury using measurable parameters. *Proceedings of the 6th Experimental Safety Vehicles Conference.* NHTSA, Washington DC. pp. 770-780.

Freid, A.M. (1978). Distribution of the bulk of the normal placenta. Review and classification of 800 cases by ultrasonography. *American Journal of Obstetrics & Gynecology*. 132(6): 675-80.

Hardy, W.N, Schneider, L.W., and Rouhana, S.W. (2001). *Impact Response of the Human Abdomen.* Report # UMTRI-2001-10. University of Michigan Transportation Research Institute, Ann Arbor, MI

Institute of Medicine (1990). *Nutrition During Pregnancy, Weight Gain and Nutrient Supplements*. Report of the Subcommittee on Nutritional Status and Weight Gain during Pregnancy, Subcommittee on Dietary Intake and Nutrient Supplements during Pregnancy, Committee on Nutritional Status during Pregnancy and Lactation, Food and Nutrition Board. Washington, DC: National Academy Press, 1990:1–233. 333–41.

Jensen, R.K., Doucet, S., Treitz, T. (1996). Changes in segment mass and mass distribution during pregnancy. *Journal of Biomechanics*, 29(2): 251-256.

King, A. I., Crosby, W. M., Stout, L. C., Eppinger, R. H. (1972). Effects of Lap Belt and Three-Point Restraints on Pregnant Baboons Subjected to Deceleration. *Fifteenth Stapp Car Crash Conference Proceedings*, SAE #710850, 68-83.

Klinich, K.D., Schneider, L.W., Moore, J.A., and Pearlman, M.D. (1999). *Investigatons of Crashes Involving Pregnant Occupants.* Report UMTRI 99-29. University of Michigan Transportation Research Institute, Ann Arbor, MI.

Klinich, K.D., Schneider, L.W., Eby, B., Rupp, J.D., and Pearlman, M.D. (1999). *Seated Anthropometry During Pregnancy*. Final Report. UMTRI 99-16. University of Michigan Transportation Research Institute, Ann Arbor, MI.

Kovanen, V.,, Suominen, H., Heikkinen, E. (1984). Mechanical Properties of Fast and Slow Skeletal Muscle with Special Reference to Collagen and Endurance Training. *Journal of Biomechanics*, 17 (10): 75-735.

McElhaney, J. H., and Byers, E. F. (1965). *Dynamic Response of Biological Materials*. ASME 65-WA-HUF-9. American Society of Mechanical Engineers.

Melvin, J.W., King, A.I., and Alem, N.M. (1988). *AATD System Technical Characteristics, Design Concepts, and Trauma Assessment Criteria.* AATD Task E-F Final Report (1985) in DOT-HS-807-224. U.S. Department of Transportation, National Highway Traffic Safety Administration, Washington, D.C.

Miller, M. A. (1989). The biomechanical response of the lower abdomen to belt restraint loading. *Journal of Trauma,* 29(11):1571-1584.

National Vital Statistics Reports. (October 5, 1999). 47(25):35-36.

Nusholtz, G., Kaiker, P. (1994). Abdominal response to steering wheel loading. *Proceedings of the 14th International Technical Conference on Enhanced*

Safety of Vehicles , pp. 118-127, US Department of Transportation, Washington DC.

Pearlman, M. D., Tintinalli, J. E., Lorenz, R. P. (1990). Blunt trauma during pregnancy. *New England Journal of Medicine,* 323(23):1609-1613.

Pearlman, M. D., Viano, D. (1996). Automobile crash simulation with the first pregnant crash test dummy, *American Journal of Obstetrics and Gynecology*, 175(4 pt 1): 977-981.

Pearlman, M.D., Ashton-Miller J.A., Dyer, T., and Reis, P. (1999). *Data Acquisition for Development to Characterize the Utero-Placental Interface for the Second-Generation Pregnant Abdomen.* Submitted to NHTSA.

Pearlman, M.D., Kinich, K.D., Schneider, L.W., Rupp, J.D., Moss, S., and Ashton-Miller, J. (2000). A comprehensive program to improve safety for pregnant women and fetuses in motor vehicle crashes: A preliminary report. *American Journal of Obstetrics and Gynecology.* 182(6):1554-1564.

Pearsall, G. W., Roberts, V. L., (1978). Passive mechanical properties of uterine muscle (myometrium) tested in vitro. *Journal of Biomechanics*, 11:167-176.

Pritchard, J.A., MacDonald, P.C., and Gant, N.F. (1985). *Williams Obstetrics.* Seventeenth Edition. Appeltic-Century-Crofts, Norwalk, CT.

Rouhana, S.W., Jedrzejczak, E.A., McCleary, J.D. (1990). Assessing submarining and abdominal injury risk in the Hybrid III family of dummies: Part II development of the small female frangible abdomen. *Proceedings of the 34th Stapp Car Crash Conference*, pp145-173, SAE Warrendale, PA.

Rouhana, S.W., Elhagediab, A. Walbridge, T., Hardy, W.N, Schneider, L.W. (unpublished) Project D.2b Development of a reusable rate-sensitive abdominal insert for the Hybrid III family of ATDs.

Schneider, L.W., Ricci, L.L, King, A.I., Neatherly ,R.F., and Beebe, M.S., (1992). *Design and development of an advanced ATD thorax system for frontal crash environments, Volume 2: Exploration of alternative design approaches.* UMTRI Report-92-22-2. University of Michigan Transportation Research Institute. Submitted to NHTSA under contract number DTNH22-83-C-07005.

Snyder, R.G., Snow, C.C., Crosby, W.M., Hanson, P., Fineg, J., and Chandler, R. (1966). Impact injury to pregnant female and fetus in lap belt restraint. *Proceedings of the 10th International Stapp Car Crash Conference*. Society of Automotive Engineers, Paper No. 660801. Warrendale, P.A.

Society of Automotive Engineers (1995). *Society of Automotive Engineers Handbook.*. Recommended Practice J211/1 March, 1995. SAE, Warrendale, PA.

Stalnaker, R. L., McElhaney, J. H. (1971). Human side impact tolerances obtained from subhuman primate scaling relationships. *Conference on Engineering in Medicine and Biology. 24th Annual. Proceedings*, Highway Safety Research Institute, Ann Arbor, Mich. 1971, p. 307.

Stalnaker, R.L., Ulman, M.S. (1985). Abdominal Trauma-Review, Response, and Criteria. *Proceedings of the 29th Stapp Car Crash Conference,* pp. 1-16, SAE, Warrendale, PA.

Trollope, M. L., Stalnaker, R. L., McElhaney, J. H., Frey, C. (1973). Injury tolerance levels in blunt abdominal trauma. *International Conference on the Biokinetics of Impacts Proceedings*, pp. 431-440.

Van Kirk, D. J., King, A. I. (1969). A preliminary study of an effective restraint system for pregnant women and children. *Thirteenth Stapp Car Crash Conference Proceedings*, SAE#690814, 353-364.

Viano, D., Smrcka, J., Jedrzejczak, E., Deng, B., Kempf, P, and Pearlman, M.D. (1996). Belt and airbag testing with a pregnant Hybrid III female dummy. *15th ESV Conference Proceedings*, Paper No. 96-S1-O-03.

Viano, D.C., Lau, I.V., Ashbury, C., King, A.I., Begeman, P.C. (1989). Biomechanics of the human chest, abdomen and pelvis in lateral impact. *The 33rd Annual Proceedings of the Association for the Advancement of Automotive Medicine* pp. 367-382, AAAM, DesPlaines, IL.

Wiechel, J. F., Sens, M. J., Guenther, D. A. (1989). Critical review of the use of seat belts by pregnant women. *Automotive Frontal Impacts*, SAE # 890752, 61-69.

Wood, C. (1964) Physiology of uterine contractions *Journal of Obstetrics and Gynecology (British Commonwealth).* 71 360-373.

Yamada, H. (1970). *Strength of biological materials.* National Institute of Health, Bethesda, Md.

APPENDIX A

EQUAL-STRESS, EQUAL-VELOCITY SCALING AS APPLIED TO THE PREGNANT DUMMY

Derivation of equal-stress, equal-velocity Scaling

The following derivation of equal-stress, equal-velocity scaling is adapted from that presented by Eppinger (1976).

Equal-stress, equal-velocity scaling is a dimensional analysis technique that assumes linear relationships between basic units (i.e., mass, length, and time) measured in a single test and the same basic units in a reference condition (Equation A1).

$$\begin{aligned} L_r &= \lambda_1 L_s \\ M_r &= \lambda_2 M_s \\ T_r &= \lambda_3 T_s \end{aligned} \tag{A1}$$

Where L, M, and T denote the basic dimensional units of Length, Mass, and Time, respectively. The subscripts r and s denote reference and subject conditions, respectively.

Assuming that the density is the same in the subject and the reference conditions allows the following relationship between the λ_1 and λ_2 to be established:

$$\rho_r = \rho_s, \text{ which implies that } \frac{M_r}{L_r^3} = \frac{M_s}{L_s^3} = \frac{\lambda_2 M_s}{\lambda_1^3 L_s^3} \tag{A2}$$

where ρ_r and ρ_s denote density in the subject and reference conditions.

$$\lambda_2 = \lambda_1^3 \text{ or } \lambda_1 = \lambda_2^{1/3} \tag{A3}$$

Assuming that the modulus of elasticity (with units of force/area) is the same in both the test and reference condition leads to the following relationship between the λ_i's:

$$E_r = E_s \Rightarrow \left(\frac{M_r L_r}{T_r^2}\right)\left(\frac{1}{L_r^2}\right) = \left(\frac{M_s L_s}{T_s^2}\right)\left(\frac{1}{L_s^2}\right) = \frac{\lambda_2 M_s}{\lambda_3^2 T_s \lambda_1 L_s} \tag{A4}$$

where E_r and E_s are the moduli of elasticity in the reference and subject conditions.

$$\lambda_3^2 \lambda_1 = \lambda_2 \tag{A5}$$

Combining Equations A3 and A5 gives the following relationship.

$$\lambda_1 = \lambda_3 = \lambda_2^{1/3} = \lambda \tag{A6}$$

where,

$$\lambda = \left(\frac{M_r}{M_s} \right)^{1/3} \tag{A7}$$

The relationships between basic units, shown in Equation A1, can now be expressed as:

$$\begin{aligned} L_r &= \lambda L_s \\ M_r &= \lambda^3 M_s \\ T_r &= \lambda T_s \end{aligned} \tag{A8}$$

When these relationships are applied to stress (M/LT^2) and velocity (L/T) scaling factors, values of unity are obtained, hence the name equal-stress, equal-velocity scaling.

Example Application of Equal Stress, Equal Velocity Scaling

A relevant example of how equal-stress, equal-velocity scaling is used is obtained from Cavanaugh at al. (1986). In this paper Cavanaugh et al. are trying to develop response corridors for the abdomen using force and deflection data from rigid-bar impacts into cadaver abdomens. To account for variations in the mass of the cadavers, equal-stress, equal-velocity scaling was used to scale the subject data (i.e., the individual cadaver data) to a 76 kg (50^{th} percentile) reference condition.

Force and deflection were the two measurements that were scaled to the 76 kg reference condition. Because deflection has units of L, its scaling factor is simply λ. That is,

$$L_r = \lambda L_s \tag{A9}$$

The scaling of force in the subject condition, F_s, to force in the reference condition, F_r, is the ratio of F_r to F_s and can be derived as follows:

$$\begin{aligned} \frac{F_r}{F_s} &= \left(\frac{M_r L_r / T_r^2}{M_s L_s / T_s^2} \right) = \frac{\lambda^3 \lambda}{\lambda^2} = \lambda^2, \text{ so} \\ F_r &= \lambda^2 F_s \end{aligned} \tag{A10}$$

If a cadaver mass, or subject mass, of 68 kg is used, equations A7, A9, and A10 become:

$$\lambda = \left(\frac{M_r}{M_s} \right)^{1/3} = \left(\frac{76}{68} \right)^{1/3} = 1.038 \tag{A11}$$

$$L_r = \lambda L_s = 1.038 L_s \tag{A12}$$

$$F_r = \lambda^2 F_s = 1.038^2 F_s \tag{A13}$$

Equal-Stress, Equal-Velocity Scaling as Applied in Pregnant Dummy Testing

Equal-stress, equal-velocity scaling was used during pregnant dummy development to scale the Cavanaugh corridor from a mass of 76 kg to the pregnant dummy mass of 58 kg. This allowed for unscaled force and deflection data to be compared to the Cavanaugh 6 m/s abdominal response corridor. Scaling of the Cavanaugh corridors was performed as follows.

$$\lambda = \left(\frac{M_{pregnant\ dummy}}{M_{unscaled\ Cavanaugh\ Corridor}} \right)^{1/3} = \left(\frac{58}{76} \right)^{1/3} = 0.9138 \tag{A14}$$

$$L_{scaled\ cavanuagh\ corridor} = \lambda L_{unscaled\ Cavanuagh\ Corridor} = 0.9318 L_{unscaled\ Cavanuagh\ Corridor} \tag{A15}$$

$$F_{scaled\ Cavanaugh\ Corridors} = \lambda^2 F_{unscaled\ Cavanaugh\ Corridors} = 0.9138^2 F_{unscaled\ Cavanaugh\ Corridors} \tag{A16}$$

APPENDIX B

PLOTS OF RELEVANT TEST SIGNALS

Table B1.
Dummy Development Test History

Test ID	Test Type	Rate	Comments
PROTOTYPE 1 25-Durometer Skin Flex Urethane. Full rigid upper and lower cradles			
GMP9901	Rigid Bar	6.0 m/s	
GMP9902	Rigid Bar	6.2 m/s	No data collected. Bladder failure due to compression against rigid upper cradle.
PROTOTYPE 2 30-durometer bladder, soft upper, full rigid lower cradle			
GMP9903	Rigid Bar	3 m/s	
GMP9904	Rigid Bar	6 m/s	Bladder failure due to shear over rigid lower cradle.
PROTOTYPE 3 25-durometer soft upper cradle, reduced profile rigid lower cradle			
GMP9905	Rigid Bar	2.2 m/s	
GMP9906	Rigid Bar	2.3 m/s	
GMP9907	Rigid Bar	3.3 m/s	
GMP9908	Rigid Bar	4.2 m/s	
GMP9909	Rigid Bar	5.2 m/s	
GMP9910	Rigid Bar	6.2 m/s	Bladder response too soft
PROTOTYPE 4 30-durometer bladder, soft upper cradle, reduced profile rigid lower cradle			
GMP9911	Belt Loading Belt	5.6 m/s	
GMP9912	Belt Loading Belt	5.6 m/s	Bladder failed due to shear over lower cradle
PROTOTYPE 5 35-durometer soft upper, soft upper cradle, reduced profile rigid lower cradle			
GMP9913	Bladder Only Sled Test	10g	
GMP9914	Bladder Only Sled Test	10g	
GMP9915	Bladder Only Sled Test	15g	
GMP9916	Bladder Only Sled Test	20g	
GMP9917	Bladder Only Sled Test	20g	
GMP9918	Bladder Only Sled Test	15g	Unrealistic distension. Concerns over urethane durability.
PROTOTYPE 6 40-durometer silicone rubber, soft upper cradle, reduced profile rigid lower cradle			
GMP9919	Belt Loading	5.0 m/s	Loading rate too high
GMP9920	Belt Loading	5.0 m/s	Loading rate too high
GMP9921	Rigid Bar	3 m/s	
GMP9922	Rigid Bar	6 m/s	
GMP9923	Rigid Bar	5 m/s	
GMP9924	Rigid Bar	4 m/s	Response too soft
GMP9925	Belt Loading	3.0 m/s	
GMP9926	Belt Loading	4.7 m/s	
GMP9927	6.2 kg Head form impact using drop tower. For FE validation.	3 m/s	
GMP9928	Same as 0027	6 m/s	

Test ID	Test Type	Rate	Comments
GMP9929	Rigid Bar. Bladder w/ inextensible wrap	4.0 m/s	Response within 6 m/s corridor
GMP9930	Rigid Bar. Bladder w/ inextensible wrap.	6.7 m/s	Response less stiff than 0029 due to loosening of wrap
PROTOTYPE 7 0.3" thick silicone rubber bladder, soft upper cradle, reduced profile rigid lower cradle			
GMP9931	Rigid Bar	3.8 m/s	Bladder rupture and was repaired for subsequent tests
GMP9932	Rigid Bar	3.7 m/s	
GMP9933	Rigid Bar	6.7 m/s	
GMP9934	Rigid Bar	6.4 m/s	Response within Cavanaugh/Hardy Corridors
GMP0001	Whole Dummy Sled. Knee bolster spacing = 70 mm. H30 = 320 mm. Wheel-to-abdomen=30 mm. Three-point belt.	20mph/ 15 g	
GMP0002	Whole Dummy Sled. Same config as 0001.	30 mph/20g	
GMP0003	Whole Dummy Sled. Airbag @ 15ms post tzero‡. Rest of setup same as 0001 and 0002	20 mph/15 g	
GMP0004	Whole Dummy Sled. Unrestr. Airbag, knee bolster, seat, same as 0001 and 0002	20 mph/15 g	
GMP0005	Sled. Repeat of GMP001.	20 mph/15 g	
GMP0006	Sled. European-style Passenger 3-point belt.	20 mph/15 g	
GMP0007	Sled. Same config as 0005.	30 mph/ 15 g	
GMP0008	Sled. Repeat of 0006.	20 mph/ 15 g	
GMP0009	Bladder-Only Sled w/Jacket Material	21 mph/16g	
GMP0010	Bladder-Only Sled w/o Jacket Material	20 mph/15g	
PROTOTYPE 8 50-durometer silicone abdomen soft upper cradle, reduced profile rigid lower cradle			
GMP0011	Rigid Bar. With chest jacket.	4.34 m/s	No data collected. Data Acquisition did not trigger.
GMP0012	Rigid Bar. With chest jacket.	4.31 m/s	
GMP0013	Rigid Bar. With chest jacket.	6.64 m/s	Validation rigid-bar test
GMP0014	Rigid Bar. No jacket.	6.51 m/s	Appropriate response. No change in response w/ jacket
GMP0015	Rigid Bar. No jacket	4.73 m/s	
GMP0016	Rigid Bar-knee impact. No jacket.	2.8 m/s	Conducted to verify that pelvic x accel can cause negative pressure in bladder
GMP0017	Belt Loading. No jacket	4.5 m/s	
GMP0018	Belt Loading . W/jacket.	3.0 m/s	Validation belt loading test
GMP0019	Belt Loading . W/o jacket.	3.0 m/s	
GMP0020	6.2 kg Head form impact using drop tower. For FE validation.	3 m/s nominal	
GMP0021	Same as 0020	3 m/s nominal	

‡ t_{zero} is defined as the moment where sled acceleration first rises above 0.5 g.

Test ID	Test Type	Rate	Comments
GMP0022	Same as 0020,21	3 m/s nominal	
GMP0023	Same as 0020-0022	3 m/s nominal	
GMP0024	Same as 0020-0023		Failed instrumentation. No data collected.
GMP0025	Same as 0020-0024		Failed instrumentation. No data collected.
GMP0026	Whole Dummy Sled w/ Airbag	20 mph/15g	
GMP0027	Instron Shape tape test		
GMP0028	Rigid Bar. Shape tape test	5.84 m/s	
GMP0029	Rigid Bar. Shape tape test	5.94 m/s	
GMP0030	Rigid Bar. Shape tape test	6.02 m/s	
GMP0031	Whole Dummy Sled. Unrestrained driver 36% risk of injury.	14.6 kph/3.2 g	
GMP0032	Whole Dummy Sled. 3-pt belt restrained driver. 9% risk	14.8 kph/3.7g	
GMP0033	Whole Dummy Sled. 3-pt belt restrained driver. 26% risk	23 kph/8.6g	
GMP0034	Whole Dummy Sled. 3-pt belt + airbag (deployed 15 ms after tzero) 26% risk.	23 kph/8.6g	
GMP0035	Whole Dummy Sled. 3-pt belt + airbag (deployed 15 ms after start of impact) Repeat of 0034 with wheel pinned. 26% risk.	23 kph/8.6 g	
GMP0036	Whole Dummy Sled. Unrestrained driver. 54% risk	19.4 kph /5.6 g	
GMP0037	Whole Dummy Sled. 3-pt belt restrained passenger. 9% risk.	15.0 kph//3.3g	
GMP0038	Whole Dummy Sled. 3-pt belt passenger 51% risk.	34.3 kph/12 g	
GMP0039	Whole Dummy Sled. 3-pt belt driver 51% risk. Repeat of 0039.	34.4 kph/12 g	
GMP0040	Whole Dummy Sled. 3-pt belt driver 51% risk.	34.5 kph/12 g	
GMP0041	Whole Dummy Sled. Unrestrained driver 86% risk.	34.1 kph/12.2 g	
GMP0042	Whole Dummy Sled. 3-pt belt driver 86% risk.	46.8 kph/15.7 g	
GMP0043	Whole Dummy Sled. 3-pt belt driver + airbag 86% risk.	46.8 kph/15.7 g	
GMP0044	Whole Dummy Sled. 3-pt belt driver. 90% risk.	52.3 kpg/17.4 g	
GMP0045	Whole Dummy Sled. 3-pt belt passenger. 90% risk.	52.6 kpg/17.5 g	
GMP0046	Bladder Only Sled. Bladder Only Sled with Shape Tape.	15 mph/ 20g	
GMP0047	Bladder Only Sled. Bladder Only Sled without Shape Tape.	15 mph/ 20g	
GMP0048	Surrogate Airbag. Fixed back pregnant dummy without jacket.	12.5 m/s	
GMP0049	Surrogate Airbag. Fixed back pregnant dummy with jacket.	12.5 m/s	Response is within the Cavanaugh/Hardy corridors

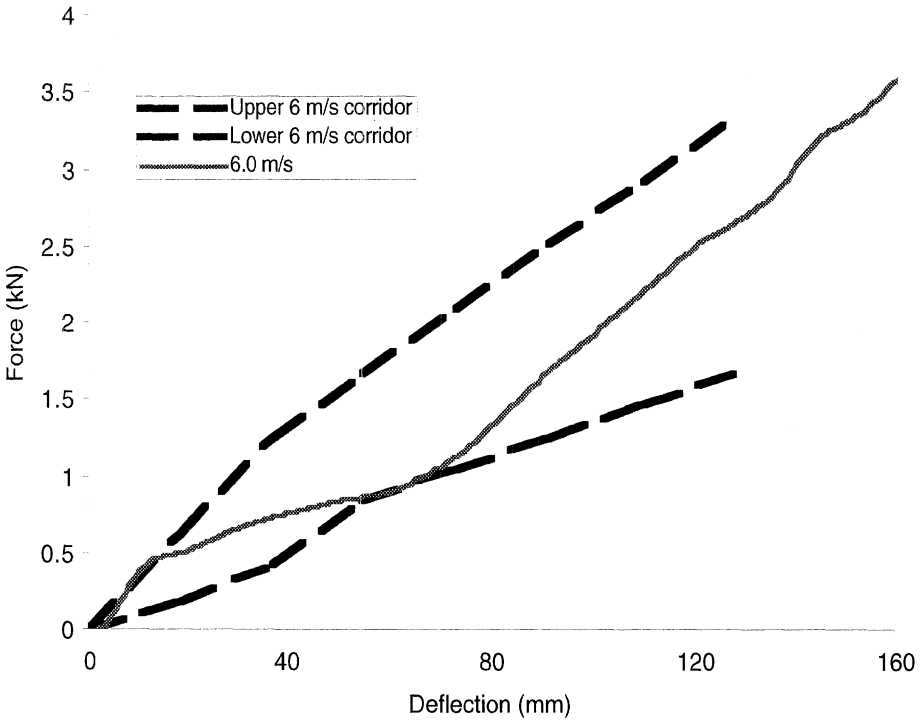

Figure B1. Force-deflection response from test GMP9901 (Bladder 1). 6.0 m/s rigid-bar impact. 25-durometer urethane bladder, full rigid upper and lower cradles.

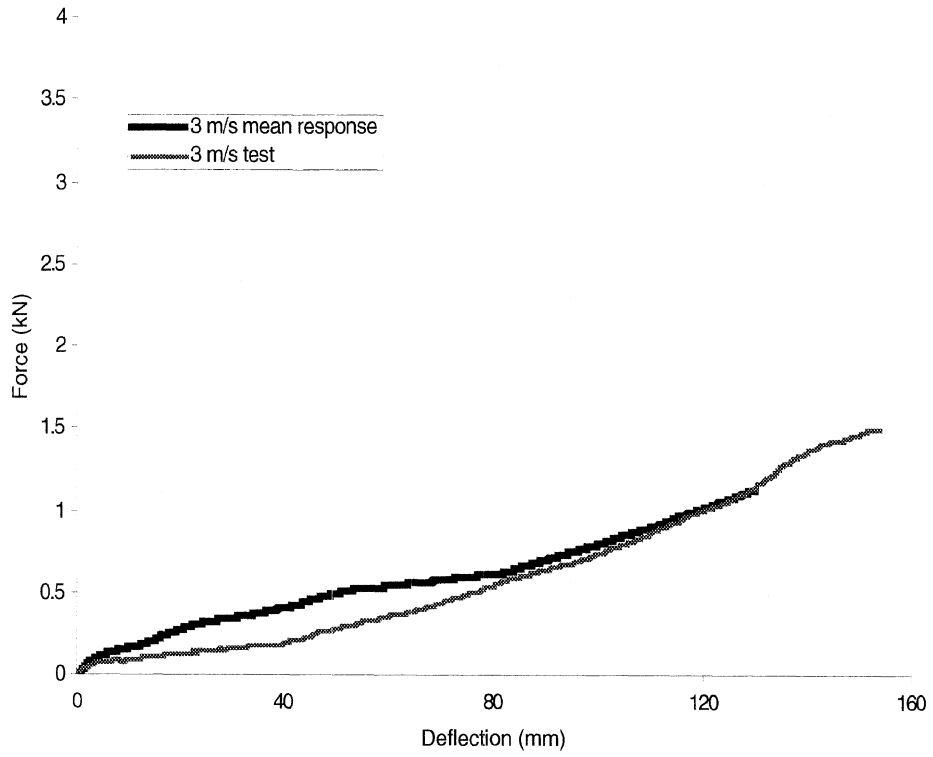

Figure B2. Force-deflection response from test GMP9903 (Bladder 2). 3 m/s rigid-bar impact. 30-durometer urethane bladder, soft upper cradle, full rigid lower cradle.

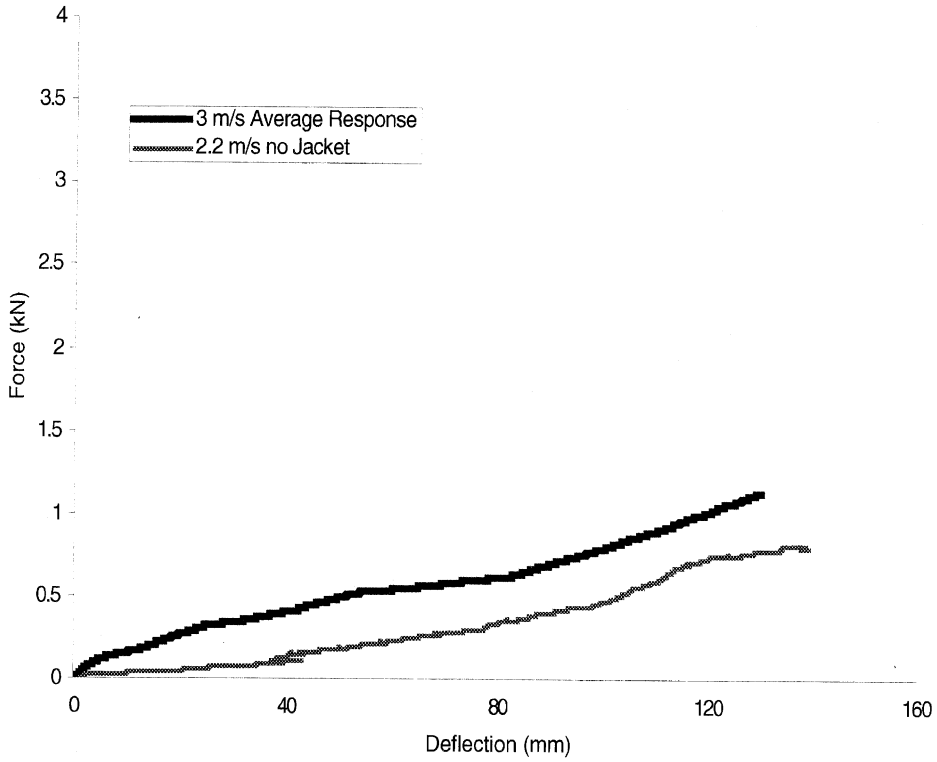

Figure B3. Force-deflection response from test GMP9905 (Bladder 3). 2.2 m/s rigid-bar impact. 30-durometer bladder, soft upper cradle, reduced rigid lower cradle, no jacket.

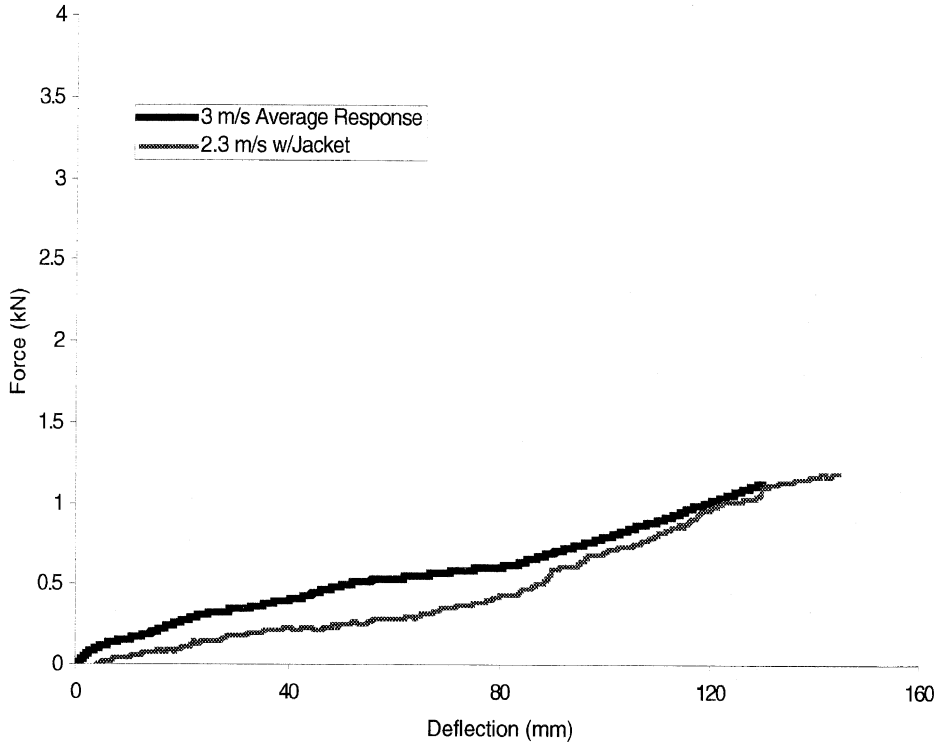

Figure B4. Force-deflection response from test GMP9906 (Bladder 3). 2.2 m/s rigid-bar impact. 30-durometer bladder, soft upper cradle, reduced rigid lower cradle, with jacket.

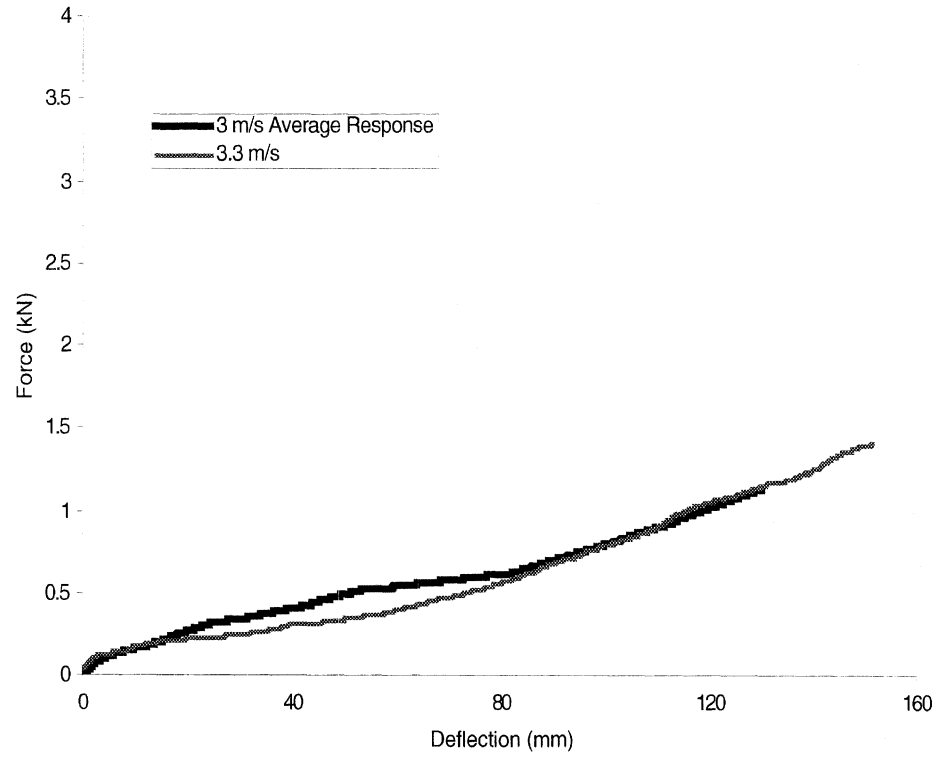

Figure B5. Force-deflection response from test GMP9907 (Bladder 3). 3.3 m/s rigid-bar impact. 30-durometer bladder, soft upper cradle, reduced rigid lower cradle, with jacket.

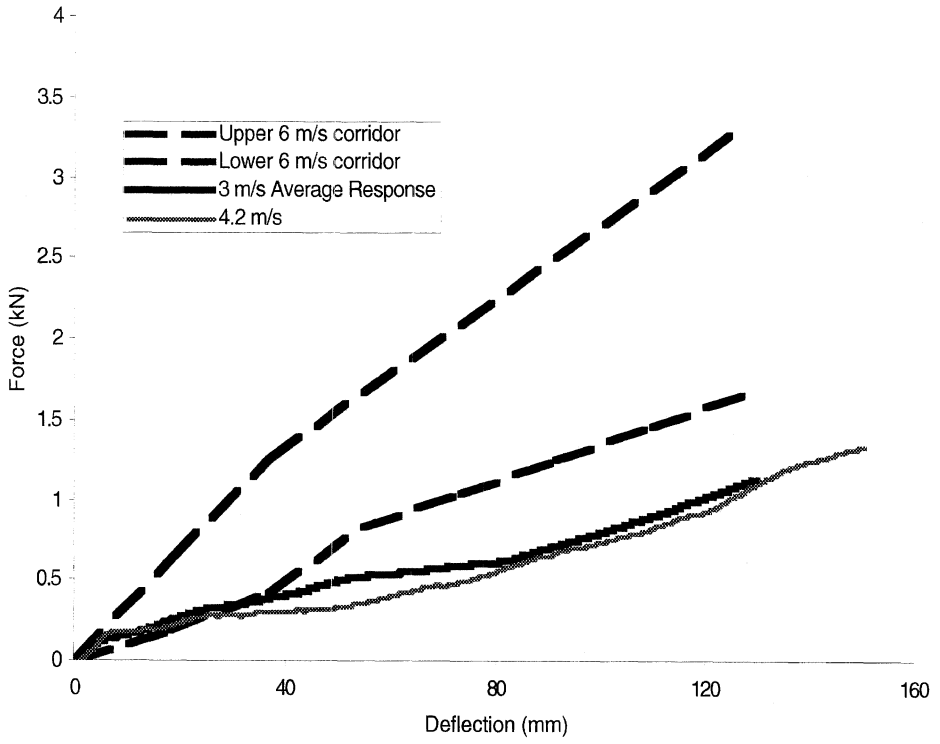

Figure B6. Force-deflection response from test GMP9908 (Bladder 3). 4.2 m/s rigid-bar impact. 30-durometer bladder, soft upper cradle, reduced rigid lower cradle, with jacket.

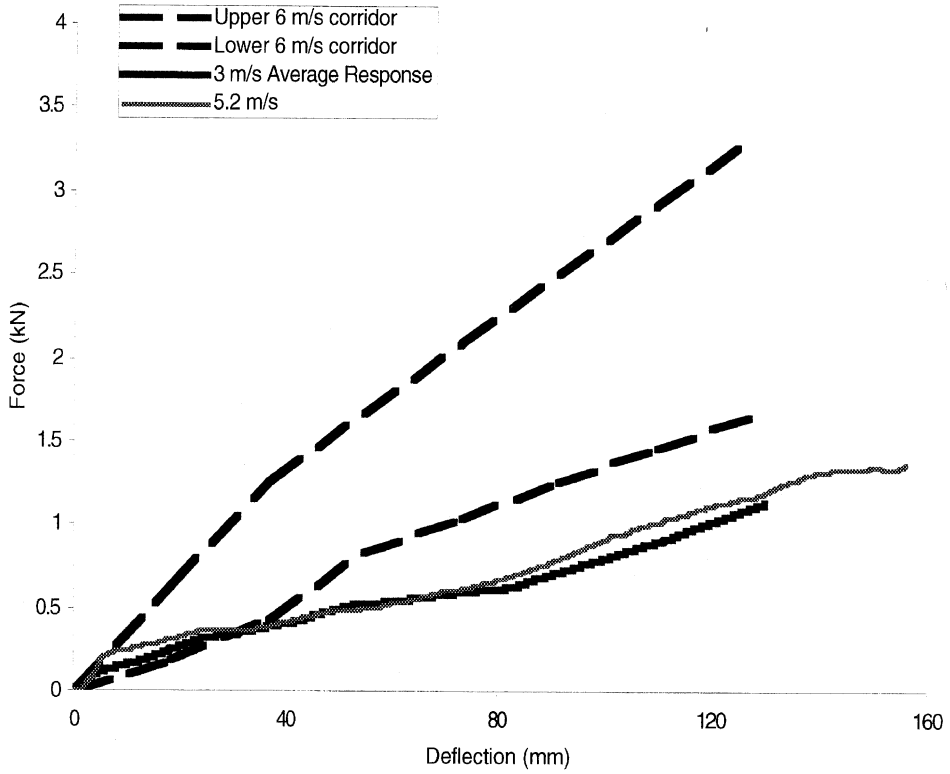

Figure B7. Force-deflection response from test GMP9909 (Bladder 3). 5.2 m/s rigid-bar impact. 30-durometer bladder, soft upper cradle, reduced rigid lower cradle, with jacket.

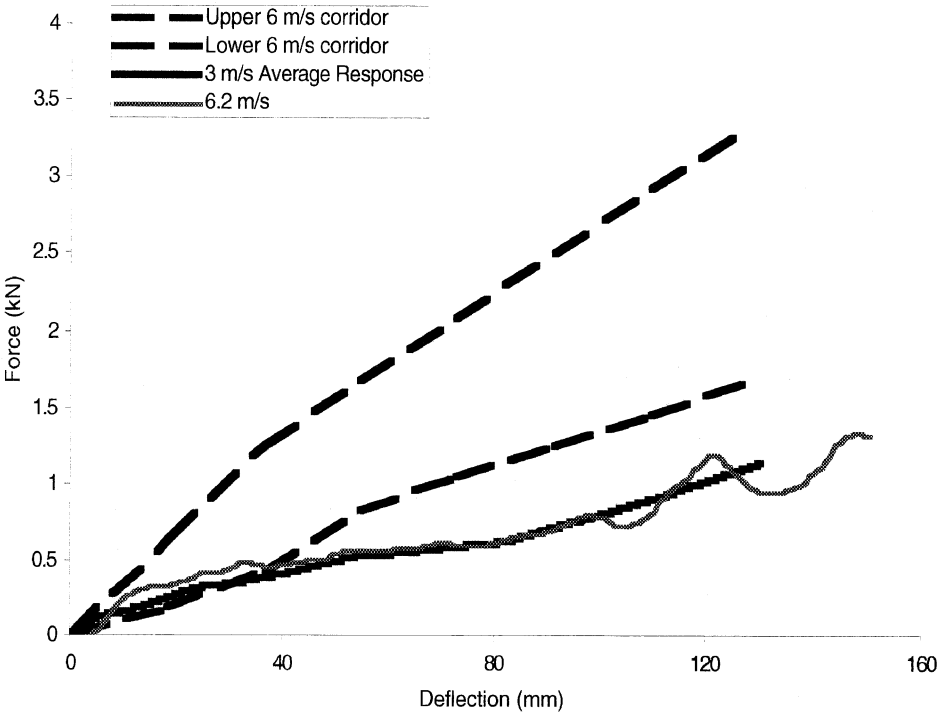

Figure B8. Force-deflection response from test GMP9910 (Bladder 3). 5.2 m/s rigid-bar impact. 30-durometer bladder, soft upper cradle, reduced rigid lower cradle, with jacket.

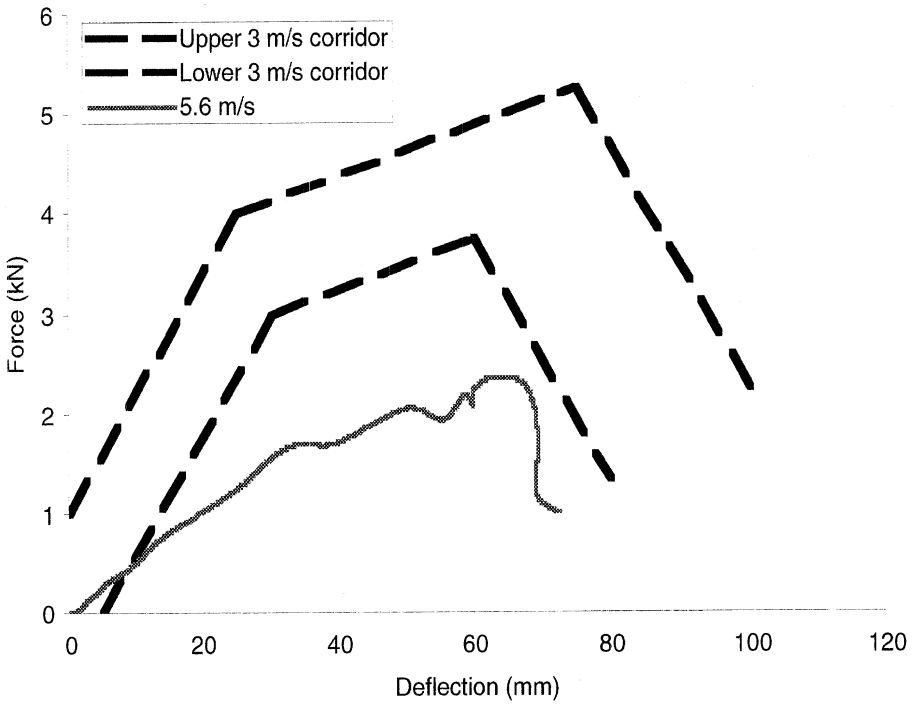

Figure B9. Force-deflection response from test GMP9911 (Bladder 4). 5.6 m/s belt loading. 30-durometer urethane bladder, soft upper cradle, reduced rigid lower cradle, with jacket.

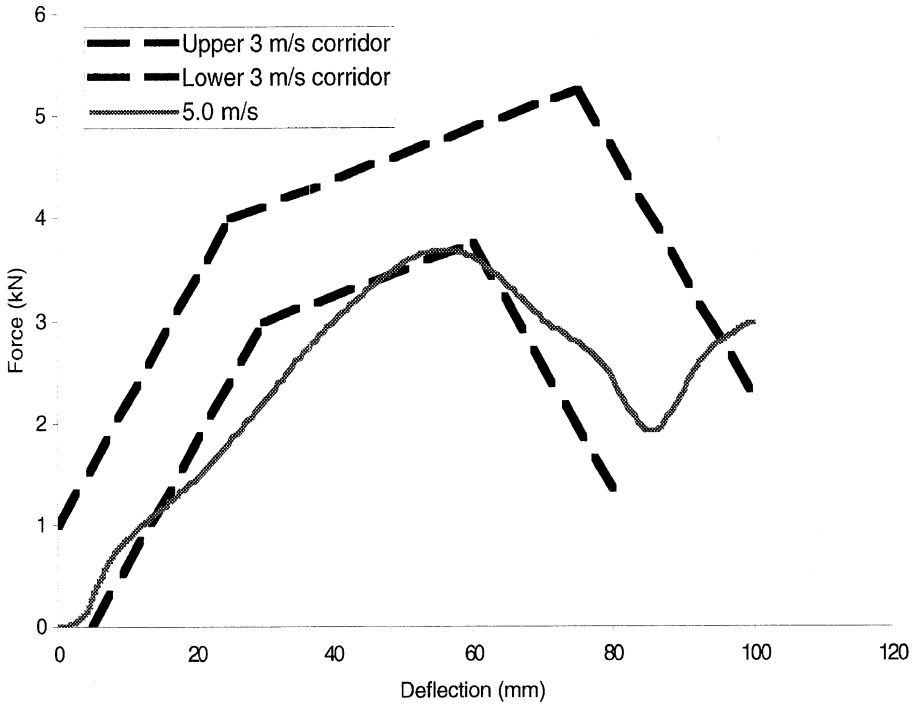

Figure B10. Force-deflection response from test GMP9919 (Bladder 6). 5.0 m/s belt loading. 40-durometer silicone bladder, soft upper cradle, reduced rigid lower cradle, with jacket.

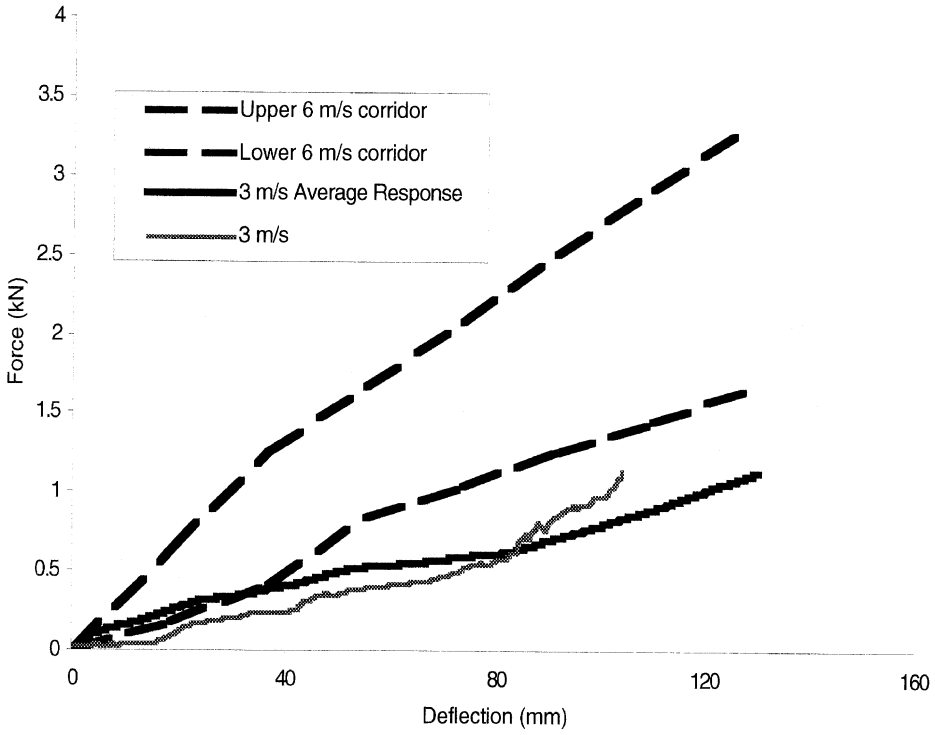

Figure B11. Force-deflection response from test GMP9921 (Bladder 6). 3.0 m/s rigid-bar impact. 40-durometer silicone bladder, soft upper cradle, reduced rigid lower cradle, with jacket.

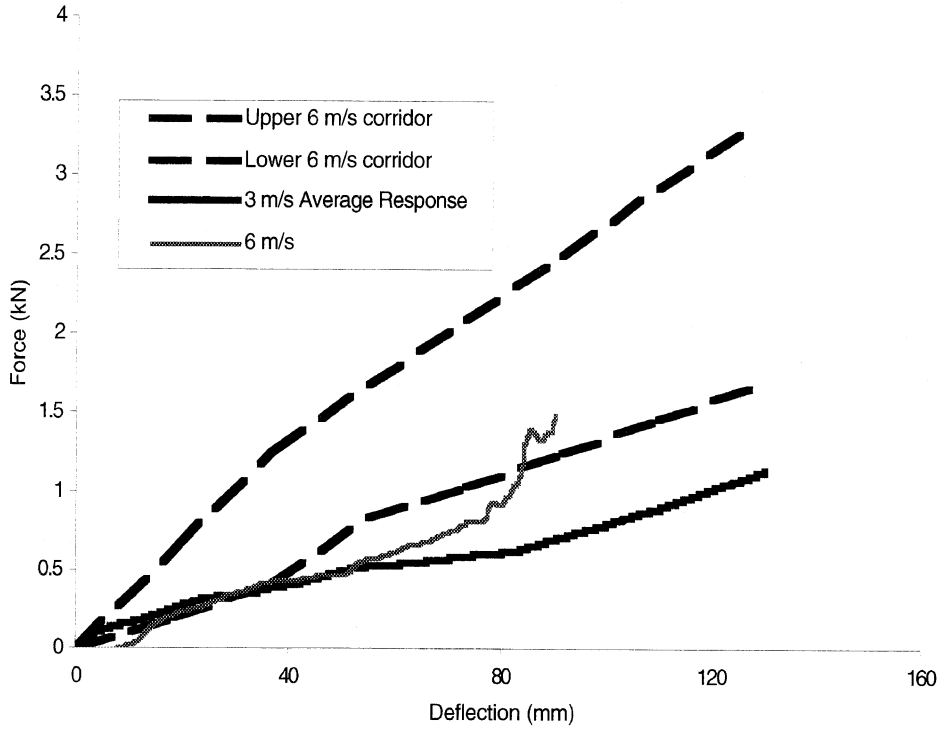

Figure B12. Force-deflection response from test GMP9922 (Bladder 6). 6.0 m/s rigid-bar impact. 40-durometer silicone bladder, soft upper cradle, reduced rigid lower cradle, with jacket.

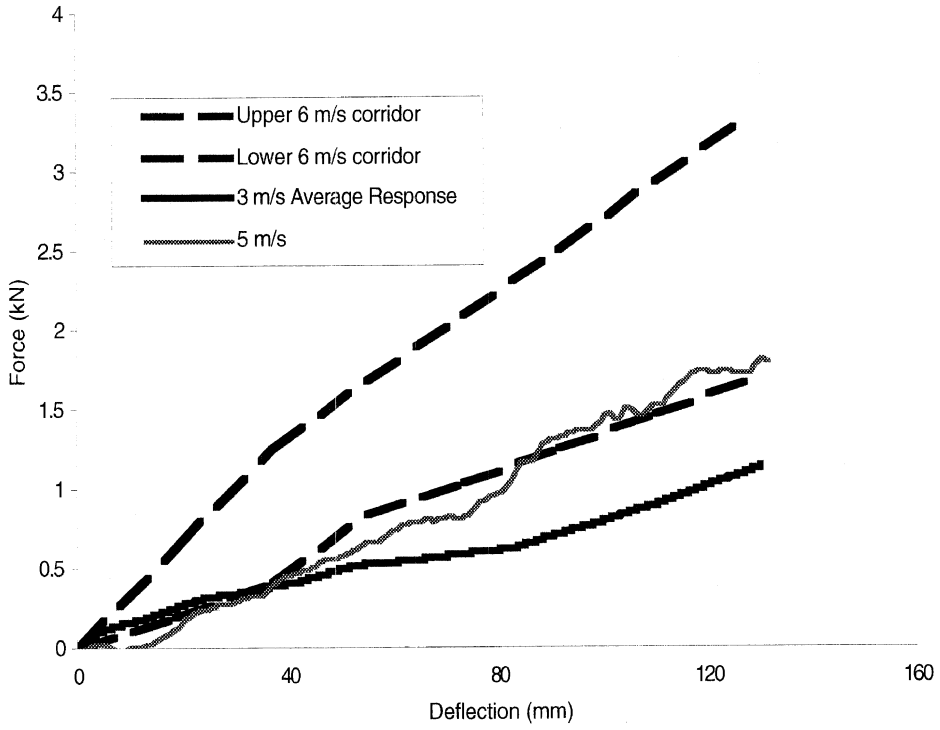

Figure B13. Force-deflection response from test GMP9923 (Bladder 6). 5.0 m/s rigid-bar impact. 40-durometer silicone bladder, soft upper cradle, reduced rigid lower cradle, with jacket.

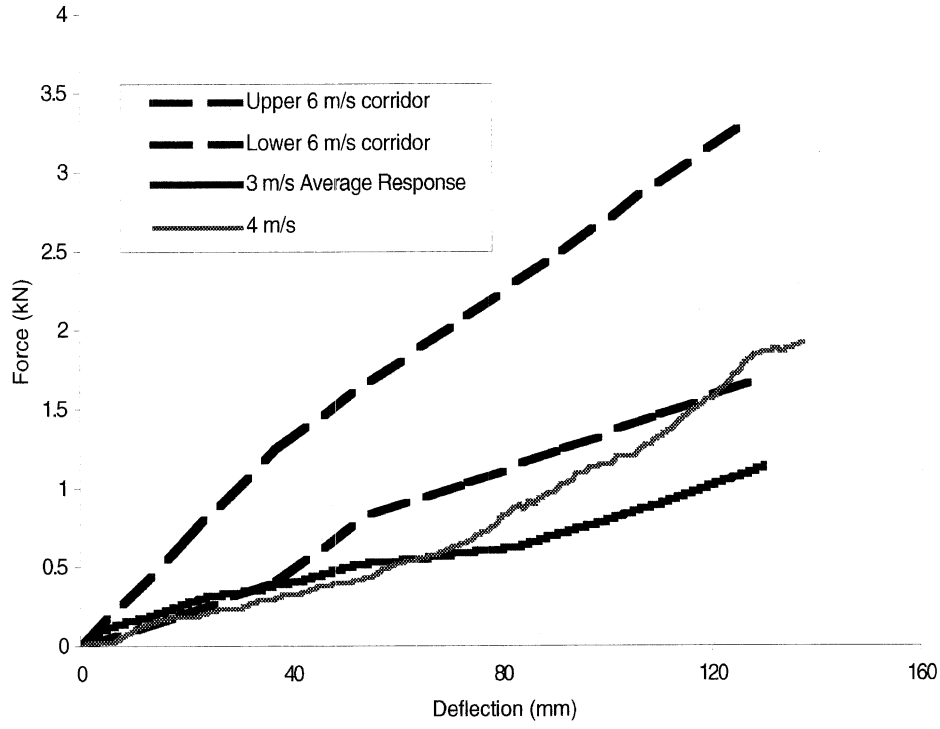

Figure B14. Force-deflection response from test GMP9924 (Bladder 6). 4.0 m/s s rigid-bar impact. 40-durometer silicone bladder, soft upper cradle, reduced rigid lower cradle, with jacket.

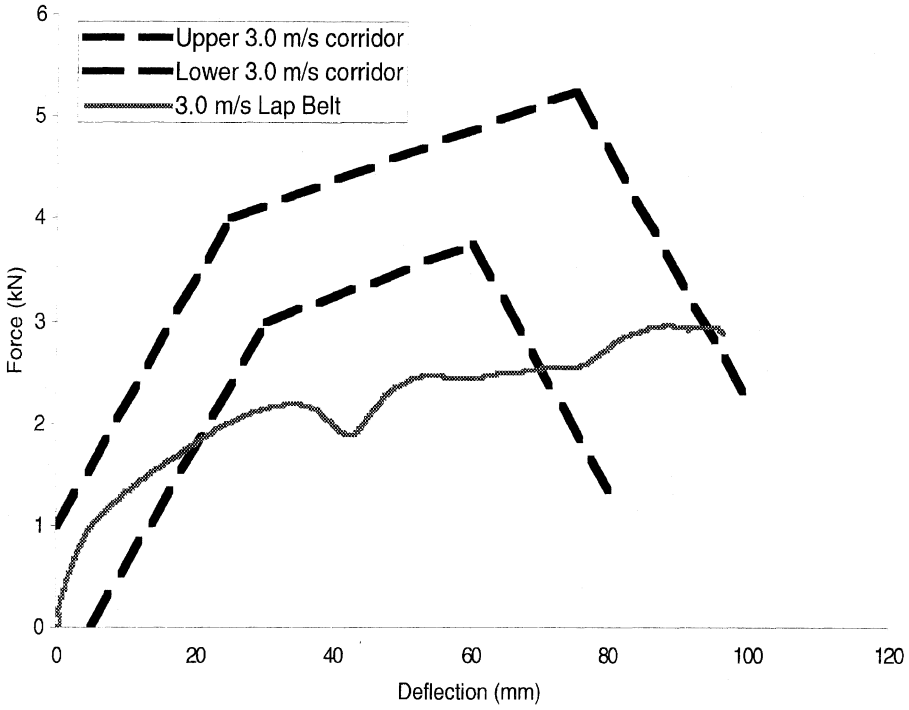

Figure B15. Force-deflection response from test GMP9925 (Bladder 6). 3.0 m/s belt loading. 40-durometer silicone bladder, soft upper cradle, reduced rigid lower cradle, with inextensible wrap.

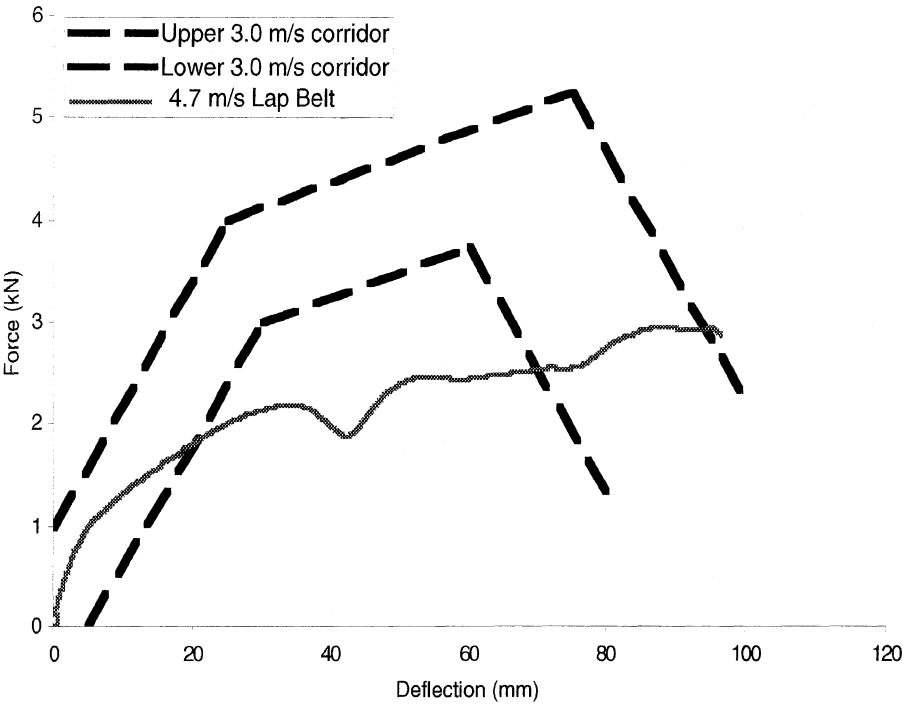

Figure B16. Force-deflection response from test GMP9926 (Bladder 6). 4.7 m/s lap-belt test. 40-durometer silicone bladder, soft upper cradle, reduced rigid lower cradle, with inextensible wrap.

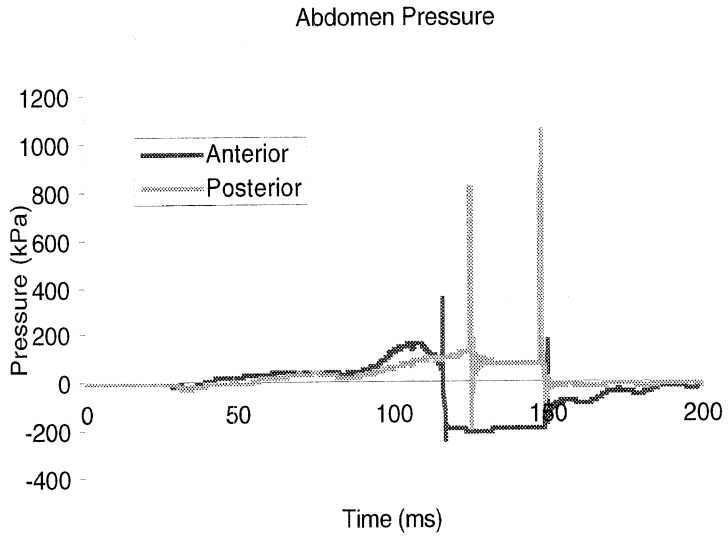

Figure B17. Bladder pressure response from test GMP9927 (Bladder 6). 3.0 m/s drop tower test performed with the 40-durometer silicone rubber bladder with inextensible wrap.

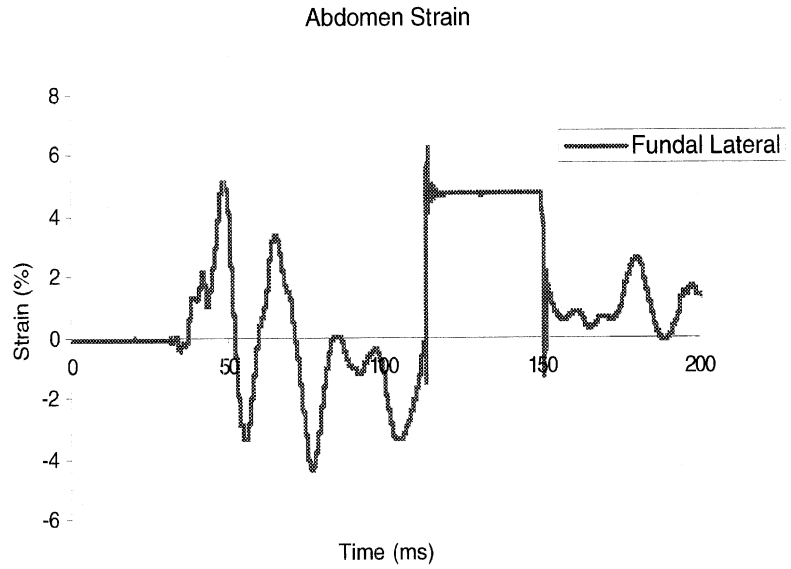

Figure B18. Bladder strain measured in a fundal location by a top-hat transducer in a lateral orientation from test GMP9927 (Bladder 6). 3.0 m/s drop tower test performed with the 40-durometer silicone rubber bladder with inextensible wrap.

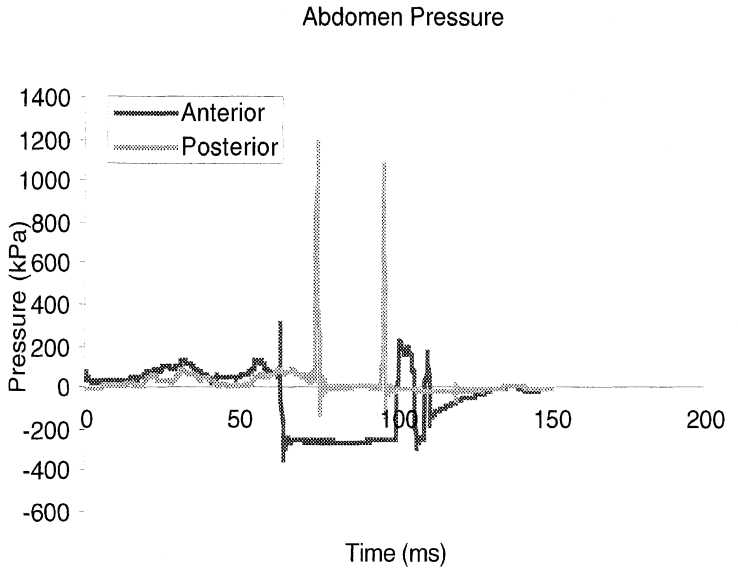

Figure B19. Bladder pressure response from test GMP9928 (Bladder 6). 6.0 m/s drop tower test performed with the 40-durometer silicone rubber bladder with inextensible wrap. Anterior top-hat transducer broke during testing at approximately 60 ms from t_{zero}.

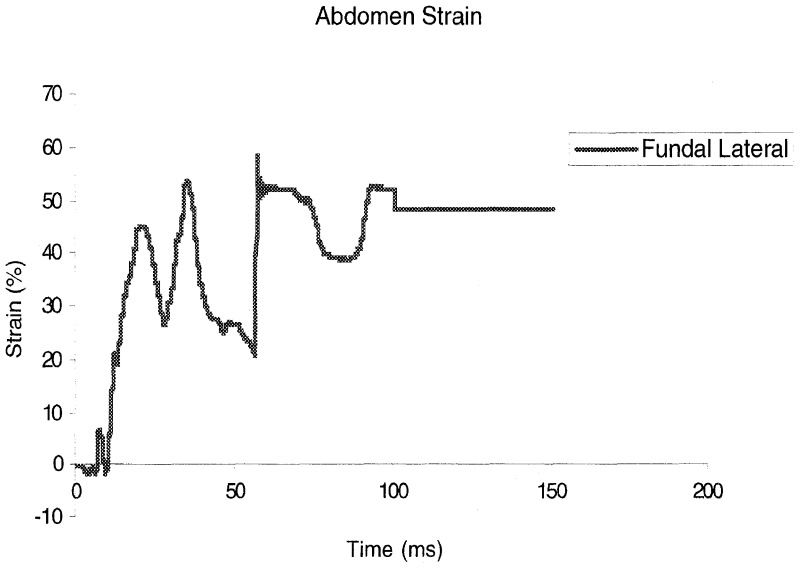

Figure B20. Bladder strain measured in a fundal location by a top-hat transducer in a lateral orientation from test GMP9928 (Bladder 6). 6.0 m/s drop tower test performed with the 40-durometer silicone rubber bladder with inextensible wrap. Anterior top-hat transducer broke during testing at approximately 60 ms from t_{zero}.

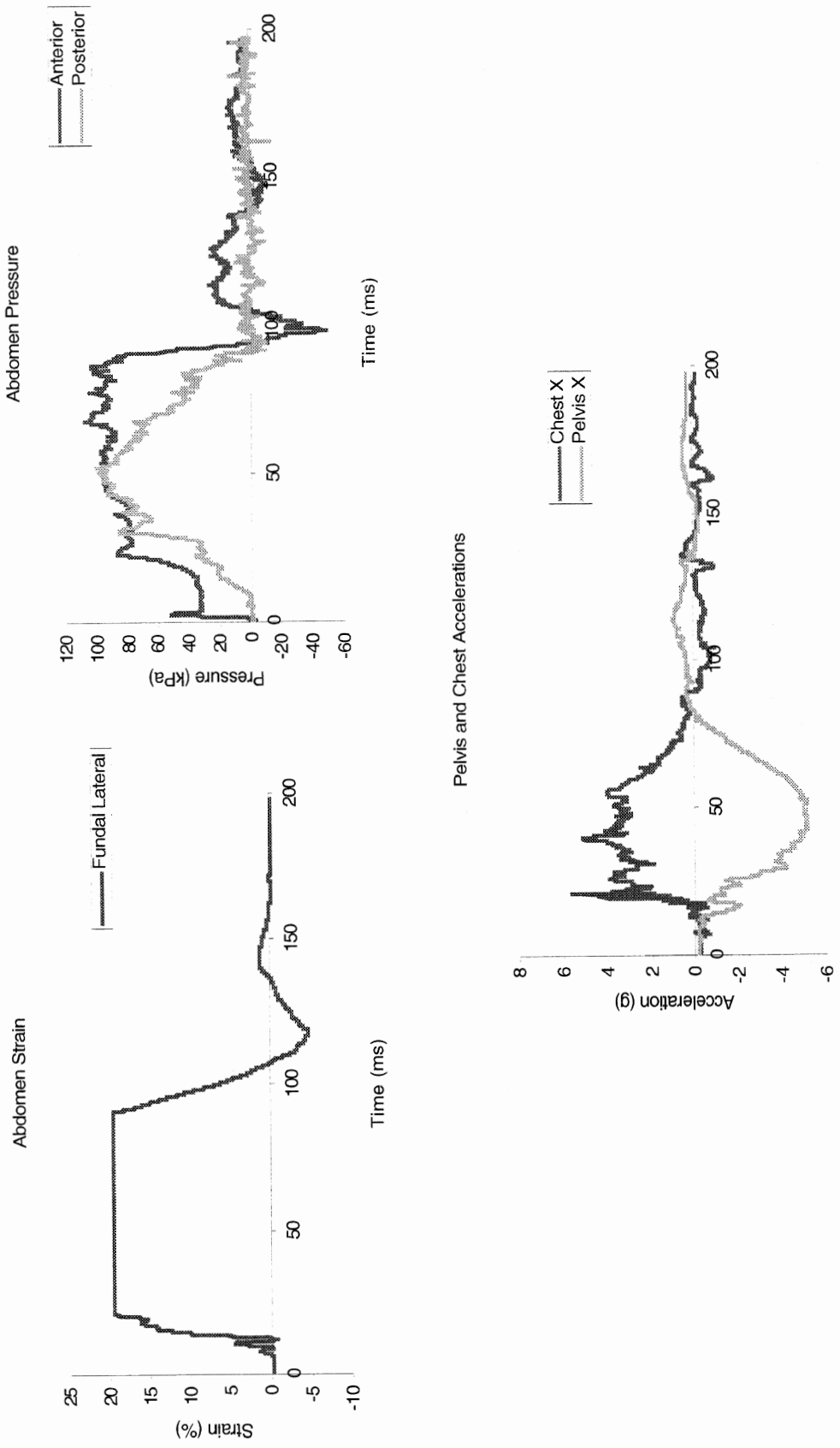

Figure B21. Signals from test GMP9929 (Bladder 6). 4.0 m/s rigid-bar impact performed with the 40-durometer silicone rubber with inextensible wrap.

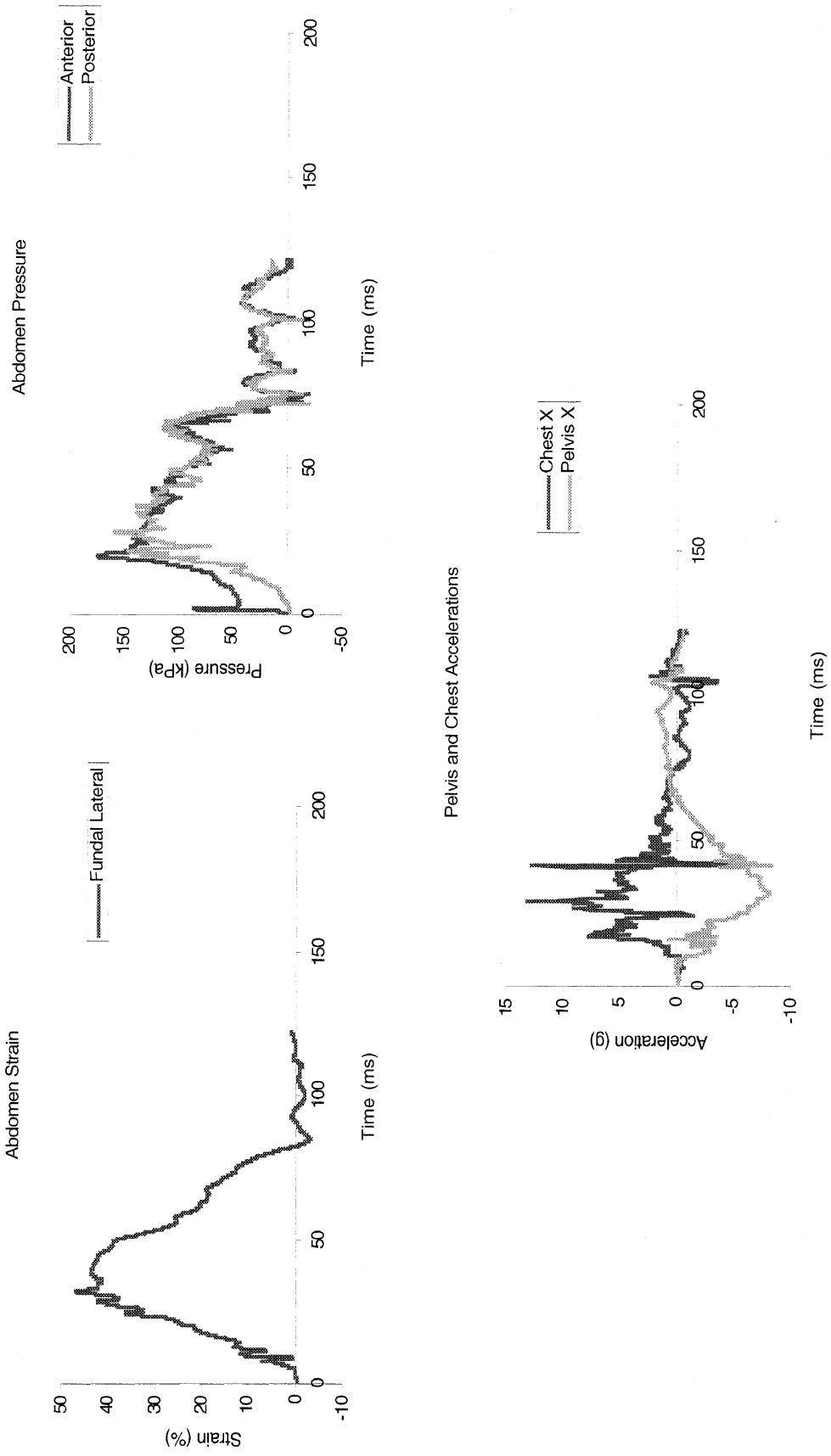

Figure B22. Signals from test GMP9930 (Bladder 6). 6.7 m/s rigid-bar impact performed with the 40-durometer silicone rubber bladder with inextensible wrap.

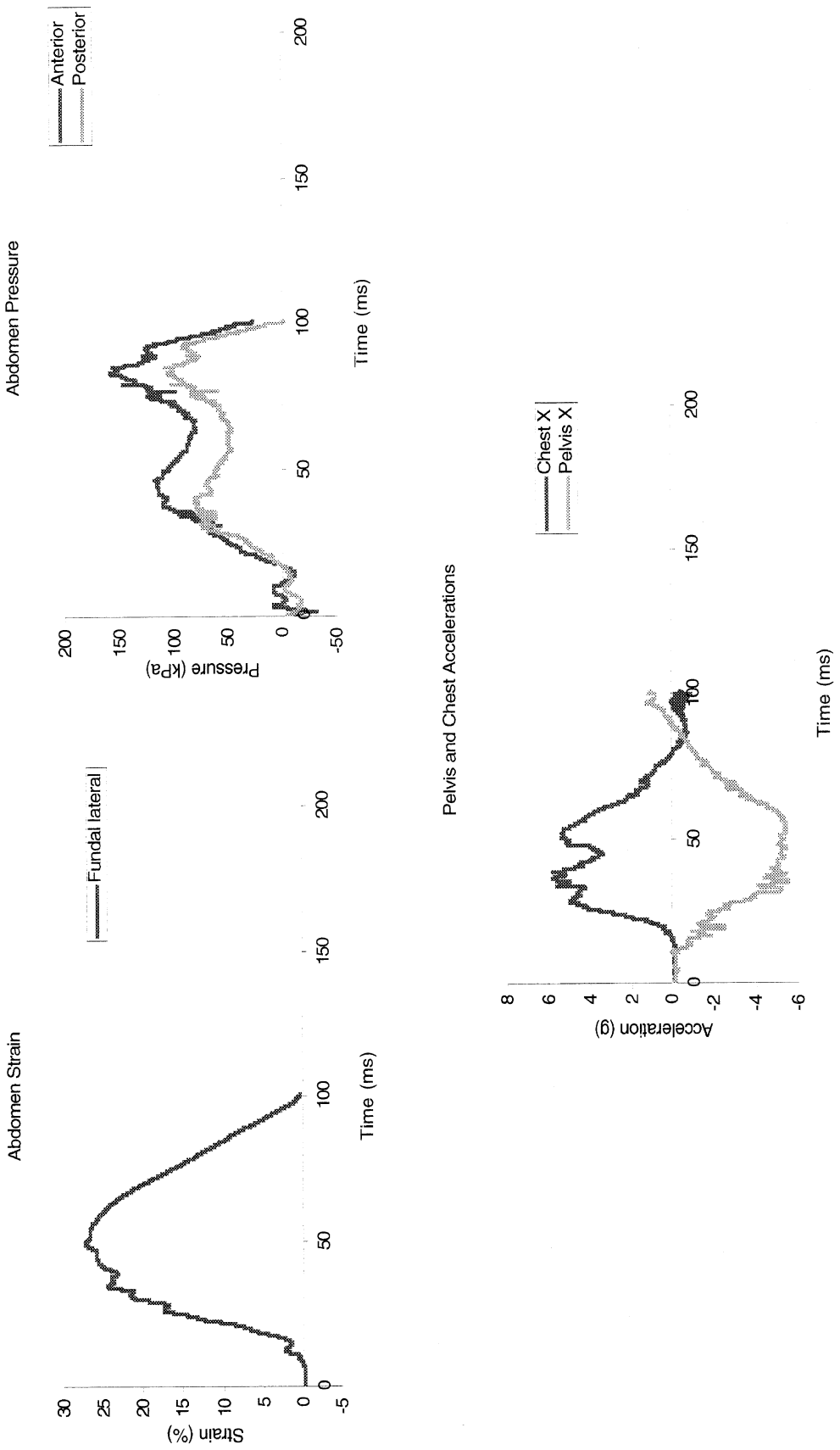

Figure B23. Signals from test GMP9932 (Bladder 7). 3.7 m/s rigid-bar impact performed with the repaired thicker 40-durometer silicone rubber bladder.

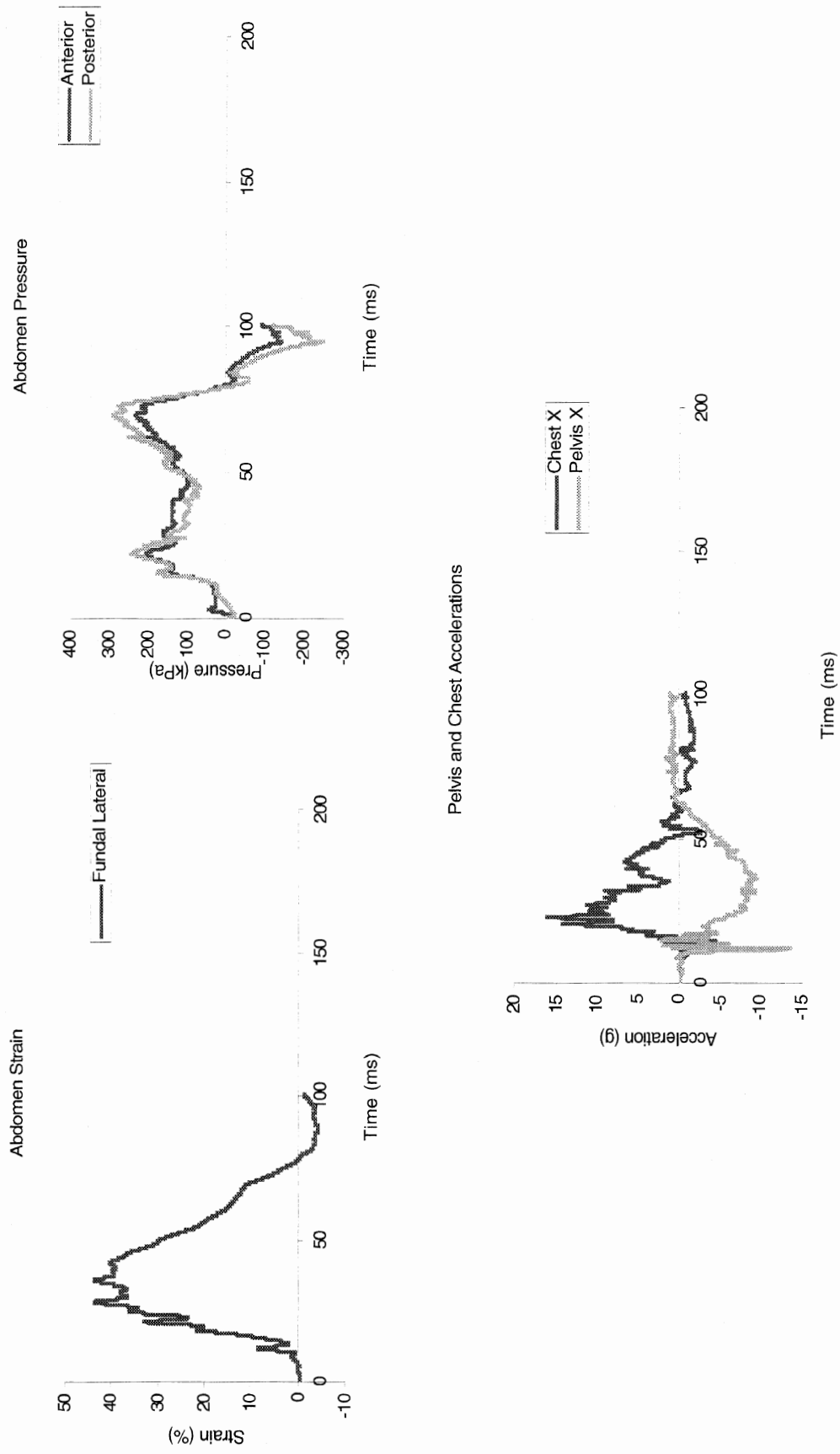

Figure B24. Signals from GMP9933 (Bladder 7). 6.7 m/s rigid-bar impact performed on the repaired, thicker 40-durometer silicone rubber bladder.

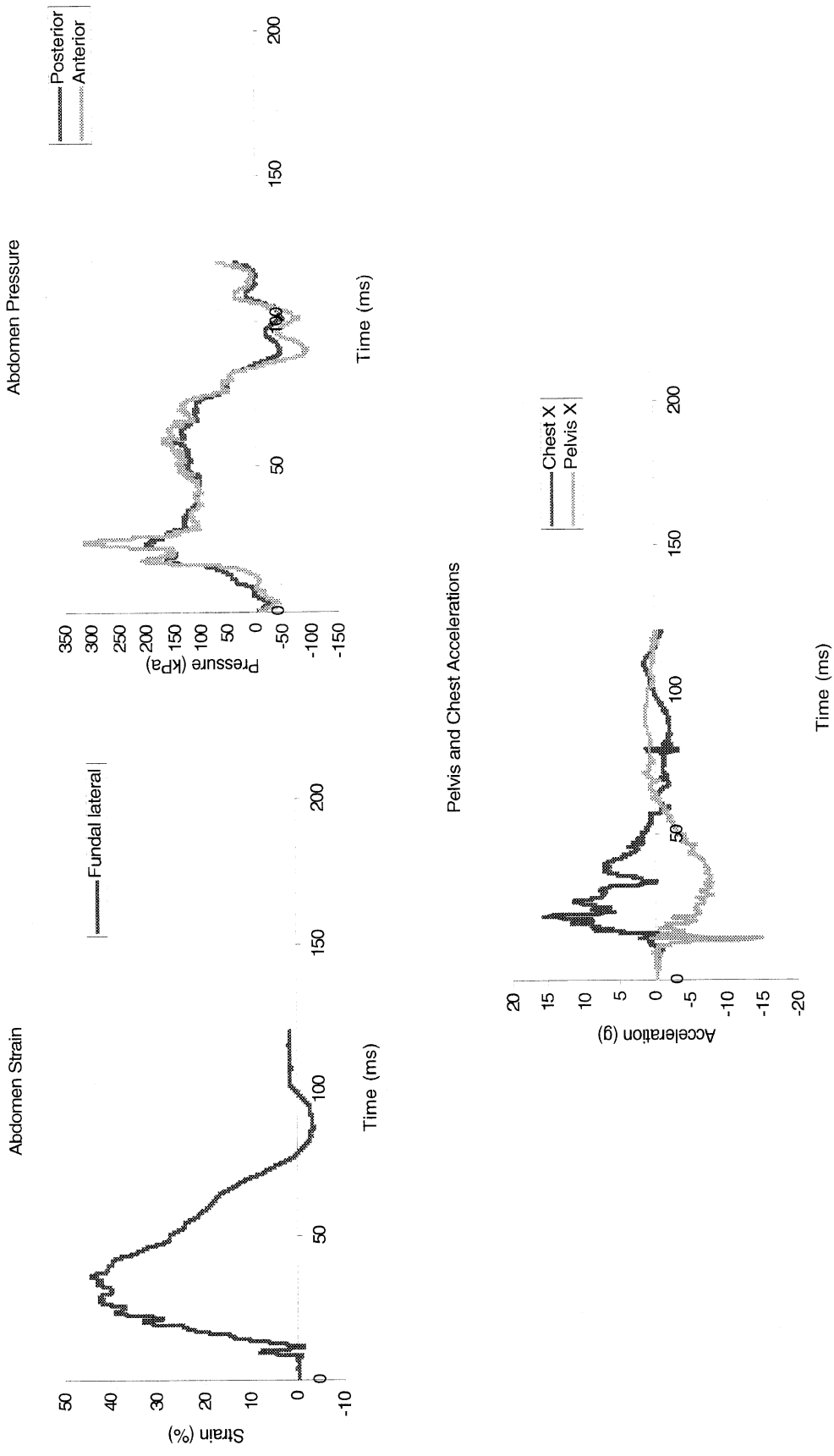

Figure B25. Signals from GMP9934 (Bladder 7). 6.4 m/s rigid-bar impact performed with the repaired, thicker 40-durometer silicone rubber bladder.

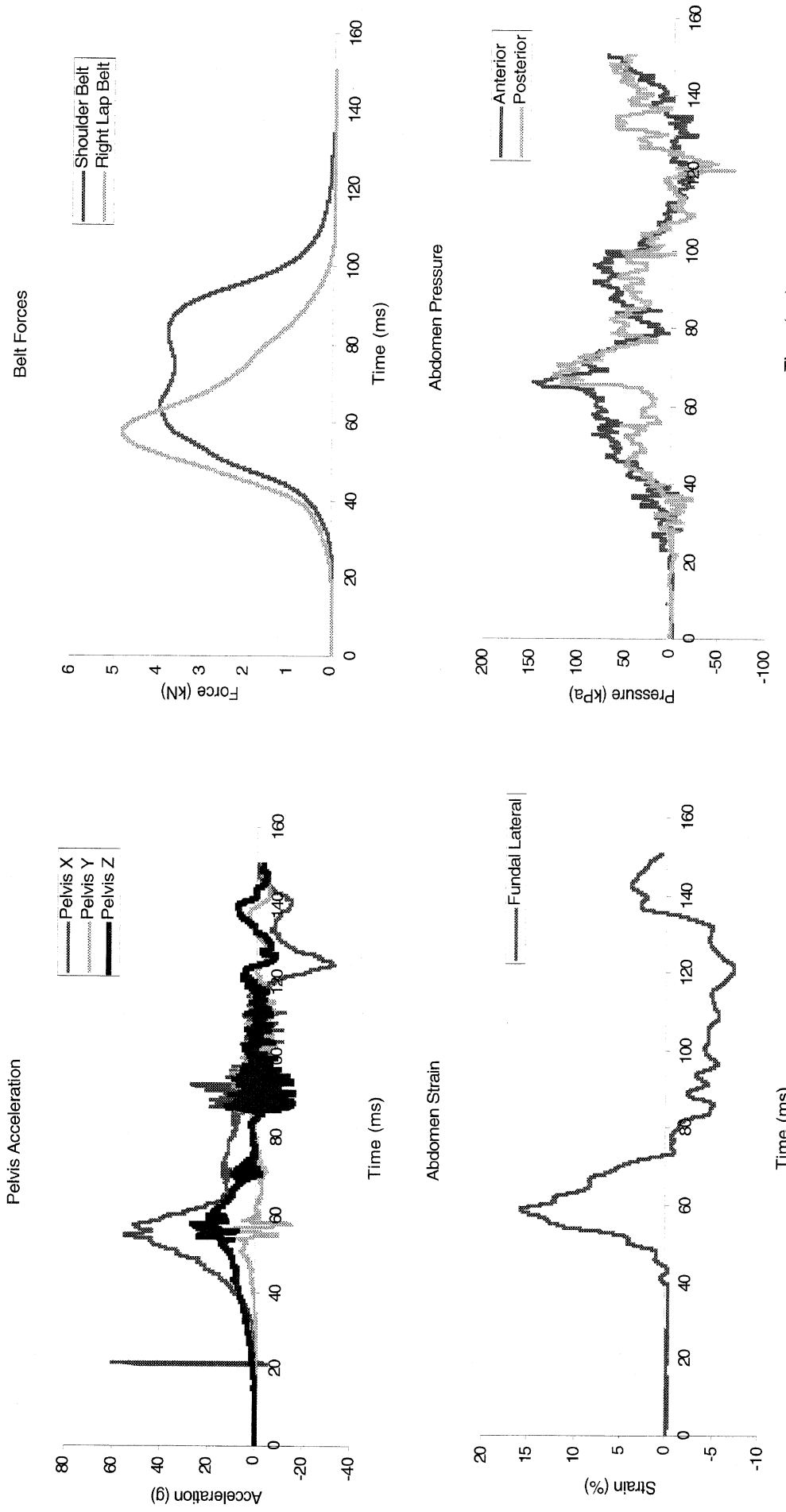

Figure B26. Signals from GMP0001 (Bladder 7). 20 mph/15 g sled test. Testing was done on a full dummy in jacket with the thicker 40-durometer silicone rubber bladder. The dummy was restrained by lap and shoulder belts.

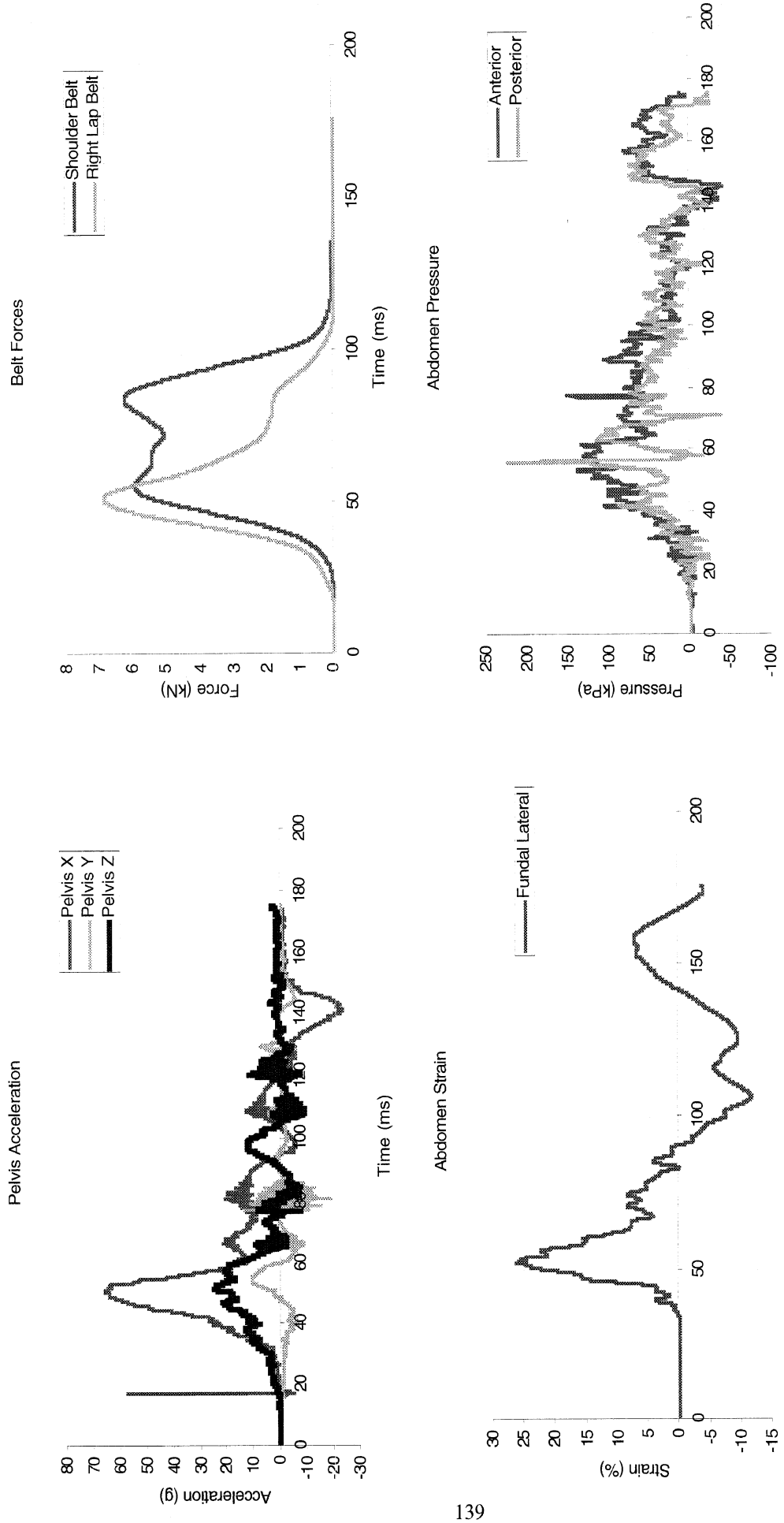

Figure B27. Signals from test GMP0002 (Bladder 7). 30 mph/20 g sled test. Full dummy with jacket and thick 40-durometer silicone rubber bladder. Restrained by lap and shoulder belts.

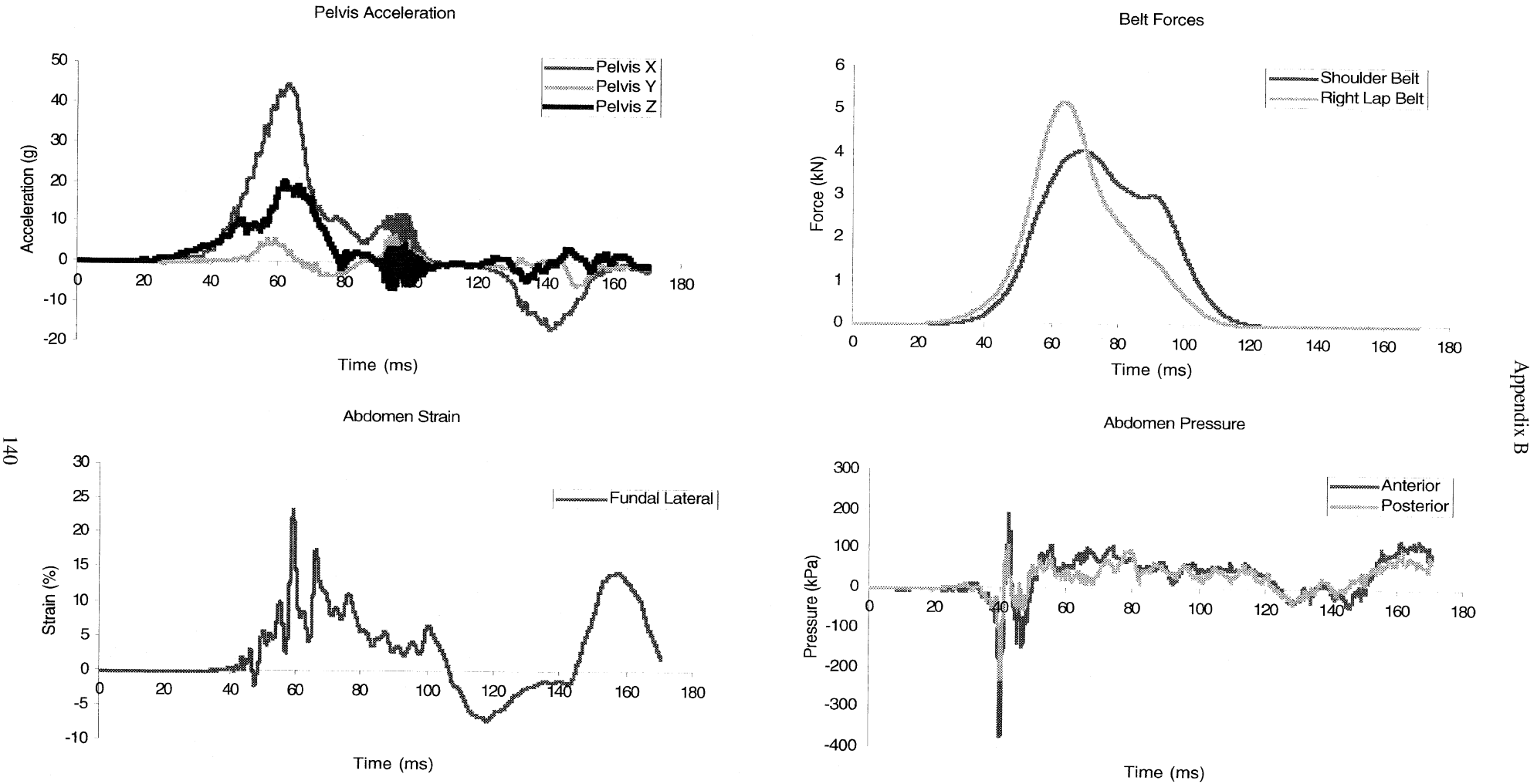

Figure B28. Signals from test GMP0003 (Bladder 7). 20 mph/15 g sled test with airbag deployment at 15 ms after t_{zero}. Full dummy with jacket and the thick 40-durometer silicone rubber bladder. Restrained by lap and shoulder belts.

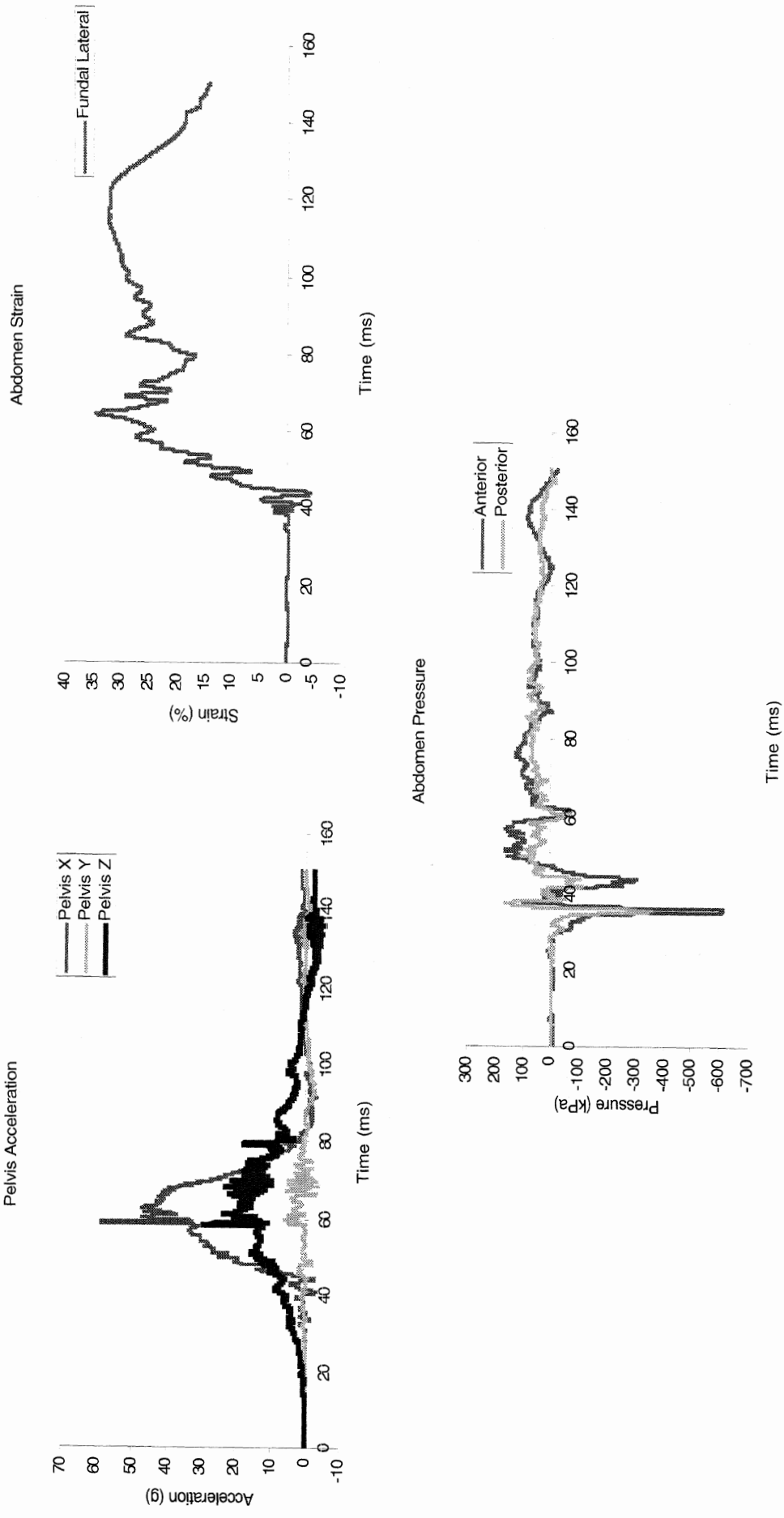

Figure B29. Signals from test GMP0004 (Bladder 7). 20 mph/15 g sled test with airbag deployment at 15 ms after t_{zero}. Unrestrained full dummy with jacket and the thick 40-durometer silicone rubber bladder.

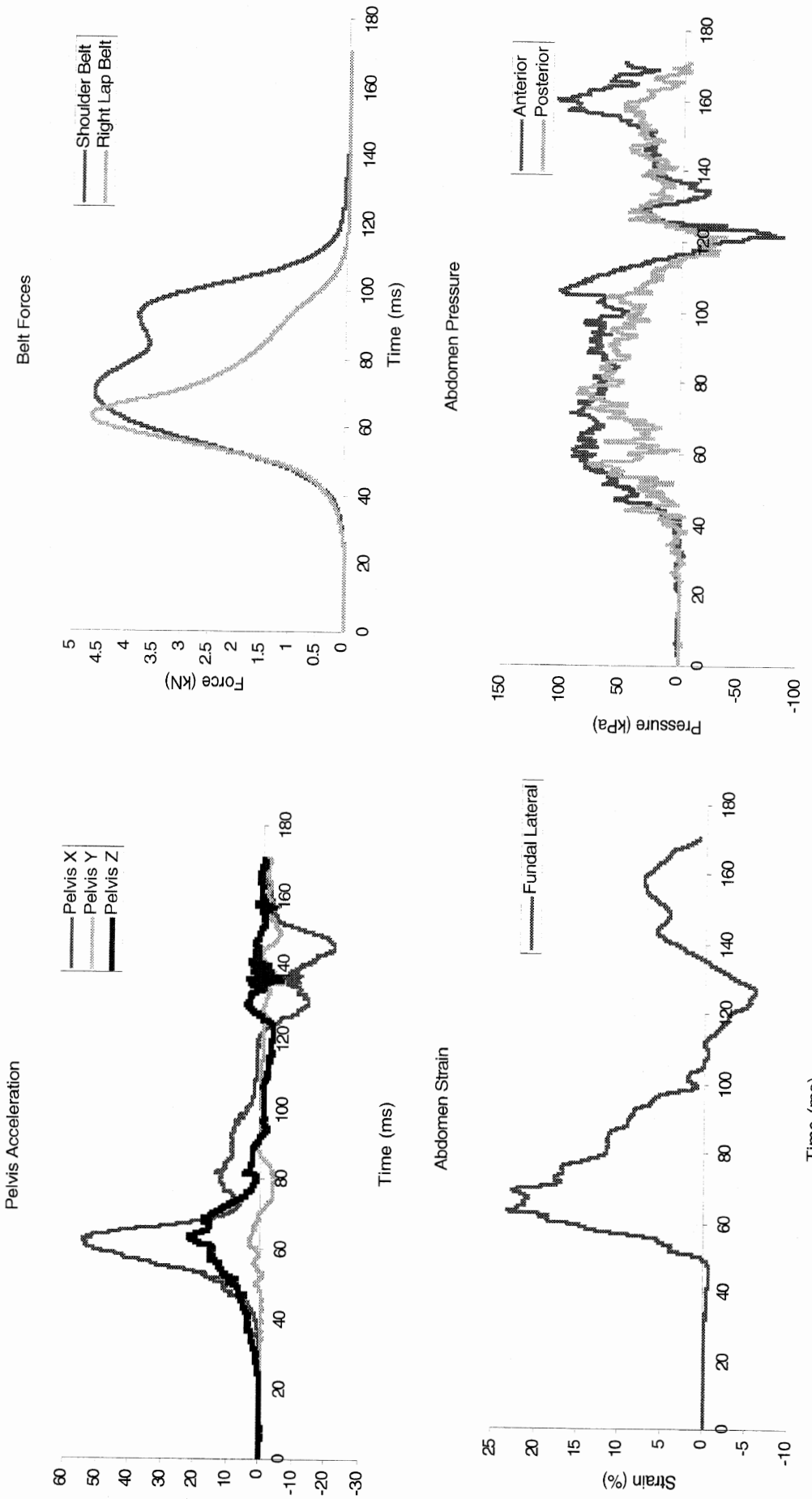

Figure B30. Signals from test GMP0005 (Bladder 7). 20 mph/15 g sled test. Full dummy with jacket and thicker 40-durometer silicone rubber bladder. Restrained by lap and shoulder belts.

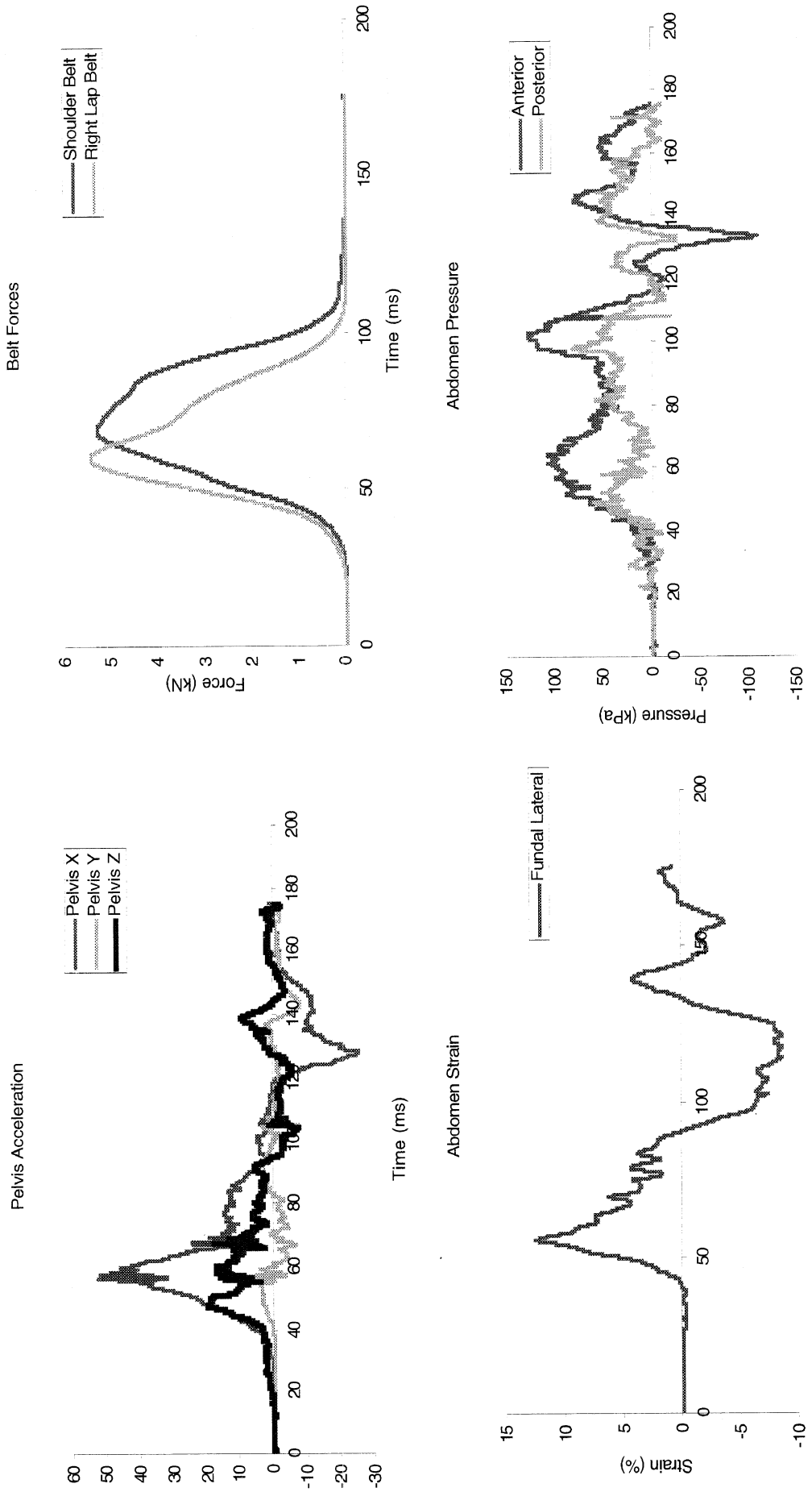

Figure B31. Signals from test GMP0006 (Bladder 7). 20 mph/15 g sled test with passenger airbag deployment. Full dummy with jacket and thicker 40-durometer silicone rubber bladder. Restrained by lap and shoulder belts.

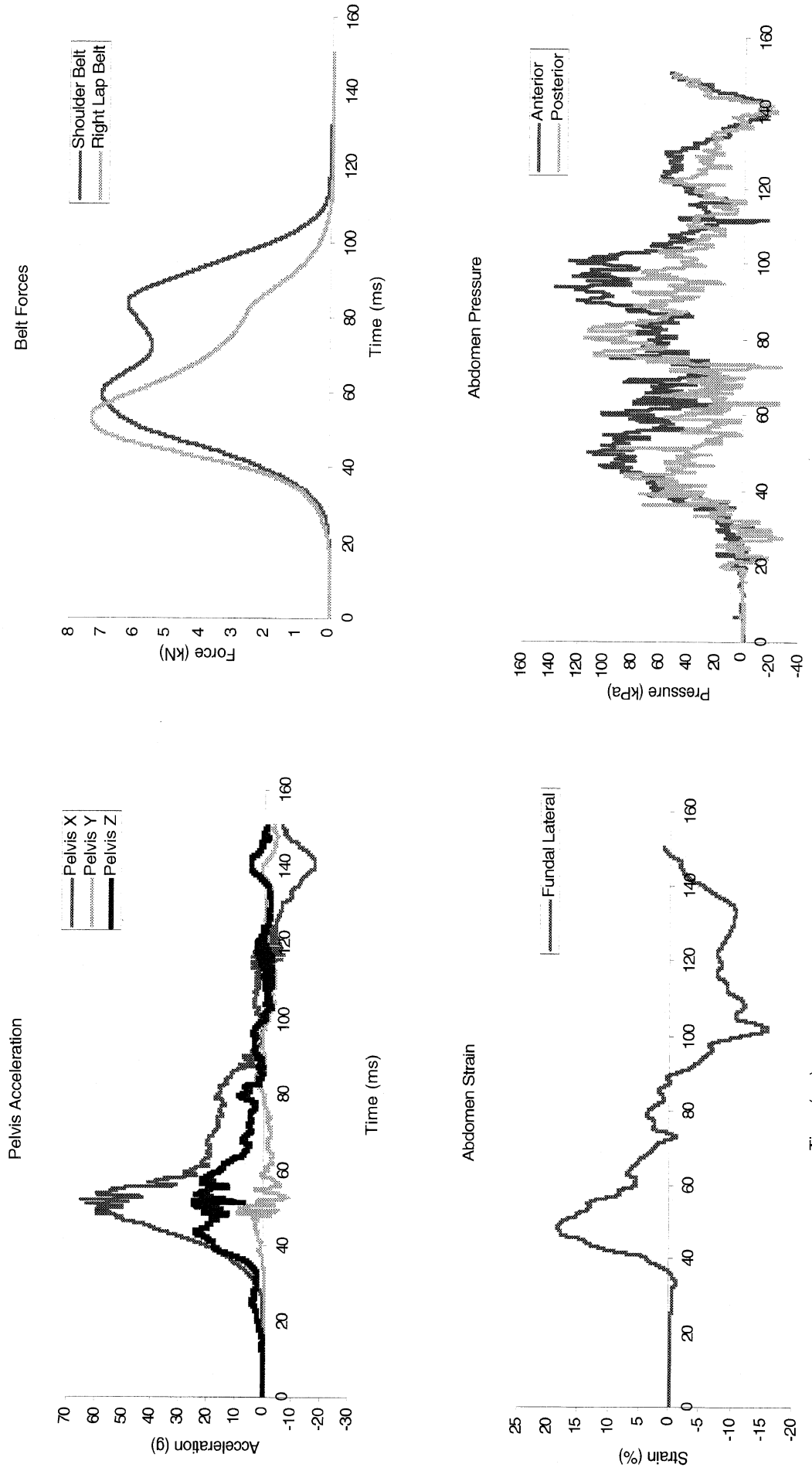

Figure B32. Signals from GMP0007 (Bladder 7). 30 mph/15 g sled test with passenger airbag deployment. Full dummy with jacket and thicker 40-durometer silicone rubber bladder. Restrained by lap and shoulder belts.

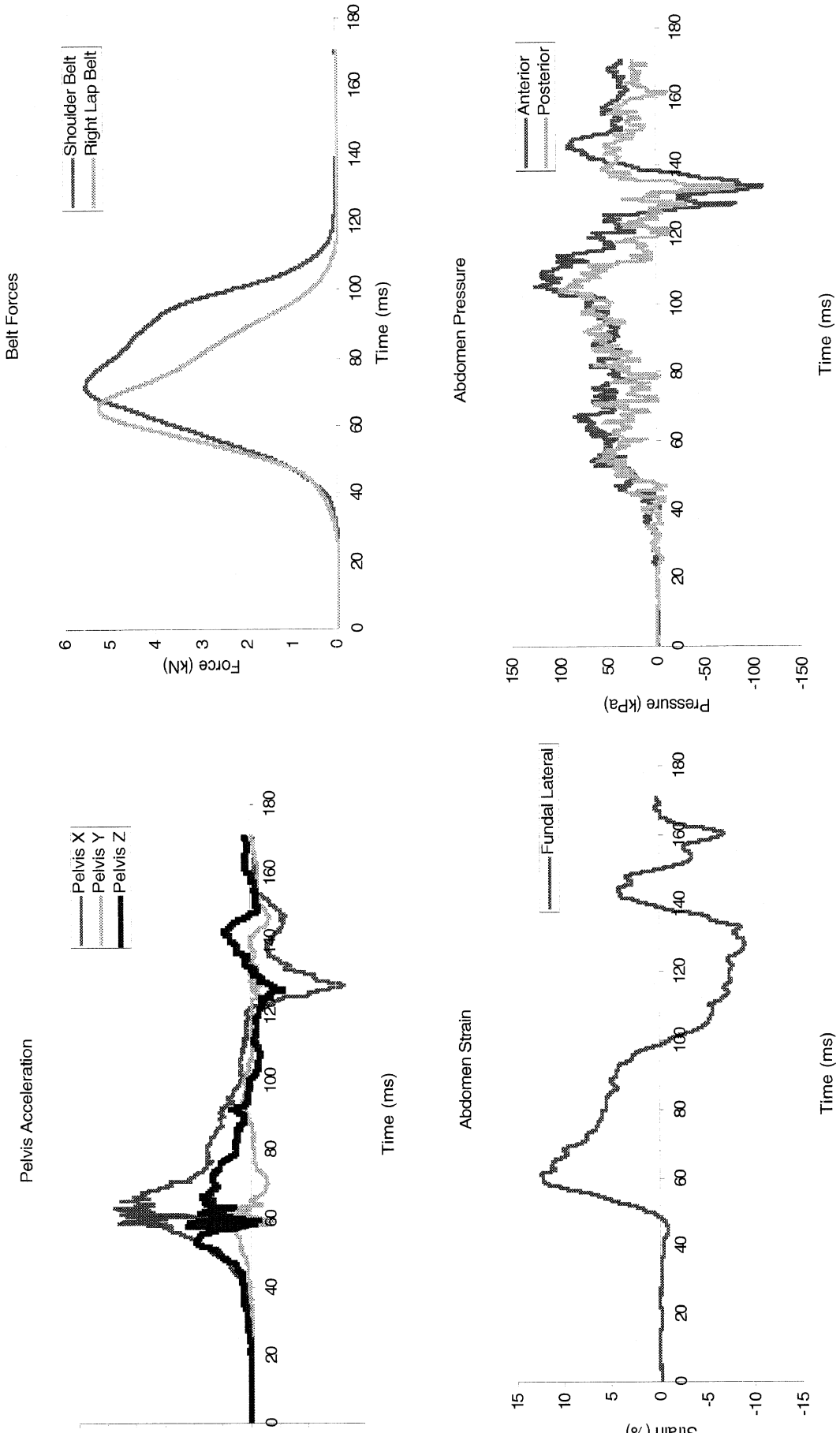

Figure B33. Signals from test GMP0008 (Bladder 7). 20 mph/15 g sled test with passenger airbag deployment. Full dummy with jacket and thicker 40-durometer silicone rubber bladder. Restrained by lap and shoulder belts.

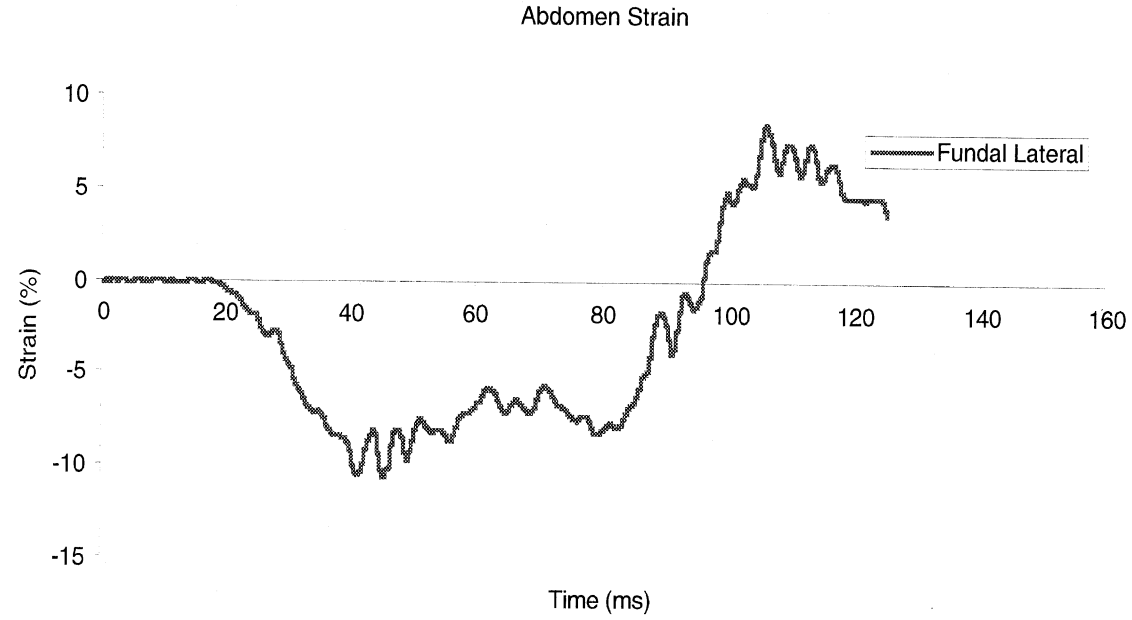

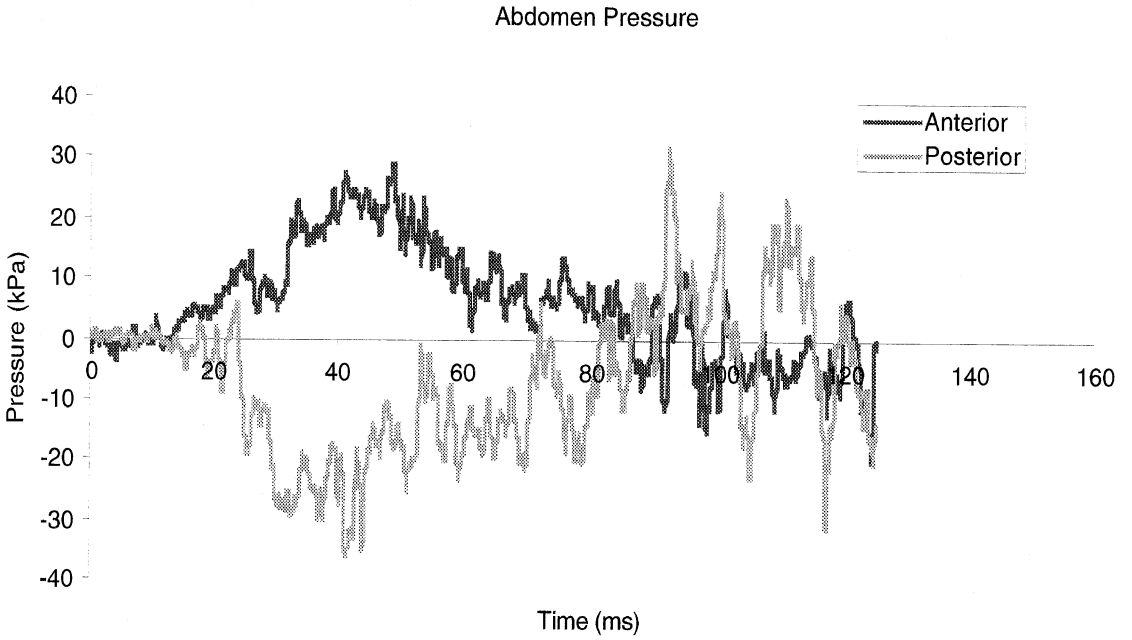

Figure B34. Signals from test GMP0009 (Bladder 7). 21 mph/16 g bladder only test with the abdomen rigidly mounted to the sled and the front of the abdomen restrained by neoprene jacket material.

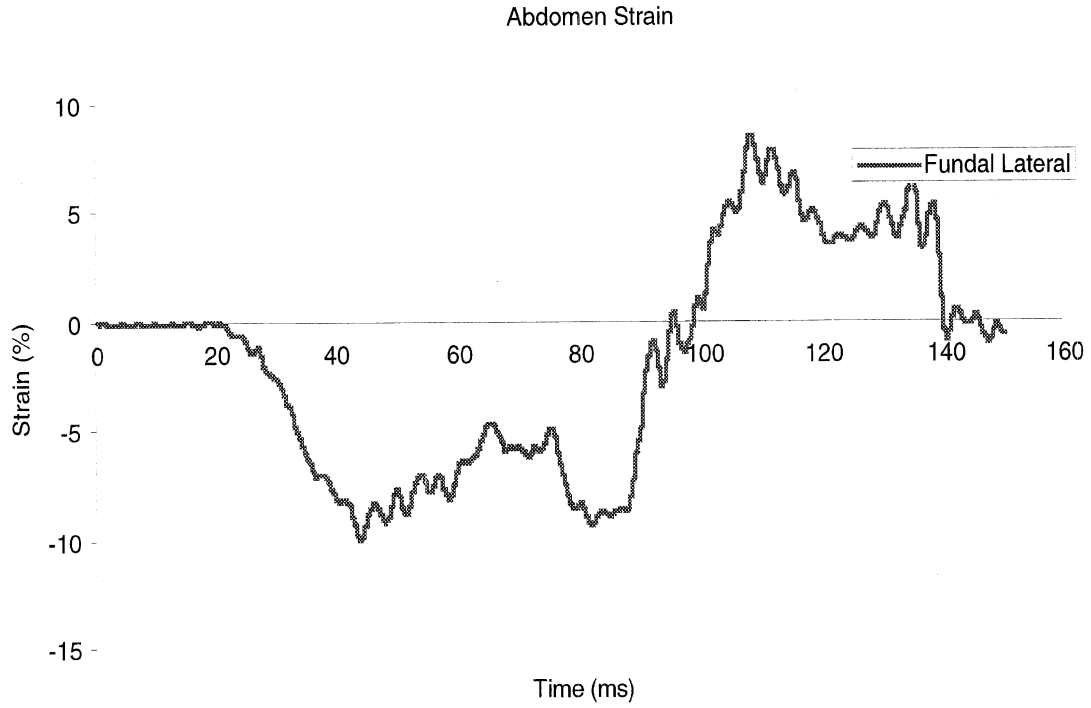

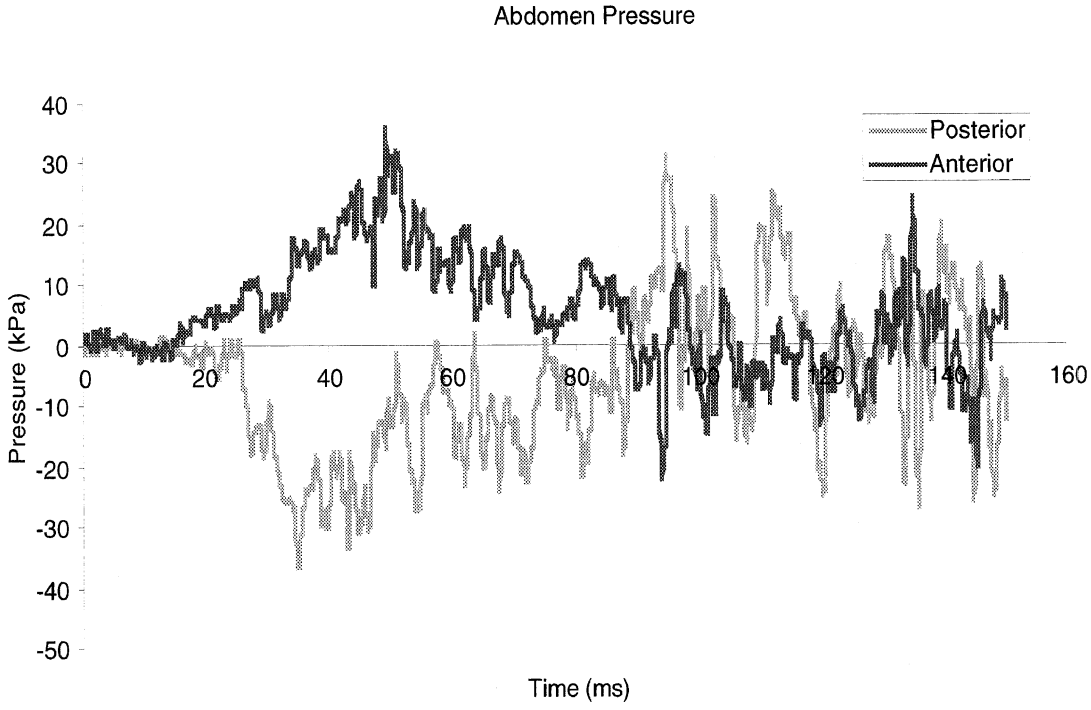

Figure B35. Signals from test GMP0010 (Bladder 7). 20 mph/15 g bladder-only sled test with the abdomen rigidly mounted to the sled and the front of the abdomen unrestrained.

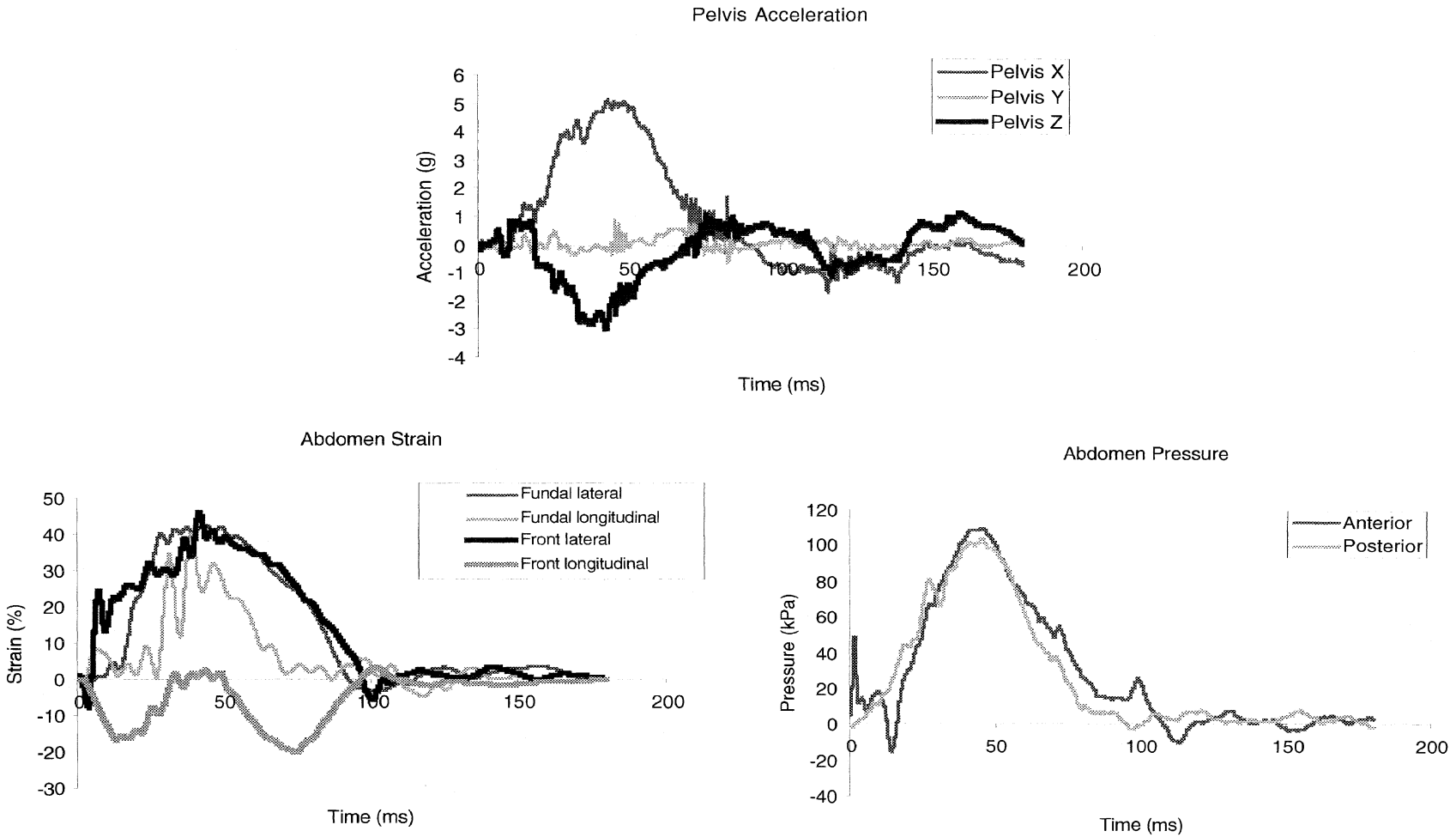

Figure B36. Signals from test GMP0012 (Bladder 8). 4.3 m/s rigid-bar impact. Full dummy with jacket and the 50-durometer silicone abdomen.

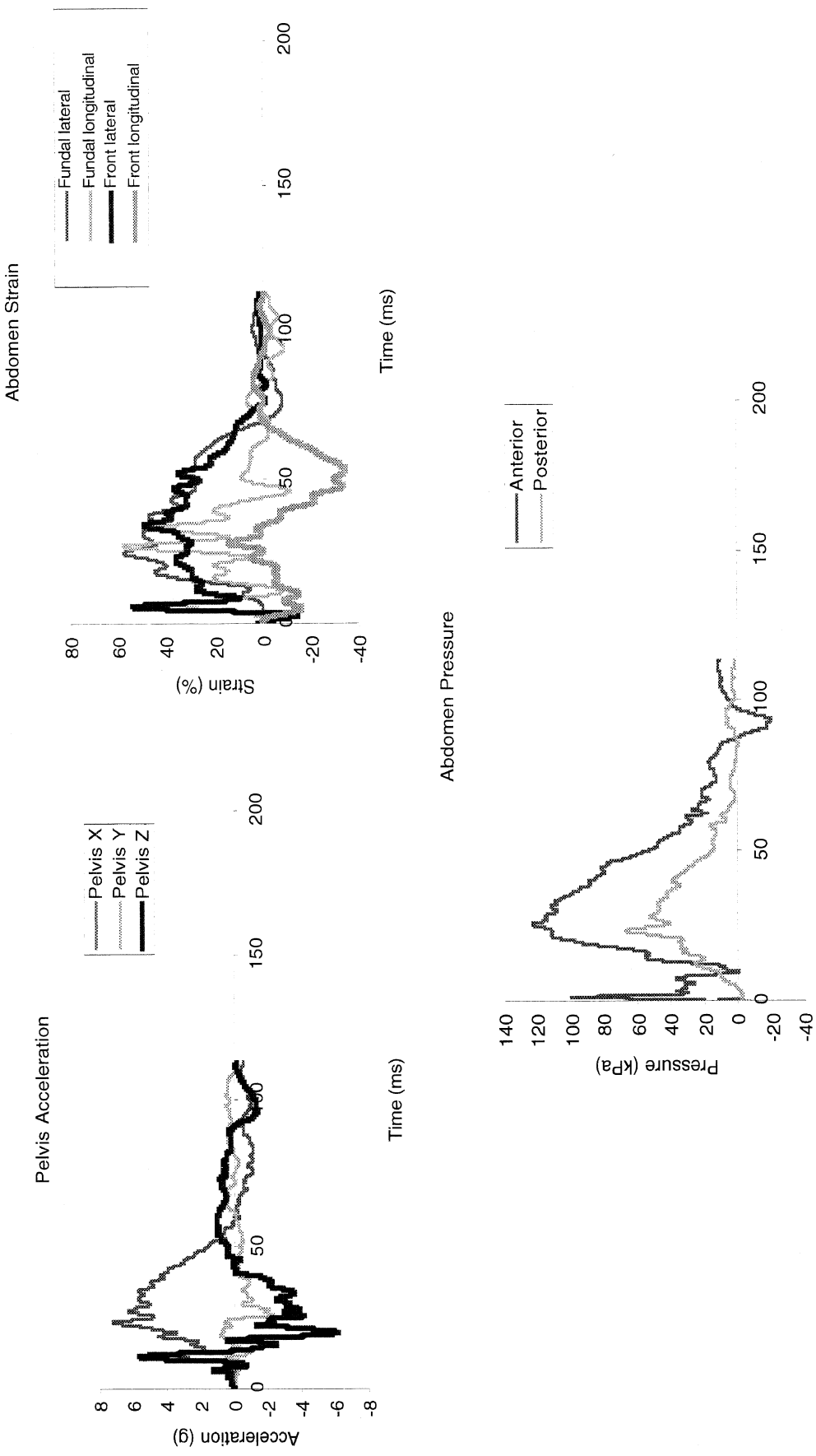

Figure B37. Signals from test GMP0013 (Bladder 8). 6.6 m/s rigid-bar impact. Full dummy with jacket and 50-durometer silicone abdomen.

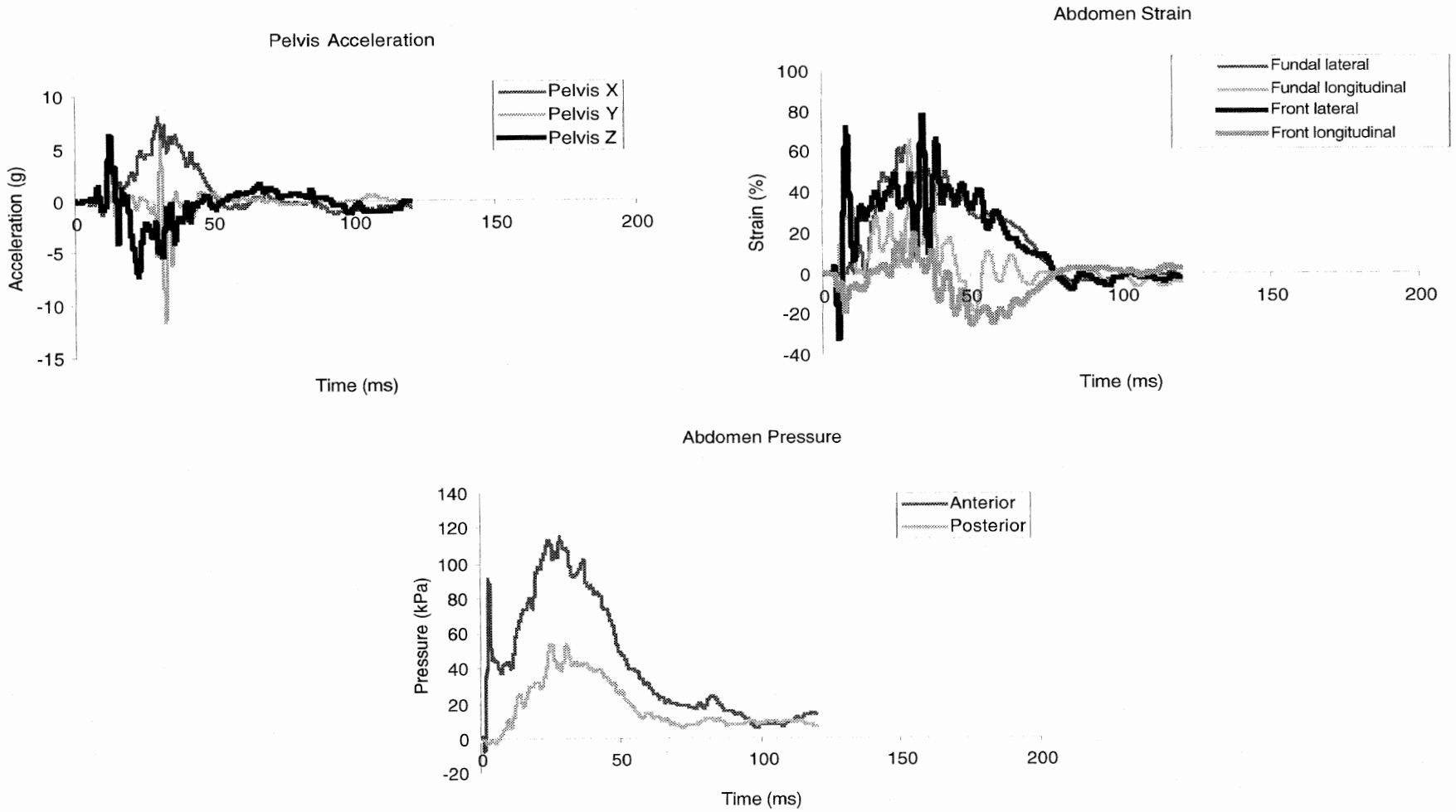

Figure B38. Signals from test GMP0014 (Bladder 8). 6.5 m/s rigid-bar impact. Full dummy without jacket and with the 50-durometer silicone abdomen.

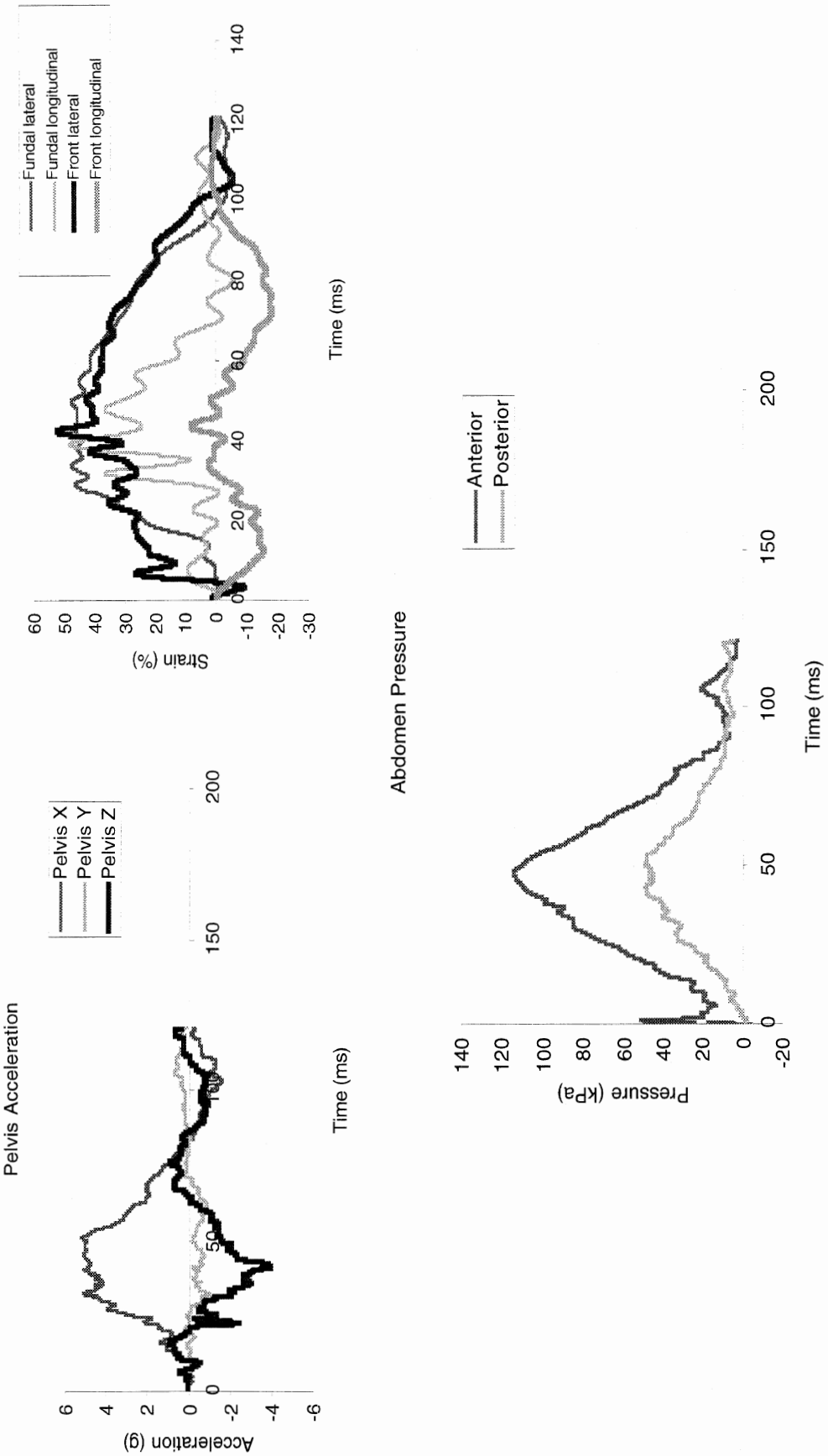

Figure B39. Signals from test GMP0015 (Bladder 8). 4.7 m/s rigid-bar impact test. Full dummy without jacket and with the 50-durometer silicone abdomen.

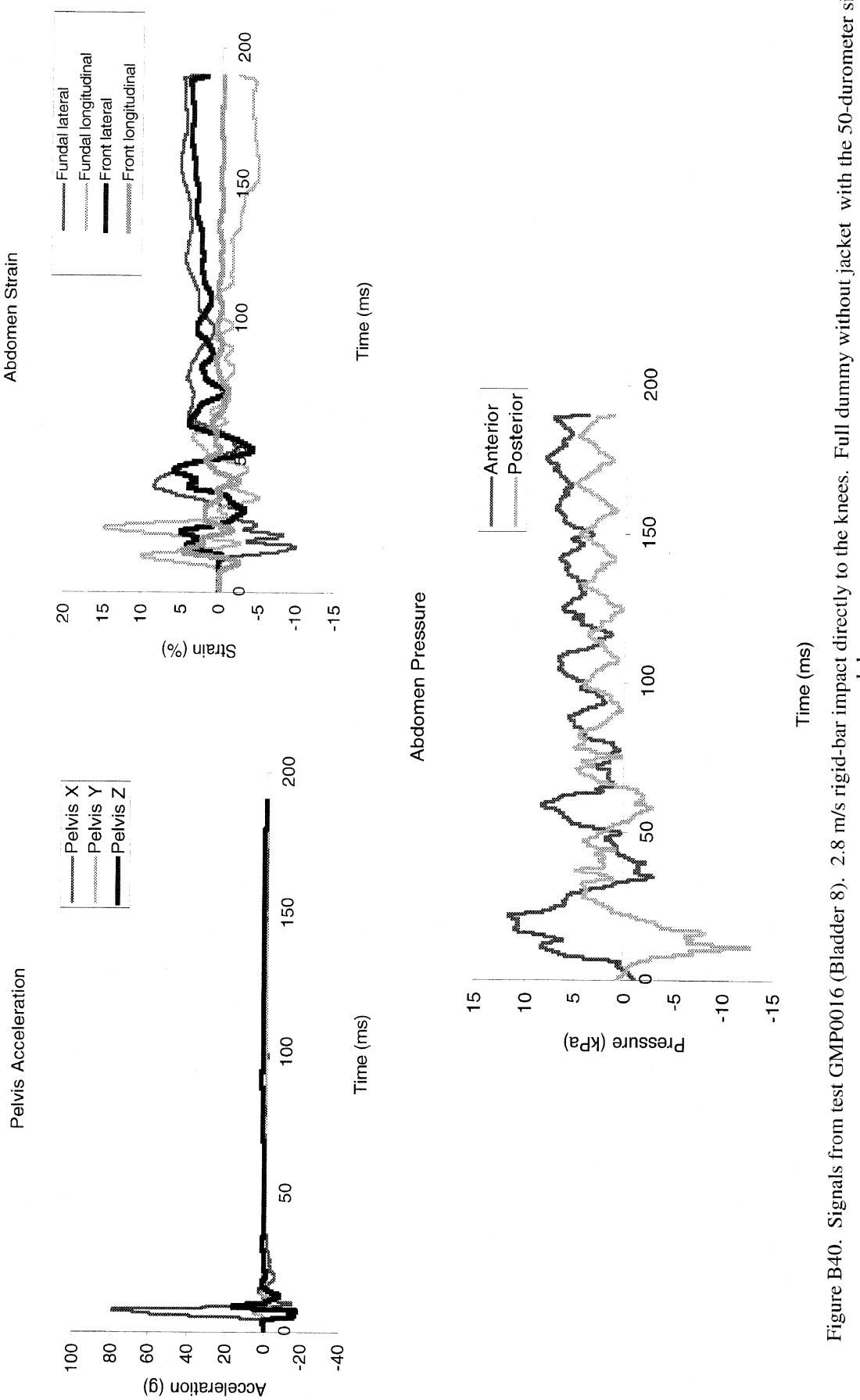

Figure B40. Signals from test GMP0016 (Bladder 8). 2.8 m/s rigid-bar impact directly to the knees. Full dummy without jacket with the 50-durometer silicone abdomen.

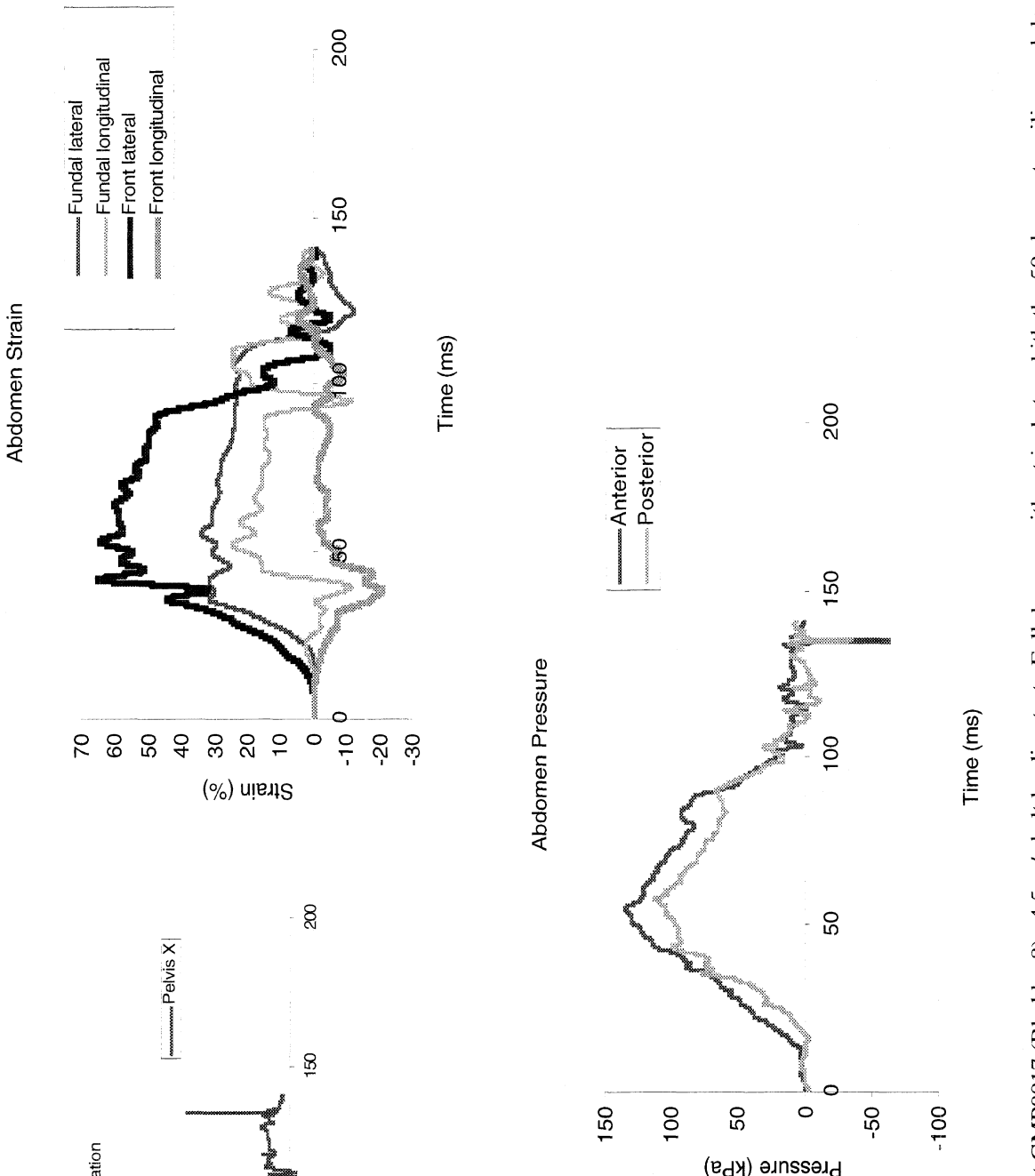

Figure B41. Signals from test GMP0017 (Bladder 8). 4.5 m/s belt loading test. Full dummy without jacket and ith the 50-durometer silicone abdomen.

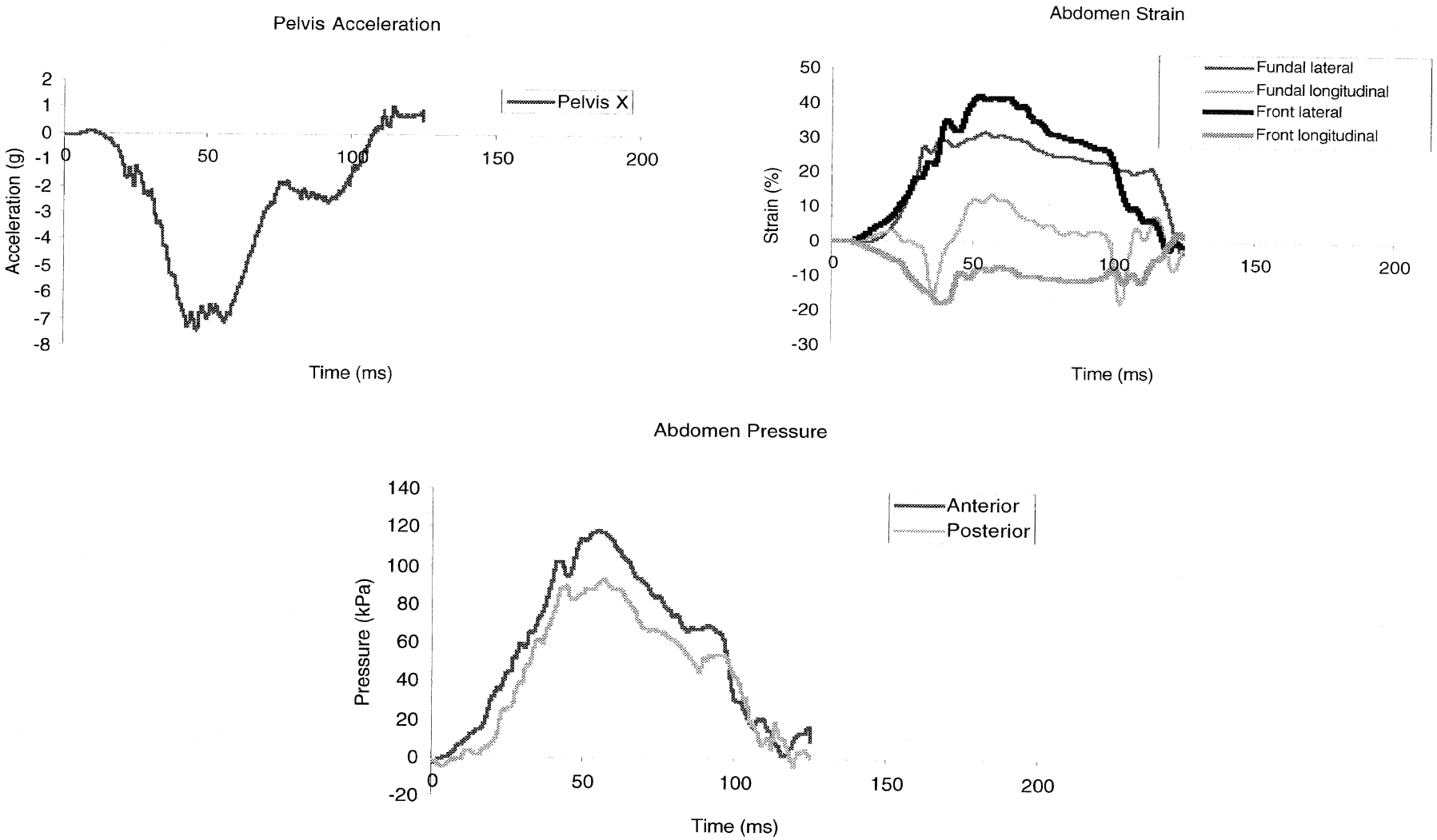

Figure B42. Signals from test GMP0018. 3.0 m/s belt loading test. Full dummy with jacket.

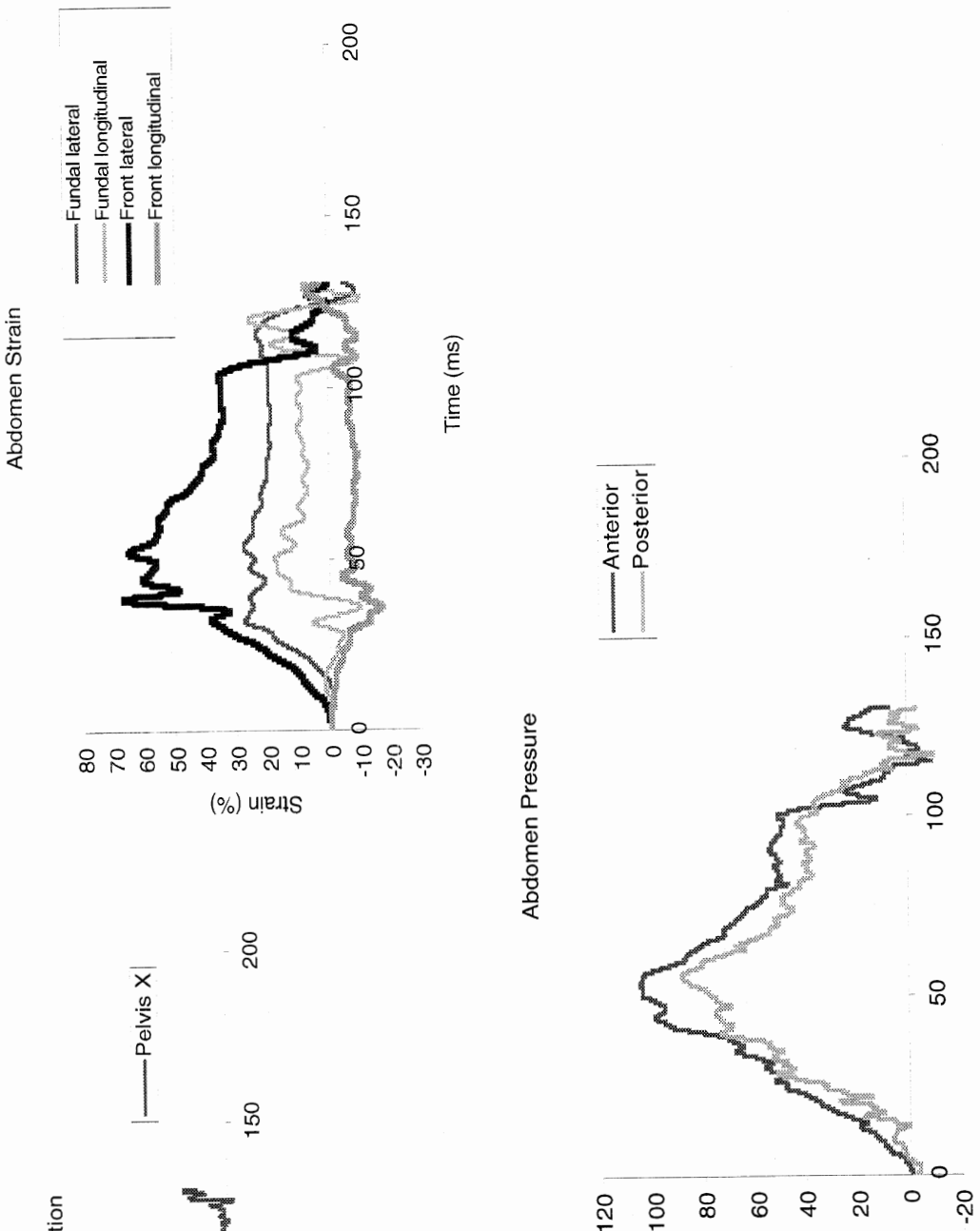

Figure B43. Signals from test GMP0019 (Bladder 8). 3.0 m/s belt loading test. Full dummy without chest jacket

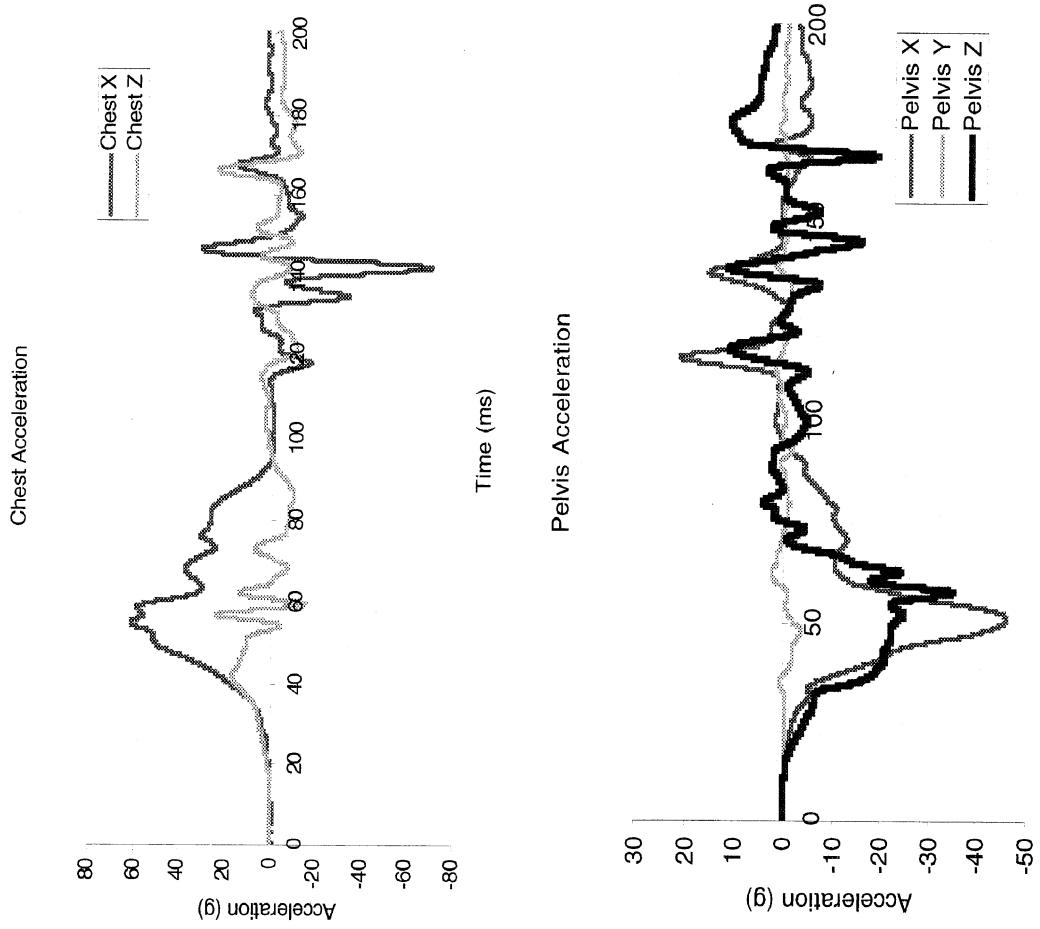

Figure B44. Accelerations from test GMP0026 (Bladder 8). 20 mph/15 g sled test with airbag deployment. Full dummy with jacket and the thick 50-durometer silicone rubber bladder. Restrained by lap and shoulder belts.

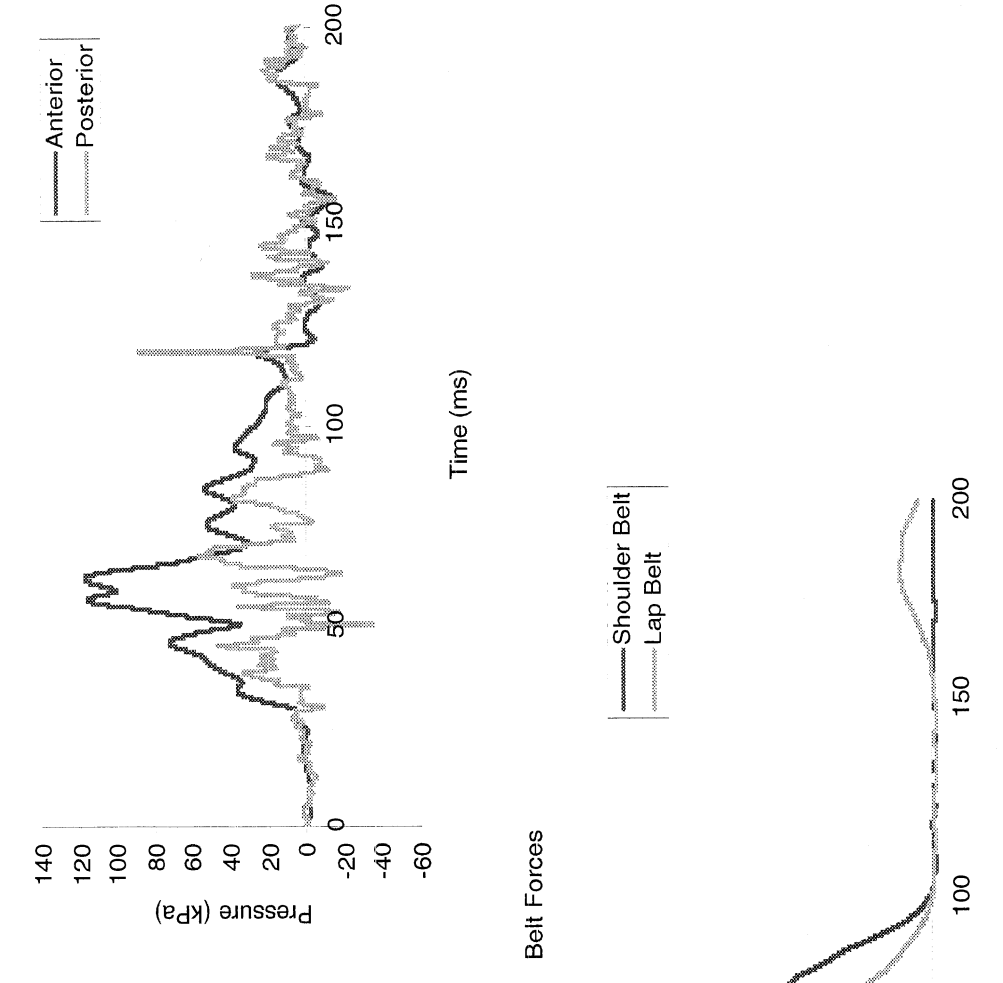

Figure B45. Signals from test GMP0026 (Bladder 8). 20 mph/15 g sled test with airbag deployment. Full dummy with jacket and thick 50-durometer silicone rubber bladder. Restrained by lap and shoulder belts.

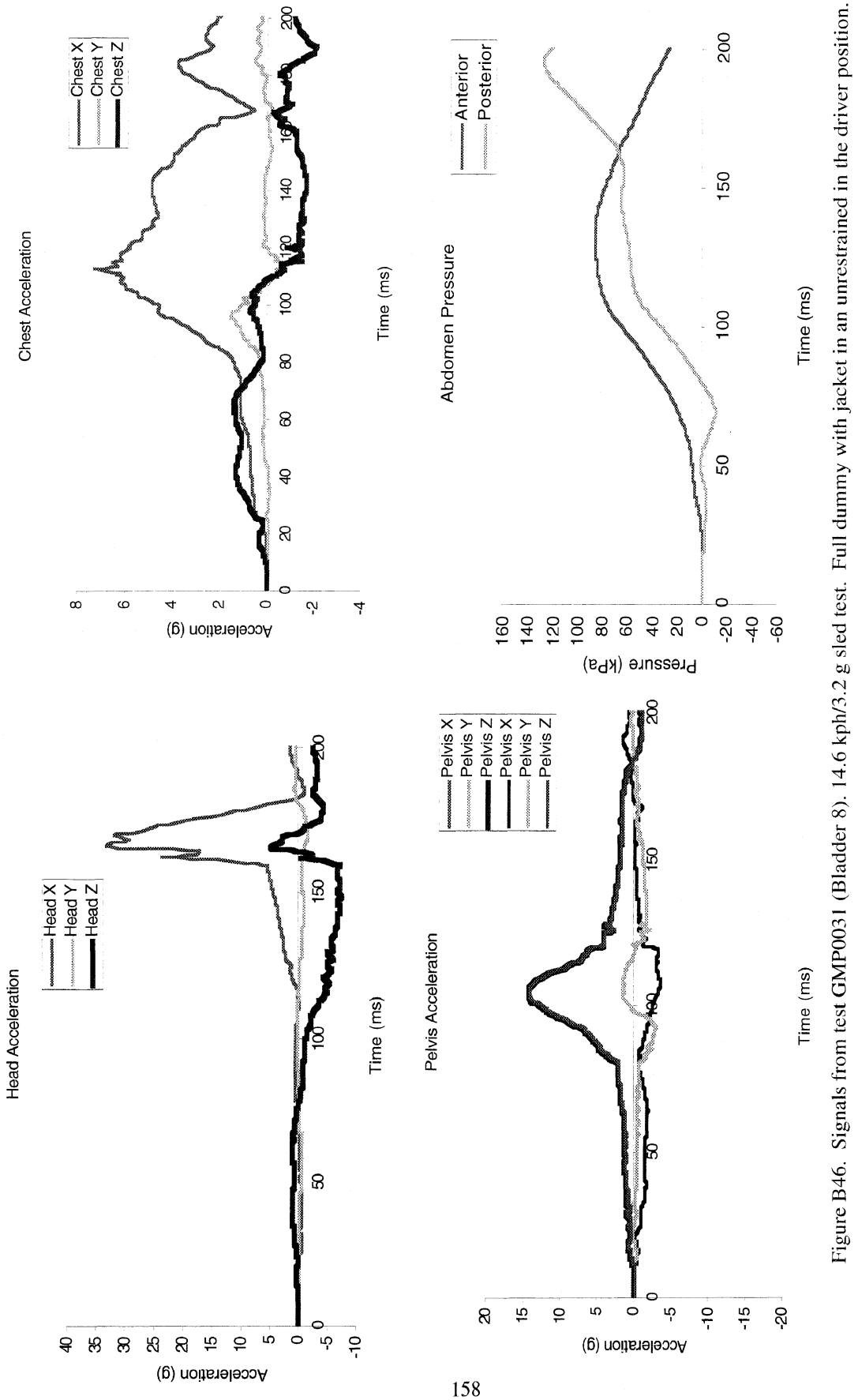

Figure B46. Signals from test GMP0031 (Bladder 8). 14.6 kph/3.2 g sled test. Full dummy with jacket in an unrestrained in the driver position.

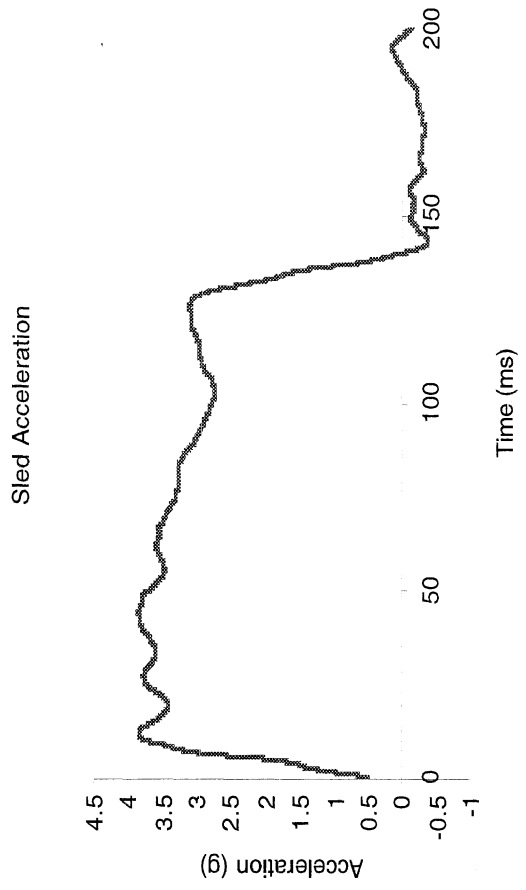

Figure B47. Sled acceleration from test GMP003114.6 kph/3.2 g sled test. Full dummy with jacket in an unrestrained in the driver position.

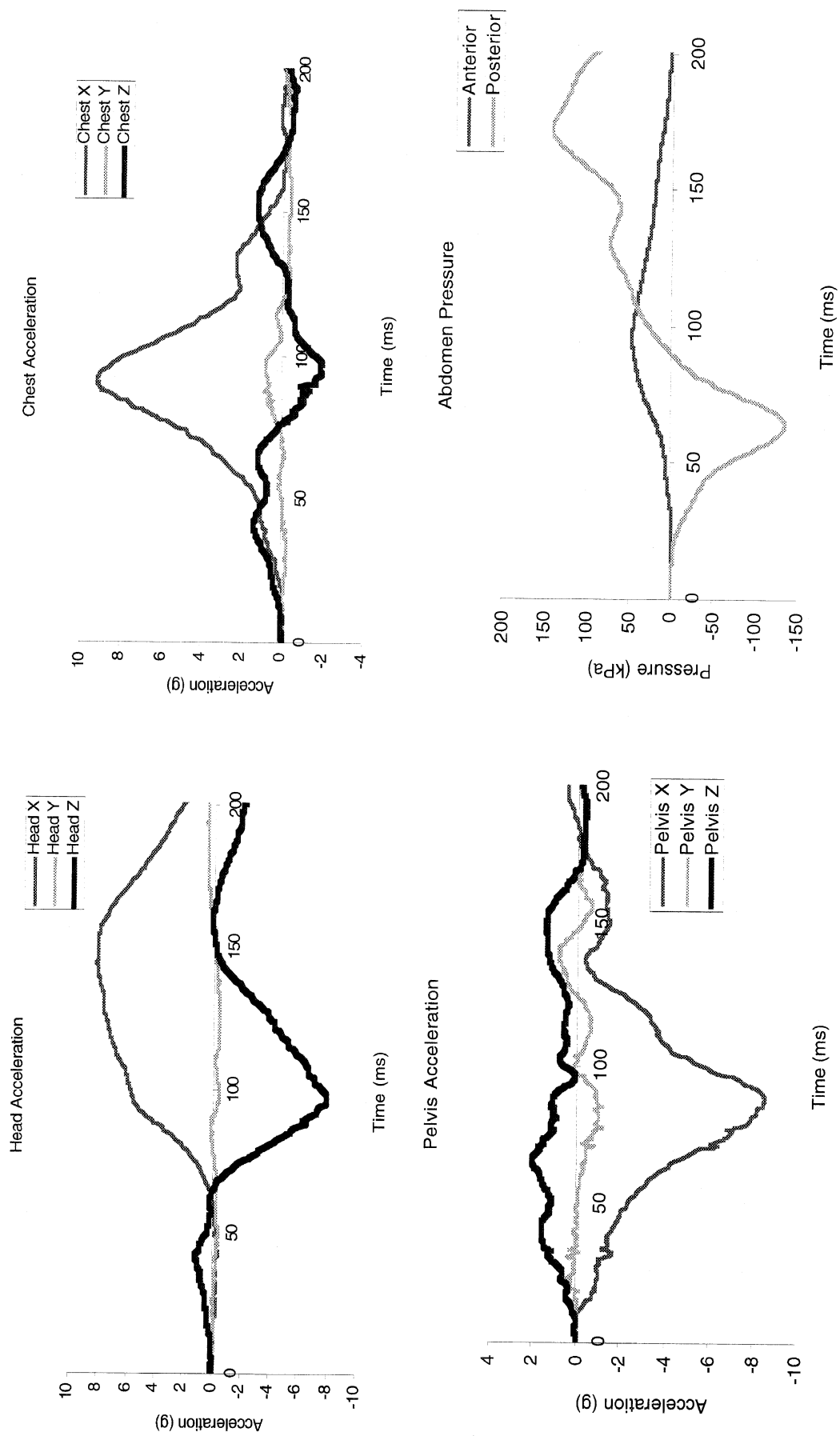

Figure B48. Signals from test GMP0032. 14.8 kph/3.7 g sled test. Full dummy with jacket restrained in the driver position with a three-point belt.

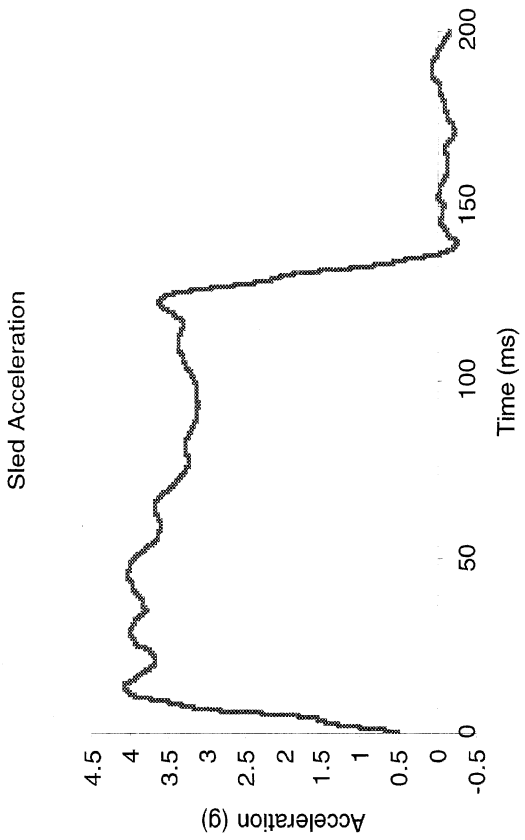

Figure B49. Sled accelerations from test GMP0032. 14.8 kph/3.7 g sled test. Full dummy with jacket restrained in the driver position with a three-point belt.

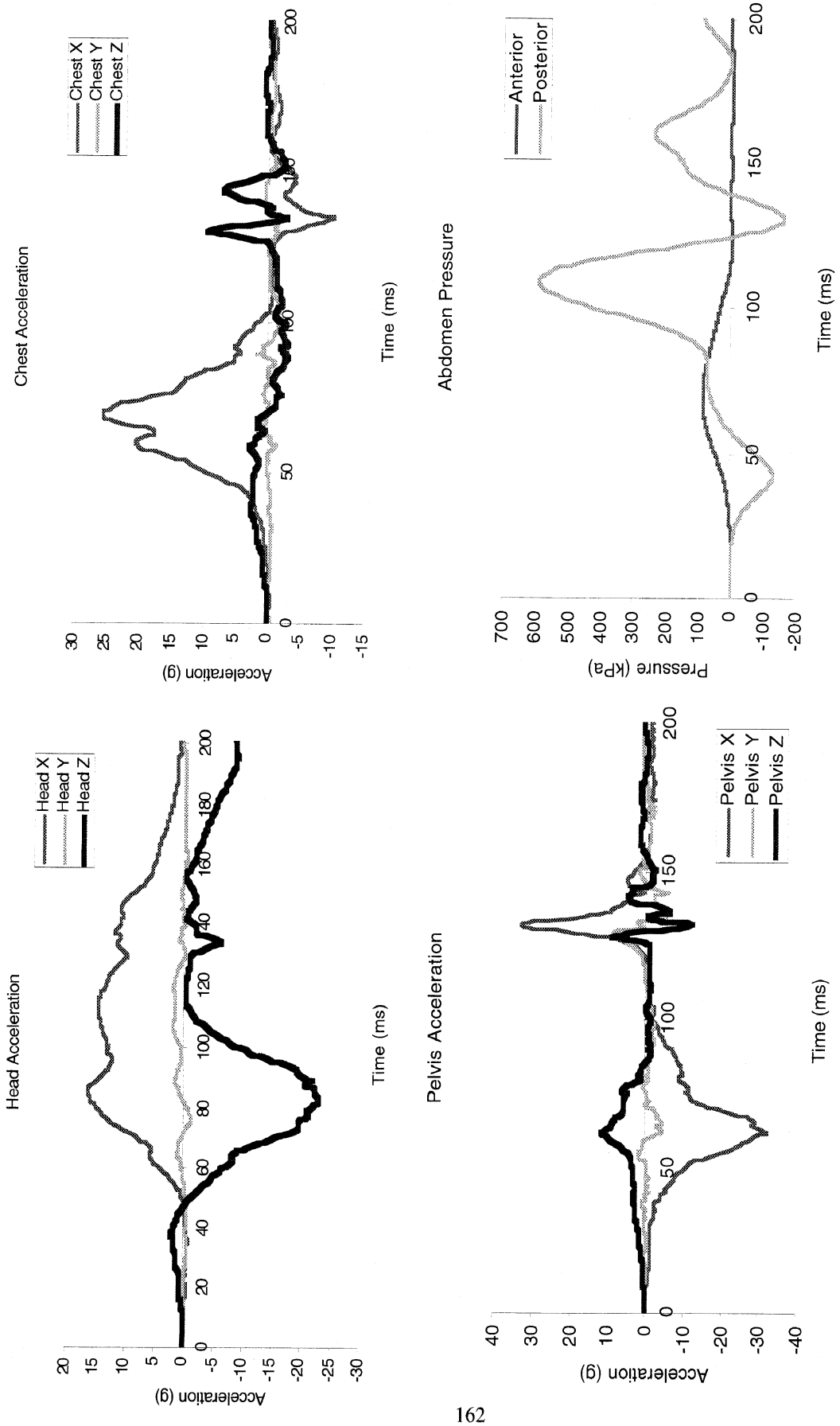

Figure B50. Signals from test GMP0033 (Bladder 8). 23.0 kph/8.6 g sled test. Full dummy with jacket in the driver position restrained by a three-point belt.

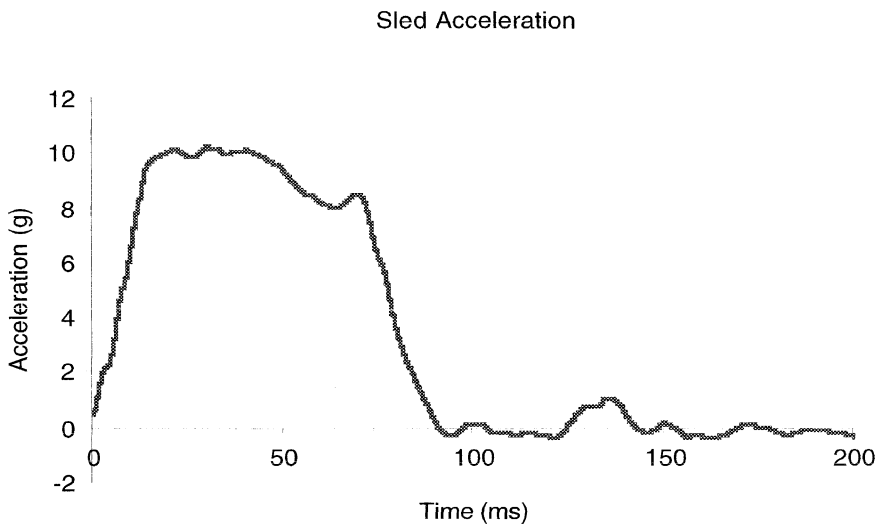

Figure B51. Sled acceleration from test GMP0033 (Bladder 8). 23.0 kph/8.6 g sled test. Full dummy with jacket in the driver position restrained by a three-point belt.

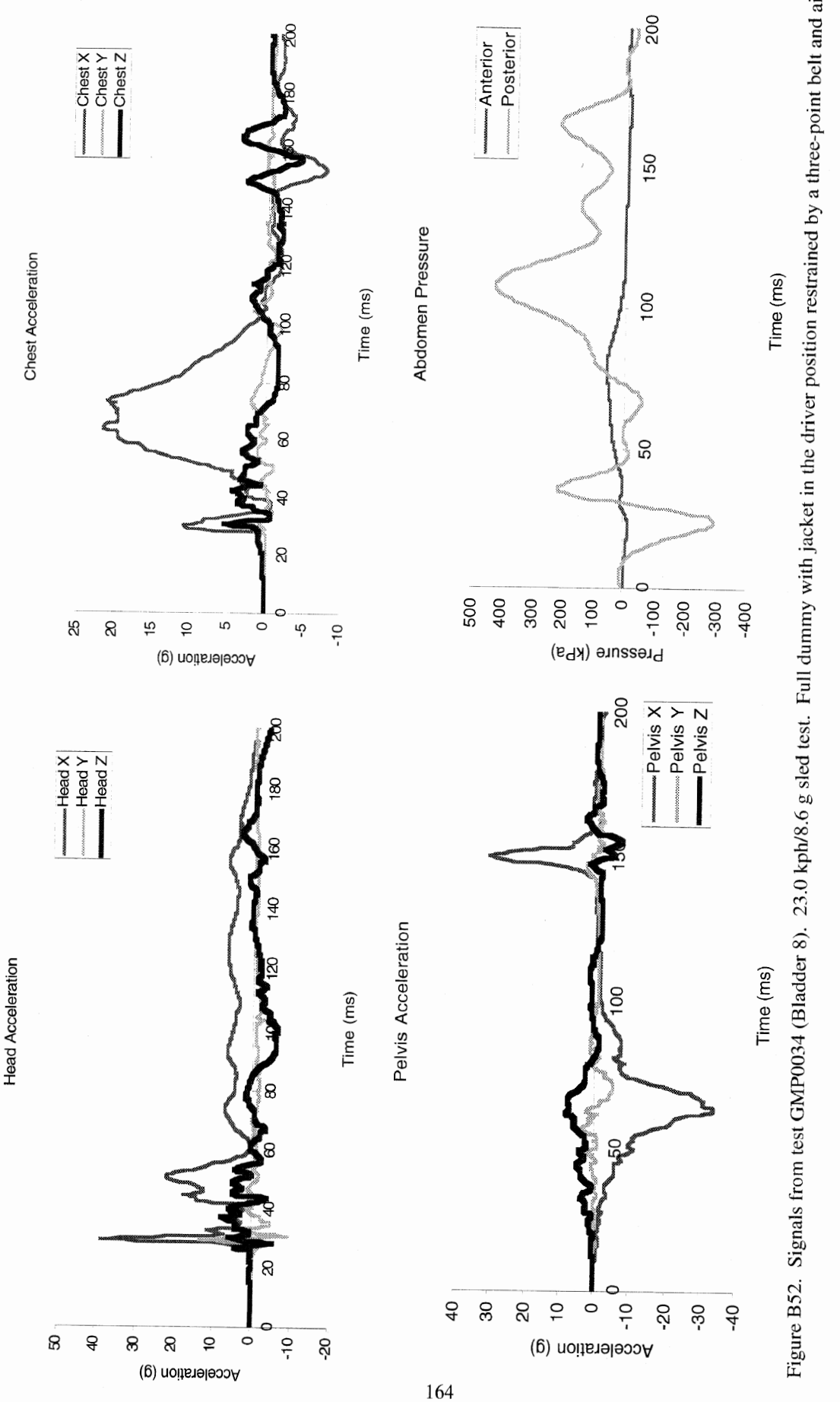

Figure B52. Signals from test GMP0034 (Bladder 8). 23.0 kph/8.6 g sled test. Full dummy with jacket in the driver position restrained by a three-point belt and airbag.

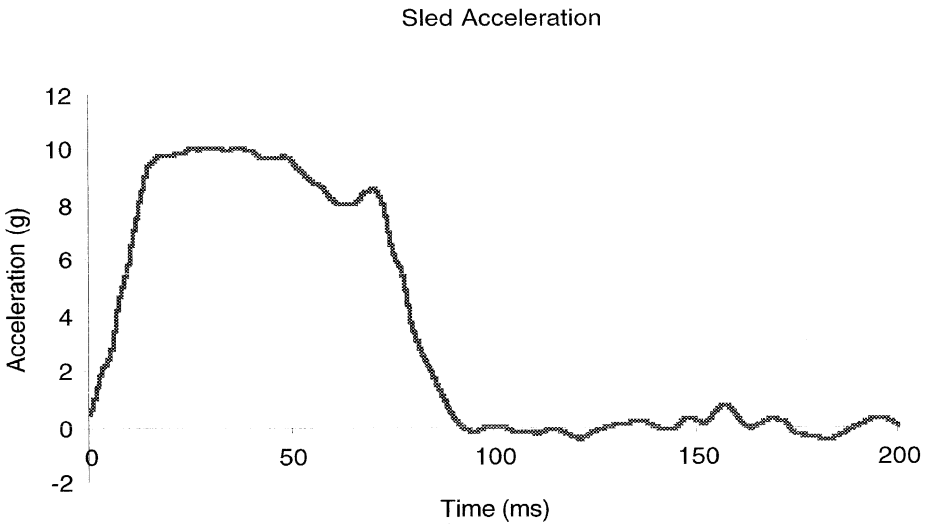

Figure B53. Sled acceleration from test GMP0034 (Bladder 8). 23.0 kph/8.6 g sled test. Full dummy with jacket in the driver position restrained by a three-point belt and airbag.

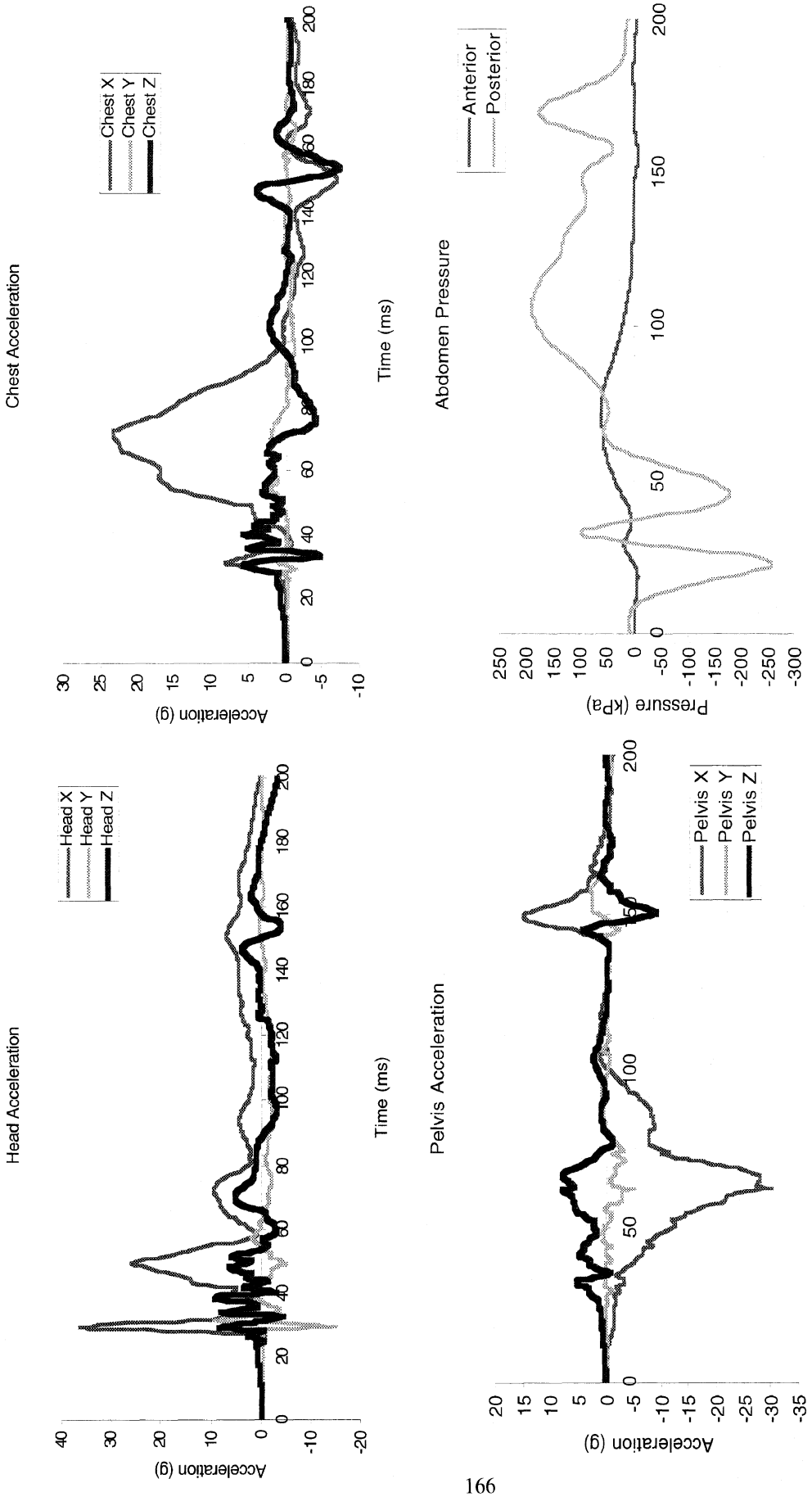

Figure B54. Signals from test GMP0035 (Bladder 8). 23.0 kph/8.6 g sled test. Full dummy with jacket in the driver position restrained by a three-point belt and airbag.

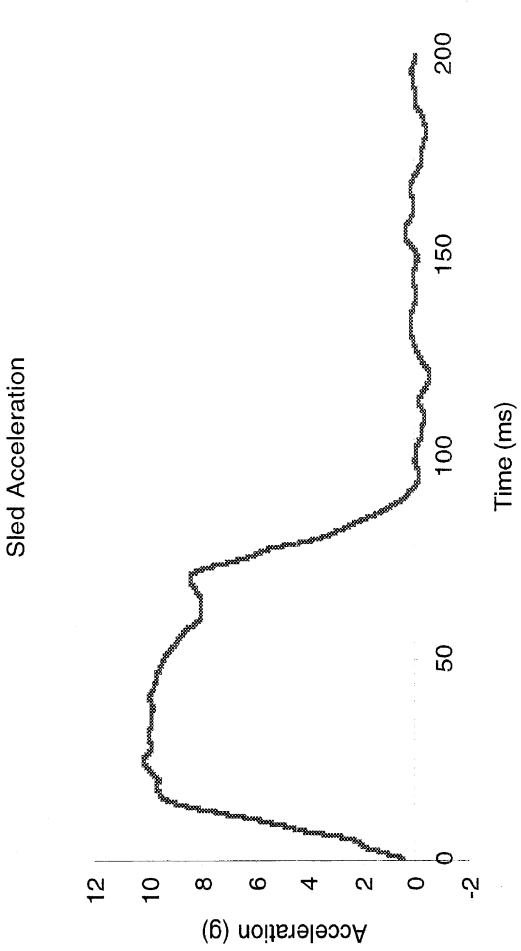

Figure B55. Sled acceleration from test GMP0035 (Bladder 8). 23.0 kph/8.6 g sled test. Full dummy with jacket in the driver position restrained by a three-point belt and airbag.

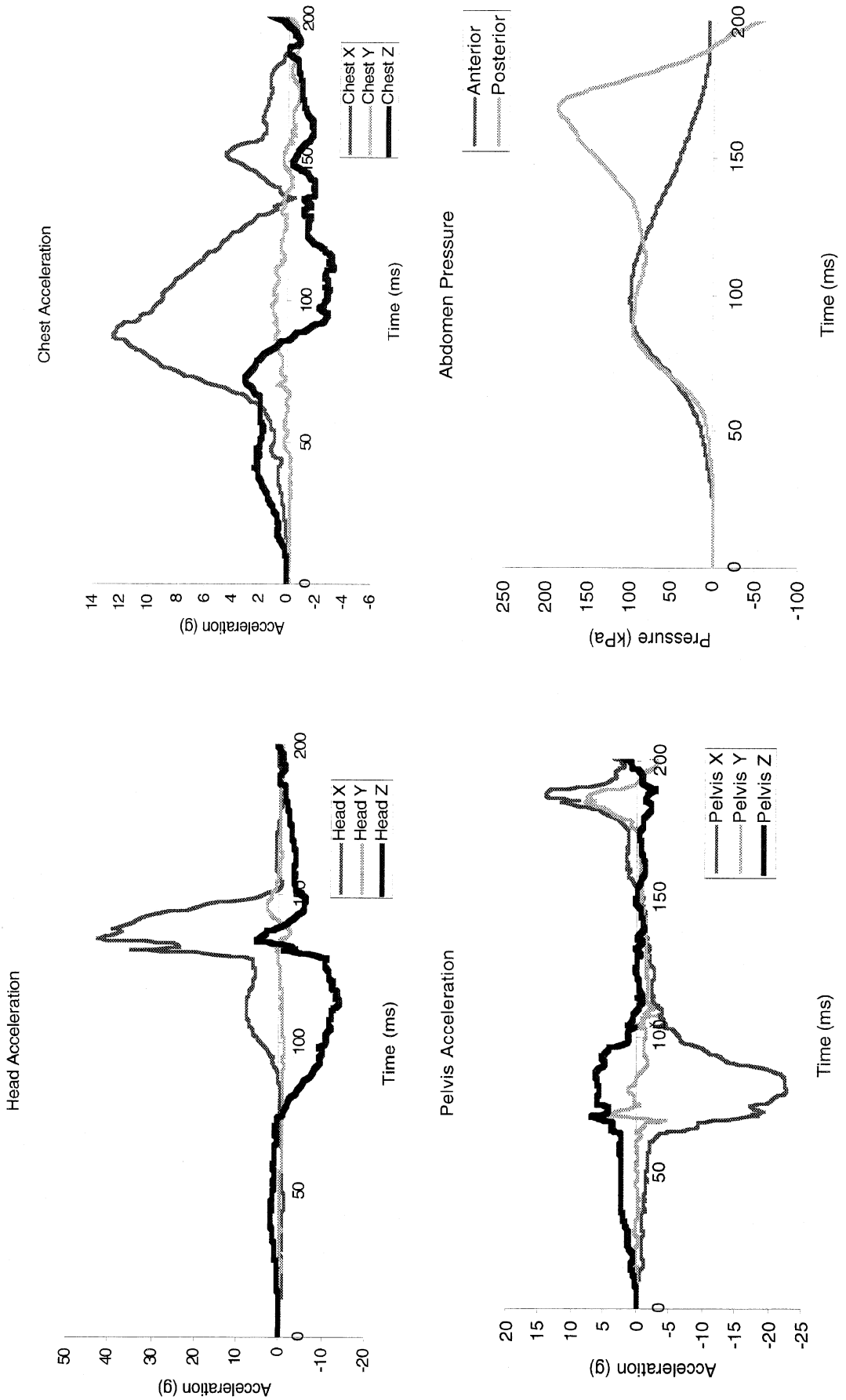

Figure B56. Signals from test GM 0036 (Bladder 8). 19.4 kph/5.6 g sled test. Full dummy with jacket in an unrestrained driver position.

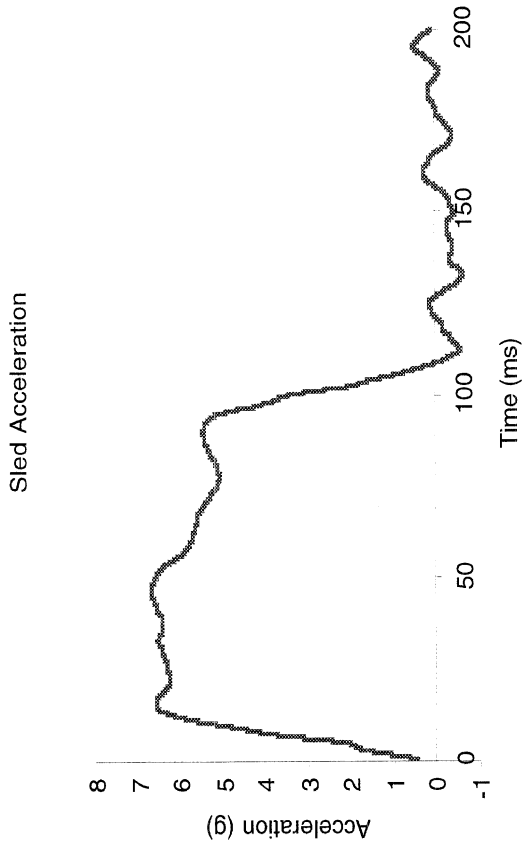

Figure B57. Sled acceleration from test GMP0036 (Bladder 8). 19.4 kph/5.6 g sled test. Full dummy with jacket in an unrestrained driver position.

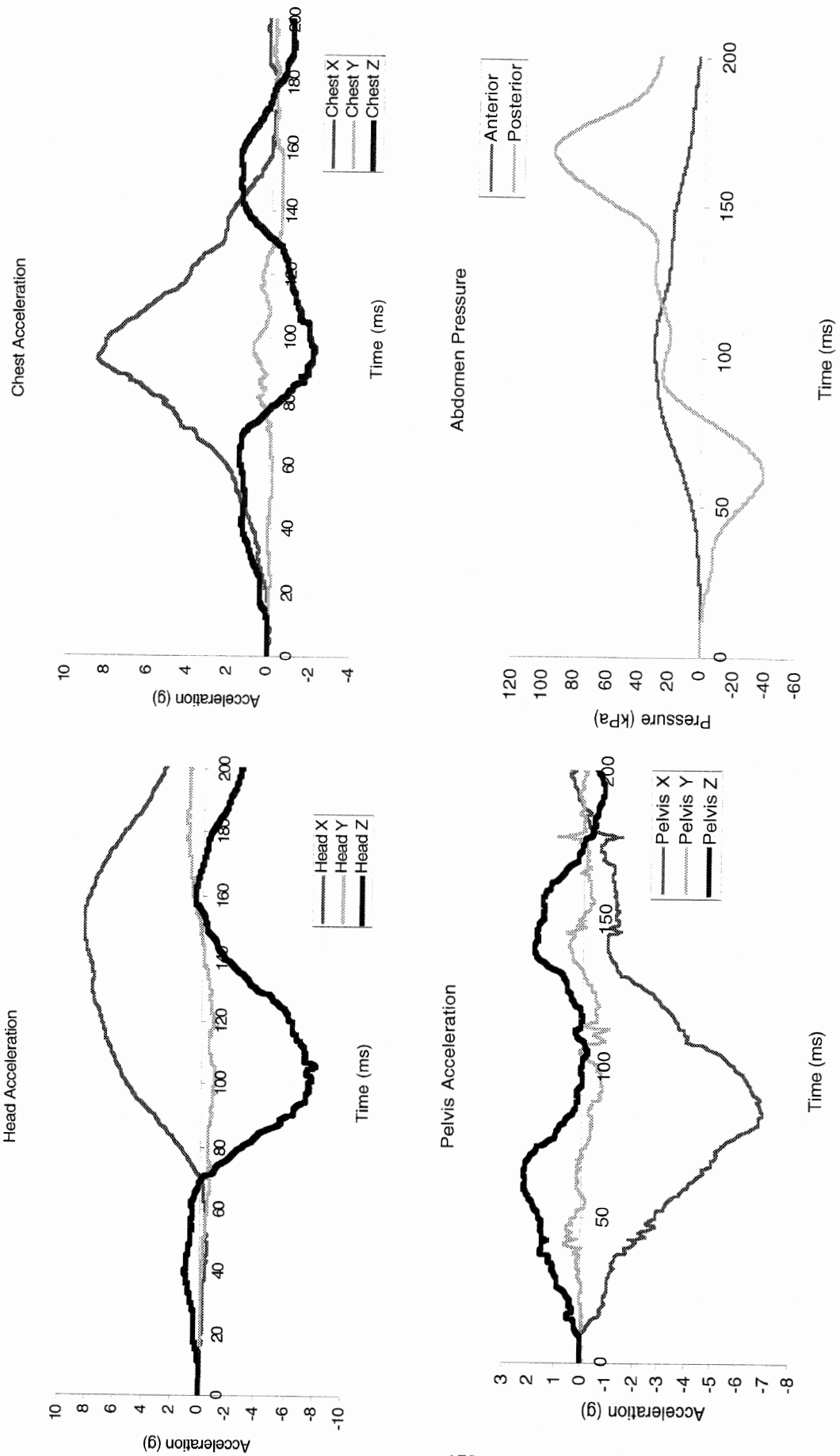

Figure B58. Signals from test GMP0037 (Bladder 8). 15.0 kph/3.3 g sled test. Full dummy with jacket in the passenger position restrained by a three-point belt.

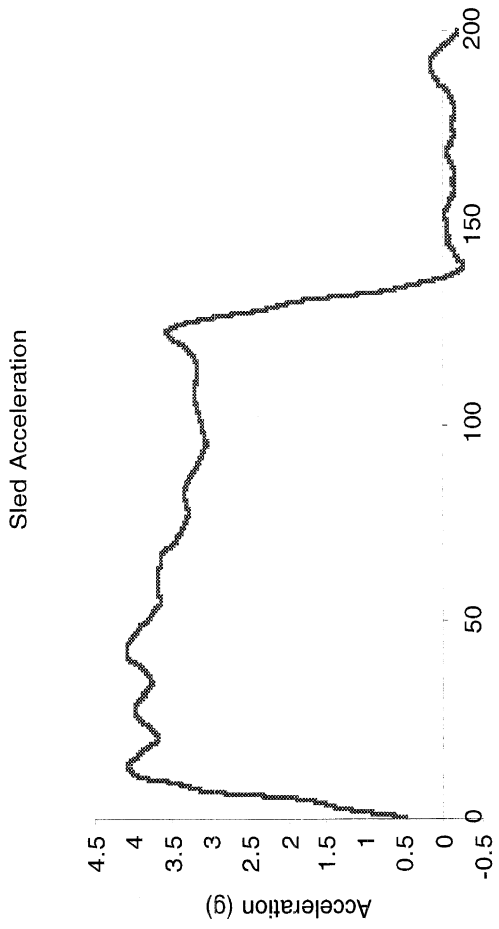

Figure B59. Sled acceleration from test GMP0037 (Bladder 8). 15.0 kph/3.3 g sled test. Full dummy with jacket in the passenger position restrained by a three-point belt.

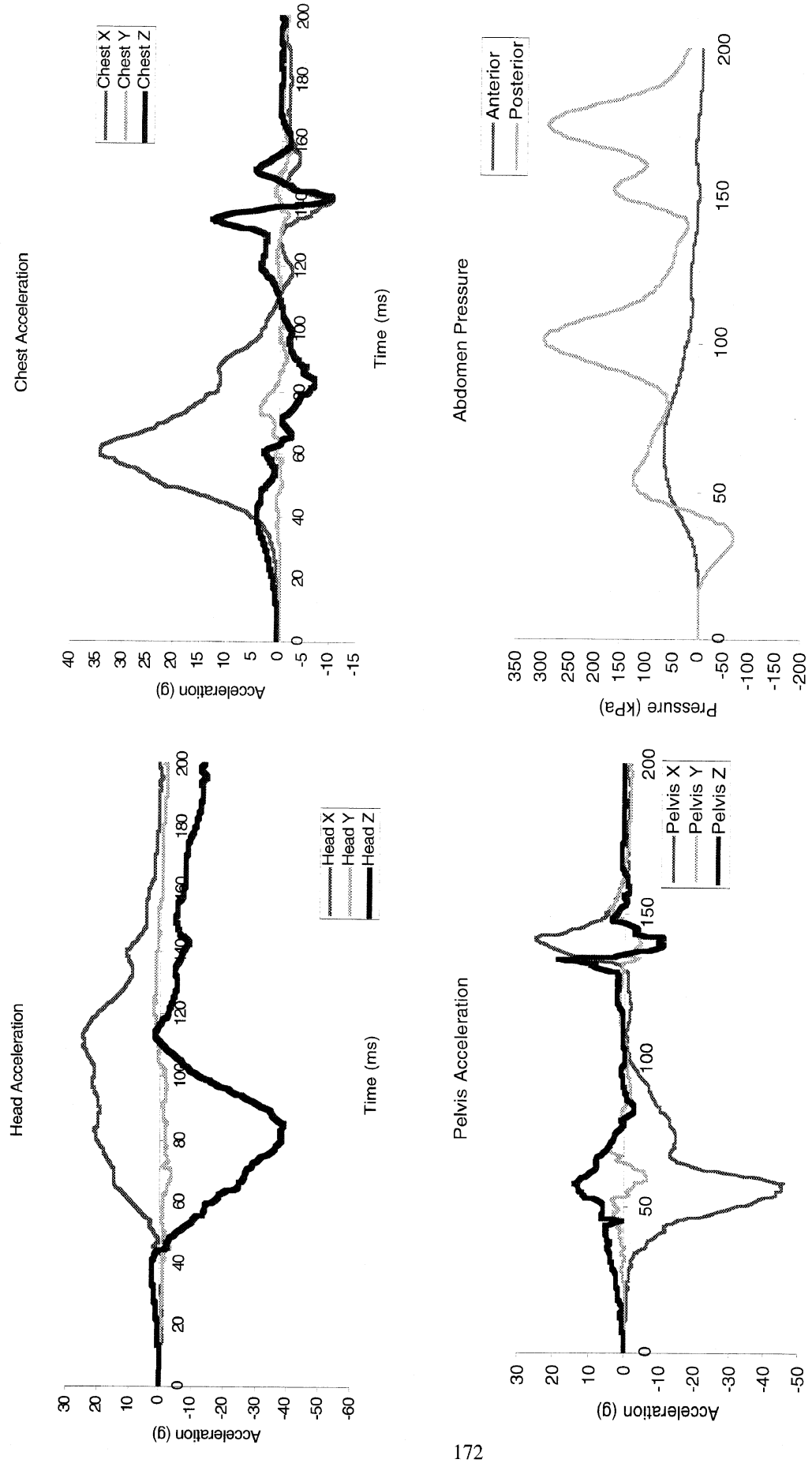

Figure B60. Signals from test GMP0038 (Bladder 8). 34.3 kph/12 g sled test. Full dummy in jacket in the passenger position restrained by a three-point belt.

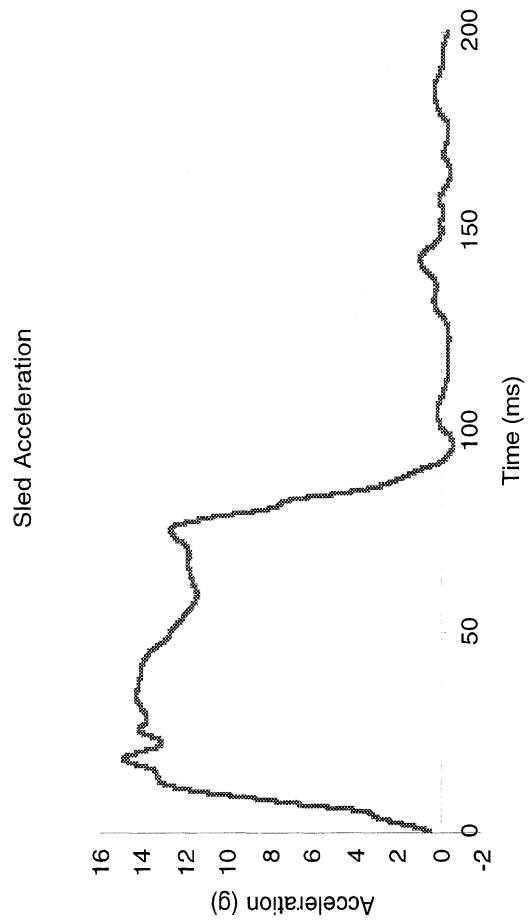

Figure B61. Sled acceleration from test GMP0038 (Bladder 8). 34.3 kph/12 g sled test. Full dummy in jacket in the passenger position restrained by a three-point belt.

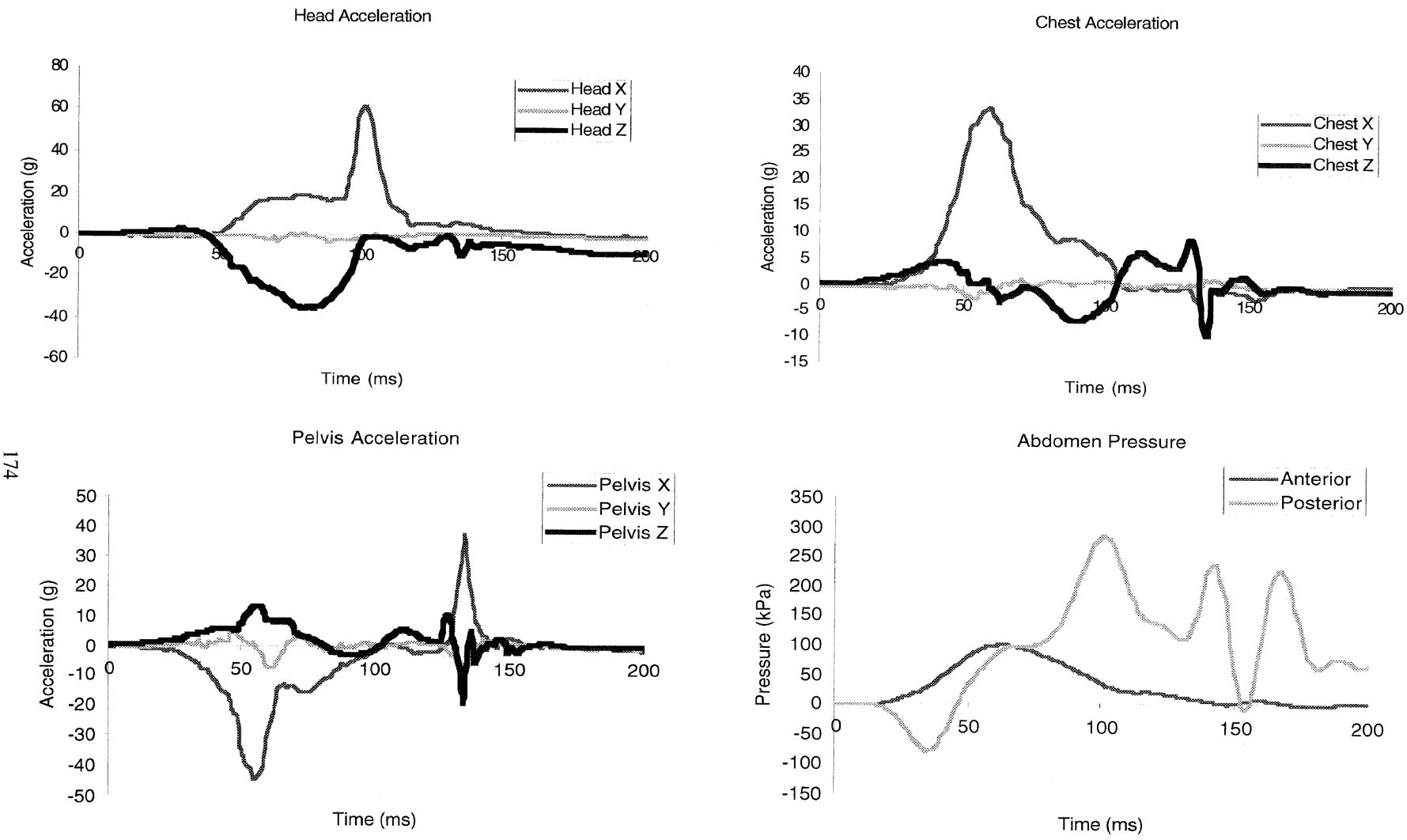

Figure B62. Signals from test GMP0039 (Bladder 8). 34.4 kph/12 g sled test. Full dummy with jacket in the driver position restrained by a three-point belt.

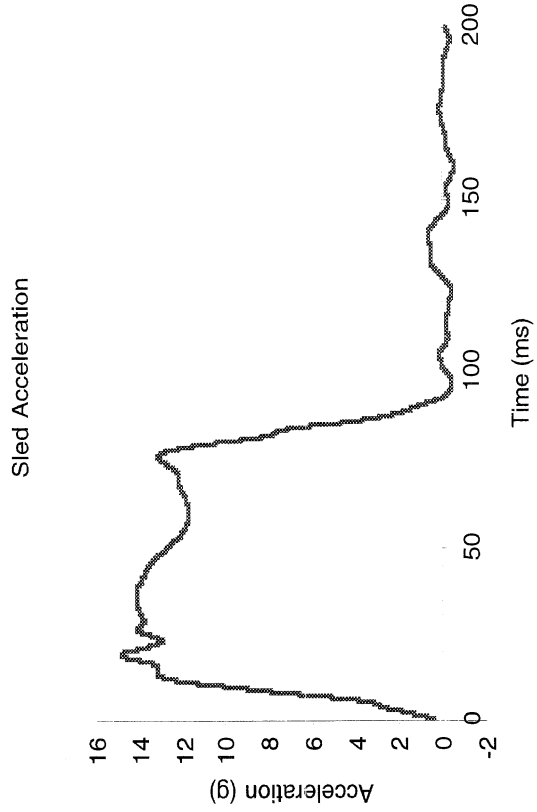

Figure B63. Sled acceleration from test GMP0039 (Bladder 8). 34.4 kph/12 g sled test. Full dummy with jacket in the driver position restrained by a three-point belt.

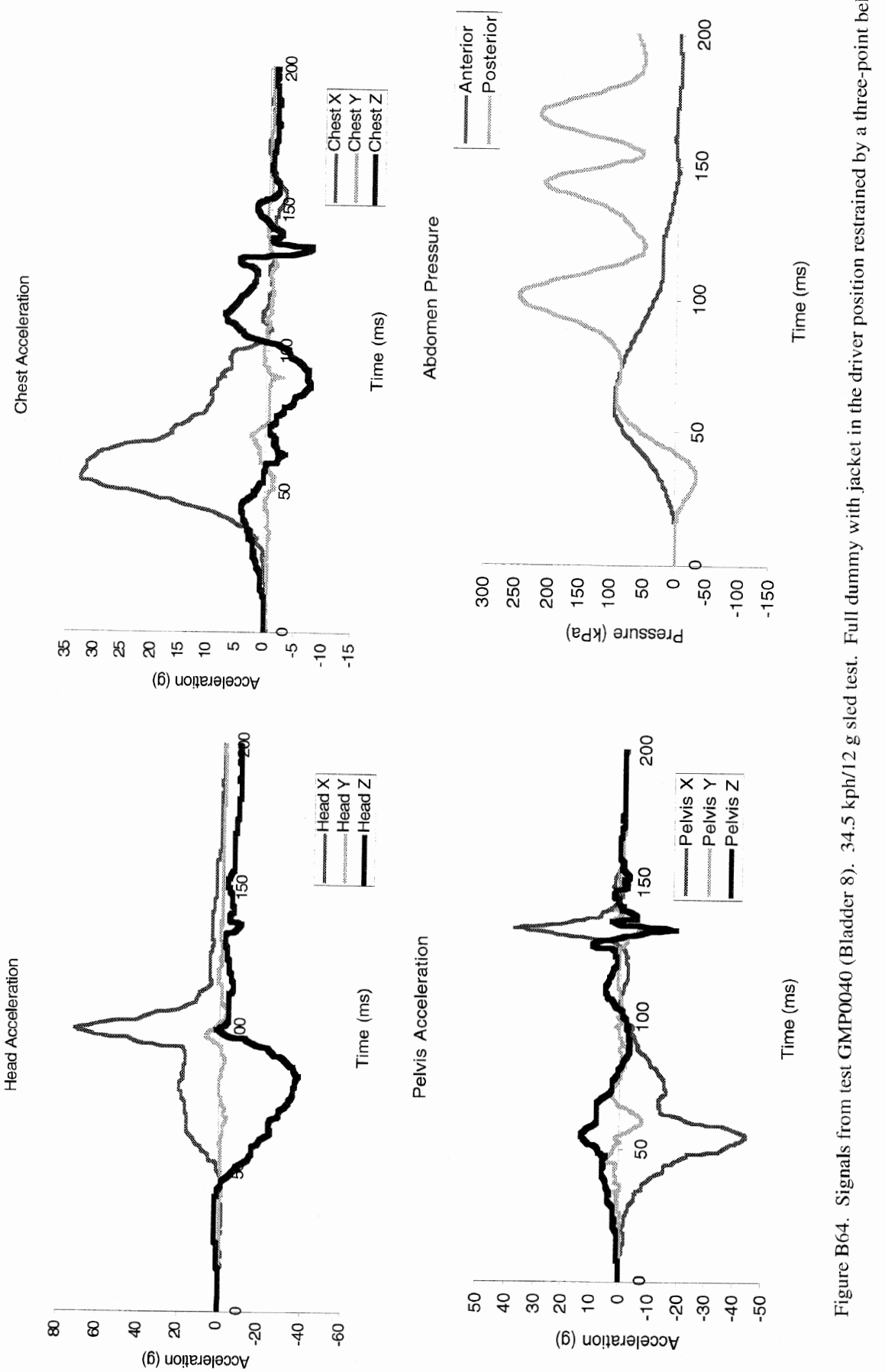

Figure B64. Signals from test GMP0040 (Bladder 8). 34.5 kph/12 g sled test. Full dummy with jacket in the driver position restrained by a three-point belt.

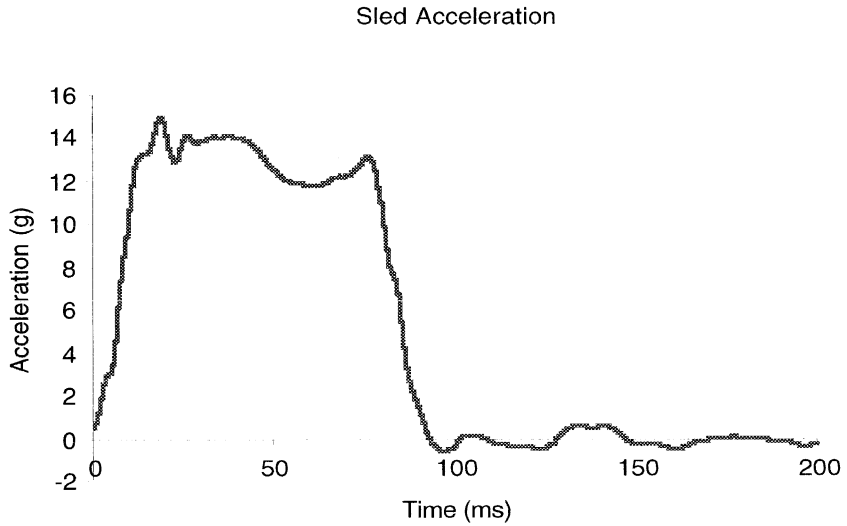

Figure B65. Signals from test GMP0040 (Bladder 8). 34.5 kph/12 g sled test. Full dummy with jacket in the driver position restrained by a three-point belt.

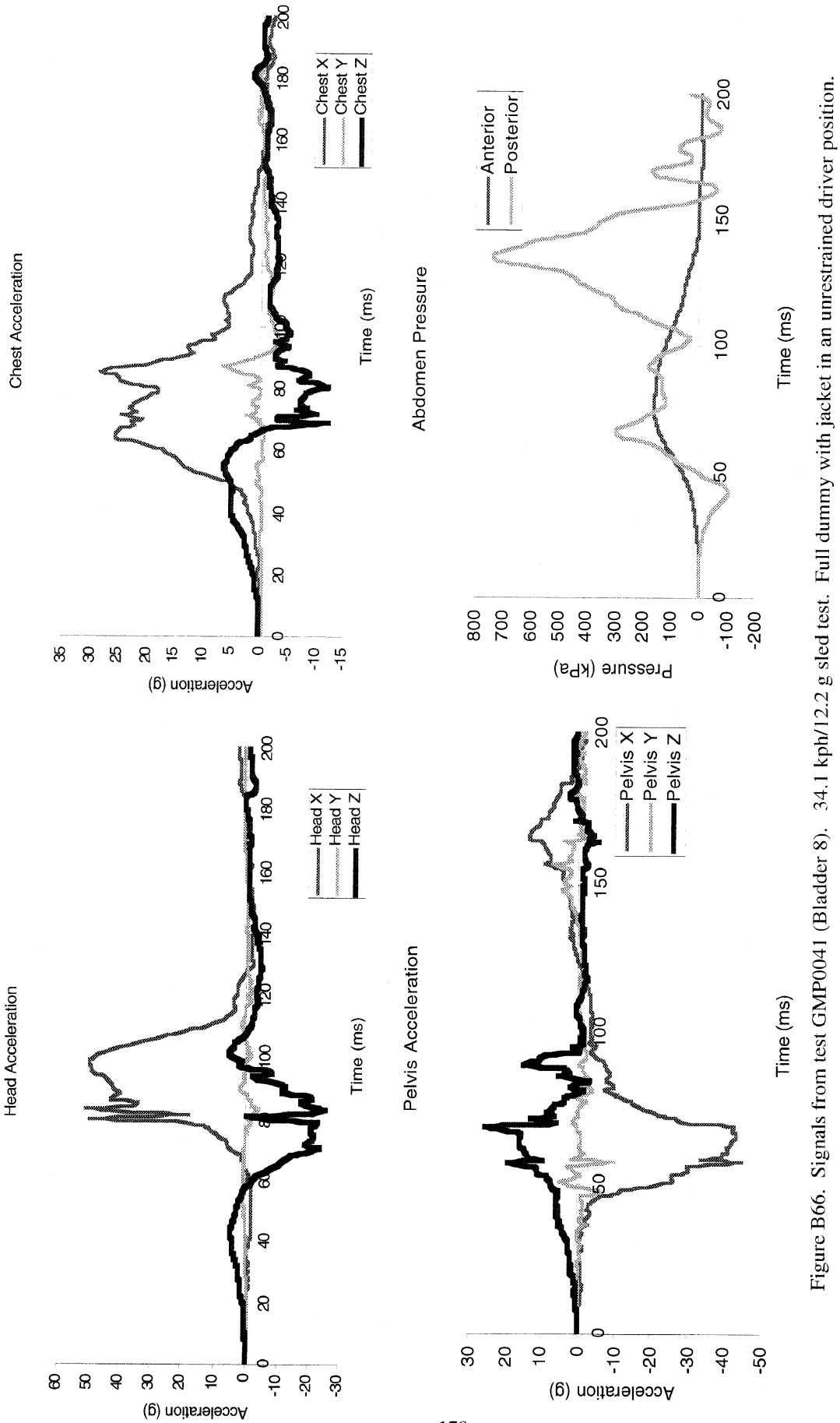

Figure B66. Signals from test GMP0041 (Bladder 8). 34.1 kph/12.2 g sled test. Full dummy with jacket in an unrestrained driver position.

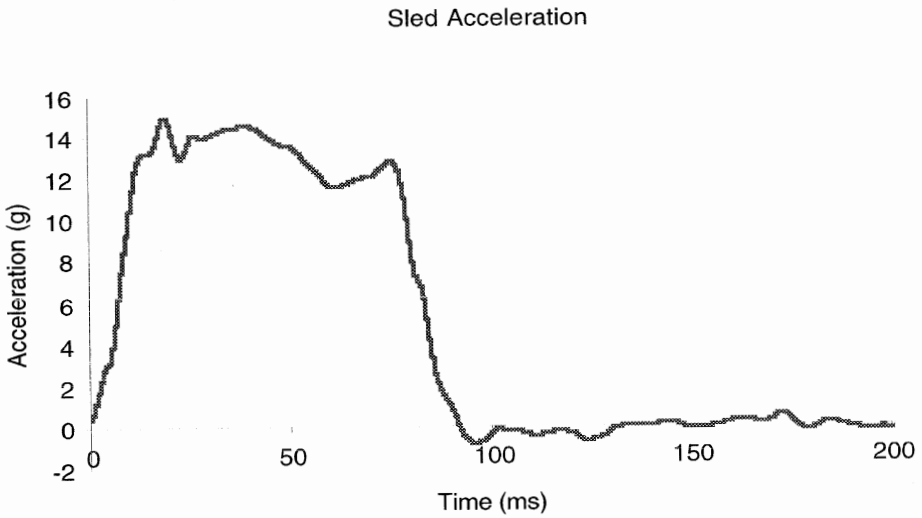

Figure B67. Sled acceleration from test GMP0041 (Bladder 8). 34.1 kph/12.2 g sled test. Full dummy with jacket in an unrestrained driver position.

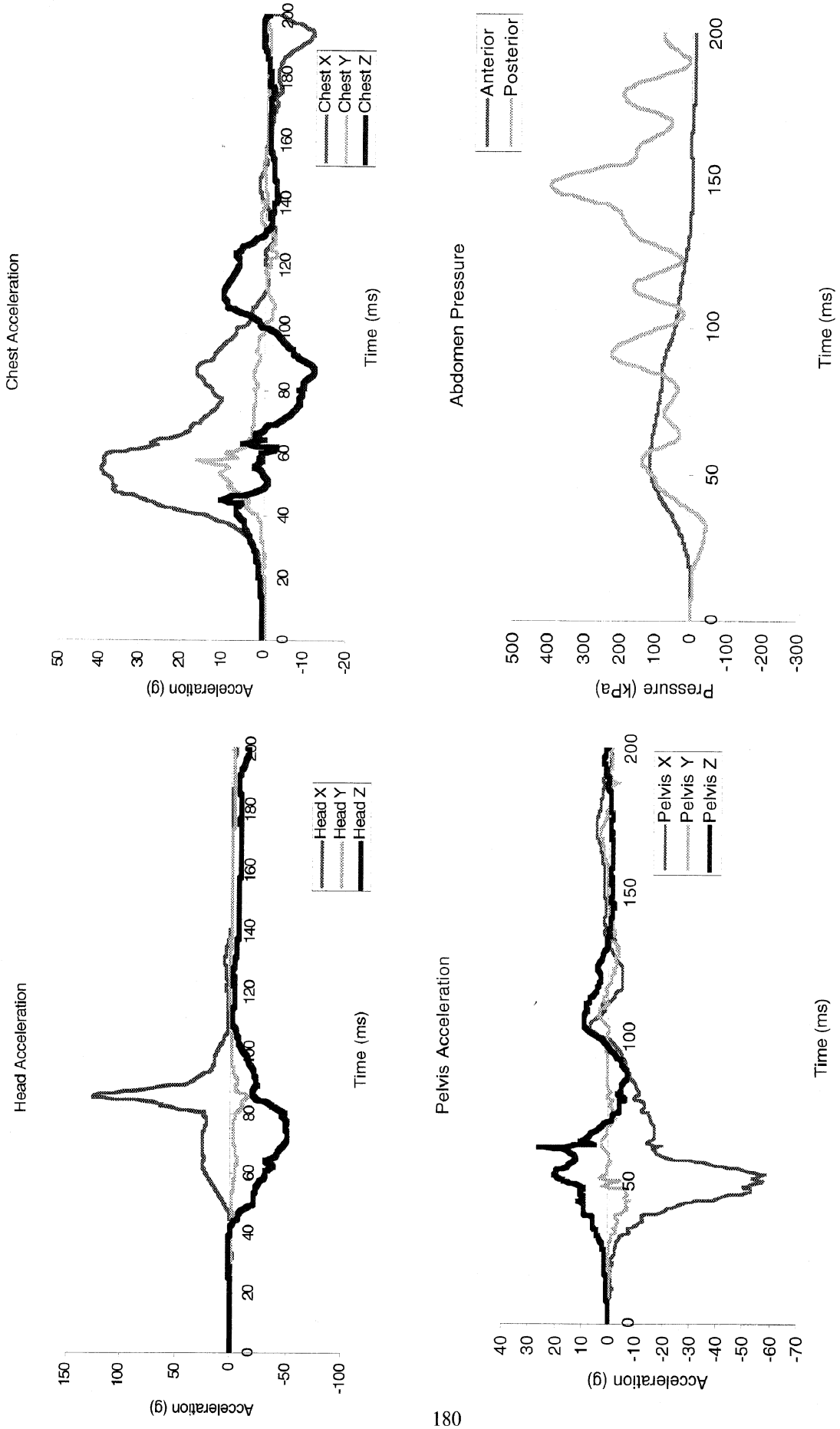

Figure B68. Signals from test GMP0042 (Bladder 8). 46.8 kph/15.7 g sled test. Full dummy with jacket in the driver position restrained by a three-point belt.

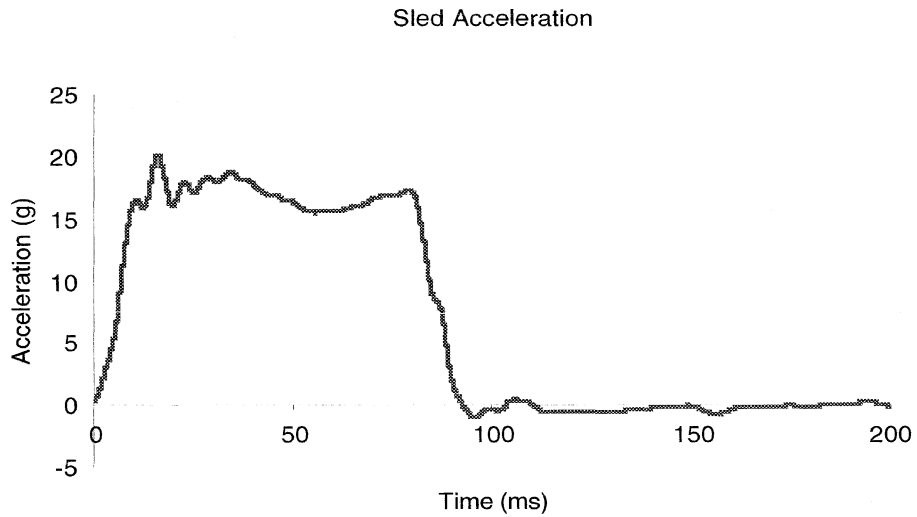

Figure B69. Sled accelerations from test GMP0042 (Bladder 8). 46.8 kph/15.7 g sled test. Full dummy with jacket in the driver position restrained by a three-point belt.

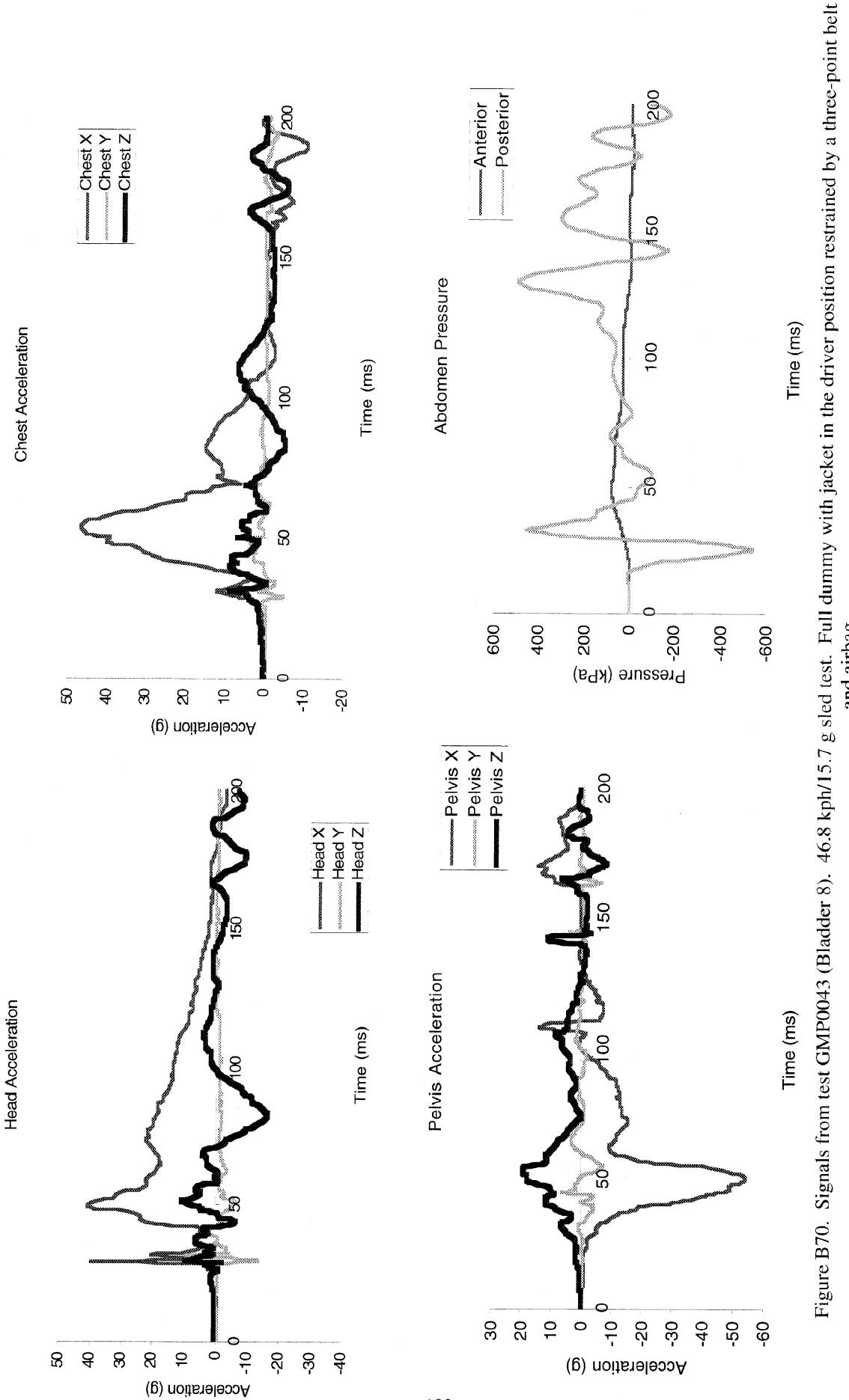

Figure B70. Signals from test GMP0043 (Bladder 8). 46.8 kph/15.7 g sled test. Full dummy with jacket in the driver position restrained by a three-point belt and airbag.

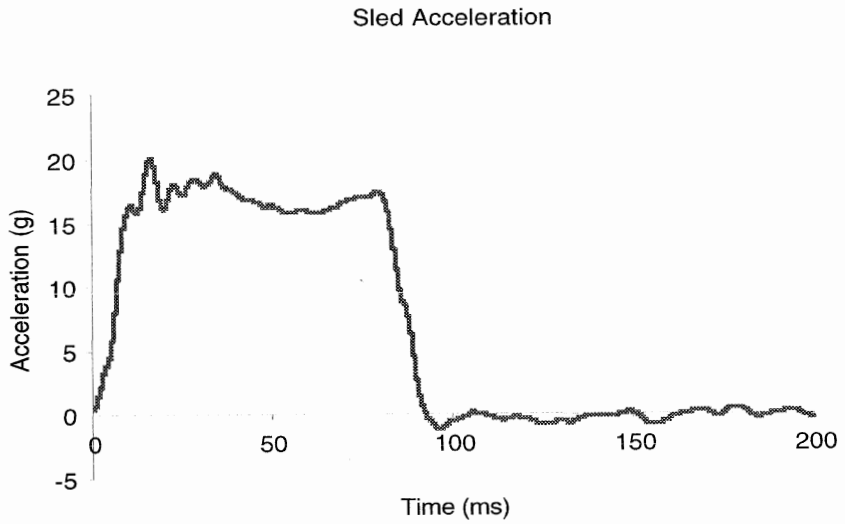

Figure B71. Sled acceleration from test GMP0043 (Bladder 8). 46.8 kph/15.7 g sled test. Full dummy with jacket in the driver position restrained by a three point belt and airbag.

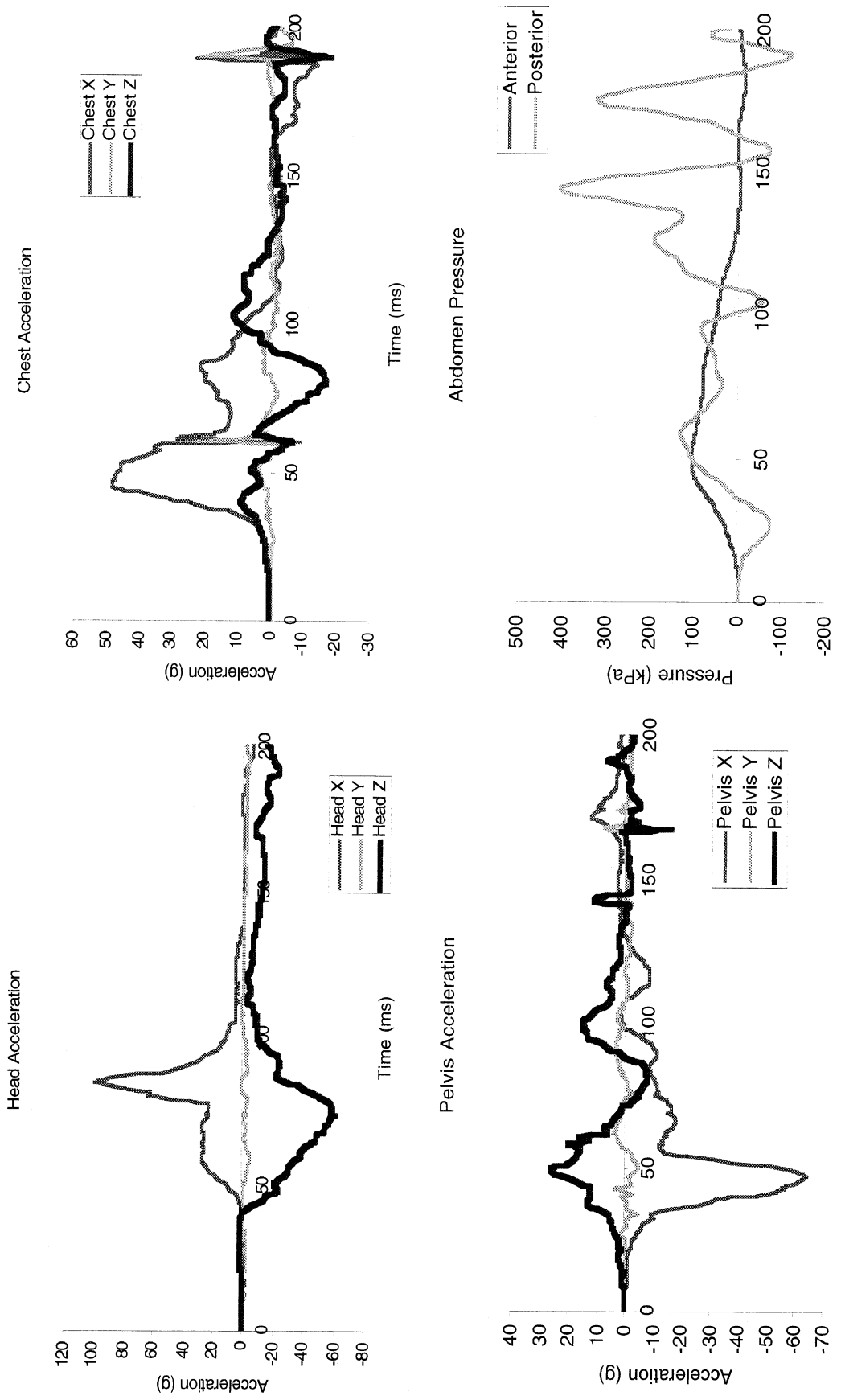

Figure B72. Signals from test GMP0044 (Bladder 8). 52.3 kph/17.4 g sled test. Full dummy with jacket in the driver position restrained by a three-point belt.

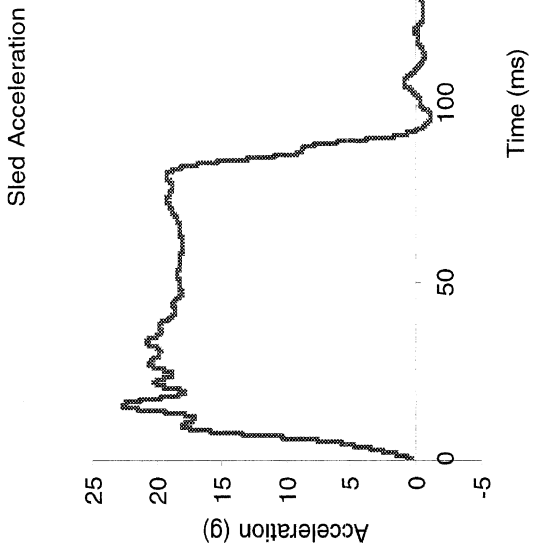

Figure B73. Signals from test GMP0044 (Bladder 8). 52.3 kph/17.4 g sled test. Full dummy with jacket in the driver position restrained by a three-point belt.

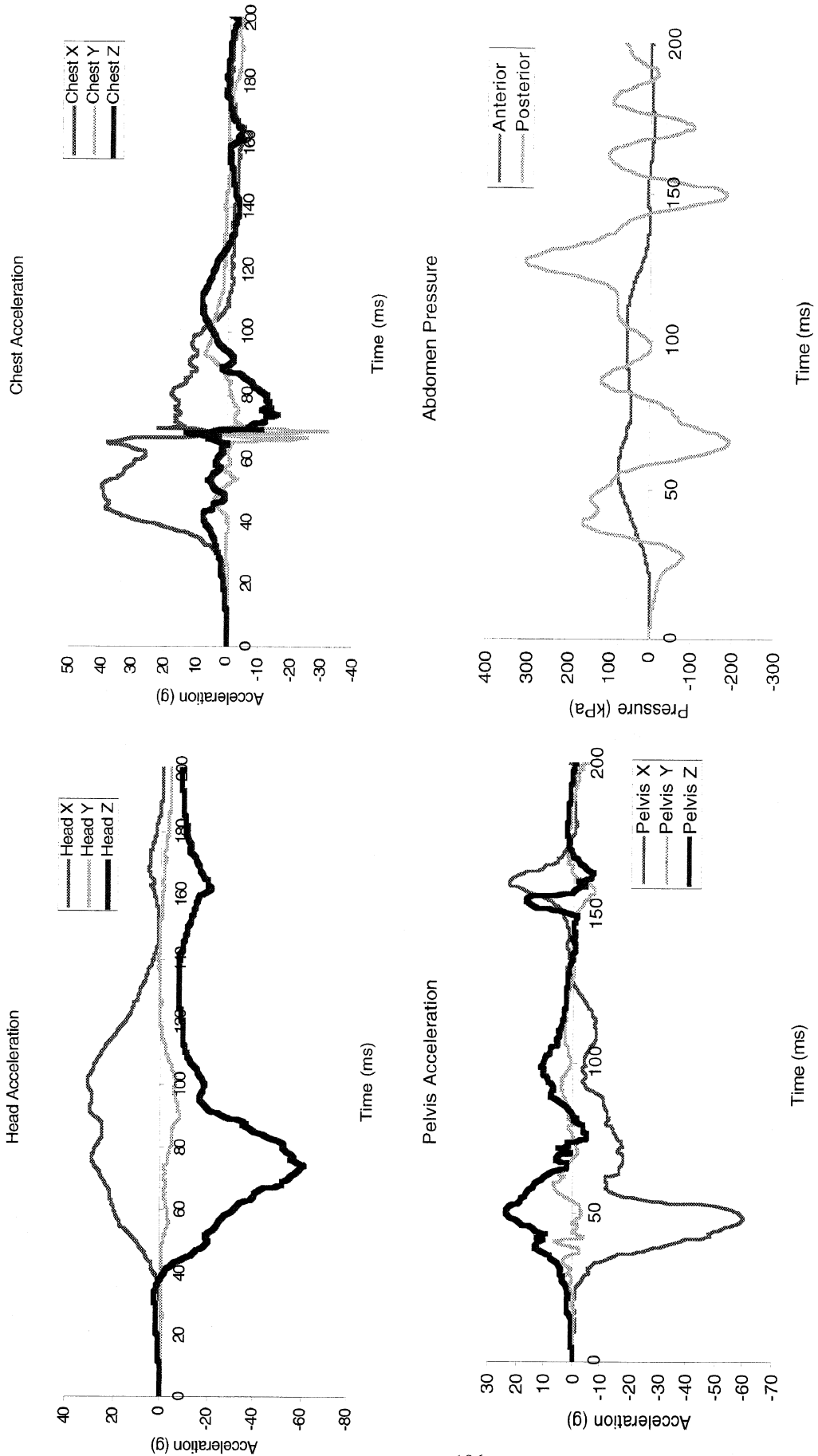

Figure B74. Signals from test GMP0045 (Bladder 8). 52.6 kph/17.5 g sled test. Full dummy in jacket in the passenger position restrained by a three-point belt.

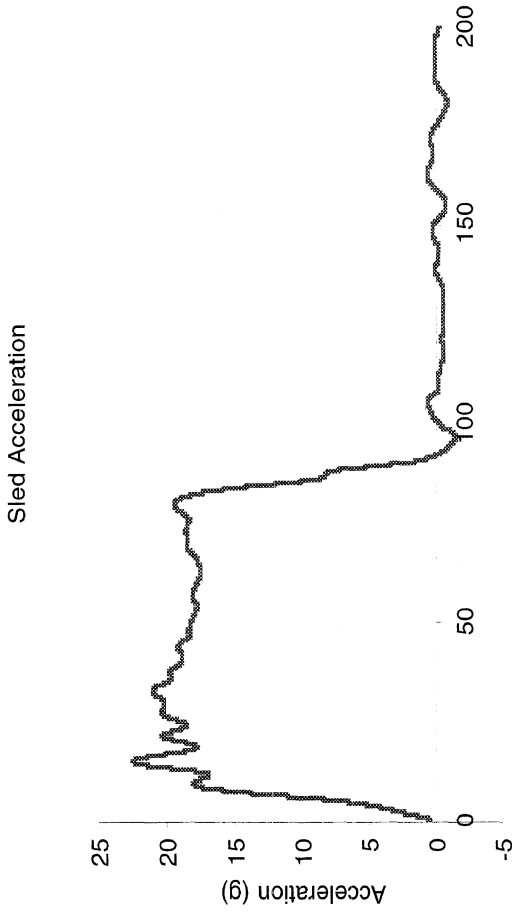

Figure B75. Sled acceleration from test GMP0045 (Bladder 8). 52.6 kph/17.5 g sled test. Full dummy in jacket in the passenger position restrained by a three-point belt.